KU LEUVEN

ARENBERG DOCTORAL SCHOOL
Faculty of Engineering Science

The effects of particles on the dynamics of sheared droplets

Helene Van Ammel

Supervisors:
Prof. dr. ir. P. Moldenaers
Prof. dr. ir. R. Cardinaels

Dissertation presented in partial fulfillment of the requirements for the degree of Doctor of Engineering Science (PhD): Chemical Engineering

June 2021

The effects of particles on the dynamics of sheared droplets

Helene VAN AMMEL

Examination committee:
Prof. dr. A. Bultheel, chair
Prof. dr. ir. P. Moldenaers, supervisor
Prof. dr. ir. R. Cardinaels, supervisor
Prof. dr. ir. M. Hendrickx
Prof. dr. ir. P. Van Puyvelde
Prof. dr. ir. S. Kuhn
Prof. Dr. ir. B. Madivala Gurappa (IIT-Madras)
Dr. ir. E. Van Hemelrijck (DSM)

Dissertation presented in partial fulfillment of the requirements for the degree of Doctor of Engineering Science (PhD): Chemical Engineering

June 2021

© 2021 KU Leuven – Faculty of Engineering Science
Uitgegeven in eigen beheer, Helene Van Ammel, Celestijnenlaan 200J box 2424, B-3001 Leuven (Belgium)

Alle rechten voorbehouden. Niets uit deze uitgave mag worden vermenigvuldigd en/of openbaar gemaakt worden door middel van druk, fotokopie, microfilm, elektronisch of op welke andere wijze ook zonder voorafgaande schriftelijke toestemming van de uitgever.

All rights reserved. No part of the publication may be reproduced in any form by print, photoprint, microfilm, electronic or any other means without written permission from the publisher.

Preface

By writing this preface and thinking back to all these good memories, I realize with a mixed feeling of relief and nostalgia, that this incredible journey is coming to an end. Of course, this journey and final thesis wouldn't be the same without the appreciated help of everybody who contributed and helped me and who I would like to thank in this preface.

I'm very grateful to my promotor Prof. Paula Moldenaers for giving me the opportunity to start a PhD, now almost 6 years ago when I was still a thesis student in the SMaRT lab. During my entire PhD, I got a lot of guidance from my co-promotor Prof. Ruth Cardinaels. Ruth, thank you for all the discussions during the weekly meetings on Friday, help with the experiments, reading of texts... I would also like to thank the members of my committee for their constructive feedback on the final manuscript.

During my research, I was able to work with different people from who I've learned a lot. During the first year, I got introduced into the world of droplet dynamics and counterrotating experiments by Dr. Yuan Mei. For the numerical simulations, I could collaborate with Prof. Simon Kuhn, Joana, and Senne. I would like to thank them for their input and the nice collaboration. During the past years, I guided several thesis students. The work of Wouter and Axel eventually became the basis for the work related to particle-filled droplets in this thesis. I would like to thank them for their effort and help with all the experimental work.

I really enjoyed working in the SMaRT lab and this was thanks to Anja and Nico who made the lab a pleasant working space as they managed the lab and were always standing by for practical help. Anja, thank you for your help and enthusiasm with the *Coole Koeler* and *Crystal trees* during P&O3. I would also like to thank Roberta for joining in this GOA-adventure. In the end, we never worked together, but I always appreciated your help and advice. The atmosphere in the SMaRT lab was always good and this was thanks to all

the SMaRT colleagues and their commitment to organize activities. I will miss the discussions during lunch breaks, the birthday cakes with cava in the afternoon, watching EK soccer in the hallway, Christmas markets and parties, Departmental dinners, beer tastings, BBQ's, lab weekends etc. Also in our office, there was always time to have a serious talk about work, let of some steam, complain, laugh or gossip. I would like to thank my office mates (Mathieu, Jasper, Moritz, An-Sofie, Alina, Charlotte, Joel, Akankshya, and Souhaila), to make our office a *sphere office* with passion hour, song of the day, cleaning (or emptying?) my desk when I was on vacation, and goodbye parties with party poppers, hats, and flags.

My colleagues have not only encouraged me in my work, but in travelling and sports as well. I don't think my high school sports teach would ever have thought that I could run 10 km, but thanks to the after work running sessions with Susanna, Anja, Jan, Irene, Maya, Jan, Avanish, Michaël, Bram, Jasper, Robin, ... I succeeded! We also spend some time together outside of Leuven, during conferences, but as well during vacations to Sweden, Portugal, Italy, ... with some memories that I will never forget! I will, for example, never forget the moment that there were suddenly 5 Christiano Ronaldo's (a.k.a. Leander, Jasper, Mathieu, Jan, and Avanish) standing in my bedroom! The highlight of these vacations was definitely the trip to India with Susanna, Greet, Jan, Mandy, Jasper, Mathieu (who I would like to thank for making the travel schedule of the entire trip with color codes and difficulty star rating included), and Avanish who I would like to thank for introducing us to India and being our tour guide and interpreter during this trip! In the past few months, I went on a few sporadic hiking trips with Robin and Susanna. Thank you, for keeping in touch in these corona times and opening up your terrace, Robin, for us on cold evenings with a warm, cosy (and smelly) fire.

Naast alle collega's op het werk, kreeg ik ook daarbuiten veel steun van vrienden en familie. Na een werkdag kon ik steeds ontspannen thuiskomen in de Paul Lebrunstraat. Céline, bedankt om steeds naar mij te luisteren na een werkdag en bedankt voor alle steun en vriendschap tijdens al die jaren (en alle jaren die nog komen). Ik stel voor dat we binnenkort (eindelijk) eens gaan brunchen in bar Stan. In het bijzonder zou ik ook graag de *Chemische Ingenieurs Toeristen* en *Furreal Friends* bedanken voor alle leuke avonden, weekendjes weg en reizen.

Mama en papa, zonder jullie onvoorwaardelijke steun was ik nooit de persoon geworden die ik nu ben. Bedankt, om steeds te zorgen voor een warme thuis in de Merellaan, steeds voor mij klaar te staan, mij al die kansen te geven en mij aan te moedigen. Charlotte, bedankt voor de gezellige tv-avondjes in Leuven en zo veel meer. Ik ben trots op je, zusje!

Tenslotte, zou ik graag nog 1 speciale persoon bedanken, ook al heb ik je al

verschillende keren hierboven vermeld. Zes jaar geleden, was jij degene die me overtuigde om te gaan informeren voor een doctoraat. ‘Want met vragen verlies je niets’, zei je. Uiteindelijk zijn we samen aan dit avontuur begonnen als collega’s. Maar je werd al snel mijn beste vriend en zo veel meer, *mijn superheld*! We hebben samen gelachen, geweend, gevloekt, ... En ook al heb je zelf ook nog een doctoraat af te ronden, toch ben je er steeds voor mij. Weet dat ik er ook steeds voor jou ben. Ik kijk er naar uit dat we samen dit hoofdstuk kunnen afsluiten met een pitcher sangria in de Werf en kunnen beginnen aan ons volgende avontuur in Kapellen.

Helene

Abstract

Polymer blending is a commonly used technique to create new polymer materials that combine the properties of their components. Polymer blends are multiphasic materials and hence, their final material properties not only depend on the type of polymers and concentration, but also on the final blend microstructure. This microstructure is formed during processing wherein a complex flow field is applied. For droplet-matrix systems, an interplay between droplet deformation, relaxation, breakup, and coalescence determines the final morphology. Hence, understanding the relation between the applied flow during processing and the structure development in polymer blends is crucial to tailor and design their material properties. Solid particles are often added to polymer blends to improve their performance, introduce an additional functionality, or manipulate the blend morphology. However, the intrinsic effects of particles on the structure development of polymer blends is still poorly understood. Therefore, the effects of particles on the structure development of blends are investigated in this dissertation by means of a fundamental study of the single droplet dynamics. The single droplet dynamics of particle-filled droplet-matrix systems are studied microscopically with a counterrotating shear cell.

The first part of this dissertation focuses on non-Brownian particles initially uniformly distributed in the droplet phase. The particle distribution development during shear flow is studied, together with the intrinsic effects of the particles on the single droplet dynamics. In this study, the matrix phase of the selected model system consists of silicon oil, whereas the droplet phase constitutes a suspension of polystyrene particles. The effects of viscosity ratio and interfacial tension are investigated by systematically varying the suspending medium of the droplet phase. The particle concentration of the suspensions ranges from 1 vol% to 20 vol%. Additionally, the effect of particle to droplet size ratio is elucidated by using different particle sizes and keeping the droplet size constant ($r/R = 0.02$, 0.1, and 0.4).

First, it was observed that particles localized inside a droplet subjected to shear flow migrate in the vorticity direction towards or away from the equatorial plane. The equilibrium particle distribution mainly depends on the system's viscosity ratio, but also the particle concentration plays a role. In contrast, the particle size and applied capillary number have no effect on the steady-state distribution, but only affect the time necessary to reach this final distribution. In order to further understand this phenomenon, numerical Volume-of-Fluid simulations of the particle-free mother system are used to identify the flow profile as well as the velocity and shear rate magnitudes to which the particles are subjected and to evaluate the presence of different possible driving forces for cross-streamline particle migration. These simulations reveal significant differences in streamline profiles and shear rate gradients which can qualitatively explain part of the observed particle migration by shear-induced migration towards zones of low shear rate and/or low streamline curvature. However, confinement inside the droplet phase, potential secondary flows, and particle disturbances probably also affect the particle cross-streamline motion. Hence, the complex flow profile inside a particle-filled sheared droplet in addition to the possible simultaneously occurrence of different migration mechanisms hampers a full quantitative understanding. In further work, it is advised to perform numerical simulations on particle-filled droplets, which is a very complex task.

Subsequently, the intrinsic effects of particles on the single droplet dynamics are systematically investigated. Therefore, the results are compared with those of reference systems with a comparable viscosity ratio. For the systems with a viscosity ratio much smaller than one, the increase in viscosity ratio caused by the addition of particles has no significant effect on the droplet dynamics. However, for the system with a viscosity ratio larger than one, the particle effects depend on the particle to droplet size ratio. The dynamics of systems with a small particle to droplet size ratio ($r/R = 0.02$) are comparable to these of the corresponding reference systems. Hence, the proposed hypothesis that the droplet can be considered as a homogenous medium characterized by its bulk viscosity governed by the particle concentration is confirmed. However, this approach is no longer applicable for higher particle over droplet size ratios. Particle-filled droplets with $r/R \geq 0.1$ behave slightly more viscous than expected based on their actual viscosity which results in more suppressed deformation and slower transient dynamics. Moreover, local particle effects such as tipstreaming resulting in particle-free satellite droplets, asymmetric, and oscillating droplet shapes are observed for particle concentrations around 15 vol% or higher. These intrinsic particle effects become more pronounced at higher particle concentrations or particle to droplet size ratios. However, no unique scaling relation could be established that captures the particle effects on the deformation, startup, retraction, and breakup behaviour of particle-filled droplets.

The second part of this work focuses on elucidating the relation between the single droplet dynamics of particle covered droplets and their interfacial properties. First, the single droplet dynamics of a silicon oil droplet covered with silica nanoparticles in a polyisobutene matrix is described. A particle network is formed at the droplet interface which is responsible for the suppression of the droplet deformation and stabilizes the droplet against breakup. Due to local instabilities in the particle network caused by the application of high capillary numbers, the droplet irregularly breaks up into several segments. Finally, the interfacial shear properties of the identical flat particle-covered interface are investigated by using a double-wall ring setup. These experiments show indeed the built-up of a viscoelastic particle network in time. However, a fully developed network is already observed after 4 h whereas, the suppression of the deformation of particle covered droplets still increases over a much longer timescale. In addition to the different time scales, also the measured yield stress does not correspond to the stress estimated to be present in the interface during droplet breakup. These results show that the interfacial shear properties alone are not able to fully quantitatively explain the observed single droplet dynamics. Hence, the dilatational properties of the particle-filled interface also play an important role. To study these effects, different material systems need to be chosen in further work.

Beknopte samenvatting

Het mengen van verschillende polymeren is een veel gebruikte techniek om nieuwe polymere materialen te creëren die de eigenschappen van hun afzonderlijke componenten combineren. Polymere blends zijn twee- of meerfasige materialen waarvan de eigenschappen niet enkel afhankelijk zijn van de verschillende types polymeren en hun concentratie, maar ook van de microstructuur of morfologie van de blend. Deze microstructuur wordt gevormd tijdens de verwerking van de materialen waarbij ze onderhevig zijn aan een complex stromingsprofiel. Een wisselwerking tussen druppelvervorming, relaxatie, opbreken en coalescentie bepaalt de morfologie voor druppel-matrix systemen. Om de eigenschappen van polymere blends op maat te maken en te ontwerpen is het zeer belangrijk om de relatie tussen de aangelegde stroming en de structuurontwikkeling in polymere blends te begrijpen. Vaste deeltjes worden vaak toegevoegd aan polymere blends om de eigenschappen te verbeteren, een extra functionaliteit toe te voegen of om de morfologie te beheersen. Maar het effect van deeltjes op de structuurontwikkeling van polymere blends is nog niet volledig gekend. Dit werk onderzoekt daarom het effect van deeltjes op de structuurontwikkeling van polymere blends door middel van een fundamentele studie van de druppeldynamica. De dynamica van druppel-matrix systemen gevuld met deeltjes wordt microscopisch onderzocht met behulp van een contraroterende afschuifcel.

Het eerste deel van dit werk focust op systemen met initieel een homogene verdeling van niet-Brownse deeltjes in de druppel. De evolutie van de deeltjesverdeling in de druppel en de intrinsieke effecten van de deeltjes op de druppeldynamica terwijl het systeem onderhevig is aan afschuifstroming worden onderzocht. De matrixfase van het onderzochte systeem is silicone olie, terwijl de druppelfase bestaat uit een suspensie van polystyreen deeltjes. Het effect van de viscositeitsratio en interfasespanning wordt bestudeerd door systematisch de vloeibare fase van de suspensie te variëren. De concentratie van de suspensies varieert tussen 1 vol% en 20 vol%. Bovendien wordt de deeltjesgrootte ook gevarieerd terwijl de druppelgrootte constant wordt gehouden om het effect van

de verhouding tussen deeltjes- en druppelgrootte te onderzoeken ($r/R = 0.02$, 0.1 en 0.4).

Wanneer een druppel gevuld met deeltjes onderhevig is aan afschuifstroming migreren de deeltjes in de vorticiteitrichting naar of weg van de centrale druppelas. De verdeling bij evenwicht is afhankelijk van de viscositeitsratio van het bestudeerde systeem, maar ook de deeltjesconcentratie speelt hierin een rol. De grootte van de deeltjes en het aangelegde capillair getal hebben geen effect op de geobserveerde deeltjesverdeling bij evenwicht. Numerieke simulaties van de deeltjesvrije systemen worden in dit werk uitgevoerd om het stromingsprofiel, snelheden en afschuifsnelheden en gradiënten in de druppels te identificeren en de verschillende mogelijke drijvende krachten voor deeltjesmigratie af te toetsen voor de verschillende bestudeerde systemen. Uit deze simulaties blijkt dat er enkele significante verschillen bestaan tussen de stromingsprofielen en afschuifsnelheden die kwalitatief deeltjesmigratie naar zones met lage afschuifsnelheid en/of kleine kromming van de stroomlijnen kunnen verklaren. Maar restrictie van de deeltjes in de druppelfase alsook potentiële secundaire stromingen en verstoring van het stromingsprofiel door naburige deeltjes hebben potentieel ook een effect op de migratie van de deeltjes in de druppel. Het complexe stromingsprofiel in een druppel gevuld met deeltjes onderhevig aan afschuifstroming en het gelijktijdig voorkomen van verschillende migratiemechanismes belemmert een volledig kwantitatieve analyse. Numerieke simulaties met druppels gevuld met deeltjes in plaats van de deeltjesvrije moedersystemen kan potentieel ook een beter begrip geven van het geobserveerde migratiegedrag. Dit is echter zeer complex, vooral bij hogere deeltjesconcentraties.

Vervolgens worden de intrinsieke effecten van de deeltjes op de druppeldynamica in detail onderzocht. De resultaten van de druppels gevuld met deeltjes worden vergeleken met deze van deeltjesvrije referentiesystemen met een vergelijkbare viscositeitsratio als de systemen met deeltjes. De resultaten zijn sterk afhankelijk van de viscositeitsratio van het onderzochte systeem. Voor de systemen met een viscositeitsratio veel kleiner dan één, heeft de stijging in druppelviscositeit door het toevoegen van deeltjes geen significant effect op de druppeldynamica. Voor het systeem met een viscositeitsratio groter dan één, is het effect van de deeltjes echter afhankelijk van de verhouding van de deeltjesgrootte tot de druppelgrootte. Voor systemen met een kleine verhouding ($r/R = 0.02$), is de druppeldynamica gelijkaardig aan deze van het deeltjesvrije referentiesysteem met een vergelijkbare viscositeitsratio. Voor deze systemen wordt de vooropgestelde hypothese dat een druppel gevuld met deeltjes beschouwd kan worden als een homogene, deeltjesvrije druppel gekarakteriseerd door de bulkviscositeit van de suspensie dus bevestigd. De bulkviscositeit van de suspensie wordt volledig bepaald door de deeltjesconcentratie. Voor druppels gevuld met grotere deeltjes is

deze hypothese echter niet langer geldig. Systemen met $r/R \geq 0.1$ gedragen zich als systemen met een iets hogere viscositeitratio dan verwacht op basis van de bulkviscositeit van de druppel. Dit resulteert in een meer onderdrukte druppelvervorming en een vertraagde transiënte druppeldynamica tijdens de opstart of relaxatie van de aangelegde stroming. Daarenboven worden ook lokale deeltjeseffecten geobserveerd voor systemen met een concentratie van 15 vol% en hoger zoals asymmetrische en oscillerende druppelvervorming alsook opbreken via *tip streaming* wat resulteert in kleine deeltjesvrije druppels. Deze geobserveerde intrinsieke deeltjeseffecten worden meer uitgesproken bij hogere deeltjesconcentraties in de druppel of een grotere verhouding van deeltjesgrootte over druppelgrootte. Er is echter geen unieke relatie gevonden om het algemene deeltjeseffect te beschrijven op zowel druppelvervorming, relaxatie als opbreken.

Het tweede deel van dit werk bestudeerd de relatie tussen de dynamica van druppels met deeltjes op de interfase en de reologische eigenschappen van de interfase bedekt met deeltjes. Eerst wordt de druppeldynamica van een silicone druppel met silica deeltjes op de interfase in een matrix van polyisobutaan gedetailleerd beschreven. Een deeltjesnetwerk wordt gevormd aan de interfase en is verantwoordelijk voor het onderdrukken van de druppelvervorming en stabiliseert de druppel tegen opbreken. Tijdens het aanleggen van hoge capillair getallen ontstaan echter lokale instabiliteiten in het deeltjesnetwerk. Deze instabiliteiten zijn verantwoordelijk voor onregelmatige druppelvervorming en het uiteindelijk opbreken van de druppel in verschillende segmenten. Tenslotte worden ook de reologische eigenschappen van de vlakke interfase bedekt met deeltjes onder afschuiving bepaald door middel van de *double-wall ring* (DWR) opstelling. Deze experimenten tonen aan dat er inderdaad een deeltjesnetwerk opbouwt aan de interfase. Maar dit deeltjesnetwerk is al volledig ontwikkeld na 4 h. Dit in tegenstelling tot het deeltjesnetwerk aan de druppelinterfase dat zich nog verder ontwikkelt na enkele dagen aangezien de vervorming na enkele dagen nog steeds verder wordt onderdrukt. Naast de verschillende tijdsschalen, komt ook de opgemeten vloeispanning niet overeen met de spanning die naar schatting aangelegd wordt op de druppelinterfase tijdens het opbreken van de druppel. Deze resultaten tonen aan dat de reologische eigenschappen van de interfasespanning onder afschuiving niet voldoende zijn om de geobserveerde druppeldynamica van druppels met een interfase bedekt met deeltjes kwantitatief te verklaren. Ook de dilatatie en bijhorende eigenschappen van de druppelinterfase spelen een belangrijke rol tijdens druppelvervorming. Om deze eigenschappen verder te bestuderen is er echter nood aan een ander model systeem.

List of Abbreviations

BBS	Bartès-Biesel and Sgaier model
CFL	Courant-Friederichs-Lewy condition
CSF	Continuum Surface Force method
DWR	Double wall-ring
MM	Maffettone-Minale model
MS	Mother system
PDMS	Poly(dimethylsiloxane)
PEG-*ran*-PPG	Poly(ethylene glycol-*ran* – propylene glycol)
PIB	Poly(isobutene)
PA6	Polyamide 6
PMMA	Polymethylmethacrylate
PP	Polypropylene
PPG	Poly(propylene glycol)
PS	Polystyrene
RS	Reference system
SEM	Scanning Electron Microscopy
VOF	Volume-of-Fluid

List of Symbols

Roman symbols

a	[m]	Radius of circulation
a_k	[m]	Fourier coefficient of approximated x-position of periodic streamline
A	[-]	Upper asymptote in Gompertz function
A'	[-]	Fitting parameter
A_0	[-]	Dimensionless constant in the Arrhenius equation
A_H	[J]	Hamaker constant
b_k	[m]	Fourier coefficient of approximated y-position of periodic streamline
B	[m]	Minor axis of deformed droplet in velocity-velocity gradient plane
Bo	[-]	Boussinesq number
c_k	[m]	Fourier coefficient of approximated z-position of periodic streamline
Ca	[-]	Capillary number
Co	[-]	Courant number
d	[m]	Gap height
d_p	[m]	Particle diameter
D	[-]	Deformation parameter
D_0	[m^2/s]	Diffusivity
D_i	[-]	Artificial divergence added to velocity component u_i
E	[Pa]	Young's modulus
$\mathbf{E}$	[s^{-1}]	Rate of deformation tensor
E_a	[J/mol]	Activation energy
f_1	[-]	Scalar coefficient in MM model
f_2	[-]	Scalar coefficient in MM model
F	[-]	Scalar second order coefficient in the model of Greco

$\mathbf{F}$	[N/m^3]	Volumetric interfacial tension force
F^{b}	[N]	Brownian force
F^{g}	[N]	Gravitational force
F^{h}	[N]	Hydrodynamic force
F^{VDW}	[N]	Van der Waals force
g	[m^2/s]	Gravitational acceleration
g($\mathbf{S}$)	[-]	Volume conservation parameter in MM model
G	[m]	Characteristic length scale of DWR geometry
G'	[Pa]	Elastic modulus
G"	[Pa]	Viscous modulus
G'_{s}	[Pa $\cdot$ m]	Interfacial elastic modulus
G"$_{\mathrm{s}}$	[Pa $\cdot$ m]	Interfacial viscous modulus
h	[m]	Particle layer or membrane thickness
H	[m]	Gap height
H_{b}	[m]	Height of simulation domain
$\mathbf{I}$	[-]	Second rank unit tensor
k	[s^{-1}]	Slope at inflection point of Gompertz function
k_{B}	[m^{2}kg/s^{2}K]	Boltzmann constant
K	[-]	Flux coefficient
L	[m]	Major axis of deformed droplet in the velocity-velocity gradient plane
L_{b}	[m]	Length of simulation domain
L_{g}	[m]	Projection of L in the velocity gradient direction
L_{p}	[m]	Projection of L in the velocity direction
$\mathbf{n}$	[-]	Normal vector
N	[m^2/s]	Particle flux
M_{n}	[g/mol]	Number average molecular weight
p	[Pa]	Pressure
r	[m]	Particle radius
R	[m]	Droplet radius
R_{g}	[J/(mol $\cdot$ K)]	Universal gas constant
Re_{p}	[-]	Particle Reynolds number
$\mathbf{s}$	[m]	Vector with same direction as $\mathbf{u}$
s_2	[-]	Scalar of second order coefficient in the model of Greco
s_3	[-]	Scalar of second order coefficient in the model of Greco
t	[s]	Time
$\mathbf{S}$	[m^2]	Droplet shape tensor
t_{b}	[s]	Breakup time
t_{f}	[s]	Final time or end time
t_{i}	[s]	Time at inflection point of Gompertz function and characteristic startup time
T	[K]	Temperature
u	[m/s]	(Relative) velocity

$\mathbf{u}$	[m/s]	Velocity field
v	[m/s]	Sedimentation or creaming velocity
$v_{\mathrm{r,centr}}$	[m/s]	Centripetal radial migration velocity
v_{θ}	[m/s]	Tangential velocity
W	[m]	Droplet axis of deformed droplet in the vorticity direction
x	[m]	First Cartesian coordinate
$\mathbf{x}$	[m]	Position vector of streamline
$\mathbf{x_r}$	[m]	Position vector of streamline of reversed velocity field
y	[m]	Second Cartesian coordinate
Y	[-]	Normalized grayscale value
$\mathrm{Y}_{\mathrm{rescaled}}$	[-]	Rescaled normalized grayscale value
z	[m]	Third Cartesian coordinate

Greek symbols

α	[-]	Phase indicator function
β	[-]	Exponent in viscosity - molecular weight relationship
γ	[-]	Strain
$\dot{\gamma}$	[s^{-1}]	Shear rate
$\Gamma_{(\mathrm{ij})}$	[N/m]	Interfacial tension (between phases i and j)
Γ_{i}^{d}	[N/m]	Polar component of the surface energy of component i
Γ_{i}^{p}	[N/m]	Dispersive component of the surface energy of component i
Δd	[m]	Distance between two particles
Δx_{c}	[m]	Side length of cubic simulation cells
ζ	[rad]	Angle between velocity vector $\mathbf{v}$ and vector $\mathbf{s}$
η	[Pa·s]	Viscosity
η_{s}^{*}	[Pa·s·m]	Interfacial complex viscosity
θ	[°]	Orientation angle
κ	[m^{-1}]	Curvature
λ	[-]	Viscosity ratio
ρ	[$\mathrm{kg/m}^3$]	Density
σ	[Pa]	Stress
τ	[s]	Characteristic relaxation time
τ_{E}	[s]	Emulsion time
τ_{M}	[s]	Characteristic time for particle migration
ϕ	[rad]	Angle periodic streamline
Φ	[-]	Volume fraction
Φ_{max}	[-]	Maximum packing fraction
ω	[rad/s]	Angular frequency
$\omega_{(\mathrm{ij})}$	[-]	Wetting parameter (between phases i and j)
$\mathbf{\Omega}$	[s^{-1}]	Vorticity tensor

Subscripts

0	Initial, at time zero
app	Apparent
b	Bottom bulk phase
c	Collision frequency gradients
corr	Corrected
crit	Critical
d	Droplet phase
eff	Effective
f	Fluid
i	Interface
l	Largest molecular weight grade
m	Matrix phase
p	Particle
r	Relative
s	Smallest molecular weight grade
ss	Steady-state
t	Top bulk phase
x	In the x-direction
y	In the y-direction
z	In the z-direction
η	Viscosity gradients
κ	Curvature gradients

Contents

Abstract v

Beknopte samenvatting ix

List of Abbreviations xiii

List of Symbols xv

Contents xix

List of Figures xxiii

List of Tables xxxi

1 Introduction 1

2 State of the art 7
2.1 Single droplet dynamics of systems with Newtonian components 8
2.1.1 Dimensionless numbers 8
2.1.2 Models 10
2.1.3 Flow profile inside a sheared droplet 13
2.2 Suspensions 14
2.2.1 Forces 14
2.2.2 Rheology 17
2.2.3 Particle migration 18
2.3 Droplet-matrix systems containing particles 21
2.3.1 Effects of particles in concentrated polymer blends . . . 21
2.3.2 Effects of particles on the single droplet dynamics . . . 24
2.3.3 Particle motion inside a sheared droplet 30
2.4 Conclusion 32

3 Materials and methods **35**
3.1 Materials . . . 35
3.1.1 Requirements . . . 35
3.1.2 Droplet and matrix phases . . . 36
3.1.3 Particles . . . 38
3.2 Suspensions . . . 39
3.2.1 Preparation . . . 39
3.2.2 Rheological characterization . . . 40
3.3 Droplet-matrix systems . . . 43
3.3.1 Mother and reference systems . . . 43
3.3.2 Particle systems . . . 44
3.4 Experimental setup and protocol . . . 48
3.4.1 Single droplet experiments . . . 48
3.4.2 Interfacial shear rheology . . . 52
3.4.3 Interfacial dilatational rheology . . . 53
3.5 Numerical simulations . . . 54
3.5.1 Theory: Governing equations . . . 54
3.5.2 Simulation domain and boundary conditions . . . 55

4 Migration of non-Brownian particles localized inside sheared droplets **59**
4.1 Particle distribution . . . 60
4.1.1 Steady-state particle distribution . . . 60
4.1.2 Time evolution of particle distribution . . . 63
4.1.3 Low particle concentrations . . . 69
4.2 Numerical simulations . . . 71
4.2.1 Steady-state deformation . . . 71
4.2.2 Velocity and shear rate profiles inside a sheared droplet 72
4.3 Possible underlying mechanisms . . . 77
4.4 Conclusion . . . 82

5 Dynamics of sheared droplets filled with non-Brownian particles **85**
5.1 Effect of particle distribution . . . 86
5.2 System with $\lambda > \mathbf{1}$ . . . 87
5.2.1 Determination of actual particle concentration . . . 87
5.2.2 Steady-state deformation and orientation . . . 89
5.2.3 Transient droplet deformation after startup of shear flow 94
5.2.4 Droplet retraction after cessation of shear flow . . . 96
5.2.5 Droplet breakup . . . 99
5.2.6 Comparison of different particle effects on droplet dynamics 104
5.3 System with $\lambda < \mathbf{1}$ . . . 107
5.3.1 Steady-state deformation, transient dynamics and droplet breakup . . . 107
5.4 Conclusion . . . 111

6 Effects of nanoparticles localized at the droplet interface 113
6.1 Effects on single droplet dynamics 114
6.1.1 Apparent interfacial tension 114
6.1.2 Steady-state deformation 115
6.1.3 Droplet breakup 117
6.1.4 Hysteresis effect 119
6.2 Link with rheological properties of the particle-covered interface 121
6.2.1 Interfacial shear rheology 122
6.2.2 Dilatational rheology 131
6.3 Conclusion 131

7 Conclusions and outlook 133

A Materials and Methods 141
A.1 Estimation of wetting parameter 141
A.2 Settling velocity of non-Brownian PS particles 142
A.3 Conservation of volume equation and the equations for projection of an ellipsoid on a plane 143
A.4 Second order coefficients in the model of Greco 143
A.5 Calculating closed streamlines from a coarse mesh velocity field 144
A.5.1 Ensuring periodic orbits 145
A.5.2 Providing the initial guess 146
A.5.3 Validation with an analytical result 147

B Migration of non-Brownian particles localized inside sheared droplets 149
B.1 Steady-state particle distribution of MS-1.4 with intermediate particle concentrations 149
B.2 Particle distribution after cessation of shear flow 150
B.3 Numerical simulations: velocity field 151
B.4 Numerical simulations: vorticity magnitude 152

C Effects of nanoparticles localized at the droplet interface 153
C.1 Hysteresis effect 153

Bibliography 155

Curriculum 173

List of Figures

1.1 Schematic representation and microscopic image of a binary polymer blend with (a) droplet-matrix and (b) co-continuous morphology. 2
1.2 Schematic representation of single droplet dynamics: droplet deformation, retraction, coalescence, and breakup of (a) particle-filled droplet and (b) droplet with particles localized at the interface. 3
1.3 Examples of oil/water emulsions including particles. (a) Oil-water emulsions used in food applications to encapsulate different types of active ingredients. Figure adapted from [142]. (b) Schematic representation of the process to create colloidosomes from oil-water emulsions and assembly of particles at the oil-water interface. Figure adapted from [36]. (c) Illustration of the use of an acoustic field to increase the particle concentration inside droplets. Figure adapted from [50]. 4

2.1 Schematic representation of an ellipsoidal droplet during shear flow in (a) top and (b) side view. 9
2.2 (a) Critical capillary number as a function of viscosity ratio. (b) Schematic representation of droplet breakup by end pinching.[179] 10
2.3 Comparison of experimental dimensionless droplet axes $L/2R$, $W/2R$, and $B/2R$ with the predictions of the MM model. [180] 12
2.4 Two-dimensional streamlines in the velocity (x) - velocity gradient (y) central plane analytically determined for a nearly spherical droplet subjected to shear flow.[10] 13
2.5 Three-dimensional streamlines inside a spherical droplet subjected to shear flow ($\lambda = 1$). [158] 14
2.6 (a-b) Droplet clustering and (c) Bridging-dewetting. [120] . . . 25
2.7 Detachment of a silicon oil droplet filled with particles.[52] . . . 27

2.8 Deformation after startup of flow of a droplet (R = 41 µm) suspended in a suspension with 2.5 wt% particles. The inset illustrates the irregular droplet shapes observed due collisions between the droplet and particles. 29
2.9 Particle-covered droplets with an irregular shape. (a-b) Non-spherical droplets with buckled interface obtained by controlled volume reduction. (c) Stable ellipsoidal droplet after squeezing between two plates. 31

3.1 Example of (a) frequency sweep data (b) steady-state viscosity of two bulk suspensions. 40
3.2 Relative viscosity of bulk suspensions consisting of different suspending media at 23 °C. 41
3.3 Particle distribution of particle systems MS-1.4 + 5 vol% PS25 and MS-0.08L + 5 vol% PS25 immediately after droplet injection and respectively, 3h50 and 300 s after droplet injection. All images are taken in the top view (velocity - vorticity plane). No shear flow is applied (Ca = 0). 46
3.4 SEM images of the particles present at the PDMS surface after curing of the PDMS bottom layer and removal of the PIB bulk suspension used as a top layer. 47
3.5 Schematic representation of the counterrotating setup. Adapted from [177]. 48
3.6 Schematic representation of the double wall-ring setup. Adapted from [182]. 52
3.7 Schematic representation of the simulation domain (H_b = L_b = 2 mm) and the imposed boundary conditions. The inset (a) depicts droplet isosurface and dimension. 56

4.1 Images of particle-filled droplets (5 vol% PS25) added to MS-1.4, MS-0.09 and MS-0.08L captured in the side view (velocity - velocity gradient plane). 61
4.2 Steady-state particle distribution of particle systems based on MS-1.4 subjected to shear flow with a capillary number of 0.15, 0.30, and 0.45. All images are taken in the top view (velocity - vorticity plane). 61
4.3 Steady-state particle distribution of particle systems based on MS-0.08L subjected to a shear flow with a capillary number of 0.15, 0.30, and 0.45. All images are taken in the top view (velocity - vorticity plane). 63

4.4 Steady-state particle distribution of particle systems based on MS-0.09 subjected to shear flow with a capillary number of 0.15, 0.30, and 0.45. All images are taken in the top view (velocity - vorticity plane). 64
4.5 Evolution of particle distribution as function of dimensionless time t/τ_E, with $t = 0$ s corresponding to the moment shear flow is started. 65
4.6 Rescaled grayscale data for MS-0.08L + 5 vol% PS25 (Ca = 0.30 and 0.50). The exponential fits are indicated by the dashed lines. 66
4.7 (a) Characteristic time scale τ_M for particle migration away from the central droplet axis as function of the applied capillary number Ca and (b) τ_M made dimensionless by dividing it with the respective emulsion time τ_E. 68
4.8 Steady-state particle distribution of MS-1.4 + 1 vol% PS25, MS-0.09 + 1 vol% PS25, and MS-0.08L + 1 vol% PS25. 70
4.9 Comparison of steady-state droplet deformation calculated from the numerical simulations and the experimental results for MS-1.4 (a, c, and d) and MS-0.08L (b, e, and f). (a-b) $L/2R$, $W/2R$, and $B/2R$ as function of capillary number. Droplet contours at Ca = 0.30 from numerical predictions (red line, $\alpha = 0.5$) and droplet images captured in the top view (velocity - vorticity plane) (c-e) and the side view (velocity - velocity gradient plane) (d-f). . . . 72
4.10 Velocity magnitude normalized by the maximum value in that slice and droplet contour at $t = 10$ s for MS-1.4 and MS-0.08L at Ca = 0.20, Ca = 0.30, and Ca = 0.40. Cross-sectional slices in the velocity (x)- velocity gradient (z) plane through the centre of the droplet. 73
4.11 Velocity magnitude normalized by the maximum value in that slice and droplet contour at $t = 10$ s for MS-1.4 and MS-0.08L at Ca = 0.20, Ca = 0.30, and Ca = 0.40. Cross-sectional slices in the velocity (x)- vorticity (y) plane through the centre of the droplet. 74
4.12 Velocity streamlines inside the droplet at $t = 10$ s (Ca = 0.30) calculated using the proposed algorithm (Appendix A.5) for (a-c) MS-1.4 and (b-d) MS-0.08L. (a-b) Cross-sectional slice in the velocity (x)– velocity gradient (z) plane through the centre of the droplet and (c-d) 3D representation with the cross-sectional slices through the centre of the droplet in the indicated directions. 75

4.13 Shear rate magnitude normalized by the maximum value in that slice and droplet contour at $t = 10$ s (Ca = 0.30) for MS-1.4 and MS-0.08L. Cross-sectional slices in the velocity (x)–vorticity (y) and velocity (x)-velocity gradient (z) planes through the centre of the droplet. 76
4.14 Shear rate magnitude normalized by the maximum value in the entire droplet and droplet contour at $t = 10$ s (Ca = 0.30) for systems MS-1.4 and MS-0.08L. Cross-sectional slices in the velocity (x)-velocity gradient (z) plane through $y = 16$ μm, $y = 48$ μm, and $y = 88$ μm. 77

5.1 Dimensionless parameter (($L_p/2R$)-1) normalized by its steady-state value (($L_{p,ss}/2R$)-1) as function of dimensionless time t/τ_E during droplet retraction of (a) MS-1.4 + 19 vol% PS25 and (b) MS-0.08L + 20 vol% PS25 with a random particle distribution and with a non homogenous steady-state particle distribution. . 87
5.2 (a) Dimensional droplet axes $L/2R$, $W/2R$, and $B/2R$ and (b) orientation angles θ of systems MS-1.4, RS-3.2 and MS-1.4 + 23 vol% PS25 as function of capillary number Ca. 90
5.3 Dimensional droplet axis $L/2R$ as function of the viscosity ratio λ. The full line indicates the MM model prediction. All data are for Ca = 0.30. 91
5.4 (a) Dimensionless parameter $L_p/2R$ of RS-3.2, MS-1.4 + 25 vol% PS5, MS-1.4 + 23 vol% PS25, and MS-1.4 + 20 vol% PS82 as function of dimensionless time t/τ_E after startup of shear flow. Images of MS-1.4 + 23 vol% PS25 (b-c) and MS-1.4 + 20 vol% PS82 (d-e) during steady-state shear. 93
5.5 (a) Dimensionless parameter (($L_p/2R$)-1) normalized by its steady-state value (($L_{p,ss}/2R$)-1) as function of dimensionless time t/τ_E after startup of shear flow for MS-1.4, RS-3.2 and MS-1.4 + 23 vol% PS25. (b) Dimensionless startup time t_i/τ_E as function of the viscosity ratio λ. The full line indicates the MM model prediction. All data are for Ca = 0.20. 95
5.6 (a) Dimensionless parameter (($L_p/2R$)-1) normalized by its steady-state value (($L_{p,ss}/2R$)-1) as function of dimensionless time t/τ_E during droplet retraction for MS-1.4, RS-3.2 and MS-1.4 + 23 vol% PS25. (b) Dimensionless relaxation time τ/τ_E as function of viscosity ratio λ. The full line indicates the MM model prediction. All data are for Ca = 0.20. 97

5.7 Revised Figure 5.6b with dimensionless relaxation time τ/τ_E as function of viscosity ratio λ of MS/RS and MS-1.4 + Y vol% PS25. Extra data points (stars) are added for MS-1.4 + 19 vol% PS25 which represent τ/τ_E as function of viscosity ratio λ calculated with the exact particle concentration of that specific droplet instead of the average particle concentration. The arrows indicate the shifting of these data points. 99
5.8 Images of MS-1.4, MS-1.4 + 25 vol% PS5, MS-1.4 + Y vol% PS25, and MS-1.4 + 20 vol% PS82 taken during droplet breakup at Ca_{crit} (indicated in the first column) in top view (velocity - vorticity plane). 100
5.9 Ca_{crit} at which breakup occurs as function of viscosity ratio λ. Inset: Comparison with experimental data of Grace [60]. 102
5.10 (a) Critical strain γ_{crit} and (b) critical droplet length $L_{p,crit}/2R$ at which breakup occurs as function of viscosity ratio λ. 103
5.11 Comparison of the viscosity ratio λ with a characteristic viscosity ratio λ^* determined for all particle systems MS-1.4 + Y vol% PSZ from experimental data of steady-state deformation, startup and retraction experiments. 105
5.12 Dimensionless droplet axes $L/2R$, $W/2R$, and $B/2R$ of systems RS-0.2L and (a) MS-0.09 (+ 20 vol% PS25) or (b) MS-0.08L (+ 20 vol% PS25) as function of the applied capillary number. 108
5.13 Steady-state droplet deformation parameter D as function of the viscosity ratio λ at Ca = 0.20. Experimental data points (x) of particle-free systems MS-0.08L, RS-0.2L, MS-1.4, and RS-3.2 together with results of numerical simulations (dots) taken from Mitrias et al. [117]. The full line represents the MM model predictions. 109
5.14 Dimensionless parameter ($(L_p/2R)$-1) normalized by its steady-state value ($(L_{p,ss}/2R)$-1) as function of dimensionless time t/τ_E after (a) startup of shear flow and (b) cessation of shear flow for MS-0.08L (+ 20 vol% PS25). All data are for Ca = 0.20. . . . 110
5.15 Images of MS-0.08L (+ 20 vol% PS25) taken during droplet breakup at Ca_{crit} (indicated in the first column) in top view (velocity - vorticity plane). 110

6.1 Apparent interfacial tension Γ_{app} of particle-covered droplets (MS-0.1 + 0.4 vol% silica). The dashed line indicates the minimum, Γ_{eff}. 115

6.2 Dimensionless droplet axes (a) $L/2R$, (b) $W/2R$, (c) $B/2R$, and (d) orientation angles θ of particle-covered droplets (MS-0.1 + 0.4 vol% silica) with a different residence time in the 0.4 vol% suspension of silica nanoparticles as function of effective capillary number Ca_{eff}. 116
6.3 Images of particle-covered droplets (MS-0.1 + 0.4 vol% silica) with a different residence time in the 0.4 vol% suspension of silica nanoparticles. Images are taken in the side view (velocity - velocity gradient plane) at $Ca_{eff} \sim 0.50$. 116
6.4 Example of buckling and wrinkling of the particle-covered interface. Image is taken in the top view (velocity - vorticity plane) at rest. 117
6.5 Critical effective capillary number at which breakup occurs for particle-covered droplets (MS-0.1 + 0.4 vol% silica). 118
6.6 Images of particle-covered droplets (MS-0.1 + 0.4 vol% silica) taken during droplet breakup at $Ca_{eff,\,crit}$ (indicated in table) in top view (velocity - vorticity plane). 119
6.7 Dimensionless droplet axes $L/2R$ of particle-covered droplets (MS-0.1 + 0.4 vol% silica) as a function of the effective capillary number Ca_{eff}. White data points refer to a droplet with a neat interface. Other measurements are performed with a droplet with a residence time of 9 h in the 0.4 vol% suspension of silica nanoparticles, immediately after droplet transfer (black data points), immediately after breakup of the particle network by shear (dark grey data points), and 1 week after breakup of the particle network (light grey data points). 120
6.8 Dimensionless droplet axes $L_p/2R$ of particle-covered droplets (MS-0.1 + 0.4 vol% silica) as function of dimensionless time t/τ_E. Measurements are performed with a droplet with a residence time of 9 h in the 0.4 vol% suspension of silica nanoparticles, immediately after droplet transfer (black data points) and 1 week after breakup of the particle network (light grey data points). Inset: Images of the droplets in the top view (velocity - vorticity plane) during steady-state deformation (i) immediately after droplet transfer and (ii) 1 week after breakup of the particle network. 122

6.9 Dimensionless droplet axes $L_p/2R$ of particle-covered droplets (MS-0.1 + 0.4 vol% silica) as function of dimensionless time t/τ_E. Measurements are performed with droplets with a residence time of 4.6-4.8 days in the 0.4 vol% suspension of silica nanoparticles, immediately after a failed droplet transfer. The insets show images during shear flow of the two droplets in the top view (velocity - vorticity plane). 123
6.10 Corrected interfacial loss modulus $G''_{s,\,corr}$ and storage modulus $G'_{s,\,corr}$ as function of time (strain amplitude of 0.025% and angular frequency of 0.5 rad/s). The dashed lines show the corrected interfacial moduli of the particle-free system as a reference. 124
6.11 (a) Deformation parameter D of particle-covered droplets (MS-0.1 + 0.4 vol% silica) with different residence times in the 0.4 vol% suspension of silica nanoparticles as function of the applied shear rate. The dashed lines indicate the corresponding linear fits. (b) Young's modulus E multiplied with particle layer thickness h determined according to the BBS model [9] from the deformation of particle-covered droplets (MS-0.1 + 0.4 vol% silica) with different residence times in the 0.4 vol% suspension of silica nanoparticles. 126
6.12 Corrected interfacial storage modulus $G'_{s,\,corr}$ as function of angular frequency (strain amplitude of 0.025%). Black data points are measured 10 h after addition of 0.4 vol% suspension of silica nanoparticles as the top phase, hence steady-state in particle interfacial coverage is reached. Grey data points are measured after breakup of the particle network by applying a shear rate of 1 s^{-1} for 60 s. Frequency sweep indicated by white data points is performed 10 h after breakup of the particle network. 127
6.13 Corrected interfacial loss modulus $G''_{s,\,corr}$ and storage modulus $G'_{s,\,corr}$ as function of strain amplitude (angular frequency of 0.5 rad/s). 128
6.14 Material response (strain γ) as function of time during the application of a shear stress σ to the interface (creep curves: a and c) and after the release of this step stress signal (recovery curves: b). 130
6.15 Example of surface pressure-area isotherm during compression of a particle laden interface. PDMS is used as bottom phase, while the upper phase consists of PIB with 0.1 vol% silica nanoparticles. 131

7.1 Schematic overview of the steady-state particle distributions in top view obtained after the application of shear flow. 135

A.1 comparison between the ordinary method for integrating a streamline inside a droplet (only upper half is shown here) and the proposed alternative method when the divergence is nonzero ($D_i = 0.05$) due to numerical errors in the calculated velocity field. 148

B.1 mages of particle-filled droplets (10 - 15 vol% PS25) added to MS-1.4 captured after droplet injection (random particle distribution) and after cessation of shear flow (Ca = 0.30) when steady-state particle distribution is reached. 150
B.2 Images of particle-filled droplets (5 vol% PS25) added to MS-1.4, MS-0.09, and MS-0.08L captured after cessation of shear flow (Ca = 0.30). 150
B.3 Steady-state velocity field and droplet contour at $t = 10$ s for MS-1.4 and MS-0.08L at Ca = 0.20, Ca = 0.30, and Ca = 0.40. Cross-sectional slice in the velocity (x)-velocity gradient (z) plane through the centre of the droplet. 151
B.4 Vorticity magnitude normalized by the maximum value in that slice and droplet contour at $t = 10$ s (Ca = 0.30) for MS-1.4 and MS-0.08L. Cross-sectional slices in the velocity (x)–vorticity (y) and velocity (x)–velocity gradient (z) planes through the centre of the droplet. 152

C.1 Dimensionless droplet axes $B/2R$ and $W/2R$ of particle covered droplets (MS-0.1 + 0.4 vol% silica) as function of effective capillary number Ca_{eff}. 154

List of Tables

3.1 Viscosity η at 23 °C and activation energy E_a of the particle-free droplet and matrix phases. 37

3.2 Viscosity η at 23 °C and activation energy E_a of the bulk suspensions.The particle diameter (Z µm) of the particles in the suspension is indicated in the suspension name as PSZ. . . 42

3.3 Characteristics of the particle-free mother systems and reference systems: droplet and matrix components, resulting viscosity ratios at 23 °C and interfacial tension (± standard deviation). . 43

3.4 Characteristics of the particle systems: viscosity ratios at 23 °C and interfacial tension (± standard deviation). 45

3.5 Maximum deviations $((y_{max} - y_{min})/y_{min})$ observed in steady-state deformation $L/2R$ at Ca = 0.30, characteristic startup time t_i/τ_E and relaxation time τ/τ_E at Ca = 0.20, and critical capillary number Ca_{crit} at breakup determined from experiments with 2-3 particle-free droplets or 2-6 particle-filled droplets. 52

4.1 Maximum velocity and maximum shear rate magnitudes observed inside the entire droplet domain or in a slice of the droplet at y = 0 (corresponding to Figure 4.10) or z = 0 (corresponding to Figure 4.11). 73

5.1 Revised Table 3.4 for systems based on MS-1.4 with actual average particle concentration inside the injected droplets (± standard deviation), viscosity ratios λ at 23 °C and range of viscosity ratios resulting from the variation in particle concentration using the Maron-Pierce equation (Equation 2.25) and the minimal and maximal particle volume concentrations observed. 88

A.1 Surface free energies Γ_i, polar and dispersive contributions of different polymers. Data from [175, 194]. 142
A.2 Wetting parameter ω_{12} for PS particles and different combinations of droplet and matrix phase materials estimated based on interfacial energy values found in literature. 142
A.3 Settling velocity of non-Brownian PS particles in the different systems calculated according to Stokes' law (Equation 2.18). A negative settling velocity corresponds to creaming, while a positive settling velocity corresponds to sedimentation of the particles. 143

Chapter 1

Introduction

Many common products and materials in our daily life are composed of different components mixed together. If these components are miscible, one homogenous phase is formed. In contrast, a mixture of immiscible components forms a multiphasic material. If we only consider two-phasic materials with a liquid as suspending medium, three different types can be distinguished. Suspensions consist of solid particles in the suspending medium. A specific example of a suspension is mud which contains sand particles in water. Emulsions, like mayonnaise and butter, on the other hand exist of two immiscible liquids, often water and oil. Finally, gas bubbles suspended in a liquid are called foams. The dispersed liquid or gas phase in, respectively, an emulsion or foam can be deformed by the application of a force, which is a major difference with the rigid particles in a suspension, which are undeformable [145].

Plastics are a type of materials which are ubiquitous in many products in industrial as well as household environments. By combining different types of polymers, a combination of properties or even improved properties can be achieved resulting in high performance materials without the expensive cost of synthesizing and developing a new polymer. In addition, the growing impact of plastic waste streams and their effect on the environment results in a need to recycle these plastic waste streams, which are often a mixture of different polymers, into materials which meet the stringent customer demands and create added value [23, 81, 66, 172, 103]. Hence, plastic materials consisting of a mixture of different polymer materials, so-called polymer blends, gain importance.

Most polymers are immiscible, or only partially miscible under certain conditions, due to their high molecular weight and absence of interacting groups. Therefore,

polymer blends are often multiphasic materials [23, 81, 140]. Polymer blends are processed at high temperatures in the melt phase. Hence, during processing, a polymer blend can be considered as an emulsion consisting of immiscible high viscous liquids [23]. An important difference with common water-oil emulsions is the higher viscosity of both polymeric phases and lower interfacial tension between the two phases [4].

In polymer blends, the final material properties not only depend on the type of polymers and their concentration, but also on the formed morphology or microstructure. Different types of microstructures can be identified, of which the droplet-matrix and co-continuous structures, both illustrated in Figure 1.1, are most common for binary polymer blends [66]. This work focuses on droplet-matrix structures. The phase morphology is formed during processing in the melt phase, for example in an extruder. During processing, the blend is exposed to complex flow fields. In these applied flow fields, an interplay between deformation, retraction, breakup, and coalescence, as schematically shown in Figure 1.2, determines the morphology. Thereafter, the material is cooled down to room temperature at which it will solidify and hence, the microstructure is fixed [23]. Therefore, a fundamental understanding of the relations between the applied flow field during processing in the melt phase and the droplet dynamics is crucial in order to predict and tailor the final material properties. Consequently, structure development and control in polymer blends during flow is already studied in detail [66, 170, 103].

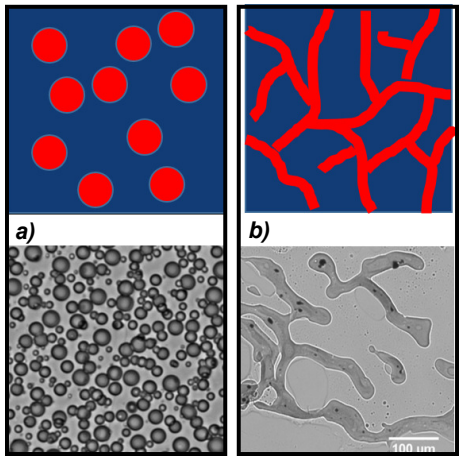

Figure 1.1: Schematic representation and microscopic image of a binary polymer blend with (a) droplet-matrix and (b) co-continuous morphology. The microscopic image in (b) is adapted from [14].

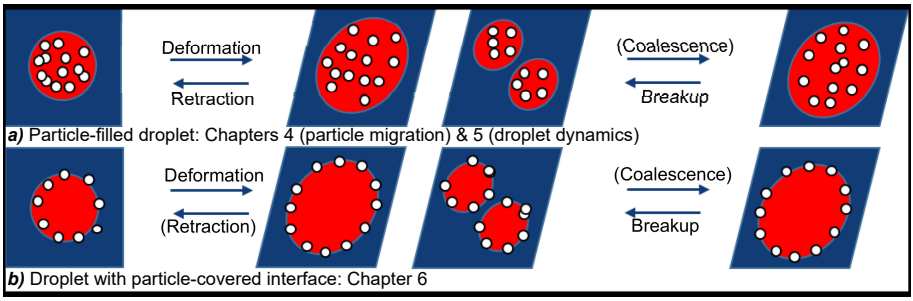

Figure 1.2: Schematic representation of single droplet dynamics: droplet deformation, retraction, coalescence, and breakup of (a) particle-filled droplet and (b) droplet with particles localized at the interface.

The incorporation of solid particles into emulsions enables the design of novel complex structures and new formulations or applications, for example for the encapsulation of active ingredients such as proteins, vitamins or flavors which is gaining importance in the food industry, but also in medical and agricultural applications [36, 142]. As illustrated in Figure 1.3a, different encapsulating strategies and resulting structures exist for oil-water emulsions depending on the nature of the active ingredient [142]. Particle-covered interfaces also occur often in the food industry to stabilize emulsions or foams. A well-known example is margarine spread in which fatty acid crystals act as stabilizers [34, 35]. However, particle-covered droplets can also be used to create colloidosomes as shown in Figure 1.3b. These are hollow, elastic capsules which can be used for the encapsulation and delivery of active ingredients [36]. In biomedical applications, particles with a functionalized surface can be used for detection of proteins for example. In order to obtain high particle concentrations, different methods are developed to increase the particle concentration inside a droplet in a microfluidic cell [25, 68, 50]. An example can be found in Figure 1.3c, where particles inside a droplet are focused with an acoustic field, resulting in higher particle concentrations when the droplet is split [50]. These techniques are also used to remove cells from their surrounding medium, for example for blood plasma analysis [68]. This last example shows that tuning the particle distribution inside droplets can be of importance.

Similar to emulsions, solid particles are also incorporated in polymer blends to improve material performance such as thermal stability [86] or to introduce an additional functionality like conductivity [75]. Furthermore, masterbatches containing inert solid particles at high concentrations are added in low amounts to a polymer matrix in industrial applications as coloring agents, stabilizers, or nucleating agents. Carbon black particles for example are often used as coloring

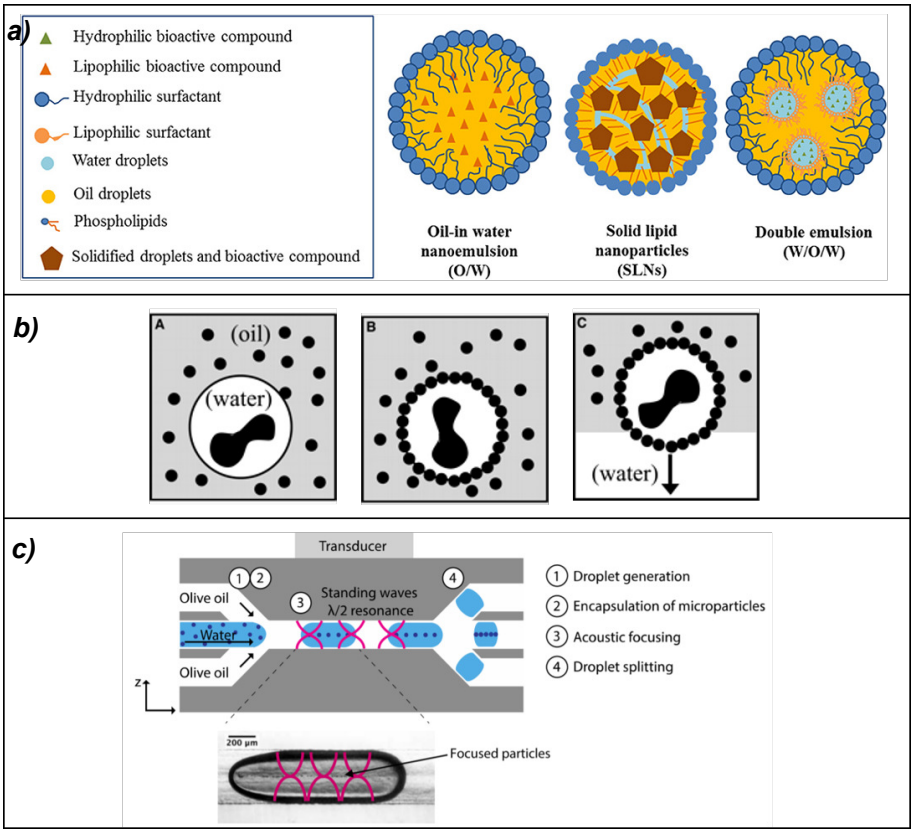

Figure 1.3: Examples of oil/water emulsions including particles. (a) Oil-water emulsions used in food applications to encapsulate different types of active ingredients. Figure adapted from [142]. (b) Schematic representation of the process to create colloidosomes from oil-water emulsions and assembly of particles at the oil-water interface. Figure adapted from [36]. (c) Illustration of the use of an acoustic field to increase the particle concentration inside droplets. Figure adapted from [50].

pigment, but also provide protection against UV-radiation. Therefore, carbon black is an often used coloring agent for polymers used in the automotive industry [94]. Masterbatches of carbon black particles dispersed at high concentrations (10 - 40 wt%) in a thermoplastic resin such as polyethylene and polypropylene are commercially available and can be added in low concentrations to different polymer matrix phases. The compatibility with the polymer matrix phase depends on the used polymer of the masterbatch. In addition, nanoparticles are

often used to manipulate the morphology as particles at the interface can refine and stabilize the blend morphology by substantially suppressing coalescence [183]. Particles can be located in the dispersed phase, matrix phase, or at the interface, but it is often difficult to predict their exact location [47]. The effects of a solid filler on the material properties depend on the particle size, concentration, localization, and the morphology [47, 144, 161]. However, a fundamental understanding of the mechanisms by which (nano)particles affect the microstructure is still lacking.

The aim of this PhD research is to study the effects of particles on the structure development of polymer blends. For this work, a model droplet-matrix polymer system subjected to simple shear flow is used. The model systems are carefully selected in order to fulfil the necessary experimental requirements and the desired location of the particles. This work focuses on the droplet dynamics (droplet deformation, retraction, and breakup) of a single droplet filled with particles (Figure 1.2a) or with a particle-covered interface (Figure 1.2b). A counterrotating shear cell equipped with an optical microscope is used in order to systematically study the single droplet dynamics in simple shear flow.

The first part of this study elaborates on droplets containing particles initially uniformly distributed in the droplet phase (Figure 1.2a). The development of the particle distribution during shear flow is studied, together with the intrinsic particle effects on the single droplet dynamics. Particles present in the droplet phase can substantially increase the droplet phase viscosity, which will also affect the droplet dynamics. Accordingly, this study focuses on the intrinsic effects of the addition of particles by comparing the particle systems with particle-free reference systems with a similar viscosity ratio. A suspension containing non-Brownian particles with Newtonian rheological behavior is used as droplet phase of the particle systems. The effects of viscosity ratio, particle size, and particle concentration are systematically studied. Additionally, the predicted velocity profiles and shear rate gradients inside the different systems are used to evaluate the possible driving forces for the particle migration behavior observed.

The main objective of the second part of this research is to study the impact of nanoparticles localized at the interface on the single droplet dynamics (Figure 1.2b), in particular on droplet deformation and breakup. Droplets with varying particle coverages at the interface are isolated and their droplet dynamics are compared. Furthermore, a double-wall ring setup is used to study the interfacial shear properties of the particle laden interface and to link the single droplet dynamics observed to these properties. Interfacial shear rheology is a useful tool to characterize the particle network and to compare different particle networks. The interfacial moduli are measured as a function of time, strain, and frequency and are compared with the Young's modulus obtained from the droplet steady-state deformation. The interfacial yield stress is also determined

by the application of creep tests and compared with the stress needed to break up the particle network in the counterrotating experiments.

The outline of this thesis is as follows. **Chapter 2** first discusses the main concepts regarding suspensions and the single droplet dynamics of particle-free polymer blend systems. Thereafter, the current state of the art concerning droplet-matrix systems containing particles is provided with the focus on particles localized in the droplet phase or at the interface. Subsequently, **Chapter 3** summarizes all different materials used in this work together with the measured properties of the droplet-matrix systems. In addition, this chapter also describes the experimental setups and followed protocols used during this research. Chapters 4, 5, and 6 present and discuss the experimental results of the different parts of this work. First, **Chapter 4** focuses on the particle migration observed in particle-filled droplets subjected to shear flow. In all systems particle migration is observed, but the final steady-state particle distribution is different. This chapter also presents the results of numerical simulations of the velocity profiles and shear rate gradients inside the droplets in order to discuss the origin of the particle migration behavior observed. **Chapter 5** quantitatively investigates the effects of particles localized in the droplet phase on the single droplet dynamics, i.e. steady-state deformation, transient deformation during startup of shear flow, droplet retraction after cessation of shear flow, and droplet breakup. The particle effects observed on the single droplet dynamics depend on the viscosity ratio of the system. Therefore, the results for the system with a viscosity ratio higher than one are first discussed. Thereafter, the results for the systems with a viscosity ratio much lower than one are presented and explained. In **Chapter 6**, the droplet deformation and breakup behavior of a droplet with its interface covered with nanoparticles is studied together with the rheological behavior of the particle covered interface subjected to shear flow or compression. Finally, the main conclusions of this work are summarized in **Chapter 7**.

Chapter 2

State of the art

This chapter introduces the main concepts and equations essential for this study by means of an extensive literature review. The first section focuses on the two-phasic system of a Newtonian droplet in a Newtonian matrix subjected to an external shear flow. This section describes the dimensionless numbers which fully determine the single droplet dynamics of such systems, followed by the most important models predicting the single droplet dynamics. The experimental data obtained in this work are compared with predictions of these models. Finally, the streamlines inside the droplet resulting from the external applied shear flow field are discussed as well.

Subsequently, the second section introduces another two-phasic system, namely suspensions, consisting of rigid particles in a fluid medium. In this work, the droplet phase consists of a suspension. The forces acting on the particles and the rheology of non-colloidal suspensions are shortly introduced. The last part of this section deals with the cross-streamline motion of particles observed when a suspension is subjected to a specific flow field.

Finally, the relevant literature available about droplet-matrix systems containing particles is reviewed in the last section. This review starts with a discussion of the general particle effects in concentrated polymer blends and continues with the effects of particles on the single droplet dynamics. The particle motion inside a sheared droplet is also discussed in this section.

2.1 Single droplet dynamics of systems with Newtonian components

2.1.1 Dimensionless numbers

The relations between the applied flow and single droplet dynamics of systems consisting of two Newtonian fluids have been studied extensively [163, 168, 134, 135, 79]. In this case, the droplet dynamics are determined by only two dimensionless numbers: the capillary number Ca and the viscosity ratio λ.

The capillary number represents the balance of the deforming viscous forces induced by the applied flow and the restoring forces of the interfacial tension. In the specific case of simple shear flow, Ca is given by:

$$\mathrm{Ca} = \frac{\eta_\mathrm{m} \cdot R \cdot \dot{\gamma}}{\Gamma} \tag{2.1}$$

with R the droplet radius, η_m the matrix viscosity, $\dot{\gamma}$ the applied shear rate, and Γ the interfacial tension.

The viscosity ratio is the ratio of the droplet phase viscosity η_d over the matrix phase viscosity η_m:

$$\lambda = \frac{\eta_\mathrm{d}}{\eta_\mathrm{m}}. \tag{2.2}$$

The characteristic time scale for droplet deformation is given by the emulsion time of the droplet:

$$\tau_\mathrm{E} = \frac{\eta_\mathrm{m} \cdot R}{\Gamma}. \tag{2.3}$$

If the applied capillary number is lower than the critical capillary number $\mathrm{Ca}_\mathrm{crit}$, the droplet starts to deform from the moment shear flow is started until a steady-state droplet shape is reached. For low and intermediate capillary numbers, this steady-state droplet shape is ellipsoidal. Figure 2.1 shows a schematic representation of a deformed droplet together with the droplet axes used to describe the droplet deformation.

The deformation parameter as first introduced by Taylor [163] is also often used to describe the steady-state droplet deformation:

$$\mathrm{D} = \frac{L - B}{L + B} \tag{2.4}$$

with L and B, respectively, the major and minor droplet axes in the velocity-velocity gradient plane (Figure 2.1). For a spherical droplet, this deformation

parameter is equal to 0. During startup of flow, the deformation parameter increases until steady-state is reached. The deformation parameter will reach a value between 0 and 1 at steady-state deformation. After cessation of shear flow, the droplet retracts back to its spherical shape and hence, the deformation parameter decreases again to 0.

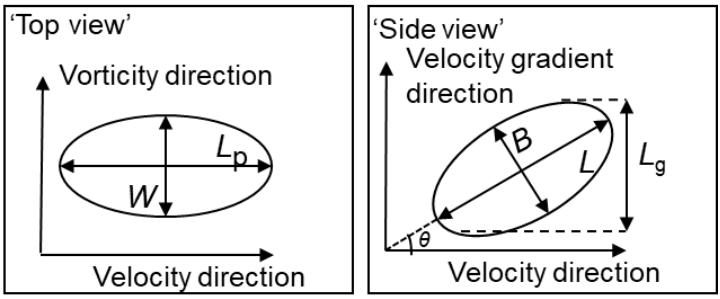

Figure 2.1: Schematic representation of an ellipsoidal droplet during shear flow in (a) the velocity-vorticity plane or top view and (b) the velocity-velocity gradient plane or side view.

When the applied capillary number exceeds the critical capillary number $\mathrm{Ca}_{\mathrm{crit}}$, the droplet will deform irreversibly until droplet breakup occurs. This critical capillary number only depends on the viscosity ratio of the system. This relationship is experimentally investigated by Grace [60]. In a later study, de Bruijn [30] numerically fitted the experimental results of Grace in shear flow in order to obtain a correlation between $\mathrm{Ca}_{\mathrm{crit}}$ and λ:

$$\log(\mathrm{Ca}_{\mathrm{crit}}) = -0.506 - 0.0994\log(\lambda) + 0.124\log^2(\lambda) + \frac{-0.115}{\log(\lambda) - \log(4.08)}. \quad (2.5)$$

A graphical representation of the de Bruijn curve and a comparison with the experimental results of Grace can be found in Figure 2.2a. A minimum in $\mathrm{Ca}_{\mathrm{crit}}$ is observed for a viscosity ratio around 0.57, while $\mathrm{Ca}_{\mathrm{crit}}$ steeply increases for larger viscosity ratios. Around a viscosity ratio of 4, droplet breakup in shear flow becomes impossible [179].

Different breakup mechanisms such as end pinching, capillary instabilities, and tip streaming are identified depending on the applied capillary number and the viscosity ratio of the system [199]. When the applied capillary number is approximately equal to $\mathrm{Ca}_{\mathrm{crit}}$, the droplet will first deform into an ellipsoid and then further stretch. Subsequently, a thinning neck at the droplet centre is

formed. Finally, the droplet will break into two equally sized daughter droplets and some smaller satellite droplets. These two daughter droplets are situated on different streamlines due to the tilted orientation of the droplet during shear flow [199]. This breakup mechanism is schematically illustrated in Figure 2.2b.

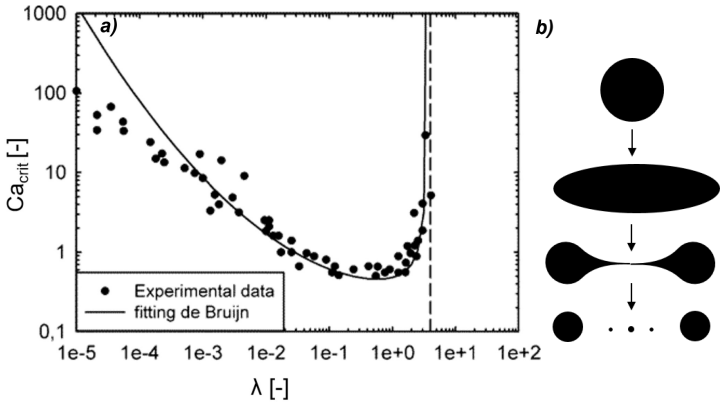

Figure 2.2: (a) Critical capillary number as a function of viscosity ratio: experimental data of Grace [60] and the de Bruijn fit [30]. Figure adapted from [179]. (b) Schematic representation of droplet breakup by end pinching ($\mathrm{Ca} \approx \mathrm{Ca}_{\mathrm{crit}}$ and $0.1 < \lambda < 4$) in the top view (velocity - vorticity plane).

2.1.2 Models

Taylor [163] was the first to develop analytical expressions of the droplet deformation D and orientation θ in shear flow by a perturbation expansion around the spherical shape:

$$\mathrm{D} = \frac{16 + 19\lambda}{16 + 16\lambda}\mathrm{Ca}, \tag{2.6}$$

$$\theta = 45^{\circ}. \tag{2.7}$$

Hence, these expressions are only valid for small deformations. Since the pioneering work of Taylor [163], numerous analytical [61, 133, 134, 8, 26, 24], phenomenological [106], and numerical [85, 79, 135] models have been developed to predict droplet deformation and orientation in shear flow.

Maffettone and Minale [106] developed a phenomenological model (MM model) which is able to describe the dynamics of ellipsoidal droplets. In this model, the droplet shape is described with a symmetric, positive-definite, second rank tensor $\mathbf{S}$ of which the eigenvalues represent $(L/2R)^2$, $(B/2R)^2$, and $(W/2R)^2$ as defined in Figure 2.1. The droplet shape and hence the evolution of $\mathbf{S}$ is determined by the competition between the viscous deforming forces and the restoring forces of the interfacial tension. By assuming that these two effects are additive and that the droplet volume is constant, following evolution equation for $\mathbf{S}$ is obtained [106]:

$$\frac{\mathrm{d}\mathbf{S}}{\mathrm{d}t} - \mathbf{\Omega}\cdot\mathbf{S} + \mathbf{S}\cdot\mathbf{\Omega} = -\frac{\mathrm{f}_1}{\tau_\mathrm{E}}(\mathbf{S} - \mathrm{g}(\mathbf{S})\mathbf{I}) + \mathrm{f}_2(\mathbf{E}\cdot\mathbf{S} + \mathbf{S}\cdot\mathbf{E}). \tag{2.8}$$

In this equation, $\mathbf{I}$ represents the second rank unit tensor, while $\mathbf{E}$ and $\mathbf{\Omega}$ are the deformation rate and vorticity tensors, respectively. Function $\mathrm{g}(\mathbf{S})$ is used for the conservation of the droplet volume.

For simple shear flow, the model predictions for the steady-state dimensionless droplet axes and orientation can be calculated with the following expressions [106]:

$$\left(\frac{L}{2R}\right)^2 = \frac{\mathrm{f}_1^2 + \mathrm{Ca}^2 + \mathrm{f}_2\mathrm{Ca}\sqrt{\mathrm{f}_1^2 + \mathrm{Ca}^2}}{(\mathrm{f}_1^2 + \mathrm{Ca}^2)^{\frac{1}{3}}(\mathrm{f}_1^2 + \mathrm{Ca}^2 - \mathrm{f}_2^2\mathrm{Ca}^2)^{\frac{2}{3}}}, \tag{2.9}$$

$$\left(\frac{B}{2R}\right)^2 = \frac{\mathrm{f}_1^2 + \mathrm{Ca}^2 - \mathrm{f}_2\mathrm{Ca}\sqrt{\mathrm{f}_1^2 + \mathrm{Ca}^2}}{(\mathrm{f}_1^2 + \mathrm{Ca}^2)^{\frac{1}{3}}(\mathrm{f}_1^2 + \mathrm{Ca}^2 - \mathrm{f}_2^2\mathrm{Ca}^2)^{\frac{2}{3}}}, \tag{2.10}$$

$$\left(\frac{W}{2R}\right)^2 = \frac{\mathrm{f}_1^2 + \mathrm{Ca}^2 - \mathrm{f}_2^2\mathrm{Ca}^2}{(\mathrm{f}_1^2 + \mathrm{Ca}^2)^{\frac{1}{3}}(\mathrm{f}_1^2 + \mathrm{Ca}^2 - \mathrm{f}_2^2\mathrm{Ca}^2)^{\frac{2}{3}}}, \tag{2.11}$$

$$\theta = \frac{1}{2}\arctan\left(\frac{\mathrm{f}_1}{\mathrm{Ca}}\right). \tag{2.12}$$

In these expressions, f_1 and f_2 are functions which only depend on the capillary number and viscosity ratio [106]:

$$\mathrm{f}_1 = \frac{40(\lambda+1)}{(2\lambda+3)(19\lambda+16)}, \tag{2.13}$$

$$\mathrm{f}_2 = \frac{5}{2\lambda+3} + \frac{3\mathrm{Ca}^2}{2+6\mathrm{Ca}^2}. \tag{2.14}$$

As illustrated in Figure 2.3, good agreement between model predictions and experimental data has been demonstrated up to intermediate capillary numbers for viscosity ratios above and below one [106, 180, 178, 63]. Therefore, the MM model is often used as a reference model as will also be the case in this work.

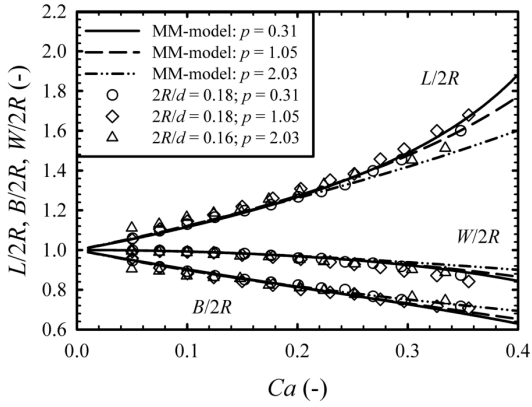

Figure 2.3: Comparison of experimental dimensionless droplet axes $L/2R$, $W/2R$, and $B/2R$ (data points) with the predictions of the MM model (lines) for 3 systems with a different viscosity ratio, indicated by p in this figure. All data points are for unconfined droplets as $2R/d$, the confinement ratio with d the gap height, is smaller than 0.2. Figure adapted from [180].

By numerically solving the set of differential equations (Equation 2.8), the MM model is also able to predict the transient droplet shapes after startup or cessation of shear flow [63]. The transient deformation parameter during droplet retraction from an ellipsoidal droplet shape towards a spherical droplet at rest can be described by a single exponential decay [63]:

$$\mathrm{D} = \mathrm{D}_{\mathrm{ss}} \exp\left(-\frac{40(\lambda+1)}{(2\lambda+3)(19\lambda+16)}\frac{t}{\tau_{\mathrm{E}}}\right) \tag{2.15}$$

with D_{ss} the deformation parameter at steady-state, just before the shear flow is stopped. A plot of $\ln(\mathrm{D}/\mathrm{D}_{\mathrm{ss}})$ versus t of different retraction experiments forms one master curve and from the slope of this straight curve, the interfacial tension of the system can be determined [63].

In addition to the analytical models, different numerical methodologies have been proposed and developed to further investigate the droplet dynamics in shear flow, including the Volume-of-Fluid method (VOF) [99, 137, 22], the Lattice Boltzmann method [51, 195, 88, 78], the Level-Set method [5, 3], and the Phase-Field method [154].

2.1.3 Flow profile inside a sheared droplet

For a system with Newtonian components, the flow profile inside a nearly spherical droplet subjected to simple shear flow is theoretically and experimentally studied in detail by several authors [169, 10, 141], who all based their analysis on the pioneering work of Taylor [162, 163]. The two-dimensional closed streamlines inside the spherical droplet are analytically calculated in the velocity - velocity gradient central plane and two different cases are identified. These two cases are visualized in Figure 2.4.

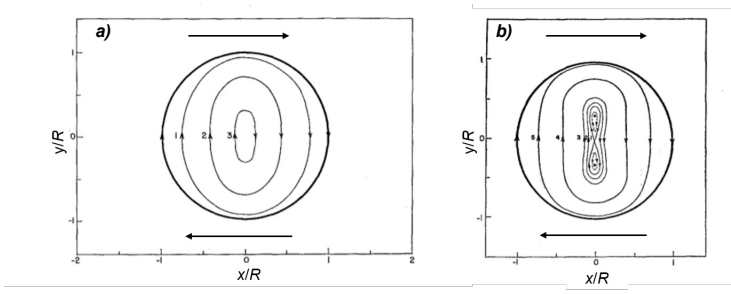

Figure 2.4: Two-dimensional streamlines in the velocity (x) - velocity gradient (y) central plane (side view) analytically determined for a nearly spherical droplet subjected to shear flow. (a) System with $\lambda > 0.5$ and (b) System with $\lambda < 0.5$. Figure adapted from [10].

For a system with a viscosity ratio higher than 0.5 ($\lambda > 0.5$), there exists one stagnation point that coincides with the droplet centre. In contrast, two stagnation points close to the droplet centre appear for systems with a viscosity ratio smaller than 0.5 ($\lambda < 0.5$) [10, 169]. The positions of these stagnation points and the shape of the streamlines become more eccentric with decreasing viscosity ratio. Outside the central plane, the eccentricity of the elliptically shaped streamlines decreases [141, 169]. Finally, Figure 2.5 shows the three-dimensional internal streamlines inside a spherical droplet subjected to shear flow, numerically calculated by Stone et al. [158] for $\lambda = 1$. During experiments by Phillips et al. [129] to investigate the internal circulation inside a droplet, tracer particles in the equatorial plane follow spherical or elliptical streamlines. However, the stagnation points and their corresponding pockets have not been observed in these experiments [129].

Kennedy et al. [85] confirmed in a numerical study that the streamlines in a deformed droplet are qualitatively similar to the streamlines calculated analytically for a spherical droplet. However, a larger droplet deformation also

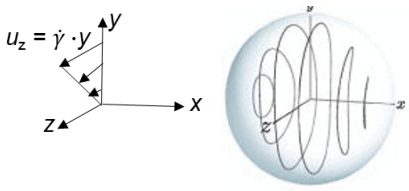

Figure 2.5: Three-dimensional streamlines inside a spherical droplet subjected to shear flow ($\lambda = 1$). x, y, and z represent in this figure the vorticity, velocity gradient, and velocity direction, respectively. Figure adapted from [158].

causes distortions in the streamline patterns. For very low viscosity ratios ($\lambda = 0.08$), the authors also noticed the existence of two near-stagnation points close to the droplet surface, which can cause the onset of internal eddies [85]. Stone et al. [157] however obtained a non-chaotic streamline pattern for a spherical droplet subjected to simple shear flow, independent of the system's viscosity ratio.

2.2 Suspensions

2.2.1 Forces

A suspension consists of particles suspended in a fluid medium. Different forces act on the individual particles or between particles in each other's vicinity. First, friction between a spherical particle moving with a constant velocity and the suspending medium results in a hydrodynamic force or drag force F^{h}, given by Stokes law [114]:

$$F^{\mathrm{h}} = 6 \cdot \pi \cdot \eta \cdot r \cdot u \tag{2.16}$$

with r the radius of the particle, η the viscosity of the suspending medium and u the relative velocity of the particle.

Depending on the density difference between the particles and the suspending fluid, the particles will settle or cream due to gravitational forces. The total gravitational force can be calculated by [114]:

$$F^{\mathrm{g}} = \frac{4}{3} \cdot \pi \cdot r^3 \cdot (\rho_{\mathrm{p}} - \rho_{\mathrm{f}}) \cdot g \tag{2.17}$$

with ρ_p and ρ_f respectively the densities of the particles and the suspending fluid, g the gravitational acceleration (9.81 $\mathrm{m/s^2}$), and r the particle radius. The creaming or sedimentation velocity v can be calculated from a force balance between the hydrodynamic drag force (Equation 2.16) and the gravitational force (Equation 2.17), resulting in [114]:

$$v = \frac{2}{9}\frac{(\rho_\mathrm{p} - \rho_\mathrm{f}) \cdot r^2 \cdot g}{\eta}. \tag{2.18}$$

The Brownian motion of the particles, which results from collisions between the particles and the suspending fluid molecules, also results in a force acting on the particles. This Brownian force is given by [114]:

$$F^\mathrm{b} = \frac{k_\mathrm{B}T}{r}. \tag{2.19}$$

with k_B the Boltzmann constant ($1.38 \cdot 10^{-23}\mathrm{m^2kg/s^2K}$), T the temperature, and r the particle radius. The average distance travelled by a particle due to this random thermal motion can be calculated by as function of the diffusion time t:

$$\lim_{t\to\infty} \langle(\Delta x(t))^2\rangle = 6 \cdot D_0 \cdot t \tag{2.20}$$

with $\langle(\Delta x(t))^2\rangle$ the mean square displacement of the particle and D_0 the diffusivity that accounts for the frictional drag. For a spherical particle this diffusion constant is given by the equation below, also known as the Stokes-Einstein-Sutherland equation [114, 139]:

$$D_0 = \frac{k_\mathrm{B}T}{6 \cdot \pi \cdot \eta \cdot r}. \tag{2.21}$$

For large non-colloical particles with a size in the micrometer range, the Brownian force can be neglected compared to the gravitational forces. In contrast, the motion of small colloidal particles with a size in the range of nanometers to one micrometer is often dominated by thermal motion and hence, the Brownian force is much larger compared to the gravitational forces. Therefore, sedimentation and creaming can often be neglected in colloidal suspensions.

Finally, also particle interactions forces should be taken into account. These interactions include hydrodynamic interactions, Van der Waals interactions, electrostatic forces, and depletion forces [114]. Hydrodynamic interactions are present in both non-colloidal as well as colloidal suspensions and are caused by the disturbance of the flow field in the vicinity of the particle which introduces hydrodynamic forces acting on the surrounding particles in the suspension.

The behavior of colloidal particles is dominated by surface forces rather than volume forces due to their large specific surface area [114, 139]. These forces can be attractive or repulsive and hence, also affect the stability of the colloidal suspension.

Van der Waals forces, dominated by dispersion forces, are always present and arise from interactions between the atoms in different particles when they come in each other's vicinity and fluctuations of the electron cloud induces polarization [114, 139]. The Van de Waals force between two identical spherical particles with radius r, separated by a distance Δd, can be calculated by:

$$F^{\mathrm{VDW}} = -\frac{\mathrm{A_H} \cdot r}{12(\Delta d)^2} \tag{2.22}$$

with $\mathrm{A_H}$ the Hamaker constant which depends on the dielectric properties of the particle material and the suspending fluid [139, 20]. These forces are attractive and act over a long range, but only dominate when the distance between the particles is small and on the order of the particle size. Consequently, colloidal particles will aggregate and eventually sediment or cream due to gravitational forces without the presence of another stabilizing mechanism [114].

The particle surface can be functionalized with charged groups or suspending particles in a polar liquid can lead to charging of the particle surface. Consequently, an electrically neutral double layer will develop and surround the particle surface. When two particles approach each other and their electrical double layers overlap, a repulsion force pushes the particles apart and hence, stabilizes the suspension against aggregation [114, 139].

Attractive depletion forces occur when two particles, suspended in a solution of macromolecules (e.g. polymer solution), approach each other. When the excluded volumes of the particles overlap, the concentration of macromolecules in the region between the particles is lower compared to that of the surrounding solution, resulting in a concentration gradient. Consequently, the osmotic pressure results in an attractive force between both particles [114, 6]. It has to be noted that the situation becomes more complex when particles are suspended in a polymer matrix [73, 74]. Finally, polymers grafted or adsorbed on the particle surface can stabilize the suspension by steric repulsion [139].

Finally, it should be noted that particles trapped at the interface can form complex 2D suspensions. In this case, additional interaction forces come into play [18, 114]. In general, additional long-range capillary interactions occur [114]. These lateral capillary forces are induced by overlap of the deformed menisci formed around two neighbouring particles [114]. The interface is deformed due to the action of a normal force on the interface. For larger non-colloidal particles, gravitational forces result in the deformation of the interface and

the capillary forces are also called flotation forces [18]. For smaller particles, these lateral capillary forces depend on the wetting properties of the particles and are also called immersion forces [91]. For two similar particles present at the interface, the capillary forces result in an attractive force between the particles. In addition, the electrostatic interactions between colloidal particles at the interface become stronger than in bulk and long-ranged [114].

2.2.2 Rheology

Non-colloidal suspensions with spherical monodisperse particles suspended in a Newtonian medium also behave as a Newtonian fluid up to moderate particle concentrations. The additional energy dissipation during flow introduced by the particles results in an increased viscosity compared to the viscosity of the suspending medium [38, 114]. This effect is characterized by the relative viscosity η_r, defined as the ratio of the suspension viscosity over the viscosity of the suspending medium. The relative viscosity is solely a function of the particle volume fraction ϕ [98, 92] and increases with particle concentration.

Einstein [40, 41] was the first to theoretically describe the relation between the relative viscosity of a very dilute suspension and the particle volume fraction ϕ:

$$\eta_r = 1 + 2.5\phi. \tag{2.23}$$

At higher particle concentrations, particle interactions will occur and influence the suspension flow and hence, viscosity. To account for these particle interactions, the relative viscosity can be determined as a Taylor expansion as function of the particle volume fraction [114]. Finally, at the maximum packing fraction ϕ_{max}, the relative viscosity curve diverges to infinity and suspension flow becomes impossible. The exact value of the maximum packing fraction depends on the particle shape, particle size distribution and the applied flow. For a random closed packing of spherical particles a value for ϕ_{max} of 0.64 can be used [38].

After the pioneering work of Einstein [40, 41], numerous semi-empirical correlations have been introduced which are all valid for a specific parameter space [38, 114]. The Krieger-Dougherty equation and the Maron-Pierce equation are two examples of these correlations which are often used to describe the relative viscosity of a non-colloidal suspension consisting of monodisperse spherical particles [114]:

$$\eta_\mathrm{r} = \left(1 - \frac{\phi}{\phi_\mathrm{max}}\right)^{-2.5\phi_\mathrm{max}}, \tag{2.24}$$

$$\eta_\mathrm{r} = \left(1 - \frac{\phi}{\phi_\mathrm{max}}\right)^{-2}. \tag{2.25}$$

At very high particle concentrations ($\phi > 0.40 - 0.45$), the flow behavior of the suspension starts to deviate from Newtonian behavior and hence, the viscosity is no longer independent of the shear rate. Additionally, at higher particle concentrations, normal stress differences become more relevant compared to shear stresses [114].

2.2.3 Particle migration

Particle migration in dilute suspensions subjected to an external flow field is a frequently discussed subject since the first observations of Segré and Silberberg [147]. No cross-streamline particle migration occurs for a neutrally buoyant suspension subjected to an unbounded, linear shear flow with no-slip conditions [153]. Segré and Silberberg [147], however, observed radial particle migration in Poiseuille flow in a tube towards an equilibrium position of 0.6 times the tube radius.

This so-called 'tubular pinch effect' can be explained by inertial effects which already appear at relatively small particle Reynolds numbers of the order $O(10^{-3})$ [148, 57]. The particle Reynolds number $\mathrm{Re_p}$ is calculated according to the formula given in Mewis and Wagner [114]:

$$\mathrm{Re_p} = \frac{\dot{\gamma} \cdot r^2 \cdot \rho_\mathrm{f}}{\eta_\mathrm{f}} \tag{2.26}$$

with ρ_f and η_f respectively the density and viscosity of the fluid phase. At these small Reynolds numbers, a particle moving in the vicinity of a wall in bounded linear flow will migrate away from this wall towards the central axis, while a particle in unbounded flow with shear rate gradients will move outward towards regions of higher shear rates [95]. Hence, particles suspended in a Newtonian fluid and subjected to a bounded flow with shear rate gradients and $\mathrm{Re_p} \sim 10^{-3} - 10^{-4}$ will accumulate at an equilibrium position due to inertia. The associated force scales with the applied shear rate to the second power ($\sim \dot{\gamma}^2$) and particle radius up to the third power ($\sim r^3$) [153, 148]. Due to inertia induced migration different coupled effects thus often result in a specific

equilibrium position depending on the applied flow field, Reynolds number, flow geometry, etc.

With increasing particle concentration, multiple particle interactions cause another migration phenomenon, also known as shear-induced migration [108] which can already be present at a particle Reynolds number of approximately zero. Particle collisions can cause the particles to deviate from their streamlines resulting in a particle flux when differences in collision frequency are present. Shear-induced migration becomes significant at higher particle concentrations and when pronounced shear rate gradients or streamline curvatures exist [96, 114]. This effect was first noticed in experiments of Gadala-Maria and Acrivos [53] where particles in a concentrated suspension migrated towards zones of low shear rate and low streamline curvature, as explained later by Leighton and Acrivos [96] and Krishnan et al. [93]. Leighton and Acrivos [96] and Abbott et al. [1] demonstrated that the migration speed in Couette flow due to shear-induced migration is proportional to the applied shear rate ($\sim \dot{\gamma}$) and particle radius to the power 2 - 2.6 ($\sim r^{2-2.6}$). Furthermore, the migration speed is a strong function of the particle concentration. However, the particle migration is independent of the suspending fluid viscosity [1].

Phillips et al. [128] composed the diffusive flux model to describe shear-induced particle migration normal to the flow direction. The model consists of two parts, each related to a different mechanism. The first term describes the particle flux N_c related to shear rate gradients and hence, differences in collision frequency:

$$N_\mathrm{c} = -\mathrm{K_c} r^2 (\phi^2 \nabla\dot{\gamma} + \phi\dot{\gamma}\nabla\phi), \tag{2.27}$$

while the second term describes the flux caused by the viscosity gradients due to the dependence on the local particle concentration (ϕ):

$$N_\eta = -\mathrm{K}_\eta \dot{\gamma}\phi^2 \left(\frac{r^2}{\eta}\right)\left(\frac{d\eta}{d\phi}\right)\nabla\phi. \tag{2.28}$$

In these equations, $\mathrm{K_c}$ and K_η are two flux coefficients of order unity and should be determined experimentally. Krishnan et al. [93] later adjusted this model with an additional term to incorporate curvature-induced migration [150]:

$$N_\kappa = -K_\kappa r^2 \dot{\gamma}\phi^2 \kappa\mathbf{n} \tag{2.29}$$

with K_κ an additional flux coefficient, κ represents the local streamline curvature and $\mathbf{n}$ is the normal vector on a curved streamline. These models describe the particle flux in unidirectional shear flows, but extension to more complex flow fields is not straightforward [128].

Furthermore, buoyancy forces, centripetal forces, secondary flows, confinement, interfaces, and a non-Newtonian suspending medium can also, directly or

indirectly, affect the trajectories of non-Brownian particles [95, 27, 69, 29]. To estimate the importance of buoyancy forces, the travel distance due to sedimentation or creaming can be estimated based on the settling velocity of a single particle according to Stokes' law (Equation 2.18). Circulation of particles introduces centripetal forces acting on the particles which can cause an additional radial motion. The corresponding migration is estimated by calculating the centripetal radial migration speed $v_{\mathrm{r,centr}}$ of a particle in simple rotational flow given by D'Avino et al. [29]:

$$v_{\mathrm{r,centr}} = \frac{2r^2(\rho_p - \rho_f){v_\theta}^2}{9a\eta}. \tag{2.30}$$

In this equation, v_θ is the tangential velocity of the particle and a represents the radius of the circular movement of the particle.

Secondary flows, defined as deviations in the flow profile from the main velocity field, can also give rise to particle migration. Moreover, due to confinement, particle motion is restricted. This confinement and the subsequent hydrodynamic interactions can also affect the particle trajectories. In addition, the jamming of particles at high particle concentrations in a certain region can inhibit further migration towards that region. Particles suspended in a non-Newtonian medium can also exhibit migration behavior induced by normal stresses or viscosity gradients [69]. In addition, particles suspended in a non-Newtonian medium align and develop string-like structures when shear flow is applied [146, 176]. Van Loon et al. [176] observed that this string formation is enhanced by normal stress differences and confinement. However, shear thinning is the key factor for particle alignment [176]. Finally, the forces and torques exerted by a deformable interface on a particle moving close to this interface can also contribute to the trajectory of that particle. A normal force directed away from the interface is exerted on a particle which translates or rotates near a deformable interface between Newtonian liquids [12].

From this overview it becomes clear that different mechanisms can be present simultaneously and can all have a different, cumulative contribution to the final particle trajectory. Consequently, complex particle distributions, which not only depend on the average particle concentration and size, but also on the Reynolds number and flow geometry, can be observed in complex flow fields. These different contributions are often difficult to separate from each other [95, 96, 1, 114, 65].

2.3 Droplet-matrix systems containing particles

Solid particles are often incorporated in polymer blends to tailor the overall material performance. The addition of particles can enhance the final material properties, such as mechanical properties [102, 189, 84, 196] or thermal stability [72, 43, 49]. Furthermore, particles can introduce additional functionalities, such as for example electrical conductivity [56, 75, 14]. Particles are also often added to control the blend morphology as they can act as compatibilizers when they are trapped at the interface [136, 198, 183, 197] and can induce cocontinuous structures [122, 49, 100]. Moreover, the presence and incorporation of particles gains importance due to the increasing fraction of recycled polymer and biocomposites [86].

Particles can be located in the dispersed phase, the matrix phase or at the interface, but it is often difficult to predict their exact location [47]. Consequently, numerous studies investigate the final blend morphology and particle distribution after blend processing. Therefore, the first part of this section focuses on the effects of particles on the morphology of polymer blends. Only a few studies report the effect of particles on the single droplet dynamics, these are discussed in the second part of this section. A distinction is made between the effects of particles present in the droplet phase, matrix phase or at the interface, respectively. Finally, the available literature about particle motions inside a sheared droplet is discussed.

2.3.1 Effects of particles in concentrated polymer blends

Particles not only cause an increase of the viscosity of the phase in which they are dispersed, they also induce other effects such as steric hindrance. As a result, particles affect the domain size, shape and stability of the dispersed phase, widen the concentration range in which a co-continuous microstructure is observed and introduce new microstructures [4, 143]. The particle effects observed depend on the nature and concentration of the blend components and particles, the particle size, shape, distribution in the blend, and their ability to form a network.

Particles can be located in the dispersed phase, the matrix phase or at the interface, but it is often difficult to predict their exact location because thermodynamic effects as well as kinetic effects can play a role [47]. The thermodynamic equilibrium position can be predicted by the interaction between the particles and the blend components, described by the wetting parameter [47, 183]:

$$\omega_{12} = \frac{\Gamma_{p1} - \Gamma_{p2}}{\Gamma_{12}} \tag{2.31}$$

with Γ_{ij} the interfacial tension between components i and j, p represents the particle, while 1 and 2 represent the two polymer components of the blend. The particles are expected to locate in phase 1 or 2 for a wetting parameter smaller than -1 or larger than 1, respectively. Intermediate values indicate an interfacial equilibrium position of the particles.

However, in order to migrate towards the equilibrium position also kinetic effects will play a role and hence, affect the final particle distribution. Therefore, component viscosity and shear history determined by mixing procedure and mixing time are also determining factors [47]. Consequently, the particle distribution and hence, blend morphology can be manipulated by thermodynamic or kinetic control [46, 131, 197, 100, 198, 71]. As a result of these various parameters and control options, numerous studies investigate the effects of the addition of a specific type of particle on the morphology of a certain polymer blend system prepared according to a specific method [4, 198, 49, 72, 90, 201, 122]. The remaining part of this section briefly discusses some general trends observed in literature, with a focus on the droplet-matrix morphology.

Particles localized in the bulk phase

In general, as already stated in section 2.2.2, the presence of particles in one of the bulk phases, matrix or droplet phase, results in a viscosity increase of the respective phase depending on the particle concentration (Equations 2.20-2.22). Additionally, the particles can also introduce other rheological flow behavior in the phases such as elasticiy by the formation of a particle network [4]. Particles present in the bulk phases can also give rise to irregular droplet shapes [122, 90, 143], a broader size distribution [59], and new microstructures [4]. Amoabeng et al. [4] systematically constructed a composition-morphology map and concluded that the effects of particles in the matrix phase stay limited, while the effects of particles in the droplet phase are larger.

Amaobeng et al. [4] and other authors [90, 72, 143, 47, 59, 84, 54] agree on the fact that the addition of particles to the dispersed phase of a polymer blend results in coarsening and an increased droplet size. According to Hong et al. [72], Kontopoulou et al. [90] and Fenouillot et al. [47], droplet breakup is hindered by the addition of particles to the dispersed phase. The particles increase the droplet viscosity and hence, the viscosity ratio λ, towards the region of inhibited or suppressed breakup [47], also indicated in Figure 2.2 of Section 2.1.1 for $\lambda > 1$. Another consequence of the reduced deformability of particle-filled

droplets is the increased efficiency of droplet collisions which also results in enhanced droplet coalescence [143]. Furthermore, co-continuous structures are more likely to develop when particles are present in the minor phase as a result of reduced droplet breakup and slower retraction due to a strong increase in droplet viscosity or elasticity [122, 4, 143, 156]. In contrast with these results, Filippone et al. [49] observed a droplet size reduction, yet only at low particle concentrations. They associated this reduction with the increased viscosity of the minor phase which hinders coalescence and coarsening. At high particle concentrations, a co-continuous structure is observed due to the formation of a particle network. Zou et al. [201] observed the opposite, i.e. a co-continuous structure at low particle concentrations and again a droplet-matrix structure at higher particle concentrations due to the formation of particle aggregates.

Particles located in the matrix phase on the other hand decrease the viscosity ratio which is expected to enhance breakup as, according to Equation 2.5, a decrease in viscosity ratio results in a smaller critical capillary number for $\lambda > 1$. This enhanced breakup results in a refined microstructure as confirmed by several studies [84, 72, 49, 90, 43, 42]. However, also coalescence is hindered due to the addition of particles into the matrix phase. Clusters of individual droplets can however be formed when particles are located in the matrix phase, but in close proximity of the droplet interface [167]. Finally, Elias et al. [43, 42] also report a reduced droplet size regardless of the location of the nanoparticles. The authors attribute this reduction to the decrease in effective interfacial tension caused by the addition of nanoparticles. However, this decrease in interfacial tension is probably caused by a small amount of nanoparticles that partially cover the droplet interface.

Particles localized at the interface

From the pioneering work of Pickering [130] it is known that particles covering the interface of oil/water emulsions can be used to stabilize the emulsion instead of surfactants. In contrast to surfactants, particles irreversibly adsorb to the oil-water interface where they form a dense film which suppresses coalescence. The three-phase contact angle which the particles make with the interface and the interfacial tension are therefore important parameters [7, 16]. An extended review about the differences between particles and surfactants as stabilizers can be found in [15].

A similar effect is observed for particles covering the interface of a polymer blend in an experimental study by Vermant et al. [187] . The authors show that the blend morphology becomes insensitive to the shear history at low particle concentrations of 1 wt% [187], and hence droplet breakup and coalescence are

altered by the particles. By shear-induced coalescence experiments, Vermant et al. [187] and other authors [183, 167, 67] demonstrate that coalescence is suppressed or inhibited in these particle-filled blends. In general, a decreased average droplet size and more uniform droplet size is found in concentrated polymer blends with particles localized at the interface [43, 72, 71, 67, 120]. Therefore, particles covering the interface can be used as a compatibilizer.

However, the stabilizing mechanisms are still unclear and under discussion [144, 2]. In most literature, the stabilizing effect and decreased droplet size is explained by the formation of a physical barrier which suppresses droplet coalescence [144, 43, 190, 67, 167, 47, 187]. In addition, the particles affect the interfacial rheology and hence, interfacial mobility and drainage during coalescence [144, 183, 187]. Finally, some authors state that a decrease in (apparent) interfacial tension is responsible for the stabilizing effect [144, 71, 47]. The modification of the interfacial tension increases the applied capillary number for a certain applied shear rate (Equation 2.1), hence droplet breakup is favoured as it occurs at lower applied shear rates. This enhanced breakup behaviour results in smaller droplet sizes [47]. Vandebril et al. [183] showed however that the formed viscoelastic interfacial particle layer is mainly responsible for the decrease in droplet size as the decrease observed in interfacial tension stayed limited for the investigated system.

Coarsening of a co-continuous blend is also suppressed by the addition of particles at the interface. By shrinkage of the interfacial area during coarsening, the particles are squeezed together at the interface until they fully cover the interfacial area and prevent further coarsening [76, 100]. In addition, a decrease in interfacial tension also stabilizes the co-continuous blend structure [122].

The effectiveness of the stabilizing effect depends on the particle size, shape, concentration, roughness, and the wetting characteristics of the particles [183, 76, 167]. It has to be noted that particle bridging can prevent further coalescence by hindering film drainage, but results in droplet clustering as illustrated in Figures 2.6a-b. Bridging-dewetting (Figure 2.6c) results in increased coalescence when particles are preferentially wetted by the dispersed phase [144, 165, 120, 121, 187].

2.3.2 Effects of particles on the single droplet dynamics

Particles localized in the droplet phase

A few studies elucidate the effects of nanoparticles localized in the dispersed phase of a polymer blend on the droplet dynamics in the blend. Gooneie

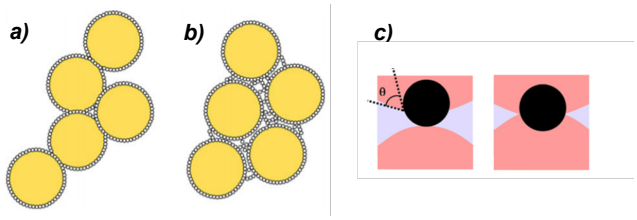

Figure 2.6: (a-b) Droplet clustering by (a) particle bridging when particles are preferentially wetted by the matrix phase and (b) particle flocculation in the matrix phase. Figure adapted from [202]. (c) Bridging-dewetting when the particle is preferentially wetted by the droplet phase. Figure adapted from [120].

et al. [58, 59] demonstrated that the addition of carbon nanotubes to the minor phase of a PP/PA6 blend suppresses droplet deformation and hinders breakup in shear flow. Droplets with a high particle load did not even deform under the applied shear rates. This increased resistance against deformation and breakup results from the elastic network formed by the nanoparticles in the droplet phase which hinders the droplet phase mobility. Additionally, the dynamics to reach a steady-state deformation are slowed down, while droplet retraction is accelerated. However, droplet retraction strongly depends on the shear history which affects the existing elastic network, and hence the elastic restoring forces [58, 59]. In contrast, Kong et al. [89] compared the theoretical calculated retraction time according to Equation 2.15 with the experimental observed retraction time and observed a retarded retraction of deformed PA6 droplets containing silica nanoparticles during annealing in a PS matrix. The dissimilarity between the results of Gooneie et al. [59] and Kong et al. [89] can be explained by the different physical origin of the elastic particle networks present in the dispersed phase [59]. Moreover, the retraction experiments by Kong et al. are performed with single droplets with a similar initial deformation, while Gooneie et al. [59] used a system with multiple droplets which have a different initial deformation [59]. Kong et al. [89] also observed an increased critical breakup aspect ratio. The authors attributed these particle effects to the improved viscoelasticity of the droplet phase introduced by the addition of nanoparticles.

Numerical simulations by Usta et al. [171] also predict a reduced droplet deformation at intermediate capillary numbers due to the additional viscous stresses introduced by the suspended particles. However, this particle effect is a function of the flow profile and the existence of an extensional flow component inside the droplet, which also depends on the droplet shape. Therefore, at low

capillary numbers when the flow profile inside the droplet is mainly rotational, the particle effect is small. At high capillary numbers, on the other hand, the applied deformational stresses dominate and hence, the extra viscous stresses introduced by the particles are negligible [171].

Besides in polymer blends, droplets encapsulating particles are also of great importance in the oil, printing, and food industry [152, 171, 33, 17, 111, 113]. Consequently, several studies focus on the droplet dynamics of water/oil systems containing particles suspended in the dispersed phase. In an early study, Powell and Mason [132] investigated the effect of high particle concentrations ($\sim$ 50 vol%) on the deformation and breakup behavior in extensional flow. Smith and Van de Ven [152] later extended this study to lower particle concentrations (0.5 vol% - 50 vol%) and simple shear flow. Both authors concluded that the effect of microsized particles is qualitatively similar to an increased fluid viscosity of the dispersed phase which is governed by the particle concentration as also stated in Section 2.2.2 (Equations 2.20-2.22), thereby resulting in a higher effective viscosity ratio. Furthermore, particles spend more time in the droplet tips during circulation at low particle concentrations. Consequently, small particle clusters are ejected from the droplet tips at shear rates that are not able to break the main particle cluster [152, 32]. This can be explained by the breakup curve in Figure 2.2 as for these system λ is smaller than one, and hence an increase in viscosity ratio by the presence of particles results in a smaller critical capillary number. However, at higher particle concentrations normal droplet breakup by end pinching (Figure 2.2) is again observed. Both studies used particles that were rather small as compared to the droplet size (particle size to droplet size ratios $r/R \sim 0.02$ - 0.11). Smith and Van de Ven [151] also performed a study with a droplet containing a single particle ($r/R \sim 0.5$) and observed an increased extension of the droplet after start-up of flow before the droplet retracts back to the steady-state deformation. When the applied capillary number is higher than the critical capillary number this behavior results in the formation of liquid threads at the droplets tips which will break up. Mehrabian et al. [111] on the other hand used higher particle over droplet size ratios ($r/R \sim 0.21 - 0.47$) at high particle concentration ($\sim$ 72 vol%) and concluded that the droplet phase can no longer be considered as a homogeneous continuum in that case. The authors concluded by variation of the viscosity ratio ($\lambda = 0.032 - 2.5$) that breakup in this case is completely governed by the viscosity of the interstitial fluid.

From studies of the detachment of droplets from a needle, it was concluded that when a thin thread is formed or when concentration gradients exist due to particle rearrangements, the droplet medium can also no longer be considered as a continuum [52, 17]. Consequently, different regimes have been identified during droplet detachment of a suspension. Figure 2.7 shows the detachment

of a particle-filled droplet in different stages. In the first stage, the system can be treated as a continuum, hence the dynamics are similar to those of a pure fluid with an increased viscosity [52, 17, 13]. Subsequently, particle rearrangements in the filament create particle-free regions which dominate and accelerate the dynamics. Furbank et al. [52], for example, noticed at higher particle concentrations (> 10 vol%) that most particles in the thin filament are forced towards the forming droplet or capillary tip. Finally, localized thinning is responsible for further accelerated droplet detachment [13, 17]. In this last regime, particles still present in the liquid thread prevent further thinning which results in shorter filaments at detachment and larger satellite droplets [174, 17, 52]. These situations also typically occur during droplet breakup, for example during breakup of droplets consisting of starch granules swollen in water and placed in a PDMS matrix phase subjected to shear flow [33]. By rearrangement of the starch granules in shear flow, the droplet can easily break up at the depleted zone between two granules which results in similar critical capillary numbers as observed for particle-free droplets with a comparable viscosity ratio. However, the yield stress present in these highly concentrated suspension droplets also inhibited breakup completely for droplets with a viscosity ratio above 0.1, at least up to the maximum applied shear stress [33].

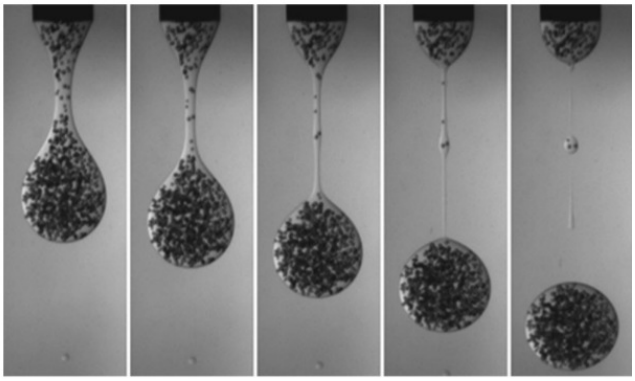

Figure 2.7: Detachment of a silicon oil droplet filled with particles. Particle radius ranges between 106 μm and 125 μm and particle concentration is equal to 5 vol%. Figure from [52].

It has to be noted that in most studies on dynamics of particle-filled droplets in shear flow, the added (nano)particles not only increase the dispersed phase viscosity, but also introduce non-Newtonian rheological behavior such as shear-thinning, viscoelasticity, and yielding [33, 32, 89, 58]. The changes observed

in deformation and breakup dynamics are then associated with these non-Newtonian properties. However, non-Newtonian behavior makes it also difficult to compare different systems at similar capillary numbers or viscosity ratios [32].

Particles localized in the matrix phase

Smith and Van de Ven [151] first studied the interactions between a single particle and a droplet. A collision of a particle with a droplet can result in a solid-liquid pair, but it is also possible that the particle and droplet separate again. The authors stated that the steady-state deformation as well as the deformation induced by the collision with the particle contribute to the total droplet deformation. Asymmetric particle trajectories due to collisions with the deformed droplet are observed. The outcome of these collisions and hence, the formation of a droplet-particle pair is however unpredictable and depends on many parameters such as the orientation and viscosity ratio [152].

In order to better comprehend the droplet dynamics in concentrated emulsions, Kaur and Leal [83] approximated the concentrated emulsion by a concentrated suspension of rigid particles and examined the effects of these particles on the deformation and breakup of a single droplet placed in this suspension. They performed an experimental study of a poly(dimethylsiloxane) (PDMS) droplet in a suspension of poly(methylmethacrylate) (PMMA) particles in planar hyperbolic flow and systematically varied the particle over droplet size ratio r/R and the particle volume fraction. The authors state that at low particle over droplet size ratios ($r/R < 0.1$) droplet deformation and breakup can be described by an effective viscosity of the suspension governed by the particle volume fraction as described in Equations 2.20-2.22, while at higher ratios the particles locally disturb the applied flow field and collide with the droplet. These last effects give rise to fluctuations in droplet deformation, asymmetric droplet shapes, asymmetric droplet breakup, increased scatter in $\mathrm{Ca}_{\mathrm{crit}}$ and a polydisperse droplet size distribution after breakup. The fluctuations increase with applied capillary number, particle concentration, and particle to droplet size ratio. An example of the fluctuations in droplet deformation and irregular droplet shapes is given in Figure 2.8 [83].

Particles localized at the droplet interface

Frijters et al. [51] performed a numerical study to investigate the effects of large particles ($r/R = 0.06$) present at the interface of a droplet subjected to shear flow. An increased droplet deformation and consequently, also enhanced droplet

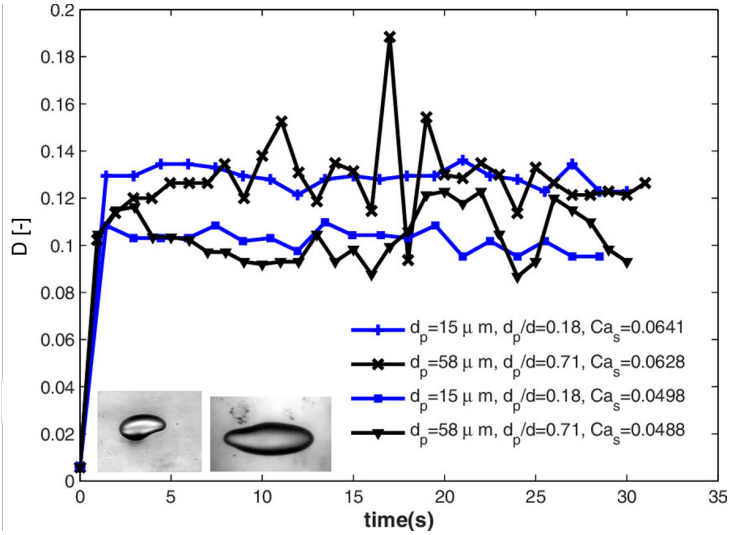

Figure 2.8: Deformation after startup of flow of a droplet ($R = 41$ µm) suspended in a suspension with 2.5 wt% particles. Different capillary numbers and particle diameters, indicated by d_p, are used. The inset illustrates the irregular droplet shapes observed due to collisions between the droplet and particles. Figure adapted from [83].

breakup is predicted and explained by the inertia of the particles. Besides the particle effects on the droplet deformation and breakup, also the particle distribution at the deformed interface is discussed. At high particle coverage a band of particles near the main droplet axis is observed together with an increased concentration of particles near the droplet tips. This distribution corresponds to the preference of the particles to locate themselves at low shear rates and to generate a high surface coverage in order to change the overall interfacial free energy [51].

However, in most experimental works a particle network is formed at the droplet interface. In prior work, Mei et al. [112] have already shown that the formation of a network of particle aggregates at the interface of a sheared droplet significantly suppresses droplet deformation and breakup. At high capillary numbers, the particle network breaks up which results in irregular droplet shapes and a hysteresis effect in droplet deformation [112]. Furthermore, a slower retraction after cessation of flow is observed by Siahcheshm et al. [149] and Mao et al. [107]. Shiahcheshm [149] calculated the nominal interfacial tension from the retraction curves described by a single exponential decay as

also explained in Section 2.2.2 in order to further assess the effects of particles covering the interface. Mao et al. [107] investigated the presence of ellipsoial particles at the droplet interface and also observed orientation in the vorticity direction.

More experiments are performed with so-called Pickering emulsions consisting of oil/water systems in which the interface is covered with nanoparticles [119, 11]. Bécu et al. [11], for example, also observed a slower droplet retraction of a water droplet covered with nanoparticles which form a solid-like network. In addition, the retraction time depends in this case on the applied strain as additional particles can migrate towards the interface during droplet deformation. Furthermore, single droplet dynamics of droplets with other complex interfaces are also studied in detail; for example droplets covered by a rigid network of globular proteins [44, 45, 80, 192]. In certain experimental conditions, globular proteins show similar behavior as particles at the droplet interface [164]. The fluctuating droplet shapes and reduced deformation observed are attributed to the formation of a viscoelastic interface and the stabilized droplet behaves similar to a soft capsule [45]. Recently, Erni et al. [45] made an attempt to link these results quantitatively with the viscoelastic shear and dilatational properties of the interface by using different hydrodynamic models.

At high particle concentrations, the particles are compressed at the interface. Consequently, the particle covered droplets start to behave as a solid-like rigid body [112, 159, 28]. In addition, different phenomena like irregular droplet shapes and buckling of the interface, illustrated in Figure 2.9, come into play in order to increase the available interfacial surface [160, 120, 144]. Different ways exist to create a stable non-spherical droplet. Datta et al. [28], for example, obtained non-spherical droplets with a buckled interface by controlled volume reduction of the droplet phase which is slightly soluble in the matrix. Subramaniam et al. [160] on the other hand created irregular droplet shapes by applying a deformation on the particle covered droplet which is unable to retract back to the spherical shape due to the jammed particle interface.

2.3.3 Particle motion inside a sheared droplet

Smith and van de Ven [152] qualitatively investigated single aqueous droplets containing polystyrene particles immersed in an oil phase ($\lambda \sim 10^{-4}$). Particle circulation on closed streamlines inside the droplet is observed at low particle concentrations. In addition, the particles accumulate in the droplet tips at high shear rates and hence, disturb the internal flow field. Similar observations are made by Desse et al. [33] for aqueous droplets containing starch granules ($\lambda \sim 2 \cdot 10^{-4} - 0.01$). The internal flow and resulting circulation of starch

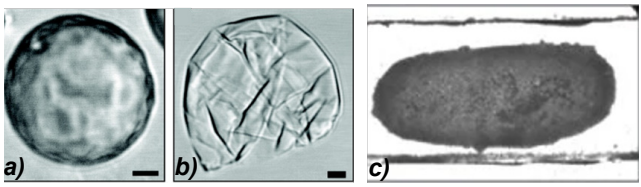

Figure 2.9: Particle-covered droplets with an irregular shape. (a-b) Non-spherical droplets with buckled interface obtained by controlled volume reduction. Figure adapted from [28]. (c) Stable ellipsoidal droplet after squeezing between two plates. Figure adapted from [160].

granules is responsible for the irregular droplet shapes observed. Moreover, the particle rearrangements enable easier droplet breakup at the depleted zones [33, 152]. However, the internal particle circulation is suppressed at higher particle concentrations (10 - 20 vol%) as a consequence of particle interactions [152].

In a numerical study, Zhu and Gallaire [200] simulated the motion of one single particle located inside a sheared droplet ($\lambda = 1$) placed at a certain distance from the droplet centre. The particle moves across the streamlines and attains different equilibrium positions depending on the applied capillary number ($\mathrm{Ca} = 0.10 - 0.35$) and particle over droplet size ratio ($r/R = 0.3 - 0.6$). The extensional part of the rate of deformation tensor is mainly responsible for this cross-streamline particle motion. The particle trajectory and the different equilibrium positions are further explained by analyzing the interplay between the internal flow field and hydrodynamic pressure forces. In addition, the particle motion is confined by the droplet interface which results in a smaller circulation radius when the particle is located further away from the central plane [200].

Liu et al. [101] on the other hand performed numerical simulations on a droplet system containing three small daughter droplets in extensional flow. The authors observed a movement of the two non-axial daughter droplets towards the droplet edge at low viscosity ratios ($\lambda = 1.2$ - 1.5), while these droplets move away from this interface at high viscosity ratios ($\lambda = 2.5$ - 5). However, the authors do not give a physical explanation for this phenomenon.

2.4 Conclusion

The incorporation of solid particles in polymer blends affects the blend morphology and hence, final material performance. Various parameters such as particle size, shape, localization, etc. determine the final blend morphology and material properties which makes it an interesting manner to tailor and enhance the material properties.

The addition of particles to the dispersed phase of a concentrated polymer blend results in general in coarsening and increased droplet sizes. However, the available literature shows that the effects strongly depend on the nature of the blend components and particles and their concentrations. Only a few studies focus on the single droplet dynamics in order to study the effects of particles in the droplet phase. However, the changes observed are mostly associated with the non-Newtonian rheological properties introduced by the particles. Moreover, most studies only compare the dynamics of the particle-filled droplets with those of the neat blend which has different viscous and/or elastic properties. Hence, these studies do not reveal the intrinsic particle effects. For oil/water systems incorporating particles, most studies suggest that particle-filled droplets can be treated as droplets with an effective viscosity governed by the particle concentration. A full quantitative study to investigate this effective droplet viscosity is still lacking. However, at high particle concentration or high particle over droplet size ratios, the available literature shows that the suspension can no longer be treated as a homogenous medium.

Concentrated polymer blends incorporating particles in the matrix phase have a reduced droplet size compared to the corresponding neat blends. However, particles localized in the matrix phase and near the droplet interface can be responsible for droplet clustering. A systematic study of the effects of particles localized in the matrix phase on the single droplet scale is already performed by Kaur et al. [83]. For small particle over droplet sizes, the system behaves as a particle-free system with an increased matrix viscosity governed by the particle concentration. At higher particle over droplet size ratios, fluctuations in droplet deformation and asymmetric droplet shapes arise due to disturbances of the flow field caused by the particles and collisions between particles and the droplet.

Finally, numerous studies demonstrate the stabilizing effects of particles localized at the droplet interface resulting in a decreased droplet size. Due to the formation of a particle network at the droplet interface, the droplet deformation and breakup is substantially suppressed and reduced droplet retraction is observed. At high particle concentration, the droplet starts to behave as a solid-like rigid body and even stable non-spherical droplets can be created. The particle effect

depends on numerous parameters such as particle concentration, size, roughness, etc. However, the stabilizing mechanisms are still poorly understood to date and will be further elucidated in this work.

In general, the intrinsic effects of particles on the single droplet dynamics are still unclear and under discussion. Therefore, we experimentally study the single droplet dynamics, i.e. steady-state deformation, transient dynamics and breakup behavior of single droplets containing particles localized in the droplet phase or at the droplet interface. The results are systematically compared with the droplet dynamics of particle-free reference systems with comparable viscosity ratios. Moreover, the effect of viscosity ratio, particle concentration, and particle size is systematically studied to gain more insight in the structure development of polymer blends containing particles. Furthermore, the stabilizing effect of particles localized at the droplet interface is further elucidated by a rheological study of the particle-filled interface.

Chapter 3

Materials and methods

This chapter first summarizes the materials used in this work together with their main characteristics (Section 3.1). Section 3.2 elucidates the preparation of the suspensions and their rheological properties in more detail. Subsequently, the different materials and suspensions are combined into droplet–matrix systems in order to perform single droplet experiments. These droplet-matrix systems are presented in Section 3.3. Finally, Section 3.4 describes the setups and experimental protocols used to perform single droplet experiments and to characterize the particle-covered interface by shear interfacial rheology. The last section (Section 3.5) of this chapter gives the main working equations and approach of the numerical Volume-of-Fluid (VOF) simulations performed to investigate the fluid dynamics inside the droplet phase in more detail.

3.1 Materials

3.1.1 Requirements

The aim of this thesis is to study the effects of particles in a model polymer droplet-matrix system. Consequently, every system in this work consists of three materials, i.e. a matrix phase, a droplet phase, and particles. These materials are carefully selected since they must satisfy certain conditions to study the single droplet dynamics.

First, the droplet and matrix phases should be completely immiscible and liquid at room temperature. In order to microscopically study the morphology, both

materials should be transparent with a substantial difference in refractive index. To limit the effect of buoyancy forces, small density differences between the different phases are necessary. Furthermore, in order to study the intrinsic effects of the added particles, the neat droplet and matrix phases preferably behave as Newtonian viscous liquids. Finally, the particles should prefer to locate in the droplet phase or at the interface, depending on the system and aim of the experiment. Hence, particle migration towards another phase during the course of the experiments should be eliminated by selection of the proper components.

3.1.2 Droplet and matrix phases

To select the components of the systems containing particle-filled droplets, the wetting parameter, defined in equation 2.31, is estimated based on values found in literature for the interfacial energies for different combinations of available polymers which also satisfy the other requirements mentioned above. An overview of different evaluated systems can be found in Appendix A.1. All estimated wetting parameters are between 0 and 1, indicating a thermodynamic equilibrium positon at the interface. Based on these values, the system of a poly(propylene glycol) droplet (PPG, Sigma Aldrich) in a poly(dimethylsiloxane) matrix (PDMS, Bluestar silicones) is selected as the wetting parameter is the closest to 1, indicating a higher preference to the droplet phase material. However, the grades and hence, viscosity range available for PPG was limited. In order to be able to also study a system with a viscosity ratio around one, a similar material was selected, namely poly(ethylene glycol-*ran*-propylene glycol) (PEG-*ran*-PPG, Sigma Aldrich) and also used as droplet phase material in combination with a PDMS matrix. Various grades of PDMS and PEG-*ran*-PPG are used in this study. For every droplet-matrix system it was verified that both components are completely immiscible. Only for a PPG droplet in a PDMS matrix a small reduction in droplet size is observed, indicating a minor miscibility of PPG in PDMS. This effect stays however limited over the time course of the experiments ($< 3\%$ in 5h) and has no significant effect on the interfacial tension. The density of PPG is equal to 1004 kg/m^3 (25 °C, data from supplier), while the density of PEG-*ran*-PPG at 25 °C slightly depends on the grade: 1095 kg/m^3 ($M_\mathrm{n} \sim 2500$) and 1092 kg/m^3 ($M_\mathrm{n} \sim 12000$) (data from supplier). The density of PDMS is equal to 973 kg/m^3 at 20 °C [116]. The refractive indices of PDMS, PPG, and PEG-*ran*-PPG are equal to 1.4 [21], 1.45 [193], and 1.466 (data from supplier), respectively.

Experiments regarding a particle-covered interface are performed with PDMS (DMPS1M, Sigma Aldrich) as droplet phase and poly(isobutene) (PIB, Glissopal V-190, BASF) as matrix phase. PDMS is completly insoluble in PIB [62].

The refractive index of PIB is equal to 1.5 [21]. A curable PDMS (Sylgard 184, Dow Corning) is used as bottom layer to visualize the flat particle-covered interface with Scanning Electron Microscopy (SEM). To perform a rheological characterization of the particle-covered interface and minimize the bulk contributions, PIB (Indopol H-7, Ineos, $\eta = 0.3$ Pa·s at 21.5 °C) and PDMS (Silicone oil 350 cSt, Sigma Aldrich, $\eta = 0.35$ Pa·s at 21.5 °C) grades with a substantially lower viscosity are selected. PIB has a density of 894 kg/m^3 [116]. Consequently, PIB has to be used as top layer and PDMS as bottom layer in the two layered systems used to perform interfacial rheology experiments and SEM.

Table 3.1: Viscosity η at 23 °C and activation energy E_a of the particle-free droplet and matrix phases.

Phase	Component	Grade	η [Pa · s]	E_a [kJ/mol]
Droplet	PEG-*ran*-PPG	$M_n \sim 12000$	40.0 / 37.4	40.2 / 40.0
	PEG-*ran*-PPG mixture	$M_n \sim 2500$ + $M_n \sim 12000$	1.1	44.2
	PPG	$M_n \sim 4000$	1.0 / 1.1	37.6 / 39.3
	PDMS 1	DMPS1M	1.0	14.6
Matrix	PDMS 12.5	Rhodorsil 47V12500	12.6	13.2
	PDMS 30	Silbione 70047 V30000	28.7	14.5
	PDMS mixture 1	Silbione 70047 V30000 + Rhodorsil 47V12500	23.1	14.0
	PDMS mixture 2	Silbione 70047 V30000 + Rhodorsil 47V12500	18.5	12.5
	PDMS mixture 3	Silbione 70047 V30000 + Rhodorsil 47V12500	11.9	12.1
	PDMS mixture 4	Rhodorsil 47V12500 + Bluesil 47V5000	6.7	11.4
	PIB 10	Glissopal V-190	14.0	66.3

In order to obtain matrix and droplet phases with a specific desired viscosity, different grades can be mixed according to the viscosity mixing rule described by Velankar and Moldenaers [184]:

$$\eta = (\phi_s \eta_s^{1/\beta} + \phi_l \eta_l^{1/\beta})^{\beta}. \tag{3.1}$$

In this formula, ϕ represents volume fraction, η viscosity and subscripts s and l respectively refer to the smallest and largest molecular weight grade. β is equal to 3.4 in the case of entangled, linear polymers [184]. The different grades are first mixed by hand for ten minutes and subsequently stored for at least one week to provide sufficient time for diffusion.

The viscosities of all fluids are measured with an AR-G2/DHR3 rheometer (TA Instruments) equipped with a cone-plate geometry. All materials behave as Newtonian viscous liquids with a constant viscosity in the shear rate range of interest (0.1 s^{-1} – 10 s^{-1}). The viscosities are measured at different temperatures and the Arrhenius equation is fitted through the data:

$$\eta = A_0 \exp\left(\frac{E_a}{R_g T}\right) \tag{3.2}$$

with η the viscosity, T the absolute temperature, and R_g the universal gas constant (8.314 J/(mol·K)). A_0 and E_a are both material constants. The viscosities η at a temperature of 23 °C and activation energies E_a of the different particle-free droplet and matrix phases used in this work are listed in Table 3.1. It has to be noted that two different batches of PEG-*ran*-PPG and PPG are used which have a slightly different viscosity. From now on, the component name as stated in Table 3.1 will be used.

3.1.3 Particles

The addition of particles to a Newtonian fluid can introduce non-Newtonian rheological effects like shear thinning and normal stresses. These effects are eliminated by selecting non-Brownian spherical particles to study the intrinsic effects of particles localized in the droplet phase. Polystyrene particles (PS, Dynoseeds) with a density of 1050 kg/m^3 at 20 °C (data from supplier) are selected as different particle sizes are available. The number average particle diameters are determined with optical microscopy and are equal to respectively 25 ± 2.7 μm, 44 ± 4.5 μm and 82 ± 5.1 μm, which is in good agreement with the information given by the supplier (respectively, 23.1 μm, 42.4 μm, and 80.4 μm). This method was not applicable for the smallest particles, hence a particle diameter of 5.3 ± 0.093 μm as given by the supplier is used for these particles.

Colloidal silica nanoparticles (TS-530, Cabot Corporation) with a diameter of 50 ± 26 nm (data from supplier) are selected for the experiments regarding the particle-covered interface. The surface of these particles is made partially hydrophobic by a treatment with hexamethyldisilazane. Consequently, these particles will locate at the PDMS-PIB interface. The density of these particles is equal to 2200-2300 kg/m^3 at 20 °C (data from supplier).

3.2 Suspensions

3.2.1 Preparation

PS particles are added to PEG-*ran*-PPG or PPG and are dispersed with a spatula for ten minutes. Thereafter, entrapped air bubbles are removed by keeping the suspension in a vacuum oven at room temperature. Suspensions with a particle volume fraction between 1 vol% and 25 vol% are prepared and used as droplet phase. No large aggregates are discovered when the suspensions are examined with a microscope.

To properly disperse the silica nanoparticles into PIB, the nanoparticles are first dispersed in cyclohexane with an ultrasonic probe (UP400S, Hielscher) for two hours, while PIB is mixed with cyclohexane for 12 hours using a magnetic stirrer. Thereafter, both mixtures are mingled and stirred for an additional hour. Finally, cyclohexane is removed again by evaporating the solvent with a rotational evaporation device (Rotavapor, Büchi) at a temperature of 60 °C and rotational speed of the sample of 10 rpm, while the pressure is decreased stepwise until 50 mbar. It is assumed that all the cyclohexane is evaporated when the sample reaches a constant weight. All prepared suspensions contain 0.4 vol% silica nanoparticles in PIB and do not have a yield stress, hence particle migration towards the droplet interface is not inhibited.

As described in Chapter 2, the forces acting on particles and particle interactions greatly depend on the particle size. The size of the PS particles is in the micrometer range and consequently, gravitational forces dominate compared to Brownian motion and other surface forces. The creaming or sedimentation velocity of the particles in the suspension is calculated using Equation 2.18 in Chapter 2. The maximum sedimentation velocity of a particle in the bulk suspension is equal to 175 μm/h and occurs for 44 μm sized particles in PPG. A summary of all the calculated sedimentation or creaming velocities of the particles in suspension can be found in Appendix A.2. In contrast, the silica nanoparticles in PIB form a colloidal suspension in which the Brownian force

dominates gravitational forces. Also surface forces such as Van der Waals forces and depletion forces should be considered in this case.

3.2.2 Rheological characterization

To verify that the suspensions with PS particles behave as purely Newtonian liquids in the shear rate range of interest, their rheological behavior is characterized by performing a strain sweep and a frequency sweep in the linear viscoelastic region as well as a steady-state flow sweep. These experiments are performed with an AR-G2 rheometer equipped with a parallel plate setup. The measuring gap is in all cases set to 1 mm.

Figure 3.1a shows the viscous (G'') and elastic (G') modulus as function of angular frequency (ω) for two different suspensions as an example. G'' linearly increases with angular frequency and G' is approximately two orders of magnitude smaller. Hence, G' is negligibly small, thereby indicating negligible elasticity. Moreover, the viscosity of these suspensions is indeed independent of the applied shear rate in the shear rate range of interest (0.1 – 10 s^{-1}), as can be seen in Figure 3.1b. In addition, the normal forces exerted are smaller than the device limits and are therefore also negligible. In general, all suspensions exert similar rheological behavior as the suspending media and hence, behave as Newtonian viscous liquids. However, due to the addition of particles, the bulk suspension viscosity is higher than the viscosity of the interstitial fluid.

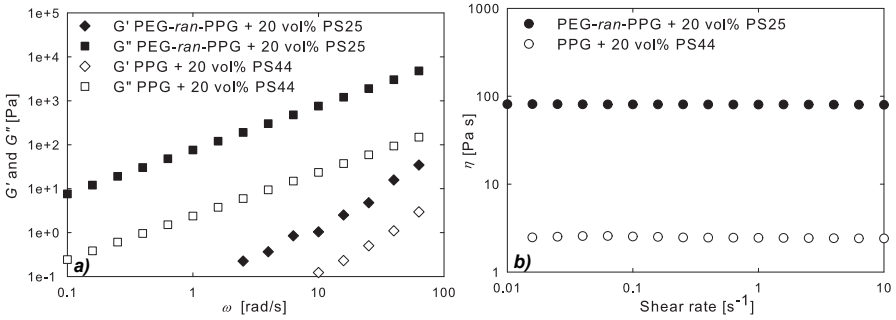

Figure 3.1: Example of (a) frequency sweep data (strain amplitude of 10%) and (b) steady-state viscosity of two bulk suspensions. The particle diameter (Z µm) of the particles in the suspensions is indicated in the suspension name as PSZ. Measurement temperature is equal to 19 °C and 23 °C for the PPG suspension and PEG-*ran*-PPG suspension, respectively.

Figure 3.2 displays the relative viscosity η_r of the suspensions as a function of their particle volume fraction ϕ at a temperature of 23 °C. The relative viscosity is defined as the ratio of the suspension viscosity over the viscosity of the suspending medium, being PEG-*ran*-PPG or PPG in this case. As expected, the suspension viscosity only depends on the particle volume fraction and is independent of the particle size and interstitial fluid. The full line in Figure 3.2 represents the Maron-Pierce equation (Equation 2.25), with 0.64 as maximum packing fraction ϕ_{max}. This model shows good agreement with the measured data and hence, can be used to estimate the viscosity of suspensions with intermediate particle volume fractions.

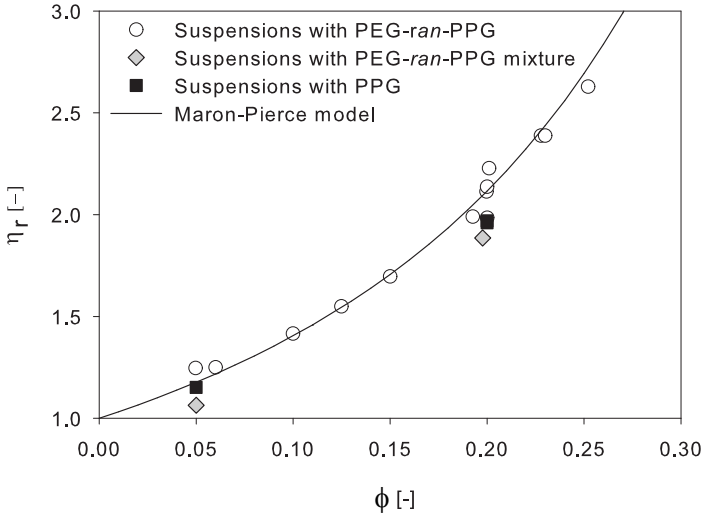

Figure 3.2: Relative viscosity of bulk suspensions consisting of different suspending media at 23 °C. The full line indicates the Maron-Pierce equation with $\phi_{max} = 0.64$.

Similar to the particle-free droplet and matrix phases in section 3.1, the different temperature dependencies of the bulk suspension viscosities are determined by using Equation 3.2. An overview of all the prepared suspensions together with the determined viscosities at 23 °C and activation energies can be found in Table 3.2.

Table 3.2: Viscosity η at 23 °C and activation energy E_a of the bulk suspensions.The particle diameter (Z µm) of the particles in the suspension is indicated in the suspension name as PSZ.

Suspension		η [Pa · s]	E_a [kJ/mol]
PEG-*ran*-PPG	+ 5 vol% PS25	46.7	38.2
	+ 6 vol% PS25	46.8	38.7
	+ 10 vol% PS25	53.0	39.3
	+ 13 vol% PS25	58.0	38.8
	+ 15 vol% PS25	63.5	39.0
	+ 19 vol% PS25	74.5	39.0
	+ 20 vol% PS25	80.4/79.1	38.3/38.8
	+ 23 vol% PS25	89.4	38.9
	+ 20 vol% PS82	81.0	38.8
	+ 20.1 vol% PS82	83.4	39.2
	+ 20 vol% PS5	74.3	39.1
	+ 25 vol% PS5	98.4	39.5
PEG-*ran*-PPG mixture	+ 5 vol% PS25	1.2	37.1
	+ 20 vol% PS25	2.1	38.4
PPG	+ 5 vol% PS25	1.1/1.2	31.8/41.2
	+ 20 vol% PS25	1.9/2.0	38.9/40.1
	+ 20 vol% PS44	1.9/2.0	41.0/40.8

3.3 Droplet-matrix systems

3.3.1 Mother and reference systems

An overview of the different droplet-matrix systems and their viscosity ratios can be found in Table 3.3. Table 3.3 also gives the interfacial tension experimentally determined as explained in Section 3.4. The system to which the particles are added is the so-called mother system MS-X with X the viscosity ratio of the system.

Table 3.3: Characteristics of the particle-free mother systems and reference systems: droplet and matrix components, resulting viscosity ratios at 23 °C and interfacial tension (± standard deviation).

Name	Droplet Component	Matrix Component	λ [−]	Γ [mN/m]
MS-1.4	PEG-*ran*-PPG	PDMS 30	1.4	8.5 ±0.1
RS-1.7		PDMS mixture 1	1.7	
RS-2.2		PDMS mixture 2	2.2	
RS-3.2		PDMS 12.5	3.2	
RS-3.4		PDMS mixture 3	3.4	
MS-0.09	PEG-*ran*-PPG mixture	PDMS 12.5	0.09	8.5 ±0.1
MS-0.08L	PPG	PDMS 12.5	0.08	3.8 ±0.3
RS-0.2L		PDMS mixture 4	0.2	
MS-0.1	PDMS 1	PIB	0.1	1.9

The first system (MS-1.4) consists of a high viscous PEG-*ran*-PPG droplet phase in a PDMS 30 matrix, which results in a viscosity ratio larger than one. The dispersed phase of the second system (MS-0.09) also consists of PEG-*ran*-PPG and hence, this system has the same interfacial tension as MS-1.4. However, the viscosity of the PEG-*ran*-PPG droplet phase of MS-0.09 is matched with that of the third system (MS-0.08L) by using the PEG-*ran*-PPG mixture described in Table 3.1. The third system (MS-0.08L) has a comparable viscosity ratio as MS-0.09, but consists of a different droplet phase, namely PPG. Hence the interfacial tension of this system is smaller compared to that of MS-1.4 and MS-0.09, which is indicated by "L" in the name (MS-0.08L). Finally, the fourth system (MS-0.1) is used to study the effect of a particle-covered droplet interface.

This system consists of a low viscous PDMS 1 droplet phase submersed in a PIB 10 matrix.

By the addition of particles to the droplet phase, the viscosity of this phase increases which affects the viscosity ratio of the system and hence, also the droplet dynamics. Therefore, the droplet dynamics of some particle systems, presented in the next section, are also compared with those of particle-free reference systems RS-X with X the viscosity ratio. These reference systems consist of the same materials as the associated mother system, but the matrix viscosity is adjusted in order to match the viscosity ratio with that of the particle systems studied.

3.3.2 Particle systems

To study the effects of particles localized in the droplet phase, experiments are performed on different particle systems. These particle systems, denoted in this work as MS-X + Y vol% PSZ, consist of the same grade matrix phase as the corresponding mother system (MS-X), but the droplet phase is produced by injection of a suspension containing Y vol% PS particles with a diameter of Z μm. The interstitial material is exactly the same as the droplet phase of the corresponding mother system.

Table 3.4 shows the main characteristics of these particle systems. The values of the viscosity ratios tabulated in Table 3.4 are based on the measured viscosities of the bulk suspensions which are used to inject the droplets into the matrix phase. Droplets produced from a 1 vol% suspension only have a few particles inside the droplet phase which have a negligible effect on the droplet phase viscosity and interfacial tension. Hence, the same viscosity ratio and interfacial tension values as those of the corresponding mother system are used. As expected, the droplet viscosity and hence the system's viscosity ratio, increases with increasing particle volume fraction, while it is independent of the particle size. The interfacial tension is determined as explained in Section 3.4. The average value of at least three preliminary experiments, as tabulated in Table 3.4, is used. However, the interfacial tension is determined separately for every investigated droplet in systems for which deviations larger than 5% were observed. By comparison of the interfacial tension values of the particle systems in Table 3.4 with those of the particle-free systems (Table 3.3), it becomes clear that the particles do not significantly alter the interfacial tension. The interfacial tension of the particle systems corresponding to MS-0.08L is therefore only verified by measuring two distinct droplets of MS-0.08L + 5 vol% PS25 and this value is also used for the other particle systems MS-0.08L + Y vol% PSZ.

Table 3.4: Characteristics of the particle systems: viscosity ratios at 23 °C and interfacial tension (± standard deviation).

Particle system	λ [−]	Γ [mN/m]
MS-1.4 + 1 vol% PS25	1.4	8.5 ±0.1
MS-1.4 + 5 vol% PS25	1.6	8.1 ±0.1
MS-1.4 + 10 vol% PS25	1.8	8.2 ±0.1
MS-1.4 + 15 vol% PS25	2.2	8.3 ±0.2
MS-1.4 + 20 vol% PS25	2.8	8.6 ±0.2
MS-1.4 + 20 vol% PS82	2.8	8.3 ±0.1
MS-1.4 + 20 vol% PS5	2.6	8.9 ±0.1
MS-0.09 + 1 vol% PS25	0.1	8.5 ±0.1
MS-0.09 + 5 vol% PS25	0.1	8.3 ±0.2
MS-0.09 + 20 vol% PS25	0.2	8.1 ±0.1
MS-0.08L + 1 vol% PS25	0.1	3.8 ±0.3
MS-0.08L + 5 vol% PS25	0.1	
MS-0.08L + 20 vol% PS25	0.2	3.9 ±0.01
MS-0.08L + 20 vol% PS44	0.2	

In a preliminary experiment, it is verified that the particles localized in the droplet phase do not migrate to the interface or matrix phase when the droplet is kept under quiescent conditions. Figure 3.3 illustrates this conclusion with images of systems MS-1.4 + 5 vol% PS25 and MS-0.08L + 5 vol% PS25 in the velocity – vorticity plane. It can also be seen on these images that the particle distribution does not change under quiescent conditions. In addition, it is verified the particles stay inside the droplet phase when shear flow is applied.

Particle-covered droplets (MS-0.1 + 0.4 vol% silica) are formed by injection of PDMS 1 droplets in a PIB 10 bulk suspension of 0.4 vol% silica nanoparticles prepared as explained in Section 3.2.1. The hydrophobic particles will migrate towards the PDMS-PIB interface. It is verified that particle motion in the PIB suspension is dominated by Brownian motion and sedimentation is negligible. After a certain residence time in the bulk suspension, the droplet is carefully transferred with a spatula to a particle-free PIB 10 matrix. Particles transferred

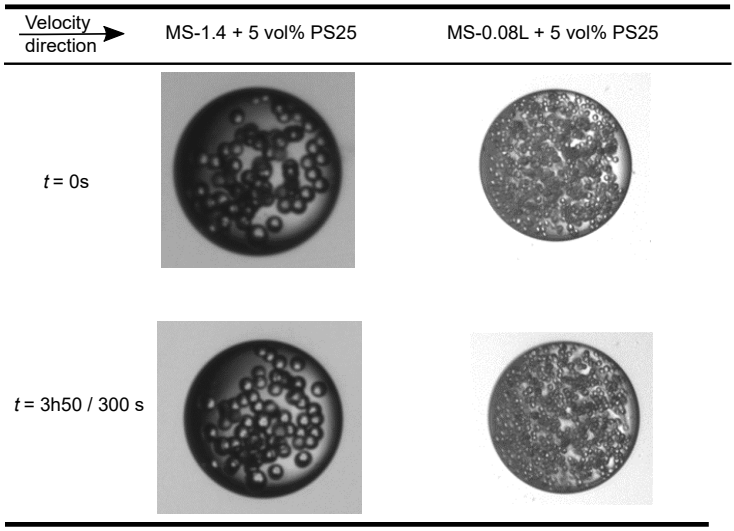

Figure 3.3: Particle distribution of particle systems MS-1.4 + 5 vol% PS25 and MS-0.08L + 5 vol% PS25 immediately after droplet injection and respectively, 3h50 and 300 s after droplet injection. All images are taken in the top view (velocity - vorticity plane). No shear flow is applied (Ca = 0).

with the droplet, but not interfacially bound to the droplet are removed by gently moving the droplet around in a particle-free matrix. Finally, the droplet is transferred to a particle-free PIB 10 matrix at room temperature to perform the single droplet experiments in the counterrotating setup. The particle concentration at the interface is altered by varying the residence time in the bulk suspension, with a longer residence time resulting in a larger interfacial coverage. However, it was not possible to determine the exact particle concentration at the droplet interface.

In order to still be able to compare the particle-covered droplet interface with the flat interface in the interfacial rheology experiments, the bulk suspension containing injected droplets is kept at an elevated temperature of 80 °C. At this temperature, the viscosities of the droplet and matrix phases are equal to 0.37 Pa·s and 0.32 Pa·s, respectively. These viscosities are similar to the viscosities of the PIB and PDMS grades used for the rheological characterization of the flat particle-covered interface at 21.5 °C. Consequently, we can assume that the particle coverage of the interfaces in the two experiments is similar as also the thickness of the PIB suspension layer, and hence travelling distance, is kept constant (1 cm) in both experiments. In a preliminary experiment, it is

verified that the storage temperature of 80 °C for several days has no effect on the single droplet dynamics, nor on the interfacial tension of the system. In the remaining text, the droplet-matrix systems containing a particle-covered interface are characterized by the residence time of the droplets in the 0.4 vol% PIB bulk suspension at 80 °C.

To study the particle structures at the interface, a two-layered system with curable PDMS as bottom layer and the same PIB bulk suspension as used in the interfacial rheology experiments with 0.4 vol% silica nanoparticles as top layer is prepared and cured at 100 °C for 1 h. Thereafter, the PIB liquid layer is removed with solvent, making it possible to visualize the particle-covered interface with SEM. Figure 3.4 shows two SEM images demonstrating the presence of silica nanoparticles at the PDMS-PIB interface and the increase of interfacial coverage with residence time. It is however not possible to determine the exact concentration of particles present at the droplet interface. Additionally, it can be seen that aggregated silica clusters are present at the interface due to particle interactions. However, this work focuses on the link between the dynamics of particle-covered droplets observed and their overall interfacial shear properties. Hence, the exact origin of the formed interfacial particle network and the existing interactions is not the scope of this work. Interesting studies regarding the relation between interfacial shear properties and 2D particle microstructure and existing interaction forces can for example be found in [104, 138, 155].

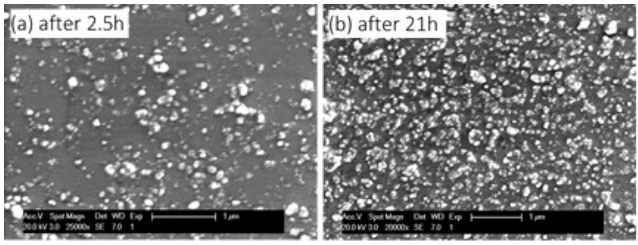

Figure 3.4: SEM images of the particles present at the PDMS surface after curing of the PDMS bottom layer and removal of the PIB bulk suspension used as a top layer. (a) Curing after 2.5h residence time and (b) after 21h residence time.

3.4 Experimental setup and protocol

3.4.1 Single droplet experiments

A counterrotating parallel plate shear cell combined with an optical microscope is used to perform the single droplet experiments. Figure 3.5 shows a schematic representation of the setup. More details about this setup can be found elsewhere [177, 31, 21, 186]. The setup consists of a stress-controlled rheometer (Anton Paar) with an upper and bottom motor which are able to rotate in opposite directions. By applying a continuous counterrotating movement a simple shear flow with a stagnation plane is created. The vertical position of the stagnation plane can be adapted in order to keep the droplet in the stagnation plane by regulating the ratio of applied rotational velocities of the top and bottom motors while keeping the total applied velocity constant. An optical setup equipped with a microscope (Wild 5MA) connected with a camera (Basler acA 1600), a prism, two light sources and a curved correction cup enables us to capture images of the droplet in two planes: the velocity-vorticity plane (top view) and the velocity-velocity gradient plane (side view). The resulting resolution is 1.4 pixels/μm. The matrix phase is contained in a glass cup to prevent sample outflow. The correction cup of the optical train compensates the curvature of this cup holder. An injection device equipped with a needle (Hamilton) and filled with the droplet phase is used to inject droplets. In order to create particle-covered droplets, the droplets are injected into the PIB bulk suspension and are transferred after a certain residence time with a spatula to the counterrotating cup containing particle-free PIB 10. In all other cases, the droplets are directly injected into the cup containing the matrix phase. The droplet size can be adjusted by regulating the pressure applied to the injection device and the injection time.

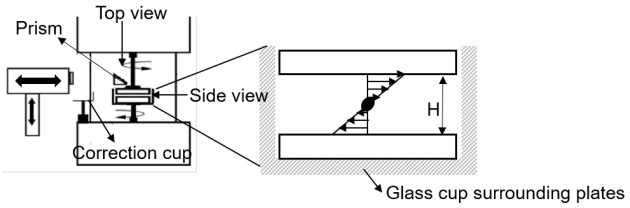

Figure 3.5: Schematic representation of the counterrotating setup. Figure adapted from [177].

The average droplet radius in the experiments regarding the particle-filled droplets is equal to 108.4 ± 4 μm. This results in a particle over droplet size

ratio (r/R) ranging from 0.02 for the 5 μm sized particles to 0.4 for the largest particles of 82 μm. In order to keep the particle over droplet size ratio constant, additional experiments with a droplet radius of 214 ± 7 μm are performed for system MS-0.08L + 20 vol% PS44. The particle-covered droplets have an average droplet radius of 100 μm. The gap height H is set to 3 mm in all experiments and the vertical position of the droplet is always checked to ensure that wall effects can be neglected.

The settling velocity of droplets in a matrix fluid is calculated with Equation 2.18 in Chapter 2. For the droplet – matrix systems the maximum sedimentation velocity exists for the particle-free reference systems containing PEG-*ran*-PPG as droplet phase. The sedimentation velocity varies from 387 μm/h for MS-1.4 to 932 μm/h for RS-3.4. For the single droplet dynamics experiments, one capillary number is applied for maximum 5 minutes, which results in a maximum sedimentation distance of the droplet of 32 μm and 78 μm, for respectively RS-1.4 and RS-3.4. However in order to study particle migration, capillary numbers are applied to the particle systems for maximum 30 minutes, which results in a maximum sedimentation distance of 200 μm. In addition, the settling of the particles inside the droplets should be considered in the time frame of the experiments, see also Appendix A.2. For system MS-1.4 the maximum estimated travel distance in 30 minutes is only 7.4 μm for the PS82 particles. This travel distance is larger for systems MS-0.09 and MS-0.08L and ranging between 25 μm for PS25 particles and 87.4 μm for PS44 particles in 30 minutes. It has to be noted however that no sedimentation or creaming of the particles inside the droplet is observed when pictures are taken in the velocity - velocity gradient plane after a steady-state distribution is already reached. Probably, the circulation flow to which the particles inside the droplets are subjected is stronger than sedimentation.

Furthermore, the radial position of the droplet is also verified before every experiment to ensure a linear shear flow field without influence of the centre or edges of the parallel plates [188]. The temperature of the sample is determined with a thermocouple for every experiment. This temperature is used to calculate the exact droplet and matrix phase viscosities according to the Arrhenius equation with the activation energy and shear viscosity at 23 °C given in Tables 3.1 and 3.2. The average experimental temperature is equal to 22.9 ± 0.5 °C.

The captured images are quantitatively analyzed using ImageJ software. The droplet axes L and W in top view and B and orientation angle (θ) in side view of the deformed droplets as defined in Figure 2.1 of Chapter 2 can be determined from these images by assuming an ellipsoidal droplet shape. An ellipse is fitted to the droplet contour in the velocity-vorticity profile to determine droplet axes W and L_p. L_p represents the projection of the droplet axis L in the velocity-vorticity plane. Regardless the use of a correction cup to compensate

the curved edge of the cup holder, the images taken in side view are still slightly disordered in the velocity direction. Therefore, these images are rescaled with a scaling factor. This scaling factor is equal to the ratio of the droplet radius determined in the velocity direction of the disordered image over de actual droplet radius determined in the velocity – vorticity plane. Subsequently, an ellipse is fitted to the droplet contours of the rescaled image to determine L, B, and θ. However, this method is inaccurate at larger droplet deformations and hence, at higher applied capillary numbers ($\mathrm{Ca} \geq 0.20$). Therefore, the droplet parameter L_g as defined in Figure 2.1 is determined from these images and the other droplet parameters (L, B, θ) are calculated with the conservation of volume equation and the equations for projection of an ellipsoid on a plane given in Appendix A.3.

The interfacial tension is determined for every system by fitting the droplet axes at small deformation to the second order theory of Greco [61]. Capillary numbers ranging from 0.05 until 0.18 are applied and the steady-state droplet shapes are captured in the velocity-vorticity plane. Thereafter, the dimensionless droplet axes $L_\mathrm{p}/2R$ are determined and plotted against the applied shear rate which results in a linear curve. The interfacial tension for a system consisting of Newtonian components can be calculated from the slope of this curve [21]:

$$\frac{L_\mathrm{p}}{2R} = 1 + \dot{\gamma}^2 \left(\frac{\eta_\mathrm{m} R}{\Gamma} \right)^2 \left(\frac{1}{4}\mathrm{F}^2 + \frac{1}{4}\mathrm{s}_2 + \frac{1}{2}\mathrm{s}_3 \right). \tag{3.3}$$

In this formula, F, s_2, and s_3 only depend on the viscosity ratio. Their exact expressions can be found in Appendix A.4.

The steady-state droplet deformation as function of the capillary number is determined by applying different constant capillary numbers ranging from 0.1 until 0.55. Images in the velocity-vorticity plane and velocity-velocity gradient plane are taken after the droplet reached a steady-state deformation. Subsequently, the transient startup and retraction behavior is observed at capillary numbers of 0.2 and 0.3 by capturing images in the velocity-vorticity plane after the startup and cessation of shear flow. Finally, the breakup behavior is studied in more detail by increasing the applied capillary number with small discrete steps until breakup occurs. After every applied capillary number, the shear flow is stopped and hence, the droplet retracts back to a spherical shape, before applying the next capillary number.

For the particle-free systems (MS and RS), the different capillary numbers are applied sequentially on the same droplet. The applied shear flow will however influence the particle distribution of particle-filled droplets or the particle network at the droplet interface of particle-covered droplets. Therefore, a strict measuring protocol is followed. For the particle-filled droplets, the steady-state

droplet deformation is measured immediately after droplet injection and hence, with still a random homogeneous particle distribution. Only for system MS-1.4 + 20 vol% PS25, different capillary numbers are applied sequentially in random order on the same droplet because no significant changes in particle distribution are observed during the experiment. Subsequently, the transient and breakup experiments are performed with a steady-state non-homogenous particle distribution. To ensure this steady-state particle distribution, a long period of shear flow is applied between the deformation experiment at a specific capillary number and the subsequent transient and breakup experiments. Finally, the evolution of the particle distribution during the application of shear flow is investigated by the injection of droplets with a random homogeneous particle distribution. Thereafter, a constant capillary number between 0.1 and 0.55 is applied and images in the velocity-vorticity plane are captured to follow the time evolution of the particle distribution. The shear flow is stopped when no more changes in particle distribution are observed and hence, a steady-state particle distribution is reached. Thereafter, the same capillary number is applied again and images of the steady-state particle distribution in the velocity-velocity gradient plane are taken. The capillary number applied to systems with a particle-covered droplet interface is stepwise increased to determine the steady-state deformation and breakup behavior.

It was not possible to repeat all experiments several times and hence, no statistical analysis could be performed on the experimental data. However, for the particle-free mother and reference systems, the steady-state deformation $L/2R$ at Ca = 0.30, the determined characteristic startup time $t_\mathrm{i}/\tau_\mathrm{E}$ and relaxation time τ/τ_E at Ca = 0.20, and the critical capillary number for breakup ($\mathrm{Ca}_\mathrm{crit}$) are determined for 2-3 different droplets. The maximum deviations ()$(y_\mathrm{max} - y_\mathrm{min})/y_\mathrm{min}$) observed are summarized in Table 3.5. An increase in fluctuations and variability is expected when particles are added to the droplet due to local intrinsic particle effects [83] and a variation in particle concentration. Therefore, the droplet dynamics of 2-6 different particle-filled droplets are measured. The deviations observed increase with particle concentration and particle to droplet size ratio r/R. The maximum deviations ($(y_\mathrm{max} - y_\mathrm{min})/y_\mathrm{min}$) observed can also be found in Table 3.5. Repeated measurements on the same droplet resulted in deviations less than 4% for the steady-state deformation $L_\mathrm{p}/2R$ for Ca = 0.30 and deviations less than 10% for the characteristic relaxation time τ/τ_E after a shear flow with Ca = 0.20 is applied.

Table 3.5: Maximum deviations $((y_{\min} - y_{\max})/y_{\min})$ observed in steady-state deformation $L/2R$ at Ca = 0.30, characteristic startup time t_i/τ_E and relaxation time τ/τ_E at Ca = 0.20, and critical capillary number Ca_{crit} at breakup determined from experiments with 2-3 particle-free droplets or 2-6 particle-filled droplets.

	Max. deviations Particle-free droplets	Max. deviations Particle-filled droplets
$L/2R$ (Ca = 0.30)	$< 2\%$	$< 5.5\%$
t_i/τ_E (Ca = 0.20)	$< 13\%$	$< 15\%$
τ/τ_E (Ca = 0.20)	$< 13\%$	$< 40\%$
Ca_{crit}	$< 5\%$	$< 28\%$

3.4.2 Interfacial shear rheology

A double wall-ring (DWR) geometry designed by Vandebril et al. [182] in combination with a stress-controlled DHR3 rheometer (TA Instruments) is used to perform interfacial shear rheology experiments. Figure 3.6 gives a schematic representation of the setup. Exact dimensions of this setup can be found in [182]. A Teflon trough is used as sample holder and placed directly on a Peltier bottom plate. PDMS ($\eta = 0.35$ Pa·s at 21.5 °C) is used as the bottom phase, while a bulk suspension of 0.4 vol% silica nanoparticles in PIB ($\eta = 0.3$ Pa·s at 21.5 °C) is used as top phase. A ring with a square-shaped cross-section is placed exactly at the planar PDMS-PIB interface.

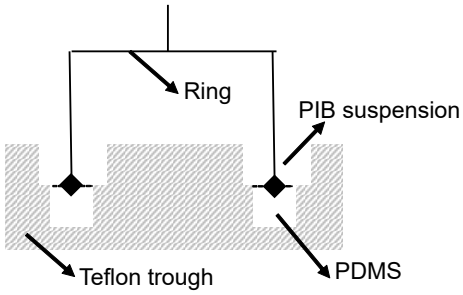

Figure 3.6: Schematic representation of the double wall-ring setup. Figure adapted from [182].

All experiments are performed at a temperature of 21.5 °C, which results in

shear viscosities of PIB and PDMS similar to those of the corresponding droplet-matrix systems (MS-0.1 + 0.4 vol% silica particles) at an elevated temperature of 80 °C. The total volume of the PIB bulk suspension is controlled in order to achieve a thickness of the top layer of 1 cm. This thickness is comparable to the thickness of the PIB suspension layer during the preparation of the particle-covered droplets. Therefore, we can assume that the flat particle-covered interface formed during the interfacial shear rheology experiments is comparable to the particle-covered droplet interfaces and hence, we can directly compare the residence times of both experiments.

The drag experienced by the ring geometry is influenced by the surface drag, but also by the drag imposed by the top and bottom bulk phases. The latter should be minimized in order to correctly characterize the interfacial rheological properties. Consequently, low viscous grades of PIB and PDMS are selected to perform these experiments. The relative importance of the interfacial effects compared to the bulk rheology is given by a dimensionless number, the Boussinesq number Bo [182, 39]:

$$\mathrm{Bo} = \frac{\eta_\mathrm{i}}{G(\eta_\mathrm{t} + \eta_\mathrm{b})}. \tag{3.4}$$

In this formula, η_i represents the interfacial viscosity, while η_t and η_b are the viscosities of the top and bottom bulk phases, respectively. G is a characteristic length scale of the geometry which is in this case approximately equal to 0.7 mm [182]. The interfacial effects dominate for a Boussinesq number much larger than 1, while the properties of the bulk fluids will influence the measurements for Boussinesq numbers close to and smaller than 1. Hence, at Boussinesq numbers close to 1 an additional correction of the raw data is necessary to take the actual velocity profiles into account [182, 39].

After sample loading a time sweep is started in the linear regime until steady-state is reached and hence, particles migrated towards the interface. Thereafter, different rheological tests are performed to further characterize the particle-covered interface. Frequency sweeps in the linear regime are performed. Furthermore, a strain sweep is executed to determine the linear strain limit. In addition, the yield stress of the particle-covered interface is determined by creep-recovery experiments. A new sample is loaded after every experiment in the non-linear regime and the moduli at steady-state are compared to ensure a similar particle-covered interface for every experiment.

3.4.3 Interfacial dilatational rheology

A liquid-liquid Langmuir trough and a Wilhelmy balance (KSV Nima NB) equipped with a platinum Wilhelmy plate are used to determine the surface

pressure-area isotherms. First, PDMS 1 is added as bottom subphase and the interfacial tension of PDMS-air is measured. An interfacial tension of 21.2 mN/m is obtained which corresponds to the value found in literature [194]. It has to be noted that a waiting time was needed before the measurement became stable and reached steady-state. Thereafter, a suspension consisting of 0.1 vol% silica nanoparticles with a diameter of 100 nm in PIB (Indopol H-7) is added as top phase. Before the start of the experiment, a resting time of 24 h is given to allow the particles to migrate towards the interface. Thereafter, the interface is compressed with a barrier speed of 1 mm/s.

3.5 Numerical simulations

3.5.1 Theory: Governing equations

For incompressible Newtonian fluids, the two-phase flow is governed by the incompressibility criterion and the conservation of momentum equation (Navier-Stokes):

$$\nabla(\mathbf{u}) = 0, \tag{3.5}$$

$$\rho\left(\frac{\partial \mathbf{u}}{\partial t} + \mathbf{u}\cdot\nabla\mathbf{u}\right) = -\nabla p + \eta\nabla^2\mathbf{u} + \rho\mathbf{g} + \mathbf{F}. \tag{3.6}$$

$\mathbf{u}$ represents the fluid velocity vector and ∇p the pressure forces. The interfacial tension force $\mathbf{F}$ is modelled as a volumetric force by the Continuum Surface Force method (CSF):

$$\mathbf{F} = \Gamma\kappa\mathbf{n} \tag{3.7}$$

where Γ is the interfacial tension, κ the interface curvature given by -$\nabla\mathbf{n}$ and $\mathbf{n}$ the interface-normal vector. In addition to the Navier-Stokes equations, the Volume-of-Fluid (VOF) method solves an advection equation for the phase indicator function α:

$$\frac{\partial \alpha}{\partial t} + \nabla\cdot(\alpha\mathbf{u}) = 0 \tag{3.8}$$

whereby α varies from 0 for the matrix phase to 1 for the droplet phase, while the grid cells in the interfacial region have an intermediate value between 0 and 1.

Finally, the Courant-Friedrichs-Lewy (CFL) condition based on the maximum Courant number Co is used to limit the time step of the simulations:

$$\mathrm{Co} = \frac{\|\mathbf{u}\|\cdot\Delta t}{\Delta x} \tag{3.9}$$

where $\|\mathbf{u}\|$ is the velocity magnitude in the cell, Δt is the time step, and Δx is the cell size in the flow direction. For all considered cases, Co is limited to 0.2 for both the bulk phase as well as the interfacial region.

3.5.2 Simulation domain and boundary conditions

The software OpenFOAM-5.x [191] is used for computations together with the *interFoam* solver and the extension of the "interfaceProperties" library [173], initially reported by Hoang et al. [70]. Ferreira et al. [48] applied this method to droplet/slug formation in flow-focusing junctions and a more detailed description can be found therein.

A schematic representation of the simulation domain and the applied boundary conditions is shown in Figure 3.7. The simulation domain consists of a 3D cubic box (2 mm × 2 mm × 2 mm) generated with the blockMesh utility. The equations discussed in the previous section are discretized on a uniform mesh in which the droplet with a radius of 100 μm is captured by approximately 25 cells in both the axial as well as the radial direction. These dimensions were selected to ensure that the droplet does not experience any confinement effects and only unbounded simple shear deformation is considered. In addition, it was found that hybrid meshes with a fine structured mesh covering the droplet deformation area surrounded by an unstructured coarse mesh disrupt the continuity of momentum fluxes. Finally, the mesh consists of 15 625 000 cubic cells with a side length of 8 μm.

The boundary conditions of the problem include a constant velocity in the x-direction ($\pm\ u_x$, 0, 0) imposed on the top and bottom faces ($z = \pm$ 1 mm). Hence the x-direction and z-direction correspond to the velocity and velocity gradient direction, respectively. On all other faces, periodic boundary conditions are applied to maintain flux continuity (Figure 3.7). These boundary conditions result in a linear steady-state velocity profile as depicted in Figure 3.7.

Precursor simulations are run to obtain the developed steady-state flow field. Thereafter, the spherical droplet is introduced to this flow field with the droplet centre at the origin of the coordinate system and thus at the zero-velocity plane. This situation corresponds to the initial condition at time $t = 0$ s. Placement at the centre of the domain induces flow symmetry in y and asymmetry in (x,z), and the droplet will not migrate.

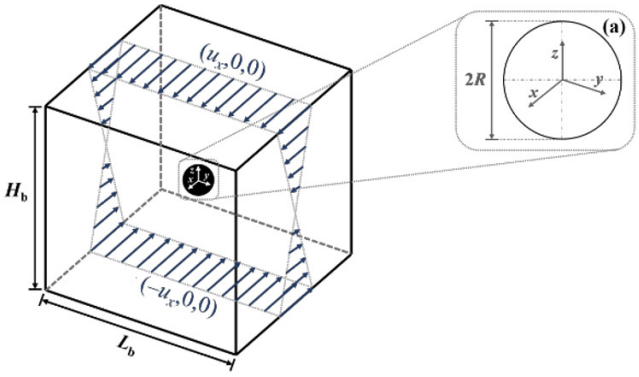

Figure 3.7: Schematic representation of the simulation domain ($H_\mathrm{b} = L_\mathrm{b} =$ 2 mm) and the imposed boundary conditions. The inset (a) depicts droplet isosurface and dimension.

The capillary number is imposed for the simulations, so that the upper and lower plate velocities are given by

$$\pm\, u_x = \dot{\gamma}\frac{H_b}{2} \tag{3.10}$$

where H_b is the height of the simulated box (2 mm) and $\dot{\gamma}$ the shear rate corresponding to a specific capillary number. For each system, three different capillary numbers are simulated: 0.2, 0.3, and 0.4.

We chose to simulate MS-1.4 ($\lambda = 1.4$, $R = 109$ µm) and MS-0.08L ($\lambda = 0.08$, $R = 105$ µm) because these two systems showed clear and unambiguous particle migration in opposite vorticity directions as will be shown in Chapter 4. The conditions for which the two systems are simulated correspond to the experimental conditions.

Steady-state for the numerical droplet deformation is reached within 10 s, even for the lowest capillary number (Ca = 0.2). However, we continued the simulation until 15 s for two of the simulated cases (MS-1.4, Ca = 0.2 and 0.3) to ensure steady-state was reached. To validate the simulation results, the droplet deformation under shear flow is compared with the experimental results. The dimensionless droplet axes are determined by fitting an ellipse through the droplet contours in the velocity-vorticity plane and the velocity-velocity gradient plane. Finally, the streamlines are also determined from the calculated

velocity field. The visualization of these streamlines is realized by an algorithm that imposes exact periodicity, despite the small loss of droplet mass due to numerical inaccuracies (see Appendix A.5). Consequently, closed streamlines are calculated which approximate the real streamlines, even when the velocity field is non-solenoidal due to small numerical inaccuracies.

Chapter 4

Migration of non-Brownian particles localized inside sheared droplets

During the CR experiments to determine single droplet dynamics of particle-filled droplets, presented in Chapter 5, it was, unexpectedly, observed that the particles inside the droplets migrate towards a non-homogenous steady-state particle distribution under the application of shear flow. Surprisingly, the final steady-state particle distribution observed differs for the different investigated systems. Based on these first observations, it was decided to also study this migration behavior in more detail in order to identify the driving mechanisms. Therefore, the evolution of the particle distribution in the different systems studied is thoroughly analysed in the first section of this chapter. In order to evaluate the possible driving forces for particle migration inside the sheared droplet, the velocity magnitudes, streamlines, and shear rate magnitudes inside the droplets of two different systems, MS-1.4 and MS-0.08L, are determined by VOF simulations. The results of these numerical predictions are discussed in detail in the second section. Finally, section 4.3 evaluates the possible driving forces, identified in literature (Section 2.2.3 of Chapter 2), using the predictions of the VOF simulations.

The following chapter is written in format of a manuscript to be submitted:

H. Van Ammel*, J. Ferreira*, A. Kruitwagen, S. Fransen, P. Moldenaers, S. Kuhn, and R. Cardinaels. Migration of non-Brownian particles localized inside sheared droplets.

H. Van Ammel designed and executed the major part of the experiments and performed the data post-processing. The numerical simulations are performed in collaboration with Prof. S. Kuhn of the section Process Engineering for Sustainable Systems (ProcESS). J. Ferreira performed the major part of the numerical simulations. S. Fransen calculated the streamlines and wrote the corresponding appendix (Appendix A.5 in this work). H. Van Ammel and J. Ferreira equally contributed to writing the major part of this manuscript.

4.1 Particle distribution

This section first focuses on the droplet-matrix systems containing high particle concentrations (5 – 20 vol%) by analyzing the steady-state particle distribution after the application of shear flow as well as the time evolution towards this equilibrium distribution. Finally, the results of experiments performed with droplets containing only 1 vol% PS25 particles are presented in order to obtain a better understanding of the underlying mechanisms affecting the particle migration behavior.

4.1.1 Steady-state particle distribution

The evolution of the particle distribution is first examined for every particle system when no shear flow is applied. As already mentioned in section 3.3.2 of Chapter 3 (Figure 3.3), the particle distribution does not change in this situation and the particles do not migrate towards the interface or matrix phase. However, during the application of shear flow, it is noticed that the random particle distribution, initially present inside the droplets, develops towards a non-homogeneous equilibrium particle distribution. These changes are especially observed in the velocity-vorticity plane (top view), while in the velocity-velocity gradient plane (side view) no significant differences are observed as can be seen in Figure 4.1. Therefore, this section only shows images captured in the velocity-vorticity plane (top view).

For particle systems based on MS-1.4 and with only 5 vol% PS25 present in the droplet phase, the particles circulate inside the droplet, but also migrate in

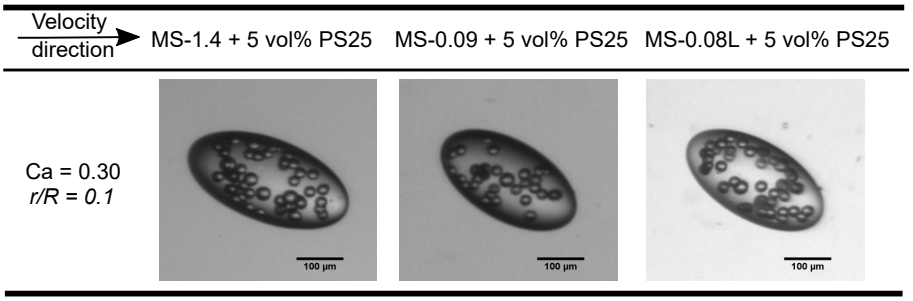

Figure 4.1: Images of particle-filled droplets (5 vol% PS25) added to MS-1.4, MS-0.09 and MS-0.08L captured in the side view (velocity - velocity gradient plane). Steady-state particle distribution is reached. All images are for Ca = 0.30.

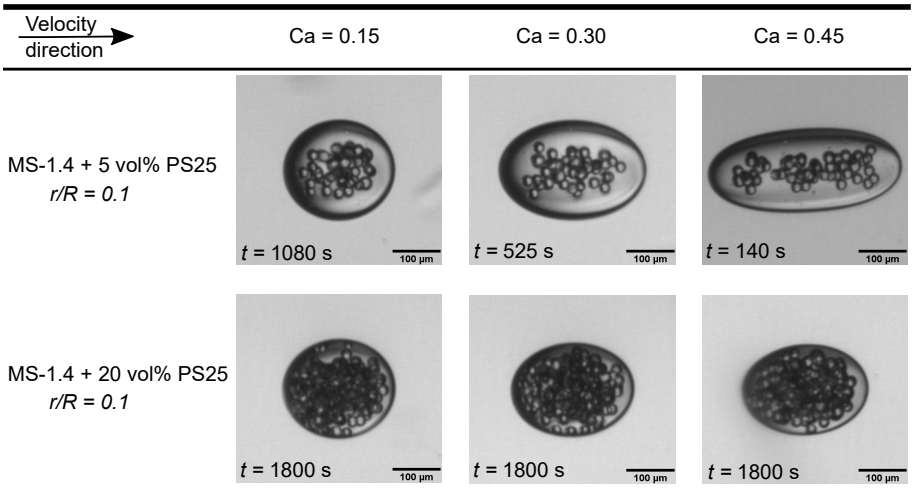

Figure 4.2: Steady-state particle distribution of particle systems based on MS-1.4 subjected to shear flow with a capillary number of 0.15, 0.30, and 0.45. Time is indicated for every image and corresponds approximately to the time at which the steady-state particle distribution is reached, with $t = 0$ s corresponding to the moment shear flow is started. All images are taken in the top view (velocity - vorticity plane).

the vorticity direction towards the central droplet axis as can be seen in Figure 4.2 for three applied capillary numbers: 0.15, 0.30, and 0.45. As a result, all the particles are situated close to the central axis after the application of shear flow. Figure 4.2 also provides the images of MS-1.4 + 20 vol% PS25 for which the particle distribution does not show significant changes over time, even if the shear flow is applied for 30 minutes. During these experiments, the only change noticed is a decrease in the amount of particles present near the droplet edges and in the droplet tips. Probably, particle migration towards the central axis is inhibited in this case because the maximum particle packing density is reached in this region. Systems with an intermediate particle concentration (10 vol% and 15 vol%) also showed significant changes in the particle distribution and a clear particle migration towards the central axis in the velocity-vorticity plane, as illustrated in Appendix B.1.

Similar to Figure 4.2, the steady-state particle distributions of the particle systems based on MS-0.08L and MS-0.09 are given in Figures 4.3 and 4.4, respectively. It is immediately clear from this overview, that a similar change in particle distribution as for particle systems based on MS-1.4 is not observed. First, the results of the systems based on MS-0.08L (Figure 4.3) are discussed which show particle migration in the vorticity direction for all applied capillary numbers, particle concentrations, and particle sizes. However, in contrast with the systems based on MS-1.4, the particles migrate away from the central axis instead of moving towards the central axis in the velocity-vorticity plane. Consequently, two regions in which the particles circulate appear, separated by a particle-free region along the central droplet axis. The width of this particle-free region ranges from approximately 15 to 36 μm ($R = 108 \pm 5\mu m$). However, the particle-free region does not always coincide exactly with the central droplet axis, as can be seen in Figure 4.3 for MS-0.08L + 20 vol% PS25 at a capillary number of 0.45. At high capillary numbers ($Ca \geq 0.45$), the particle-free region along the central axis of MS-0.08L + 20 vol% PS44 with a particle over droplet size ratio of 0.2 is less clear due to the lack of space to develop a particle-free region. This conclusion is supported by the results of the droplets which consist of the same system (MS-0.08L + 20 vol% PS44) but with a particle over droplet size ratio of 0.1. This system, also displayed in Figure 4.3, shows a clear particle-free region along the central axis, also at high capillary numbers.

Finally, systems based on MS-0.09 (Figure 4.4), which have a similar viscosity ratio as systems based on MS-0.08L, but consist of PEG-*ran*-PPG as interstitial fluid in the droplet phase, are discussed. MS-0.09 + 5 vol% PS25 shows similar changes as the systems based on MS-0.08L at intermediate and high capillary numbers ($Ca \geq 0.30$). However, an intermediate behavior is seen at low capillary numbers: most of the particles migrate away from the central axis, but some

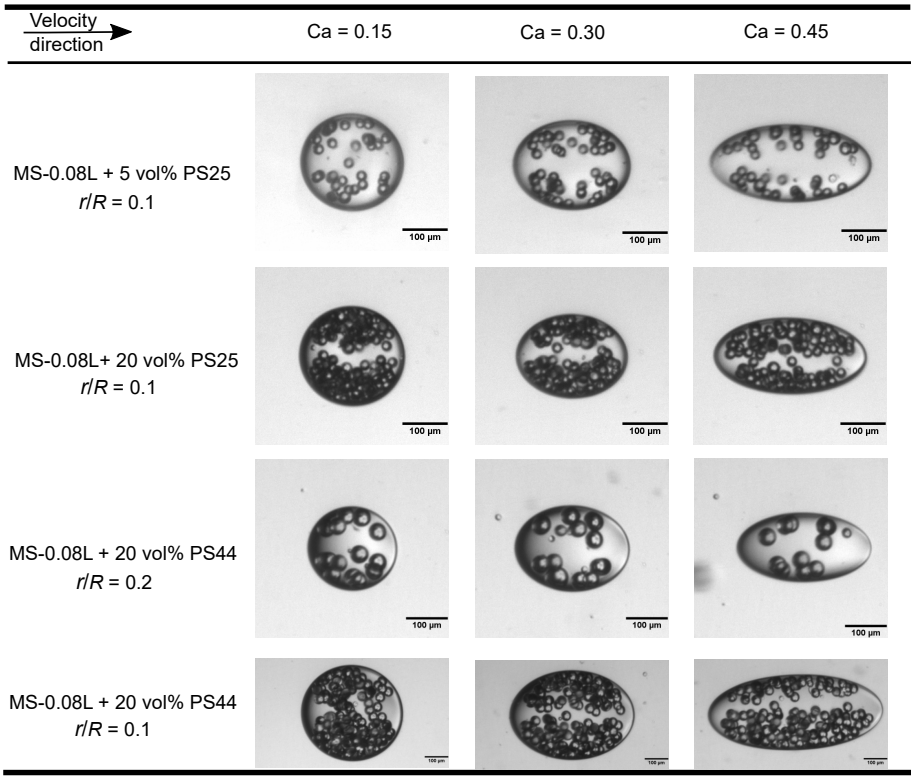

Figure 4.3: Steady-state particle distribution of particle systems based on MS-0.08L subjected to a shear flow with a capillary number of 0.15, 0.30, and 0.45. All images are taken in the top view (velocity - vorticity plane).

particles are still situated along the central droplet axis, like we observed for systems based on MS-1.4. The changes of MS-0.09 + 20 vol% PS25 particles are less clear and only a very small particle-free zone arises.

4.1.2 Time evolution of particle distribution

In addition to the steady-state particle distributions, Figure 4.5 compares the time evolution of the particle distribution of the different systems containing 5 vol% PS25 particles at Ca = 0.30. The dimensionless time t/τ_E, with τ_E the emulsion time of the system, is indicated for every image. Time $t = 0$ s corresponds to the moment shear flow is started and hence, the particle

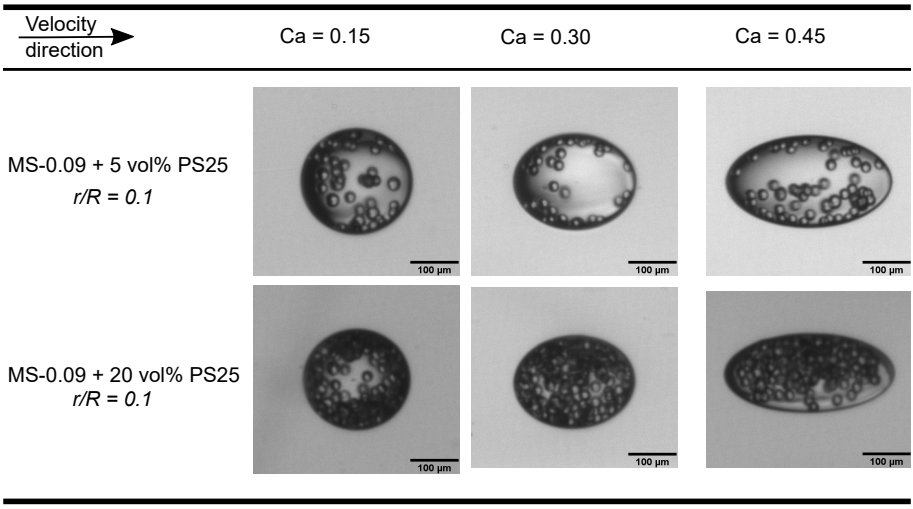

Figure 4.4: Steady-state particle distribution of particle systems based on MS-0.09 subjected to shear flow with a capillary number of 0.15, 0.30, and 0.45. All images are taken in the top view (velocity - vorticity plane).

distribution is still random as shown in the first column for every system. Thereafter, the particle distribution evolves towards the steady-state particle distribution.

For particle systems based on MS-1.4, the particles gradually move away from the droplet edges, closer towards the central droplet axis. From the moment shear flow is applied, no particles are present in the droplet tips. For systems based on MS-0.08L, two particle-free zones are observed near the droplet tips almost immediately after shear flow is started. These zones evolve and grow over time along the central axis towards the droplet centre. The evolution towards this particle-free central region is slightly different for particle systems based on MS-0.09 as more particles are present close to the droplet tips during shear flow and particles mainly migrate towards the outer edges of the droplet. Furthermore, the steady-state particle distribution is reached considerably faster in systems based on MS-0.08L.

The particle distribution after cessation of shear flow is not shown in Figure 4.5, but can be found in Appendix B.2. The droplets relax back to a spherical shape as expected, but the particle distribution does not relax back to a random distribution, as expected for non-Brownian particles.

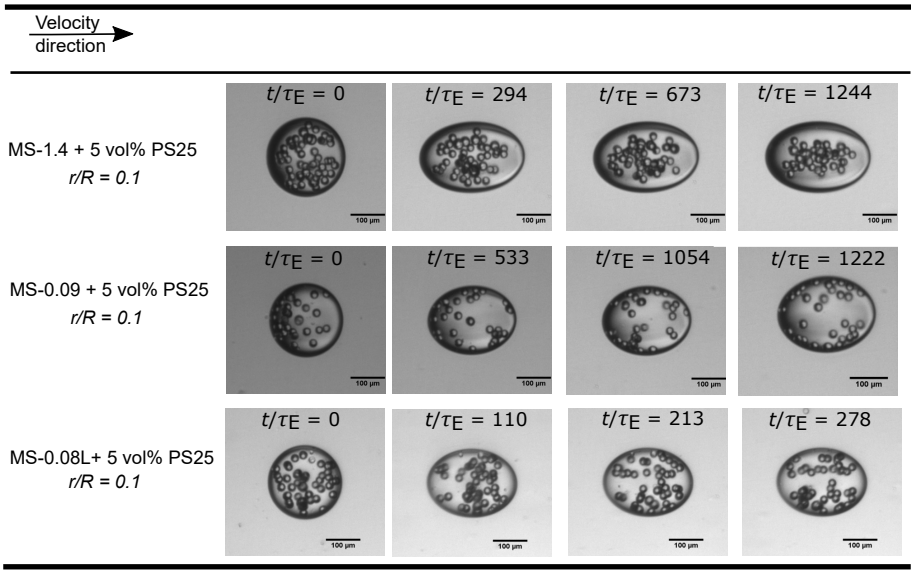

Figure 4.5: Evolution of particle distribution as function of dimensionless time t/τ_{E}, with $t = 0$ s corresponding to the moment shear flow is started. All droplets are subjected to shear flow with Ca = 0.30. All images are taken in the top view (velocity - vorticity plane).

To further understand the particle migration away from the central droplet axis and to gain insight in the underlying mechanisms, the transient particle distributions of the particle systems which show a clear particle-free zone along the central droplet axis in the velocity-vorticity plane are quantitatively analyzed using the following method, also schematically explained in Figure 4.6. First, the sum of the grayscale values over a horizontal line along the velocity direction and through the droplet centre is determined using ImageJ, with a higher grayscale value corresponding to a lighter pixel. This value is then normalized with the background value by dividing it with the sum of grayscale values over a reference line. An example is shown in the inset of Figure 4.6. As already discussed in Figure 4.3, the particle-free region is not always exactly situated along the central droplet axis. Therefore, normalized grayscale values are calculated for 7 different horizontal lines inside the droplet at specific positions along the vorticity axis. Subsequently, the normalized grayscale curve which reaches the highest plateau value is selected for further analysis.

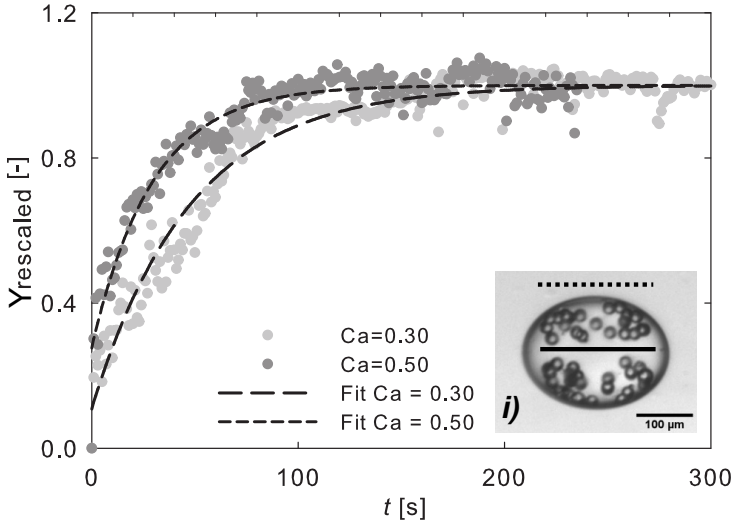

Figure 4.6: Rescaled grayscale data for MS-0.08L + 5 vol% PS25 (Ca = 0.30 and 0.50). The exponential fits are indicated by the dashed lines. Inset (i): Horizontal line inside a droplet over which the sum of grayscale values is calculated (full line) and the corresponding reference line indicated by the dashed line outside the droplet.

It is always verified that this line corresponds to the particle-free region. Thereafter, the normalized grayscale curve is rescaled as follows:

$$\mathrm{Y}_{\mathrm{rescaled}}(t) = \frac{\mathrm{Y}(t) - \mathrm{Y}_0}{\mathrm{Y}_{\mathrm{ss}} - \mathrm{Y}_0}. \tag{4.1}$$

With $\mathrm{Y}(t)$ the normalized grayscale value at time t, Y_0 the normalized grayscale value at the time shear flow is started and Y_{ss} the average plateau value when a steady-state particle distribution is reached. An exponential function (1 - A' $\cdot$ $e^{-t/\tau_{\mathrm{M}}}$) is fitted through the data with A' and τ_{M} as fitting parameters. As an example, Figure 4.6 presents the rescaled grayscale data $Y_{\mathrm{rescaled}}(t)$ of MS-0.08L + 5 vol% PS25 for capillary numbers 0.30 and 0.50 together with the exponential fits obtained indicated by the dashed lines.

From the example in Figure 4.6, it becomes already clear that, as expected, the time necessary to achieve a particle-free region decreases with increasing capillary number. Hence, the particles reach their steady-state position faster if higher shear rates are applied. This conclusion is also valid for particle systems in which the particles migrate towards the central axis. For every image of MS-1.4 + 5 vol% PS25 in Figure 4.2 of the previous section, the time is given

when the image is taken with $t = 0$ s corresponding to the moment shear flow is started. This time corresponds approximately to the time at which the steady-state particle distribution is reached. For low capillary numbers (Ca = 0.15), changes in the particle distribution are only noticed after approximately 10 – 15 minutes, while for high capillary numbers (Ca = 0.45), changes are already visible after less than 2 minutes. The particle distribution changes thus faster with time at higher capillary numbers and hence, the steady-state distribution is also reached faster for these systems. A further quantitative analysis is not made for these systems as it is difficult to quantify when the steady-state particle distribution is reached with image analysis because the particle-free zone in these systems is small and close to the droplet edges.

In addition to Figure 4.6, the characteristic time constants obtained for particle migration as a function of the applied capillary number are compared in Figure 4.7a. The time constants of the different systems show comparable trends as function of the capillary number. From this figure it becomes clear that there exists no linear relationship between the applied shear flow and the time necessary to reach a steady-state particle distribution, which is also expected as Megias-Alguacil [110] demonstrated a qualitatively similar relation between the droplet surface rotation period and the applied shear rate for different droplet-matrix systems with varying viscosity ratios. However, comparing the characteristic time constants τ_M of different systems also allows us to identify the effect of particle size and particle concentration on the particle migration observed which will help to further identify the possible driving mechanisms. It should however be noticed that these data do not provide the migration speed of the individual particles, but the kinetics of the overall microstructure change.

The effect of particle concentration is studied by comparing the data points of MS-0.08L + 5 vol% PS25 in Figure 4.7a with MS-0.08L + 20 vol% PS25. The time constants of both systems first decay considerably with the applied capillary number. At these low and intermediate capillary numbers, the time constants of MS-0.08L + 20 vol% PS25 are slightly higher. The decrease stagnates for both systems at a capillary number of 0.40 and a plateau value is reached. The differences between the characteristic time constants of systems MS-0.08L + 5 vol% PS25 and MS-0.08L + 20 vol% PS25 almost vanish at these high capillary numbers, although the time constant of MS-0.08L + 20 vol% PS25 stays slightly larger as compared to that of MS-0.08L + 5 vol% PS25. The particle-free zone is thus achieved faster at lower particle concentrations. However, at higher particle concentrations, more particles have to migrate away from the central droplet axis. Furthermore, confinement and particle jamming in the other regions can possibly slow down the particle migration at these higher particle concentrations.

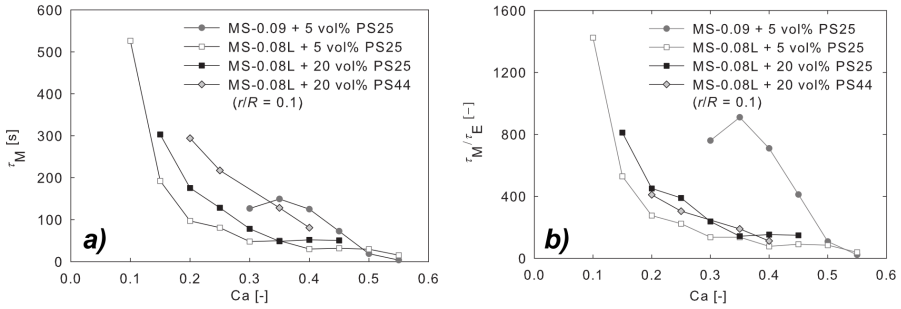

Figure 4.7: (a) Characteristic time scale τ_M for particle migration away from the central droplet axis as function of the applied capillary number Ca and (b) τ_M made dimensionless by dividing it with the respective emulsion time τ_E. For all data r/R is equal to 0.1. Lines are to guide the eye.

The effect of particle size, while the particle over droplet size ratio remains constant ($r/R = 0.1$), is also illustrated in Figure 4.7a. The results show that the time constants of the systems with larger particles (PS44) are larger as compared to those of the systems with smaller particles (PS25) at a constant capillary number. However, the applied shear rates are smaller for the system with larger particles due to the larger droplet size required to to keep $r/R = 0.1$. To eliminate these differences in applied shear rate, the characteristic time constant τ_M is made dimensionless by dividing it with the respective emulsion time τ_E, which is equivalent to multiplying the time constant with the applied shear rate. The dimensionless time constant is shown in Figure 4.7b. The results show that the dimensionless time constants for both particle sizes are similar in the studied range.

Finally, the effect of the droplet phase material and hence, interfacial tension, can be examined by comparing the time constants of MS-0.09 + 20 vol% PS25 with those of MS-0.08L + 20 vol% PS25. The time constants for particle migration in MS-0.09 + 20 vol% PS25 ($\Gamma = 8.5$ mN/m) are significantly larger than those of the equivalent system (MS-0.08L + 20 vol% PS25) with lower interfacial tension ($\Gamma = 3.8$ mN/m). Hence, particles are migrating slower away from the central axis in a PEG-*ran*-PPG droplet as compared to a PPG droplet. The differences become even larger when we compare the dimensionless time constants in order to eliminate differences the in applied shear rate (Figure 4.7b). This result is unexpected as the surface rotation period according to Megias-Alguacil [110] is smaller for a droplet of system MS-0.09 + 20 vol% PS25 as compared to system MS-0.08L + 20 vol% PS25 at a constant capillary number. However, at very high capillary numbers (Ca $\geq$ 0.45), the time constants of the

PEG-*ran*-PPG system become comparable to the time constants observed for PPG systems.

4.1.3 Low particle concentrations

In order to obtain a better understanding of the particle concentration effects on the particle migration, the particle concentration is further reduced to 1 vol% PS25. Consequently, only 5 – 10 particles are present in the droplet phase and hence, the frequency of particle collisions strongly decreases.

During the application of shear flow a clear swinging motion of the particles is observed in the velocity-vorticity plane for the systems with a low viscosity ratio (MS-0.09 + 1 vol% PS25 and MS-0.08L + 1 vol% PS25). Furthermore, the particle circulation speed differs between the different systems with the lowest circulation speed occurring in MS-1.4 + 1 vol% PS25 and the highest circulation speed occurring in MS-0.09 + 1 vol% PS25, which is in agreement with the magnitude of the applied shear rates. Different capillary numbers ranging from 0.30 to 0.45 are applied, but the final steady-state particle distribution is similar for all applied capillary numbers. Therefore, Figure 4.8 gives an overview of the results for Ca = 0.40 as a representative case. The images in the top view (velocity-vorticity plane) are taken during shear flow after a steady-state particle distribution is achieved, while the images in the side view (velocity-velocity gradient) are taken after shear flow is stopped.

Particle migration in the vorticity direction is observed during all the performed experiments, but the steady-state particle positions are different from those observed in the previous section for more concentrated systems. As can be seen in the first column of Figure 4.8, the particles of MS-1.4 + 1 vol% PS25 do not migrate and align around the central droplet axis as is the case for MS-1.4 + 5 vol% PS25. Instead, the particles align symmetrically at both sides of the central axis in the velocity-vorticity plane. This symmetry is confirmed by the images in the side view where all particles seem to be positioned at the same streamline. The particles align on one streamline similar to the regular alignment and spacing of particles in the flow direction of Poiseuille flow observed due to inertia effects [148, 64]. By this alignment, collisions between particles at different streamlines are eliminated, which may suppress further migration.

A different particle distribution appears for MS-0.09 + 1 vol% PS25 and MS-0.08L + 1 vol% PS25. Some particles, indicated by the dashed red lines and circles in Figure 4.8, migrate and align at both sides of the central axis, similar to the particles in MS-1.4 + 1 vol% PS25. However, the other part of the particles present in the droplet, indicated by the full blue circles, migrate away from the central droplet axis towards the droplet edge in the top view, which is similar

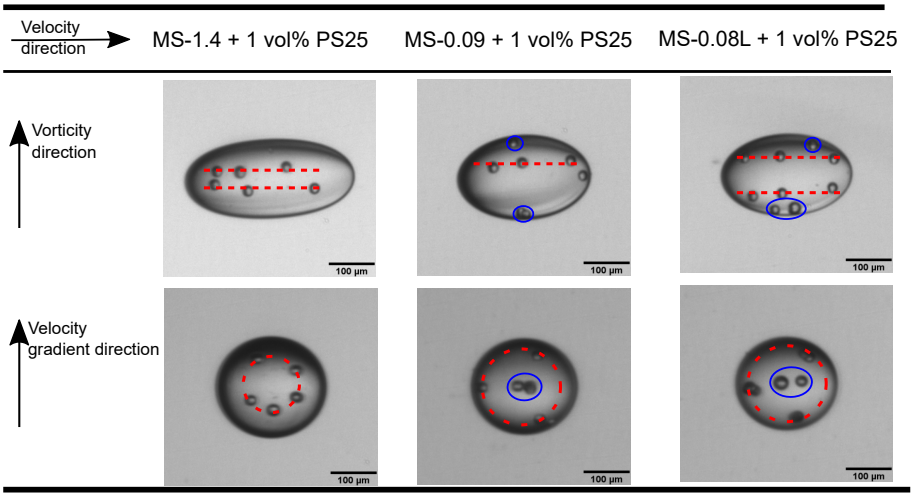

Figure 4.8: Steady-state particle distribution of MS-1.4 + 1 vol% PS25, MS-0.09 + 1 vol% PS25, and MS-0.08L + 1 vol% PS25. Images in the top view (velocity - vorticity plane) are taken during shear flow (Ca = 0.40) after a steady-state particle distribution is achieved, images in side view (velocity - velocity gradient plane) are taken after the shear flow is stopped.

to the migration behavior observed for the more concentrated particle-filled systems based on MS-0.09 and MS-0.08L. At higher applied capillary numbers, more particles migrate towards the droplet edges. These particles are then situated close to the droplet centre in the velocity-velocity gradient and circulate on a streamline with a small radius as the movement is restricted by the droplet edge. This confinement effect is also mentioned by Zhu and Gallaire [200] for a single particle moving towards the droplet edge.

A full quantitative comparison of the particle migration time scales between 1 vol% systems and higher particle concentrations is not possible because the particles migrate to a different location. Determination of the individual particle migration speed in the vorticity direction on the other hand is not possible for systems with a particle concentration of 5 vol% or higher. The time necessary to achieve a steady-state particle distribution is however higher at low particle concentrations for the particle systems based on MS-1.4 and MS-0.08L. Hence, particle collisions enhance particle migration in these systems.

4.2 Numerical simulations

The performed numerical simulations are first validated by comparing the steady-state deformation with the experimental results. These experimental results will be further elucidated in Chapter 5. Thereafter, the velocity profile, streamlines, and shear rate profiles inside a sheared droplet of MS-1.4 and MS-0.08L are compared in detailed.

4.2.1 Steady-state deformation

First, the numerical VOF simulations are validated by comparing the predictions with the dimensionless droplet axes of MS-1.4 and MS-0.08L determined with the single droplet experiments in figure In Figure 4.9. The experimental results will be discussed in more detail in Chapter 5. The droplet contours with α equal to 0.5 are used to determine $L/2R$, $W/2R$, and $B/2R$. Figures 4.9c-f also compare the droplet contours (in red) with the experimental images, these results are for a capillary number of 0.30. For MS-1.4, the numerical predictions coincide with the experimental data for the three investigated capillary numbers (deviations $< 3\%$). As can be seen in Figure 4.9b, the deviations between the experimental results and the numerical predictions are larger for MS-0.08L. At low and intermediate capillary numbers (Ca = 0.20 - 0.30), the deviations are still limited ($< 7\%$), but at a capillary number of 0.40, the numerical prediction of $L/2R$ is 20% higher than the experimental value. However, the predicted droplet shape at this high capillary number shows clear deviations from the ellipsoidal shape and pointed droplet tips. These deviations are caused by numerical inaccuracies during the calculations of the droplet curvature and normal vectors. Therefore, additional difficulties emerge at low interfacial tension values and/or by a sudden jump in the physical properties at the interface (i.e. viscosity, density). Even though the VOF function is smoothed over a finite region around the droplet interface, the particular challenges of a numerical study at low interfacial tension and/or low viscosity ratio still remain. These deviations, attributed to the inaccurate calculation of the surface tension force at high curvature, should be solved by increasing the mesh resolution. Hence, there exists no optimal solution without compromising the computational cost [99]. Despite the large deviation at Ca = 0.40, the numerical results of MS-0.08L are still used to evaluate the driving forces for particle migration because the deviations at Ca = 0.20 and Ca = 0.30 are still limited ($< 7\%$).

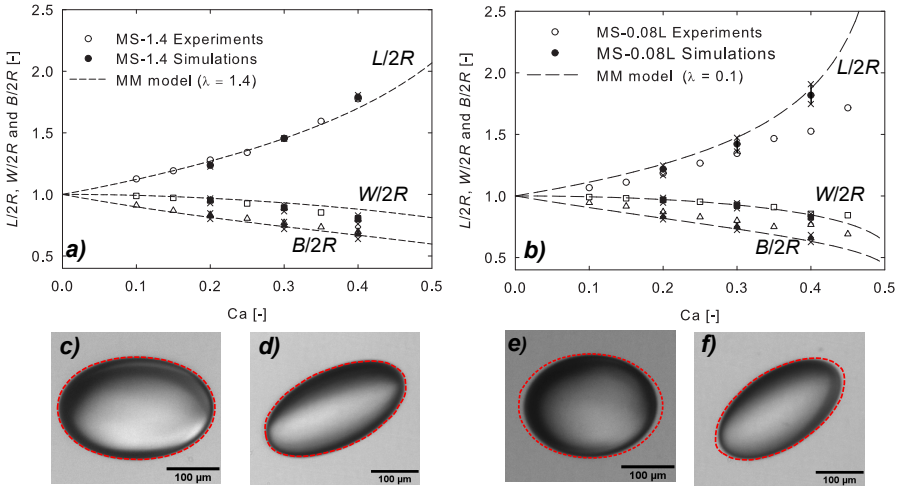

Figure 4.9: Comparison of steady-state droplet deformation calculated from the numerical simulations and the experimental results for MS-1.4 (a, c, and d) and MS-0.08L (b, e, and f). (a-b) $L/2R$, $W/2R$, and $B/2R$ as function of capillary number. Data points of numerical predictions are calculated for contours with $\alpha = 0.5$. The error bars represent the results for $\alpha = 0.1$ and $\alpha = 0.9$. Droplet contours at Ca = 0.30 from numerical predictions (red line, $\alpha = 0.5$) and droplet images captured in the top view (velocity - vorticity plane) (c-e) and the side view (velocity - velocity gradient plane) (d-f).

4.2.2 Velocity and shear rate profiles inside a sheared droplet

The velocity magnitude inside the droplet, shown in Figures 4.10 and 4.11, is normalized by the maximum velocity magnitude observed in that particular slice($y = 0$ or $z = 0$). The values of these maximum velocity magnitudes are summarized in Table 4.1 together with the maximum velocity magnitudes inside the entire droplet domain. In addition, Figures 4.10 and 4.11 show the droplet shapes ($\alpha = 0.5$) predicted by the numerical simulations. At a fixed viscosity ratio, the typical trend of larger droplet deformations with increasing the capillary number follows the previous results reported in the literature [99, 88, 78, 3]. Droplets tend to deform into an ellipsoidal shape following the flow direction, with the deformation level being mainly dependent on the applied shear rate. In the Stokes flow regime with high capillary number, after reaching steady-state, the droplet deviates from the ellipsoidal shape [78], as observed for both systems at Ca = 0.40. At a lower capillary number, the droplet is less oriented towards the flow direction as compared to the droplet orientation at

higher capillary numbers, and the flow field inside the droplet also follows this change.

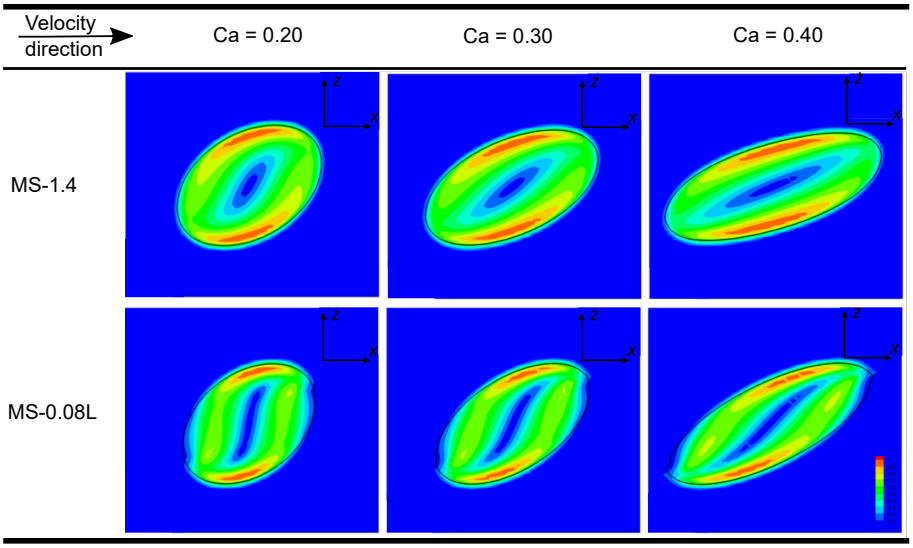

Figure 4.10: Velocity magnitude normalized by the maximum value in that slice and droplet contour at $t = 10$ s for MS-1.4 and MS-0.08L at Ca $= 0.20$, Ca $= 0.30$, and Ca $= 0.40$. Cross-sectional slices in the velocity (x)- velocity gradient (z) plane through the centre of the droplet.

Table 4.1: Maximum velocity and maximum shear rate magnitudes observed inside the entire droplet domain or in a slice of the droplet at $y = 0$ (corresponding to Figure 4.10) or $z = 0$ (corresponding to Figure 4.11).

System	Ca	$\|\mathbf{u}\|^{\max}_{\text{drop}}$	$\|\mathbf{u}\|^{\max}_{y=0}$	$\|\mathbf{u}\|^{\max}_{z=0}$	$\|\dot{\boldsymbol{\gamma}}\|^{\max}_{\text{drop}}$	$\|\dot{\boldsymbol{\gamma}}\|^{\max}_{y=0}$	$\|\dot{\boldsymbol{\gamma}}\|^{\max}_{z=0}$
	[-]	$[10^{-5}$ m/s]			$[\text{s}^{-1}]$		
	0.20	2.73	2.73	1.91	0.51	0.51	0.32
MS-1.4	0.30	4.13	4.13	2.83	0.89	0.89	0.47
	0.40	5.24	5.24	3.50	1.29	1.29	0.75
	0.20	4.05	4.05	2.58	1.86	1.85	0.79
MS-0.08L	0.30	6.64	6.64	4.36	3.48	3.30	1.19
	0.40	9.51	9.51	6.47	5.60	5.52	1.62

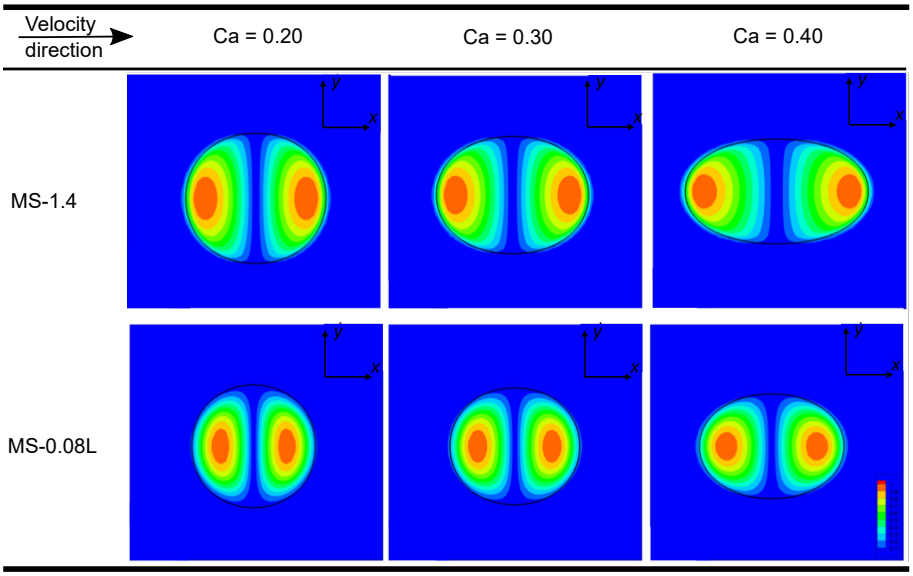

Figure 4.11: Velocity magnitude normalized by the maximum value in that slice and droplet contour at $t = 10$ s for MS-1.4 and MS-0.08L at Ca = 0.20, Ca = 0.30, and Ca = 0.40. Cross-sectional slices in the velocity (x)- vorticity (y) plane through the centre of the droplet.

The velocity field, shown in in Appendix B.3, is tangential to the interface near the droplet, where the velocity vectors follow the droplet contour, while far away from the droplet, the flow moves towards the u_x-direction and $-u_x$-direction at the upper and lower plates, respectively. By the competition between the externally imposed shear flow and the surface tension driven flow, an internal circulation flow develops inside the droplet. A stronger vortex flow is present in droplets subjected to higher capillary numbers. For system MS-0.08L the droplet phase is less viscous than the matrix phase ($\lambda < 1$), and hence the surface shear will drastically intensify the internal flow as compared to that in MS-1.4. This is observed in the velocity vectors inside the droplet, and in the values of the maximum velocity magnitude given in Table 4.1, while the applied shear rates, and hence velocities in the matrix phase are only slightly higher in system MS-0.08L to maintain a similar capillary number.

Another apparent difference between the two simulated cases is observed from the velocity field and the calculated streamlines in the velocity (x) - velocity gradient (z) plane (Figures 4.12a-b), which varies from a single vortex to a double vortex structure for systems MS-1.4 and MS-0.08L, respectively. The

vorticity magnitude (Appendix B.4) confirms this difference. This effect is also predicted for decreasing viscosity ratios in previous numerical simulations [85, 3] as well as analytical calculations [10, 169]. Furthermore, Figures 4.12c-d shows the 3D representation of the streamlines in MS-1.4 and MS-0.08L for Ca = 0.30. The 3D shape of the streamlines is similar to a saddle shape which is more curved in the vorticity direction for system MS-0.08L. The swinging motion of the particles observed in the experiments of MS-0.08L + 1 vol% PS25 is caused by this more pronounced curvature in the vorticity direction.

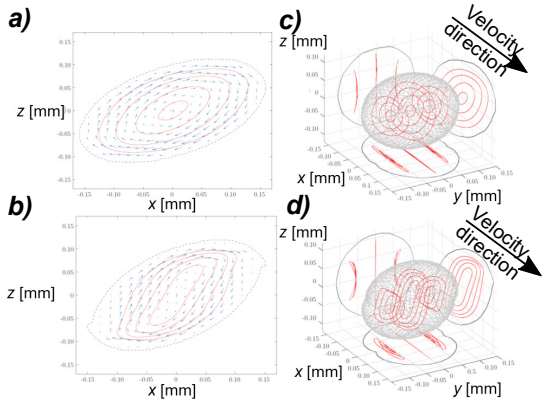

Figure 4.12: Velocity streamlines inside the droplet at $t = 10$ s (Ca = 0.30) calculated using the proposed algorithm (Appendix A.5) for (a-c) MS-1.4 and (b-d) MS-0.08L. (a-b) Cross-sectional slice in the velocity (x)– velocity gradient (z) plane through the centre of the droplet and (c-d) 3D representation with the cross-sectional slices through the centre of the droplet in the indicated directions.

As already mentioned in section 2.2.3 of Chapter 2, the shear rate magnitude constitutes an additional tool for interpreting the particle migration. For this reason, the shear rate magnitude is further analyzed. An increase of the capillary number shows a higher deformation for both systems, with an alignment of the droplet along the shear direction. This suggests that increasing the capillary number leads to an increase of the shear rate magnitude, which is confirmed by the increasing trend of the maximum shear rate magnitude with increasing capillary number (Table 4.1). The minimum shear rate magnitude inside the droplet is also calculated for every simulated case and is of the order of 10^{-13}s^{-1} to 10^{-19}s^{-1}. Hence, this minimum shear rate magnitude is negligibly small as compared to the maximum shear rate magnitude inside the droplet. Therefore, the total gradient in shear rate magnitude present inside the droplet is approximately equal to the maximum shear rate magnitude mentioned in

Table 4.1. The maximum shear rate magnitude is higher in system MS-0.08L as compared to MS-1.4. However, it has to be noted that the droplet viscosity of system MS-1.4 is much larger as compared to this of MS-0.08L, which results in higher shear stresses inside droplets of systems MS-1.4 as compared to those in MS-0.08L.

In both systems, a region of high shear rate magnitude exists near the droplet tips as can be seen in Figure 4.13 which shows the shear rate magnitude of both systems in the velocity (x) – vorticity (y) and velocity (x) – velocity gradient (z) planes for Ca = 0.30, normalized by the maximum shear rate magnitude in that particular slice. However, this region is much more extended for system MS-1.4.

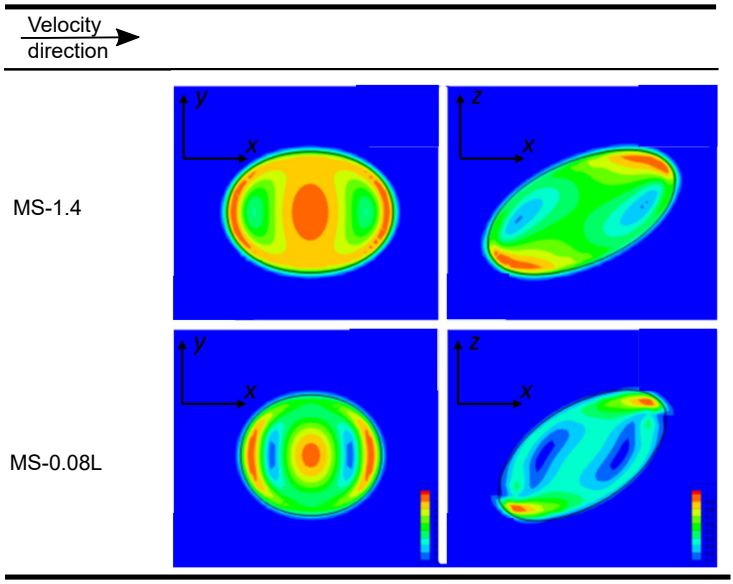

Figure 4.13: Shear rate magnitude normalized by the maximum value in that slice and droplet contour at t = 10 s (Ca = 0.30) for MS-1.4 and MS-0.08L. Cross-sectional slices in the velocity (x)–vorticity (y) and velocity (x)-velocity gradient (z) planes through the centre of the droplet.

In order to better interpret the particle migration behavior in the vorticity (y) direction, additional slices in the velocity (x) – velocity gradient (z) plane are made at different values of y (vorticity direction). Figure 4.14 displays these slices. Due to symmetry, only slices through the positive vorticity axis (y) are plotted. The shear rate magnitude is, in this case, normalized by the maximum shear rate observed in the entire droplet. From these results it is clear that

there exist some differences in the shear rate profile and shear rate gradients between systems MS-1.4 and MS-0.08L which can result in different particle migration behavior as will be elucidated in more detail in the next section. On the one hand, system MS-1.4 has a significantly larger area of high shear rate magnitudes in the droplet tips. Furthermore, across the different slices, excluding the droplet tips, an almost uniform shear rate magnitude is observed. On the other hand, for system MS-0.08L, distinct regions of high shear rate magnitude (closer to the droplet tips) are intercalated by regions of low shear rate magnitude, resulting in a more non-uniform distribution of the shear rate field.

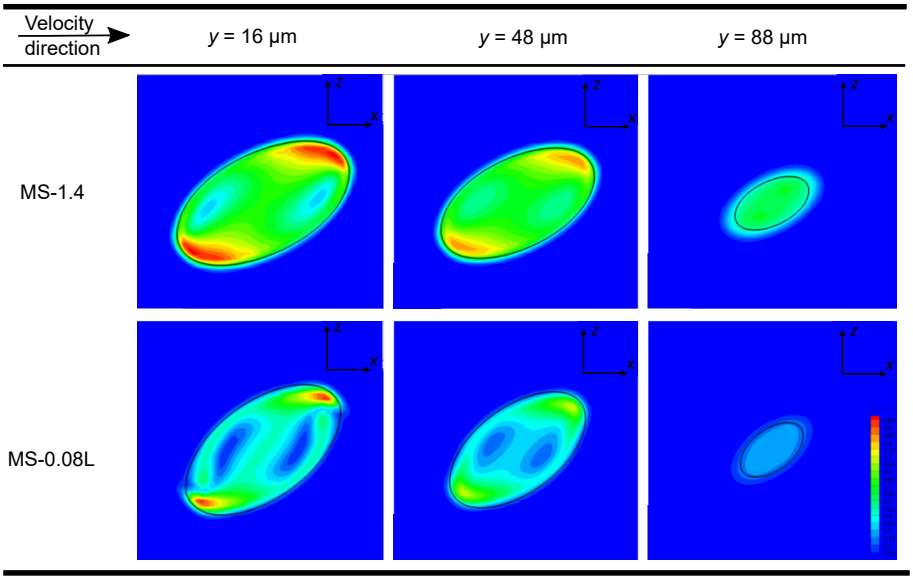

Figure 4.14: Shear rate magnitude normalized by the maximum value in the entire droplet and droplet contour at $t = 10$ s (Ca = 0.30) for systems MS-1.4 and MS-0.08L. Cross-sectional slices in the velocity (x)-velocity gradient (z) plane through $y = 16$ µm, $y = 48$ µm, and $y = 88$ µm. The droplet radius is 109 µm (MS-1.4) and 105 µm (MS-0.08L).

4.3 Possible underlying mechanisms

When shear flow is applied, particle circulation on closed streamlines is observed in all systems studied similarly to the observations of Smith and van de Ven

[152] and Desse et al. [33]. However, the particles migrate in the vorticity direction away or towards the central axis depending on the system. A similar observation is made by Liu et al. [101] who performed numerical simulations on a droplet system containing three smaller daughter droplets in extensional flow. The authors observed a movement of the two non-axial daughter droplets towards the droplet edge at low viscosity ratios, while these droplets move away from this interface at higher viscosity ratios. Zhu and Gallaire [200] on the other hand reported cross-stream motion of a single particle in the vorticity direction inside a sheared droplet which depends on the applied capillary number and the particle over droplet size ratio. However, in our experiments the equilibrium position is independent of the applied capillary number. Different particle migration mechanisms can be responsible for the migration behavior observed. In this section, the possible driving forces are evaluated by using the results of the VOF simulations.

Buoyancy forces, centripetal forces, and secondary flows can be responsible for particle motion across streamlines. The settling velocity of a single particle inside the droplet is calculated according to Stokes' law (Equation 2.18). Subsequently, the travel distance due to sedimentation in the time frame of our experiments is estimated by multiplying the settling velocity with the time necessary to reach a steady-state particle distribution. The estimated travel distances are relatively small, in the range from -0.3 μm for particle systems based on MS-1.4 to 25 μm for particle systems based on MS-0.08L containing PS44 particles. However, it should be noted that no settling of the particles is observed in the velocity – velocity gradient plane after steady-state distribution is already reached, as can be seen in Figure 4.1. Furthermore, buoyancy forces cause the particles to migrate in the vertical direction, the velocity gradient direction in our case. Consequently, we can conclude that buoyancy forces only have a minor effect on the particle trajectories and are not the driving force of the particle migration observed in the vorticity direction.

The migration attributed to centrifugal forces is estimated by calculating the centripetal radial migration speed of a particle in simple rotational flow (Equation 2.30). A worst-case scenario is calculated by taking the velocity equal to the maximum velocity occurring in the droplet of MS-0.08L (Table 4.1) whereby the particle's radial position is varied. The estimated migration velocities are of the order of 10^{-4}μm/s and are therefore negligible.

Secondary flows, defined as deviations in the flow profile from the main velocity field, can also give rise to particle migration. From the velocity fields observed, we can state that, if secondary flows exist in the system, they are very small. However, it has to be noted that the streamlines are calculated by using an algorithm that eliminates divergence by imposing exact periodicity. Hence, this method can possibly also eliminate the onset of secondary flows which

makes it impossible to reveal secondary flows with the current simulations. In literature, Kennedy et al. [85] stated that internal eddies arise in systems with a low viscosity ratio ($\lambda = 0.08$) induced by two near-stagnation points on the droplet surface. In addition to the minimum velocity magnitude close to the droplet centre, we notice in Figure 4.10 for MS-0.08L also a very small velocity magnitude (dark blue) close to the droplet edge, which is not the case for MS-1.4. Furthermore, the addition of particles can possibly also induce secondary flows.

Particles suspended in a non-Newtonian medium can also exhibit migration behavior induced by normal stresses or viscosity gradients [69]. However, the suspending media used in this work (PEG-*ran*-PPG and PPG), as well as the suspensions, behave as Newtonian viscous fluids. Additionally, the normal forces exerted during rheological experiments are smaller than the device limit and are therefore negligible.

Inertia induced migration is another common driving force for particle migration in suspension flow. In this case, different coupled effects often result in a specific equilibrium position depending on the applied flow field, Reynolds number, flow geometry, etc. To eliminate inertia as a driving force for the particle migration observed, the particle Reynolds number $\mathrm{Re_p}$ is calculated (Equation 2.26). Particle Reynolds numbers of the order $O(10^{-3})$ can already give rise to cross-stream motion of particles [57]. The maximum shear rates obtained from the VOF simulations for Ca = 0.40 (Table 4.1) are used to estimate the particle Reynolds number. MS-0.08L + 20 vol% PS44 has the highest particle Reynolds number which is of order $O(10^{-6})$. Hence, inertia induced particle migration can be eliminated as underlying migration mechanism.

The trajectory of a particle moving near a deformable interface is affected by the induced deformation of that interface [12]. However, during most experiments no outwards bulging of the particles and subsequent interface deformation is observed as most particles are not localized near the droplet interface. Only for MS-0.08L + 20vol% PS44 with a high particle to droplet size ratio ($r/R = 0.2$) outwards bulging of the particles is observed at higher capillary numbers (Ca ≥ 0.40). The particles are on the other hand still confined inside the droplet phase domain and hence, their motion is restricted. This confinement and the subsequent hydrodynamic interactions can also affect the particle trajectories. In addition, the jamming of particles at high particle concentrations in a certain region of the droplet can inhibit further migration towards that region. However, confinement in the systems containing only 1 vol% PS25 is limited, and yet particle migration in the vorticity direction is observed in these systems. Consequently, we can conclude that confinement will definitely have an effect on the steady-state particle distribution in our systems, especially at large volume fractions or large particle to droplet size ratios, but is not the main driving

force.

Finally, shear-induced migration is a migration mechanism that originates from particle interactions and therefore particularly dominates at higher particle concentrations and when pronounced shear rate gradients or streamline curvatures exist [96, 114]. In general, particles will migrate towards zones of low shear rates and less streamline curvature [96, 93]. The VOF numerical simulations in section 4.2 revealed that shear rate gradients and streamline curvatures are present in MS-1.4 and MS-0.08L. For both systems, the droplet tips are the region with the highest shear rate, but the extent of this high shear rate zone strongly differs between MS-1.4 and MS-0.08L. If we compare the slices of the shear rate magnitude along the vorticity direction (Figure 4.14), we notice that this high shear rate region in the droplet tips vanishes further away from the central plane. Furthermore, the particles circulate on closed elliptical streamlines in the velocity-velocity gradient plane. As already observed earlier in literature [10, 169], the eccentricity of the elliptically shaped streamlines decreases along the vorticity direction further away from the droplet centre and hence, the streamlines become more spherical shaped. The curvature in the vorticity direction increases further away from the central plane. The streamlines of MS-0.08L clearly show more curvature in the vorticity direction as well as in certain regions of the closed streamlines in the velocity-velocity gradient plane as compared to the streamlines of MS-1.4. However, this curvature of circulation is higher than the curvature in the vorticity direction. From this discussion, it becomes clear that shear-induced and curvature-induced migration can play an important role in the systems studied. It is however difficult to quantitatively evaluate the criteria for minimum shear rate and streamline curvature because the particles are not stationary, but continuously circulate on closed streamlines inside the droplet and these streamlines have a complicated 3D shape as illustrated in Figure 4.12.

In the following, the steady-state particle distributions experimentally observed are compared with the identified regions of minimum shear rate and streamline curvature. The identified region of maximum shear rate is for all systems in the droplet tips. This corresponds to the experimental observations that from the moment shear flow is started no particles are observed in or close to the droplet tips in MS-1.4 + 5 vol% PS25. Similarly, the particle separation observed for particle systems based on MS-0.08L also originates from the droplet tips. The simulations reveal symmetry in the flow profiles which is also observed in the particle distributions inside the droplets containing 1 vol% PS25 particles. In these systems, particles align and circulate on a streamline between the central plane ($y = 0$) and the droplet edge. This region of circulation qualitatively agrees with a combined optimization of minimized shear rate and streamline curvature. The streamlines that go through the area of minimum shear rate

magnitude in the central plane ($y = 0$), will also go through the high shear rate zones located in the droplet tips whereas the more outward streamlines have on average a higher curvature. By migration in the vorticity direction towards an intermediate slice the particles avoid these high shear rate regions, while still minimizing the curvature of its streamline. For MS-0.09 + 1 vol% PS25 and MS-0.08L + 1 vol% PS25, part of the particles migrate in the vorticity direction towards the droplet edges. This region corresponds to the low shear rate zone close to the droplet edge for MS-0.08L (slice $y = 88$ μm in Figure 4.14) where the high shear rate region in the droplet tips completely disappeared.

At higher particle concentrations, particles added to MS-1.4 migrate towards the central axis in the velocity-vorticity plane, the zone with the least streamline curvature, but avoid the high shear rate zones located in the droplet tips. In contrast, the particles added to MS-0.09 and MS-0.08L migrate away from this central axis to zones where the curvature of the streamlines in the vorticity direction increases, while the streamlines become more spherical shaped avoiding the regions with high curvature in the elliptically shaped streamlines of the central plane. In addition, the high shear rate regions in the droplet tips disappear in these slices.

The differences and trends observed can not be fully explained, especially if we look in more detail to the quantitative results. Shear-induced migration originates from particle interactions and is therefore a strong function of the particle concentration. If the timescales of the 1 vol% PS25 experiments are compared with the timescales of the 5 vol% PS25 experiments, we can conclude that particle interactions definitely accelerate the migration process for particle systems based on MS-1.4 and MS-0.09. In contrast, the time scale of MS-0.08L + 20 vol% PS25 is even larger as compared to that of MS-0.08L + 5 vol% PS25, which means a longer time is needed to reach the steady-state distribution. A full quantitative comparison is however not possible because the particles migrate to different locations (1 vol% vs. $\geq$ 5 vol%) and it is not possible to determine the individual particle migration speed from the experiments with 5 vol% particles or more. The flux associated with shear-induced migration is also a function of the particle size, but in these experiments almost no difference in the migration time scale is observed between PS25 and PS44 particles at a concentration of 20 vol%. It is however possible that other effects i.e. confinement start to interfere at these high particle concentrations. In addition, the differences in migration speed and particle distribution between MS-0.09 and MS-0.08L are not completely understood yet.

In general, shear-induced migration is probably one of the driving mechanisms of the particle migration observed as well as migration induced by streamline curvature. However, the flow profile and conditions inside the droplet are very complex and therefore other factors, including confinement and possible

secondary flows, might also play a role. Consequently, the steady-state distributions observed are a result of different effects that occur simultaneously and compete with each other. It also has to be noticed that the current VOF simulations and discussion do not take into account the disturbance flow inside the droplet induced by the particles which will also affect particle migration phenomena. However, including these effects is not feasible with the current numerical model.

4.4 Conclusion

During preliminary experiments, it was noticed that the random particle distribution inside a particle-filled droplet significantly changes when the droplet is subjected to simple shear flow. In general, the particles migrate in the vorticity direction, but the final steady-state particle distribution surprisingly differs between the different systems studied. Therefore, it was decided to study this unexpected phenomenon in more detail in order to identify the possible driving mechanisms.

At very low particle concentrations (1 vol% PS25), most particles align on a streamline between the central plane ($y = 0$) and the droplet edge in the vorticity direction. Additionally, some particles in systems with a very low viscosity ratio ($\lambda = 0.08$), migrate in the vorticity direction towards the droplet edge. At higher particle concentrations, the particles in systems with a high viscosity ratio ($\lambda \sim 1.4$) migrate towards the central axis in the velocity–vorticity plane, while particles localized in droplets of systems with a very low viscosity ratio ($\lambda = 0.08$) migrate away from this central axis. The latter results in a particle-free region along the central droplet axis in the velocity–vorticity plane. This effect is more pronounced in the system with a lower interfacial tension in which the steady-state distribution is also achieved faster.

Numerical VOF simulations on the particle-free droplet-matrix systems revealed differences in streamlines and shear rate gradients between MS-1.4 ($\lambda = 1.4$) and MS-0.08L, which has a lower viscosity ratio and smaller interfacial tension. The streamlines of the latter system show the existence of a double vortex as compared to that of a single vortex for MS-1.4 as expected based on previous results found in literature (Section 2.1.3 in Chapter 2).. In addition, the saddle-shaped streamlines are more curved in the vorticity direction for MS-0.08L. Finally, the shear rate magnitudes and hence, shear rate gradients, are larger in the system with the lower viscosity ratio (MS-0.08L). However, for both systems, the maximum shear rate magnitude occurs in the droplet tips.

Using the predictions of these simulations, we evaluated the different possible driving forces of particle migration. Buoyancy forces, centripetal forces, inertia, and elasticity could be eliminated as main particle migration mechanism occurring in the vorticity direction. Shear-induced migration towards zones of lower shear rate and less streamline curvature can qualitatively explain part of the experimental results observed. However, additional effects like confinement inside the droplet, potential secondary flows, and particle disturbance flow can also affect the cross-streamline motion of particles. Hence, the simultaneous occurrence of different effects in addition to the very complex flow profile and geometry hampers a full quantitative analysis and in-depth interpretation of the particle trajectories observed inside the droplet. Furthermore, a detailed quantitative comparison of the experimental results is currently not possible because particles migrate towards different steady-state locations and the individual particle migration speed cannot be determined at particle concentrations of 5 vol% or higher. In further work, numerical simulations of the actual three-phase systems consisting of particle-filled droplets, is indispensable.

Chapter 5

Dynamics of sheared droplets filled with non-Brownian particles

The literature review in Chapter 2 demonstrates that most studies compare the dynamics of the particle-filled droplets with those of the neat blend and the effects observed are mainly attributed to the non-Newtonian rheology introduced by the addition of particles. Hence, the intrinsic effects of particles localized in the dispersed phase on the single droplet dynamics of polymer blends remain poorly understood to date. For oil/water systems, qualitative studies conclude that a particle-filled droplets can be treated as a homogeneous medium characterized by its viscosity which is governed by the particle concentration. The aim of this study is to verify this hypothesis by a quantitative study of the steady-state deformation, transient dynamics, and breakup behavior of single droplets containing microsized particles that do not introduce non-Newtonian properties. Therefore, the results are systematically compared with the droplet dynamics of particle-free reference systems with comparable viscosity ratios. The first section examines the effect of the particle distribution on the droplet dynamics observed. In the second section, the effects of the addition of particles to a system with a viscosity ratio larger than one, namely MS-1.4, are discussed. The third section describes the effects of particles added to a system with a viscosity ratio much smaller than one (MS-0.09 and MS-0.08L). The steady-state deformation, start-up, retraction, and breakup behavior of the particle systems are described in detail.

Part of this chapter was previously published and adapted for this dissertation:

H. Van Ammel, P. Moldenaers, and R. Cardinaels. Dynamics of sheared droplets filled with non-Brownian particles. *Rheologica Acta*, 59:935-949, 2020.

H. Van Ammel designed and executed the experiments, performed the data post-processing and wrote the major part of the manuscript.

5.1 Effect of particle distribution

The previous chapter described the migration of particles localized inside a droplet. The non-homogenous steady-state particle distribution is independent of the applied shear rate. For particle systems based on MS-1.4, the particles migrate towards the central droplet axis in the top view (velocity - vorticity plane), while for particle systems based on MS-0.08L, the particles migrate away from this central axis. For the work presented in this chapter, it is verified that the particle distribution has no significant effect on the droplet dynamics. Therefore, the effect of the particle distribution on the droplet dynamics is examined in different verification experiments.

For example, two retraction experiments are performed for every system: (i) one with a random particle distribution and (ii) one with the same droplet but after applying shear for a longer time and hence, after a non-homogeneous steady-state particle distribution is reached. Results are comparable for all systems, an example for system MS-1.4 + 19 vol% PS25 and MS-0.08L + 20 vol% PS25 can be found in Figures 5.1a and 5.1b, respectively. As shown in Figure 5.1, the retraction curve of the droplet with a random particle distribution completely coincides with the retraction curve of the same droplet with a non-homogeneous steady-state particle distribution. The deviations between the determined characteristic relaxation times in these two examples are smaller than 2.5% and 3% for, respectively, system MS-1.4 + 19 vol% PS25 and MS-0.08L + 20 vol% PS25. The same method is applied for steady-state deformation experiments and startup experiments.

In general, we never noticed any significant effect of the particle distribution on the relaxation time, nor on the steady-state deformation or startup results. Additionally, the variability observed for a droplet with a random particle distribution is similar to the variability of a droplet with a non-homogenous steady-state particle distribution.

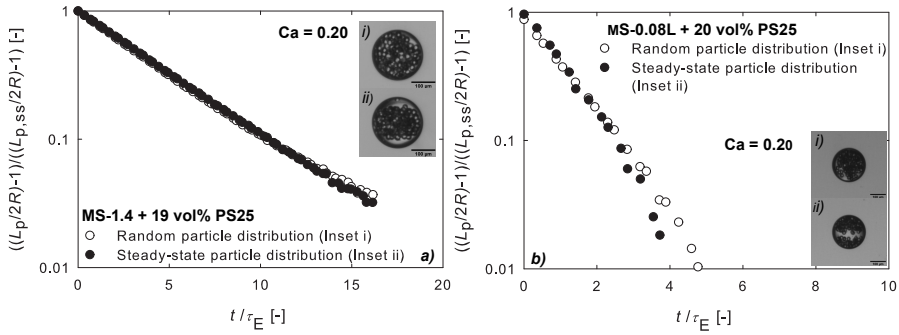

Figure 5.1: Dimensionless parameter $((L_\mathrm{p}/2R)\text{-}1)$ normalized by its steady-state value $((L_\mathrm{p,ss}/2R)\text{-}1)$ as function of dimensionless time t/τ_E during droplet retraction of (a) MS-1.4 + 19 vol% PS25 and (b) MS-0.08L + 20 vol% PS25 with a random particle distribution (open symbols) and with a non homogenous steady-state particle distribution (filled symbols). Inset: Images of the droplets in the top view with (i) random particle distribution immediately after droplet injection and (ii) steady-state particle distribution.

5.2 System with $\lambda > 1$

5.2.1 Determination of actual particle concentration

During the injection of particle-filled droplets, it was noticed that some small particle-free satellite droplets are formed. Consequently, the particle concentrations inside the injected droplets differ significantly from the concentrations of the prepared suspensions. This particle concentration has a significant effect on the viscosity ratio of the particle systems and hence, on the droplet dynamics. Therefore, we determined the actual particle concentration of the injected particle-filled droplets of systems MS-1.4 + Y vol% PSZ.

To determine the particle concentration of the droplets, an average of at least 8 single droplets is investigated. First, the droplet size is determined and thereafter, the single droplet is transferred with a spatula to a microscope slide. Subsequently, the droplet is carefully squeezed between two microscope slides which makes it possible to count the number of particles present in the droplet. Hence, with the particle size, droplet size, and number of particles known, the particle concentration in the droplet can be calculated. However, this method is not applicable for the system which contains 5 µm-sized particles (MS-1.4 + 20 vol% PS5) because the particles are too small to individually count

them at a magnification that allows seeing the complete droplet in the field of view. For this reason, the particle concentration of this system is determined by using confocal microscopy. Droplets containing 20 vol% fluorescent silica particles with a similar particle diameter (7 μm) as system MS-1.4 + 20 vol% PS5 are injected into PDMS and scanned in 3D to determine the actual particle volume fraction with image analysis. We assume that the determined particle volume fraction of the droplets filled with fluorescent silica particles is similar to that of the droplets containing polystyrene particles with a similar size.

The actual particle concentration of the particle-filled droplets is summarized in Table 5.1 which is a revised version of Table 3.4 of Chapter, but with the actual particle concentration instead of the particle concentration of the suspension used to inject the droplet. To avoid confusion, the name of these particle systems is also changed in this chapter to include the actual particle concentration.

Table 5.1: Revised Table 3.4 for systems based on MS-1.4 with actual average particle concentration inside the injected droplets (± standard deviation), viscosity ratios λ at 23 °C and range of viscosity ratios resulting from the variation in particle concentration using the Maron-Pierce equation (Equation 2.25) and the minimal and maximal particle volume concentrations observed.

Particle system	Particle concentration [vol%]	λ [−]	Range λ [−]
MS-1.4 + 6 vol% PS25	6.0 ±1.0	1.6	1.5-1.7
MS-1.4 + 13 vol% PS25	12.5 ±2.3	2.0	1.8-2.2
MS-1.4 + 19 vol% PS25	19.3 ±2.2	2.6	2.3-3.1
MS-1.4 + 23 vol% PS25	22.8 ±1.5	3.1	2.8-3.5
MS-1.4 + 20 vol% PS82	20.1 ±0.3	2.9	2.7-2.8
MS-1.4 + 25 vol% PS5	25.2 ±1.4	3.4	3.1-3.8

The viscosity of the particle-filled droplets is then determined by measuring the viscosity of a suspension with a particle concentration equal to the average particle concentration of the droplets. These data are also included in Figure 3.2 of Chapter 3. Finally, the viscosity ratio λ is determined and listed in Table 5.1. In all further figures, this value of the viscosity ratio is used. In Table 5.1, we also estimated a corresponding viscosity ratio with the Maron-Pierce model (Equation 2.25), indicated by the full line in Figure 3.2, for the minimal and maximal particle concentrations observed.

5.2.2 Steady-state deformation and orientation

The dimensionless droplet axes ($L/2R$, $W/2R$, and $B/2R$) and orientation angles θ, as defined in Figure 2.1, of deformed droplets of MS-1.4 + 23 vol% PS25 are compared with in Figure 5.2 those of the particle-free reference systems MS-1.4 and RS-3.2 as function of the capillary number. In addition, predictions of the MM model [106] are shown as dashed lines in Figure 5.2.

As expected, $L/2R$ of MS-1.4 and RS-3.2 agrees well (deviations $< 5\%$) with the corresponding MM model up to relatively high capillary numbers, as can be seen in Figure 5.2a. In addition, the model is able to accurately predict the droplet orientation of systems with a viscosity ratio around one, as can be seen in Figure 5.2b for MS-1.4. However, for viscosity ratios much higher than one (RS-3.2), the model predicts more orientation towards the flow direction than experimentally observed [106, 180].

The steady-state deformation observed for MS-1.4 + 23 vol% PS25 does not correspond to that of MS-1.4. The particle-filled droplets of MS-1.4 + 23 vol% PS25 deform less and orient more towards the flow direction compared with MS-1.4. A reduced deformation is also observed experimentally in nanoparticle-filled blends [58] and in numerical simulations [171]. The addition of (nano)particles introduces additional viscous and/or elastic stresses resisting droplet deformation [171].

The data for MS-1.4 + 23 vol% PS25 (Figure 5.2) are also not in agreement with the data of the corresponding particle-free system with the same viscosity ratio (RS-3.2). The deviations between particle system MS-1.4 + 23 vol% PS25 and RS-3.2 are relatively small ($\leq$ 7 %) at low and intermediate capillary numbers ($\mathrm{Ca} \leq 0.30$), but become more pronounced at higher capillary numbers (14% at $\mathrm{Ca} = 0.45$). The MM model is fitted through the $L/2R$ data of MS-1.4 + 23 vol% PS25 with the viscosity ratio λ as fitting parameter. The resulting fit ($\lambda = 4.9$) is also depicted in Figure 5.2 as a full line. According to the MM model, the steady-state deformation of system MS-1.4 + 23 vol% PS25 is thus similar to the steady-state deformation of a particle-free droplet with a viscosity ratio of 4.9, which is higher than the viscosity ratio of this system ($\lambda = 3.1$).

The effect of particle concentration and particle size on the steady-state droplet deformation is summarized in Figure 5.3, which gives an overview of $L/2R$ at $\mathrm{Ca} = 0.30$ as a function of the viscosity ratio λ. For every reference system, three droplets with similar parameters are measured and indicated as separate data points in Figure 5.3. Analogously, experiments with 3–6 droplets are performed for the particle systems because the behaviour of these particle systems is less reproducible than that of the reference systems, but differences between different droplets remain smaller than 5.5%. Repeated measurements on the

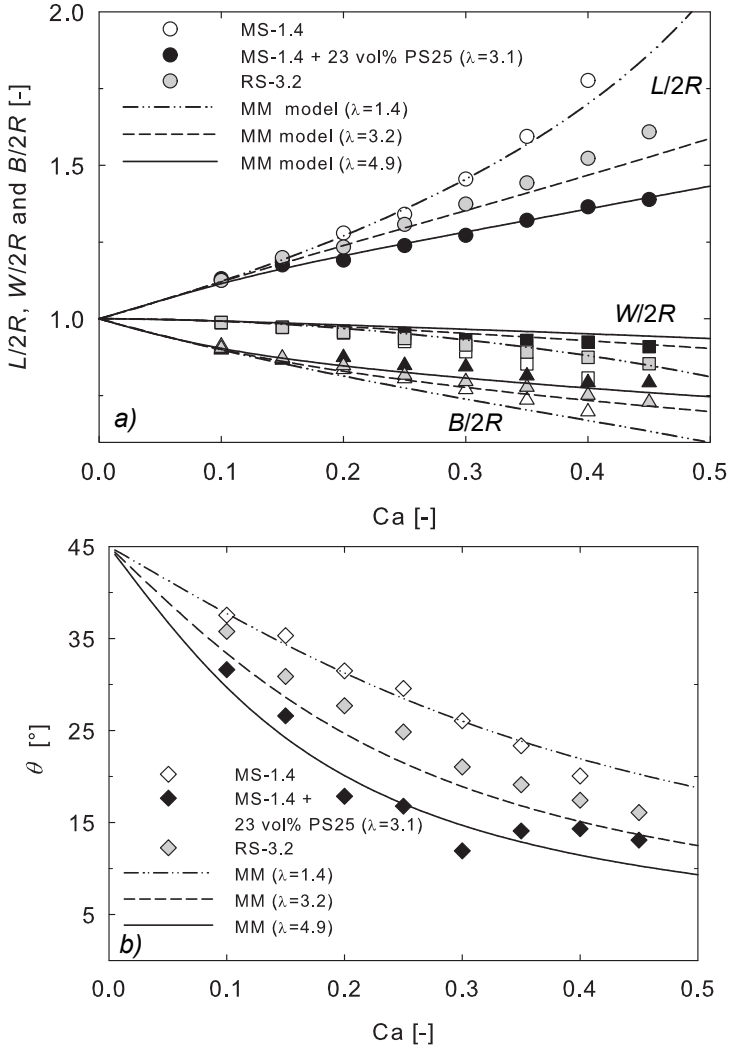

Figure 5.2: (a) Dimensional droplet axes $L/2R$, $W/2R$, and $B/2R$ and (b) orientation angles θ of systems MS-1.4, RS-3.2 and MS-1.4 + 23 vol% PS25 as function of capillary number Ca.

same droplet show a deviation in $L_p/2R$ of less than 4%. It has to be noted that Figure 5.3 is a detailed figure compared with Figure 5.2a as the $L/2R$-axis in Figure 5.3 only spans a very small range (1.20–1.50). All measured values of the mother and reference systems (MS/RS) are slightly larger than the MM model predictions, although deviations are small (< 2.5%).

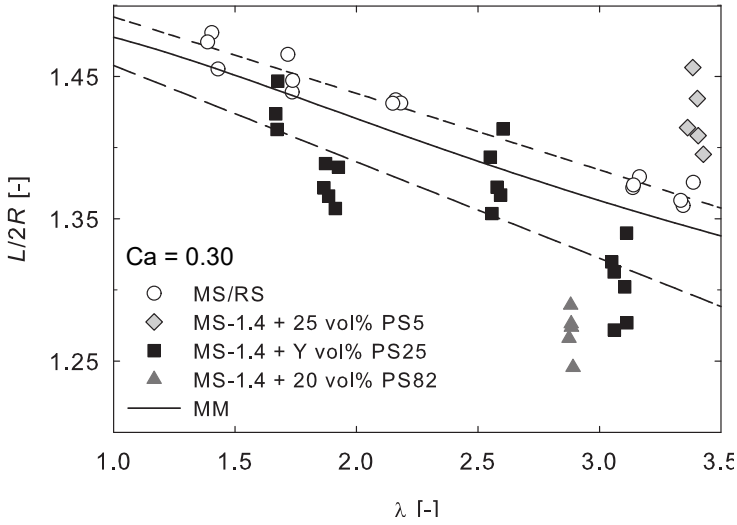

Figure 5.3: Dimensional droplet axis $L/2R$ as function of the viscosity ratio λ. Data points with approximately the same viscosity ratio represent different droplets of the same system. Linear fits through the data points of MS/RS and MS-1.4 + Y vol% PS25 are shown by dashed lines to guide the eye. The full line indicates the MM model prediction. All data are for Ca = 0.30.

The effect of particle concentration is studied by means of the systems MS-1.4 + Y vol% PS25 in Figure 5.3. Figure 5.2 already demonstrated that MS-1.4 + 23 vol% PS25 behaves as a system with a viscosity ratio higher than its viscosity ratio. Figure 5.3 confirms this trend for other particle concentrations as most particle-filled droplets of MS-1.4 + Y vol% PS25 show a reduced deformation compared with droplets from the corresponding reference system. This effect increases with increasing particle concentration, but remains relatively small for a capillary number of 0.30. Deviations of MS-1.4 + 23 vol% PS25 from RS-3.2 range from 2% to 7% (Ca = 0.30). However, Figure 5.2 already illustrated that this effect becomes more pronounced at higher capillary numbers. Figure 5.3 also illustrates the effect of particle size. Similar to MS-1.4 + 23 vol% PS25, also MS-1.4 + 20 vol% PS82 shows a reduced dimensionless droplet axis $L/2R$. This reduction is even more pronounced for MS-1.4 + 20 vol% PS82 than for

MS-1.4 + 23 vol% PS25, which shows that the particle effect depends on particle size. On the other hand, MS-1.4 + 25 vol% PS5 has an average deformation even slightly larger (2.4%-6.8%) than the reference system with the same viscosity ratio, but still smaller or equal to that of the original mother system MS-1.4 (deviations: 0% - 6%).

An additional particle effect observed during steady-state deformation is illustrated in Figure 5.4. Figure 5.4a shows the dimensionless parameter $L_\mathrm{p}/2R$, as defined in Figure 2.1 after startup of shear flow at Ca = 0.30, followed by a period of steady shear flow. Time is made dimensionless by dividing it with the respective emulsion time τ_E. The startup dynamics will be discussed in detail in the next section, here we focus on the steady-state behavior after startup ($t/\tau_\mathrm{E} > 20$).

As expected, the particle-free systems (MS/RS) have a stable ellipsoidal droplet shape during steady shear flow and hence, also constant values of $L_\mathrm{p}/2R$. As illustrated in Figure 5.4a, MS-1.4 + 25 vol% PS5 behaves in a similar way. This is in contrast to systems MS-1.4 + 23 vol% PS25 and MS-1.4 + 20 vol% PS82, which clearly show a small overshoot in $L_\mathrm{p}/2R$ after startup of shear flow followed by small-amplitude oscillations ($(L_\mathrm{p,max}–L_\mathrm{p,min})/L_\mathrm{p,ss} \leq 1.1\%$). The oscillations observed in our experiments are still present after several minutes of shearing. For the same particle system, it was qualitatively observed that the time period of the oscillations decreases with increasing capillary number and the oscillations become more pronounced at higher capillary numbers, higher particle concentrations, or higher particle over droplet size ratios. A similar phenomenon has been reported for droplets submersed in a suspension in which the particles in the matrix phase cause local flow disturbances [83]. An overshoot during startup of shear flow is also observed by Smith and Van de Ven [151] for a droplet containing a single particle.

In general, the rotational flow inside the droplet causes the particles to circulate. At high particle concentrations and high particle over droplet size ratios, particle confinement during this circulation results in outwards bulging of the particles. This also results in considerable deviations from the assumed ellipsoidal droplet shape as can be seen in Figures 5.4b-e. Desse et al. [33] also mentioned irregularities in droplet shape when starch granules are added to a water in oil droplet. These irregularities are attributed to the internal circulation of the granules inside the droplet. For system MS-1.4 + 20 vol% PS82, the oscillations are caused by individual particles bulging out of the droplet, while for system MS-1.4 + 23 vol% PS25, the irregular shape of the large particle cluster is responsible for the oscillations and deviations in droplet shape. Consequently, the oscillations observed for MS-1.4 + 20 vol% PS82 have a larger amplitude and smaller time period. However, considering the limited amplitude of the oscillations and lack of regularity, a full quantitative analysis of these oscillations

is considered beyond the scope of the experiments.

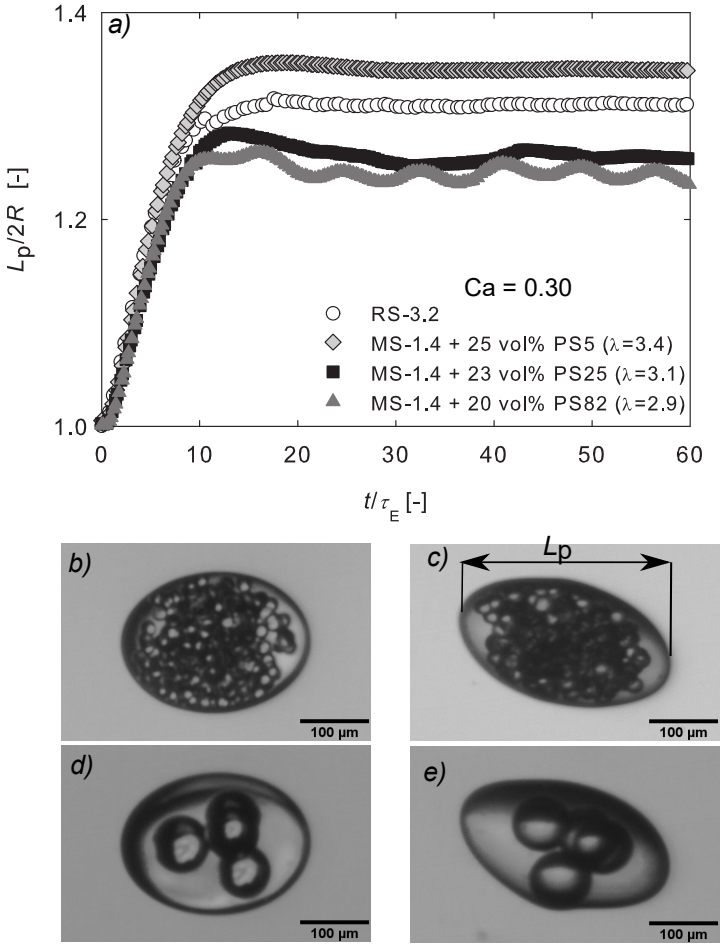

Figure 5.4: (a) Dimensionless parameter $L_p/2R$ of RS-3.2, MS-1.4 + 25 vol% PS5, MS-1.4 + 23 vol% PS25, and MS-1.4 + 20 vol% PS82 as function of dimensionless time t/τ_E after startup of shear flow. Images of MS-1.4 + 23 vol% PS25 (b-c) and MS-1.4 + 20 vol% PS82 (d-e) during steady-state shear. Images are taken in the top view (velocity - vorticity plane)(b-d) and the side view (velocity - velocity gradient plane) (c-e). All data are for Ca = 0.30.

5.2.3 Transient droplet deformation after startup of shear flow

The startup curves show the time evolution of the dimensionless parameter $((L_p/2R)\text{-}1)$ is shown from the moment shear flow is started until a steady-state deformation is reached. However, as discussed in the previous section, the systems attain different steady-state values for the droplet axes. To be able to adequately compare the startup dynamics of the different systems, we therefore normalize $((L_p/2R)\text{-}1)$ by its steady-state value $((L_{p,ss}/2R)\text{-}1)$. In addition, time is made dimensionless by dividing it with the respective emulsion time τ_E. The results for systems MS-1.4, RS-3.2, and MS-1.4 + 23 vol% PS25 are shown and compared with the corresponding predictions of the MM model in Figure 5.5a.

Differences between the startup curves in Figure 5.5a remain limited, and the overall shapes are similar. MS-1.4 reaches its steady-state deformation somewhat later than expected from the MM model prediction, while the MM model prediction for the high viscosity ratio system (RS-3.2) is in good agreement with the experimental data. The startup curve measured for MS-1.4 + 23 vol% PS25 clearly deviates from the curves measured for the reference systems. The particle system reaches its steady-state value at a later time. Hence, it is characterized by slower startup dynamics. This result is similar to the findings of Gooneie et al. [58] who reported a decreased droplet deformation rate when carbon nanotubes are added to a PP/PA6 blend and hinder the mobility of the dispersed phase.

To be able to compare the different systems in a more quantitative way, a characteristic time scale for the startup curves is determined. All startup curves at Ca = 0.20 have a sigmoidal shape which is very similar to the shape of the Gompertz function [166]. Therefore, the startup curves are fitted with the following equation:

$$\frac{\frac{L_p}{2R} - 1}{\frac{L_{p,ss}}{2R} - 1} = A \cdot e^{-e^{(-k(t-t_i))}}, \tag{5.1}$$

in which k is the slope at the inflection point, t_i the time at inflection, and A the upper asymptote, which is in our case equal to one. A two-parameter fit of Equation 5.1 is made through all the startup curves, including the MM model predictions and t_i is selected as the characteristic time scale for the startup process. The resulting values of k are also compared, but no significant differences or clear trends could be observed. A summary of the resulting t_i values for the different systems can be found in Figure 5.5b. Note that the characteristic time scale t_i is made dimensionless with the corresponding emulsion time τ_E.

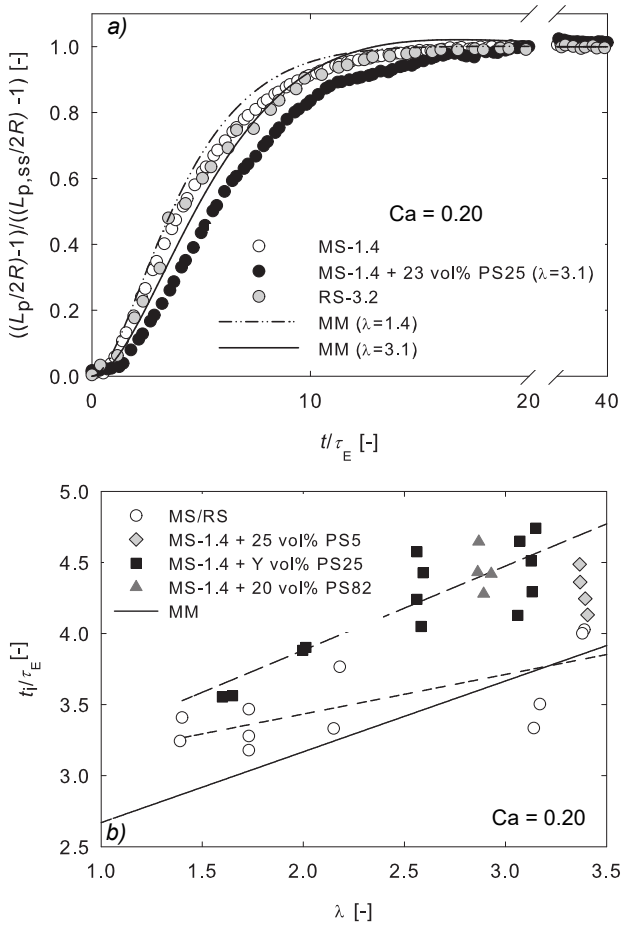

Figure 5.5: (a) Dimensionless parameter $((L_p/2R)\text{-}1)$ normalized by its steady-state value $((L_{p,ss}/2R)\text{-}1)$ as function of dimensionless time t/τ_E after startup of shear flow for MS-1.4, RS-3.2 and MS-1.4 + 23 vol% PS25. (b) Dimensionless startup time t_i/τ_E as function of the viscosity ratio λ. Data points with approximately the same viscosity ratio represent different droplets of the same system. Linear fits through data points of MS/RS and MS-1.4 + Y vol% PS25 are shown by dashed lines to guide the eye. The full line indicates the MM model prediction. All data are for Ca = 0.20.

The characteristic time scales calculated from the experimentally determined curves of the reference systems do not always agree with the MM model prediction, approximated by the full line in Figure 5.5b. Therefore, caution is recommended during the interpretation of these results. Additionally, there exists quite some variability on the fitted t_i values, yet some general conclusions can be made. The characteristic time scales of all particle systems are larger than those of the corresponding reference systems. This confirms the conclusion, already made from Figure 5.5a for system MS-1.4 + 23 vol% PS25, that the startup dynamics are slowed down by the addition of particles, more than could be expected on the basis of the viscosity ratio. This effect increases with particle concentration. Surprisingly, the characteristic time scales for all systems containing approximately 20 vol% particles are in the same range and thus independent of particle size. Hence, the kinetics towards steady-state are almost independent of the particle over droplet size ratio, while the reduction in steady-state deformation increases significantly with this ratio.

5.2.4 Droplet retraction after cessation of shear flow

The shape retraction is represented as the time evolution of $((L_p/2R)\text{-}1)$ normalized by its steady-state value during shear flow $((L_{p,ss}/2R)\text{-}1)$. Time is made dimensionless by dividing it with the respective emulsion time τ_E, and time zero corresponds to the moment shear flow is stopped. The flow is stopped when a steady-state droplet deformation is reached. All retraction experiments are performed after applying a shear flow corresponding to Ca = 0.20. Figure 5.6a illustrates the shape retraction of systems MS-1.4, RS-3.2, and MS-1.4 + 23 vol% PS25. As expected, the retraction curves of MS-1.4 and RS-3.2 correspond well with the MM model predictions.

On the other hand, MS-1.4 + 23 vol% PS25 retracts significantly slower as compared to the corresponding reference system with a similar viscosity ratio, namely RS-3.2. Thus, MS-1.4 + 23 vol% PS25 retracts in a similar way as a particle-free system with a higher viscosity ratio. The system studied by Kong et al. [89] also showed slower retraction dynamics of single droplets containing silica nanoparticles. In contrast, Gooneie et al. [59] found an accelerated retraction process of PA6 droplets filled with carbon nanotubes which form an elastic network. However, the particle-filled blends exhibit in both cases viscoelastic behavior which is not the case in our study. In addition, both studies only compared the retraction behavior of the particle-filled droplets with those of the neat blend which has different viscous and elastic properties.

From each retraction curve in Figure 5.6a, a single characteristic relaxation time scale τ can be calculated by fitting an exponential function ($e^{-t/\tau}$). Figure

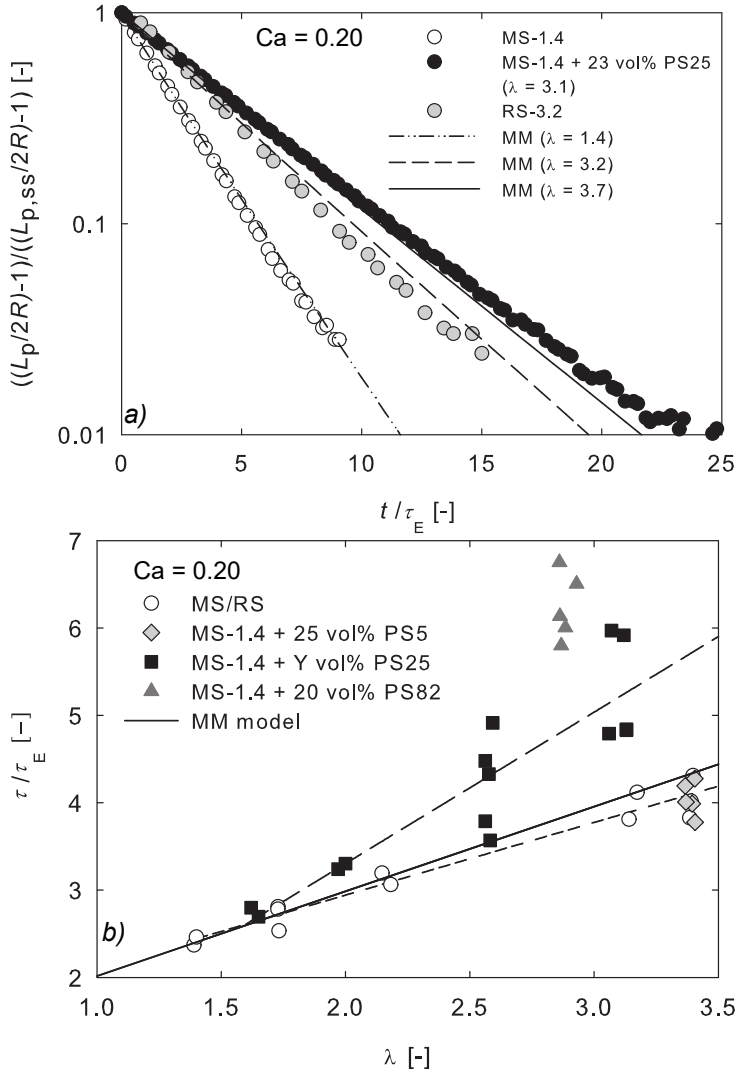

Figure 5.6: (a) Dimensionless parameter $((L_p/2R)\text{-}1)$ normalized by its steady-state value $((L_{p,ss}/2R)\text{-}1)$ as function of dimensionless time t/τ_E during droplet retraction for MS-1.4, RS-3.2 and MS-1.4 + 23 vol% PS25. (b) Dimensionless relaxation time τ/τ_E as function of viscosity ratio λ. Data points with approximately the same viscosity ratio represent different droplets of the same system. Linear fits through the data points of MS/RS and MS-1.4 + Y vol% PS25 are shown by dashed lines to guide the eye. The full line indicates the MM model prediction. All data are for Ca = 0.20.

5.6b provides a summary of these relaxation times, scaled by the respective emulsion time τ_E, as function of the viscosity ratio λ. The qualitative trend observed in Figure 5.6a is confirmed by this overview. The experimentally determined relaxation times of the reference systems agree well with the MM model predictions, while particle systems MS-1.4 + Y vol% PS25 and MS-1.4 + 20 vol% PS82 show longer relaxation times when the particle concentration is 10 vol% or higher. Hence, these particle-filled droplets retract slower and thus behave similar to systems with a higher viscosity ratio. This effect becomes again more pronounced at higher particle concentrations and higher particle to droplet size ratios. In contrast, the relaxation times of MS-1.4 + 25 vol% PS5 are in good agreement with those of the respective reference system (RS-3.4). At this low particle to droplet size ratio, the particle suspension that constitutes the droplet can thus be considered as a homogeneous medium characterized by the viscosity ratio governed by the particle concentration.

It has to be noted that significant deviations (13%-38%) in relaxation time are observed between different experiments with droplets containing 15 vol% or more particles. However, different retraction experiments at $Ca = 0.20$ and $Ca = 0.30$ performed with the same droplet of MS-1.4 + Y vol% PS25 resulted in one retraction master curve, and hence a reproducible value (deviations $< 10\%$) of the relaxation time per droplet. This suggests that the variability in relaxation time is caused by variations in particle concentration between different droplets.

To verify this hypothesis, the exact particle concentration of different droplets of MS-1.4 + 19 vol% PS25 is determined after the performed experiments, using the method explained in section 5.2.1. The viscosity ratio of that particular system is then calculated with the Maron-–Pierce equation (Equation 2.25). However, as illustrated in Figure 5.7, the trend with viscosity ratio does not become clearer when the results are plotted as a function of the calculated viscosity ratio per droplet instead of the average viscosity ratio as tabulated in Table 5.1. Hence, the variation in particle concentration can only partially explain the increase in variability for concentrations above 15 vol%. Probably, local intrinsic particle effects cause an additional variation in droplet behavior.

On the other hand, for system MS-1.4 + 20 vol% PS82, experiments at different capillary numbers on the same droplet already give rise to slightly different retraction curves. From these results, we can assume that at high particle over droplet size ratios, droplet retraction is affected by local particle effects which cause an increase in variability. This interpretation is supported by the deviations in droplet shape and resulting oscillations observed during steady-state shear flow in Figure 5.4, which could be linked to the particle circulation inside the droplet.

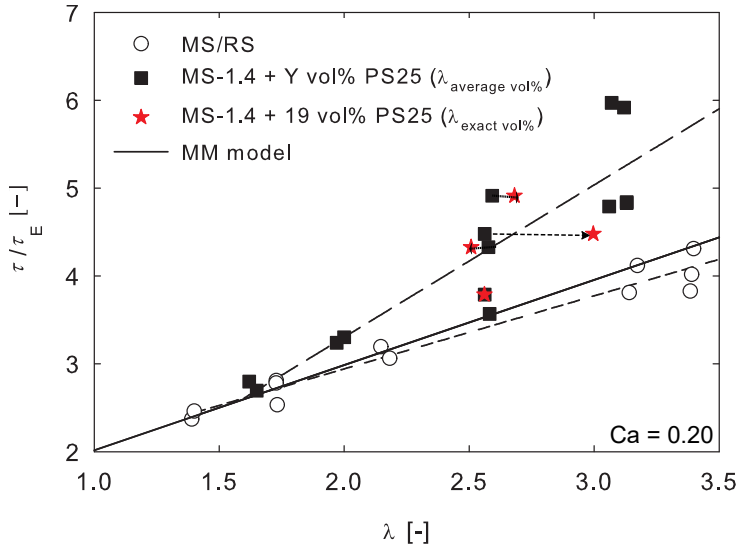

Figure 5.7: Revised Figure 5.6b with dimensionless relaxation time τ/τ_E as function of viscosity ratio λ of MS/RS and MS-1.4 + Y vol% PS25. Extra data points (stars) are added for MS-1.4 + 19 vol% PS25 which represent τ/τ_E as function of viscosity ratio λ calculated with the exact particle concentration of that specific droplet instead of the average particle concentration. The arrows indicate the shifting of these data points.

5.2.5 Droplet breakup

Droplet breakup is studied by increasing the applied capillary number with small discrete steps until breakup occurs. Thereby, after every applied capillary number, the shear flow is stopped and, hence, the droplet starts from a spherical shape.

An overview of the observed breakup mechanisms can be found in Figure 5.8 which provides images taken in the top view (velocity - vorticity plane) at Ca_{crit}. As expected, all particle-free systems break up by necking, which results in two identical daughter droplets and some small satellite droplets. This is illustrated in Figure 5.8 for system MS-1.4. The breakup modes observed for MS-1.4 + 25 vol% PS5, MS-1.4 + 6 vol% PS25, and some droplets of MS-1.4 + 13 vol% PS25 are similar to those of the particle-free systems. However, satellite droplets of MS-1.4 + 6 vol% PS25 and MS-1.4 + 13 vol% PS25 do not contain any particles, while satellite droplets of MS-1.4 + 25 vol% PS5 are partially filled with particles. For larger particles, the neck width during

thinning becomes comparable with the particle diameter, and particles are forced towards the larger daughter droplets. Hence, a particle-free neck is created where droplet breakup occurs. Similar behavior is observed by Furbank and Morris [52] during droplet formation of concentrated suspensions from a needle ($\geq$ 15 vol%), yet with a lower particle over droplet size ratio.

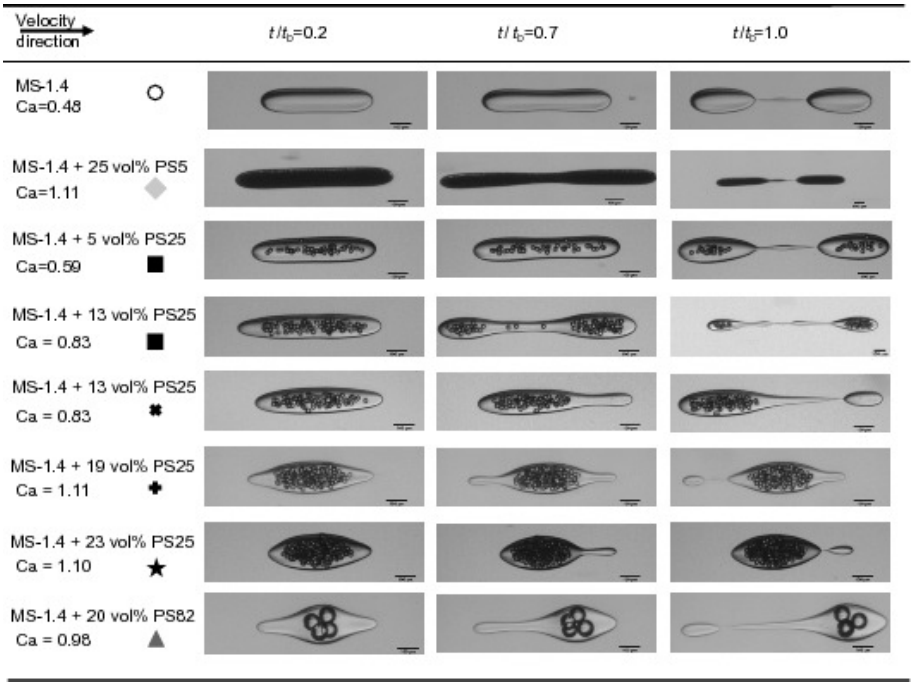

Figure 5.8: Images of MS-1.4, MS-1.4 + 25 vol% PS5, MS-1.4 + Y vol% PS25, and MS-1.4 + 20 vol% PS82 taken during droplet breakup at $\mathrm{Ca}_{\mathrm{crit}}$ (indicated in the first column) in top view (velocity - vorticity plane). Second and third column show images taken at time $t/t_{\mathrm{b}} = 0.2$ and $t/t_{\mathrm{b}} = 0.7$, respectively, with t_{b} the breakup time. Last column shows the droplets just after breakup ($t/t_{\mathrm{b}} = 1$). The symbols in the first column refer to the symbols used in Figures 5.9 and 5.10.

On the other hand, MS-1.4 + 19 vol% PS25, MS-1.4 + 23 vol% PS25, MS-1.4 + 20 vol% PS82, and some droplets of MS-1.4 + 13 vol% PS25 show a completely different breakup behavior. As can be seen in Figure 5.8, the particle-filled droplets do not break into two identical daughter droplets, instead particle-free droplets are released from the droplet tips. Attempts to break the remaining particle cluster by immediately applying a very high shear rate only

resulted in the release of more and smaller particle-free satellite droplets from the tips. In blends and emulsions, this different breakup mechanism may lead to a broader droplet size distribution and an inhomogeneous distribution of the particles over the droplets.

This breakup mechanism is comparable with tip streaming which is observed for systems with an interfacial tension gradient [30], although the physical origin is different. During shear flow, no particles are present in the droplet tips due to the particle clustering around the droplet center. As a result, a lower viscosity ratio, which is comparable with the viscosity ratio of MS-1.4, exists locally in the droplet tips. This lower viscosity ratio gives rise to easier breakup of the particle-free droplet tips as compared to the particle-filled cluster in the droplet center. Consequently, only satellite droplets without particles are formed. As a result, the particle concentration of the remaining particle cluster is higher than the particle concentration of the original droplet. This effect stabilizes the droplet against further breakup [132]. The opposite behavior is observed for water in oil systems with particle-filled droplets with low viscosity ratios [152, 32] (Smith and van de Ven 1985b; Desse et al. 2011). In these systems, particles spend more time in the droplet tips during circulation. Consequently, particle clusters are ejected from the droplet tips at high shear rates.

A quantitative analysis is made by comparing the critical capillary number at which breakup occurs ($\mathrm{Ca}_{\mathrm{crit}}$), the critical strain γ_{crit} ($=\dot{\gamma}_{\mathrm{crit}} \cdot t_{\mathrm{b}}$, with t_{b} the breakup time), and the dimensionless critical droplet length $L_{\mathrm{p,crit}}/2R$. However, results have to be interpreted with caution because the breakup mechanisms differ among the different particle systems, as already presented and discussed in Figure 5.8. Therefore, data points in Figures 5.9 and 5.10 of droplets that break up according to the tip streaming breakup mechanism are marked in the figure legend. The symbols refer to the symbols used in the first column of Figure 5.8.

$\mathrm{Ca}_{\mathrm{crit}}$ values measured for the particle-free systems (MS/RS) agree with the de Bruijn [30] curve at viscosity ratios around 1, but deviate when reaching viscosity ratios close to 4. It has to be noted however that Figure 5.9 is a detailed figure because only a limited range of viscosity ratios is shown and both scales are linear. The inset of Figure 5.9 therefore shows a complete breakup diagram of the critical capillary numbers determined in this work and the experimental data of Grace [60] together with the de Bruijn curve [30]. This inset shows that the experimental data of Grace show similar deviations from the de Bruijn fit in the investigated viscosity ratio range. Furthermore, the experimentally determined critical capillary numbers in the work of Zhao [199] are also consistently lower than the predictions of de Bruijn [30]. The authors attributed these discrepancies to the fact that the gradual increase in capillary number used by Grace [60] leads to higher critical capillary numbers than direct

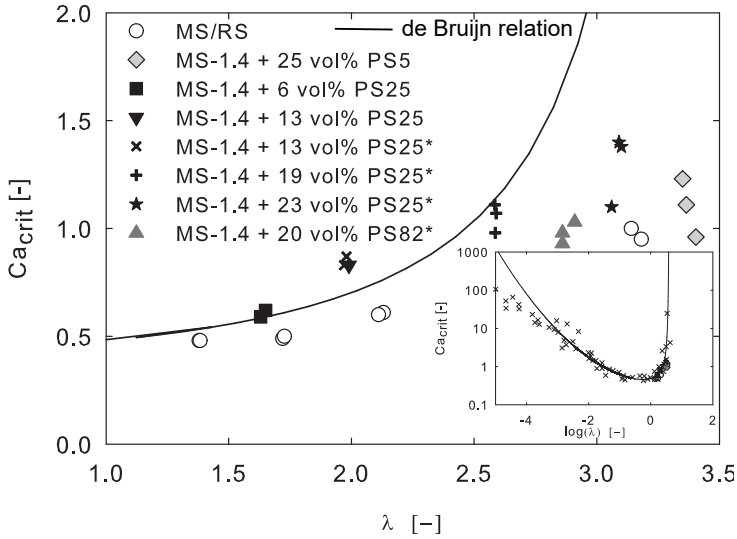

Figure 5.9: Ca_{crit} at which breakup occurs as function of viscosity ratio λ. Data points with approximately the same viscosity ratio represent different droplets of the same particle or reference system. Entries indicated with * refer to the tip streaming breakup mode. The same symbols are used in Figure 5.8 to indicate the specific breakup modes. Inset: Comparison with experimental data of Grace [60].

startup of flow, as applied here and in the work of Zhao [199].

After the addition of high particle concentrations ($\geq$ 15 vol%), the breakup behavior shows more variability. In general, the viscosity ratio is increased by the addition of particles compared with the original system MS-1.4 which results in this case in a higher value of Ca_{crit}. Therefore, particle-filled droplets are more difficult to break and larger average droplet sizes are expected in blends. This particle effect is already extensively studied in literature for concentrated polymer blends [201, 59] and diluted oil in water emulsions [113]. In addition, Kong et al. [89] observed a higher critical breakup aspect ratio for single PA6 droplets containing silica nanoparticles which introduce viscoelastic effects in the dispersed phase. However, most of these works only compare the droplet size of particle-filled blends with that of the neat blend which has different viscous and/or elastic properties.

When we compare the Ca_{crit} values of MS-1.4 + 6 vol% PS25 and MS-1.4 + 13 vol% PS25 with the Ca_{crit} values of the corresponding reference systems with matched viscosity ratios, a slight increase is still observed. Hence,

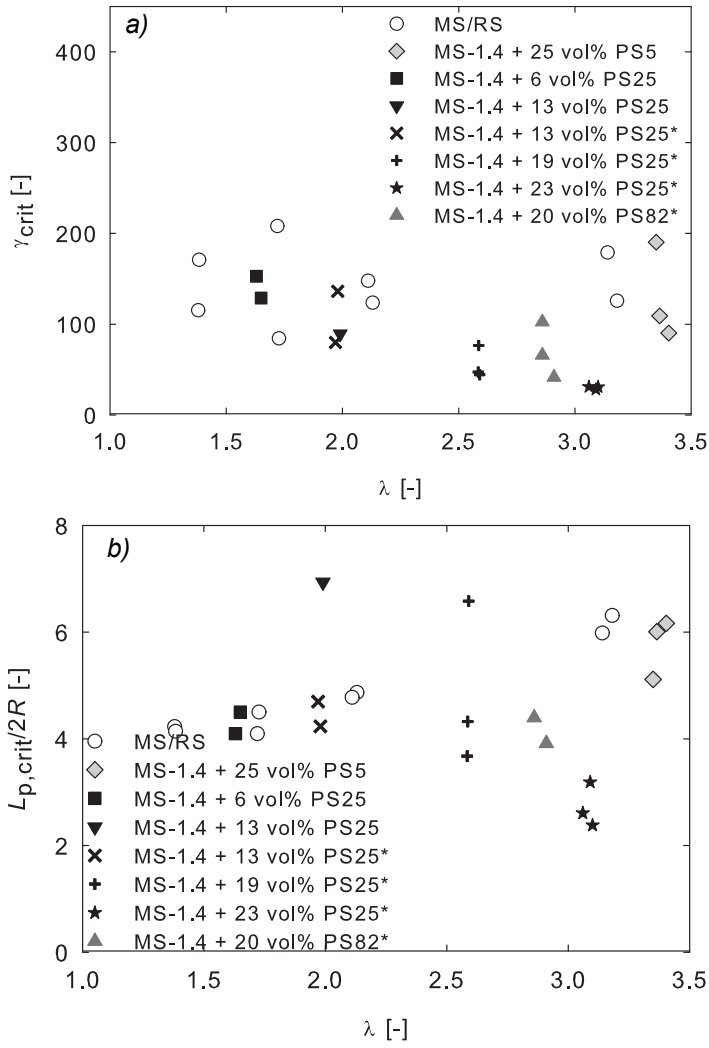

Figure 5.10: (a) Critical strain γ_{crit} and (b) critical droplet length $L_{\text{p,crit}}/2R$ at which breakup occurs as function of viscosity ratio λ. Data points with approximately the same viscosity ratio represent different droplets of the same particle or reference system. Entries indicated with * refer to the tip streaming breakup mode. The same symbols are used in Figure 5.8 to indicate the specific breakup mode.

there is a small additional intrinsic effect of the particles that stabilizes the droplets further against breakup. Figure 5.10 shows that the critical strain and critical droplet length are in the same range as those of the respective reference systems. At higher particle concentrations (MS-1.4 + 19 vol% PS25 and MS-1.4 + 23 vol% PS25), droplets break up according to the tip streaming mechanism, which results in a lower critical droplet length and lower critical strain. $\mathrm{Ca}_{\mathrm{crit}}$, on the other hand, is equal to or higher than $\mathrm{Ca}_{\mathrm{crit}}$ observed for RS-3.2 (see Figure 5.9). Hence, even though the central particle cluster does not break, the shift of the necking from the droplet center to the droplet tips caused by its presence, postpones breakup as compared with that in the neat MS-1.4 system. Similar conclusions can be made for MS-1.4 + 20 vol% PS82, which also shows breakup by tip streaming. However, if smaller particles are added to the droplet phase (MS-1.4 + 25 vol% PS5), the breakup process is in most aspects comparable to the breakup behavior of the particle-free system RS-3.2 which approximately matches the viscosity ratio of MS-1.4 + 25 vol% PS5.

5.2.6 Comparison of different particle effects on droplet dynamics

In this section, the particle effects in the different experiments (steady-state deformation, transient droplet dynamics, and breakup behavior) are quantitatively compared with each other in order to verify if a general scaling law based on a corrected viscosity ratio can be composed to predict the complete droplet dynamics.

From the previous sections, we can state that the particle systems behave in a similar way as a particle-free system with a higher viscosity ratio λ^*. For every data point of MS-1.4 + Y vol% PS25, MS-1.4 + 25 vol% PS5, and MS-1.4 + 20 vol% PS82 presented in Figure 5.3 ($\lambda^*_{\mathrm{deformation}}$), Figure 5.5b ($\lambda^*_{\mathrm{startup}}$), and Figure 5.6b ($\lambda^*_{\mathrm{retraction}}$), λ^* is determined as the viscosity ratio which gives the same deformation ($L/2R$) or characteristic time scale (t_{i} or τ) according to the MM model, shown as a full line in Figures 5.3, 5.5b, and 5.6b. λ^* is not determined for the breakup experiments because a different breakup mode is observed for MS-1.4 + 19 vol% PS25, MS-1.4 + 23 vol% PS25, and MS-1.4 + 20 vol% PS82, which makes direct comparison difficult. For these systems, only tip streaming was observed, and it was impossible to break the particle cluster within the shear rate range that could be reached in the experiments. Therefore, we assume λ^* for these systems larger than 3.8, which is the upper viscosity limit to break droplets in shear flow [60, 30].

To verify the hypothesis that particle-filled droplets can be treated as a homogeneous medium characterized by its viscosity, λ^* has to be compared

with the viscosity ratio λ of the particle systems. Figure 5.11 summarizes the results. The error bars represent the minimal and maximal determined λ^*.

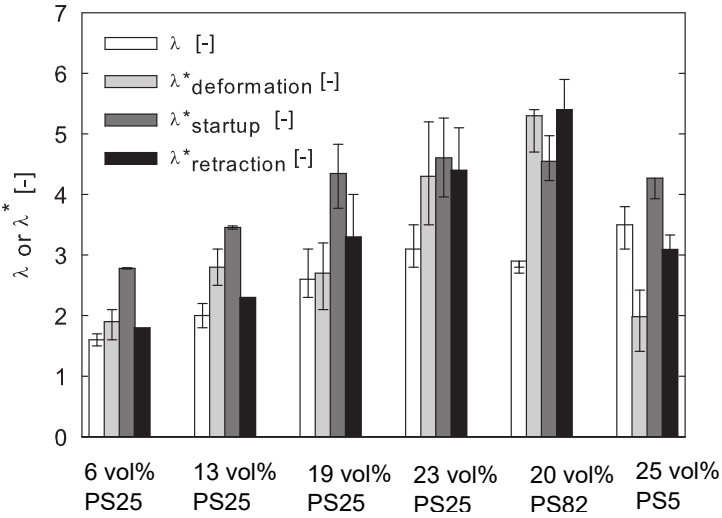

Figure 5.11: Comparison of the viscosity ratio λ with a characteristic viscosity ratio λ^* determined for all particle systems MS-1.4 + Y vol% PSZ from experimental data of steady-state deformation, startup and retraction experiments. The error bars represent the minimal and maximal determined λ.

First, we focus on MS-1.4 + 25 vol% PS5, a system with a low particle over droplet size ratio ($r/R = 0.02$). As discussed in Figure 5.3, the deformation of this system is slightly larger than the deformation of the corresponding reference system (RS-3.4), but still smaller than MS-1.4. Hence, $\lambda^*_{\text{deformation}}$ is smaller than the viscosity ratio λ of MS-1.4 + 25 vol% PS5. Figure 5.11 also confirms that the retraction behavior of MS-1.4 + 25 vol% PS5 is comparable to the retraction behavior of a particle-free system with approximately the same viscosity ratio ($\lambda^*_{\text{retraction}} \approx \lambda$). As mentioned in section 5.2.5, also the breakup behavior of MS-1.4 + 25 vol% PS5 agrees well with that of the corresponding reference system. These findings support the hypothesis that particles only influence the droplet dynamics by increasing the overall viscosity ratio of the system to the viscosity ratio λ determined by the particle concentration. Only for the startup experiments, the value of λ^* is significantly higher than the viscosity ratio λ and more comparable with the other 20 vol% particle systems (MS-1.4 + 23 vol% PS25 and MS-1.4 + 20 vol% PS82).

Secondly, higher particle over droplet size ratios ($r/R \geq 0.1$) are studied by MS-1.4 + Y vol% PS25 and MS-1.4 + 20 vol% PS82. In contrast to MS-

1.4 + 25 vol% PS5, these systems behave in a similar way as a particle-free system with a viscosity ratio slightly higher than their actual viscosity ratio ($\lambda^* > \lambda$). In addition, the particle clusters of MS-1.4 + 19 vol% PS25, MS-1.4 + 23 vol% PS25, and MS-1.4 + 20 vol% PS82 could not be broken, and hence, $\lambda^*_{\text{breakup}}$ is larger than 3.8, which is in all cases also larger than the viscosity ratio λ. Furthermore, additional intrinsic particle effects like oscillations in deformation, asymmetrical droplet shapes, and tip streaming occur in these systems at high particle concentrations.

These particle effects become more pronounced at higher particle concentrations or higher particle over droplet size ratios. Only the values of λ^* determined from the startup experiments are independent of the particle size as MS-1.4 + 25 vol% PS5, MS-1.4 + 23 vol% PS25, and MS-1.4 + 20 vol% PS82 show similar values for $\lambda^*_{\text{startup}}$. Consequently, it seems that the startup dynamics are mainly governed by the particle concentration present in the droplet phase. It has to be noted however that the startup dynamics of the reference systems do not always agree with the MM model predictions. Therefore, we have to be careful with the interpretation of $\lambda^*_{\text{startup}}$.

Despite the fact that different experiments (steady-state deformation and transient dynamics) show similar trends, the exact values of λ^* differ. Therefore, no general scaling law based on a corrected viscosity ratio can be composed to predict the complete droplet dynamics based on particle concentration and particle over droplet size ratio.

Kaur and Leal [83] made similar conclusions in their paper about the effect of particles in the matrix phase on droplet deformation and breakup. The authors stated that at low particle over droplet size ratios droplet deformation and breakup can be described by taken the viscosity of the suspension as the matrix viscosity, while at higher ratios the particles locally disturb the applied flow field and collide with the droplet. These last effects give rise to more fluctuations, asymmetric droplet shapes, and scatter in the measured deformation and breakup behavior [83].

In our case, particles are located inside the droplet phase, and hence at higher particle over droplet size ratios or higher particle concentrations, also particle confinement inside the droplet will play a role. It is well-known that confinement leads to an increase of the viscosity of non-Brownian suspensions [127]. Moreover, particles will be excluded from a volume near the droplet interface as they do not cross the interface, which results in a higher particle concentration. Both types of confinement effects will be more pronounced for larger particles. As a result, these systems behave similar to a particle-free system with a viscosity ratio slightly higher than their viscosity ratio λ. This effect is even observed at low particle concentrations, although very limited, and increases with particle

concentration and particle size. Since the flow profile in the droplet is rather complex and may vary depending on whether steady-state conditions, startup, or retraction is considered, the effects of the particles on each of these processes can be slightly different, as demonstrated in this study.

5.3 System with $\lambda < 1$

5.3.1 Steady-state deformation, transient dynamics and droplet breakup

The dimensionless droplet axes ($L/2R$, $W/2R$, and $B/2R$) of systems MS-0.09 (+ 20 vol% PS25), MS-0.08L (+ 20 vol% PS25), and RS-0.2L are shown in Figure 5.12. Two seperate experiments are conducted for the particle-free systems (MS-0.09, MS-0.08L, and RS-0.2L). The results are reproducible (deviations $< 5\%$), but do not completely agree with the MM model [106]. In general, the systems show less deformation for $L/2R$ and $B/2R$ as compared to the model, while $W/2R$ agrees well with the model. However, the pure PDMS–PIB system with a viscosity ratio of 0.07 measured by Mei et al. [112] shows similar or even larger deviations from the MM model.

We also noticed that droplets of MS-1.4, which have a higher viscosity ratio, deform more than droplets of systems MS-0.09 and MS-0.08L at a constant capillary number. This is indicated by the data points in Figure 5.13. These results seem inconsistent with the findings that the steady-state deformation should decrease with increasing viscosity ratio [85]. However, the MM model as well as numerical simulations of Mitrias et al. [117], indicated by full lines in Figure 5.13, show that the deformation parameter D (Equation 2.4) as function of the viscosity ratio has a maximum around $\lambda = 1$ for $\mathrm{Ca} = 0.20$. These results also predict a larger deformation parameter for systems with a viscosity ratio around 1.4 as compared to systems with a much lower viscosity ratio ($\lambda = 0.1$). Additionally, the experimental results presented by Vananroye et al. [180] show similar trends at high capillary numbers for the measurements of pure PDMS-PIB systems with viscosity ratios of 0.31 and 1.05.

In contrast with the systems based on MS-1.4, the polystyrene particles do not affect the deformation behavior of systems based on MS-0.09 or MS-0.08L and hence, the dimensionless droplet axes of the particle systems agree well with those of the mother system as well as with those of the reference system. The largest deviations occur for $L/2R$ at higher capillary numbers ($\mathrm{Ca} > 0.35$), as can be seen in Figure 5.12, but these are limited (< 9 %) and still smaller than the deviations between the reference system and the mother system.

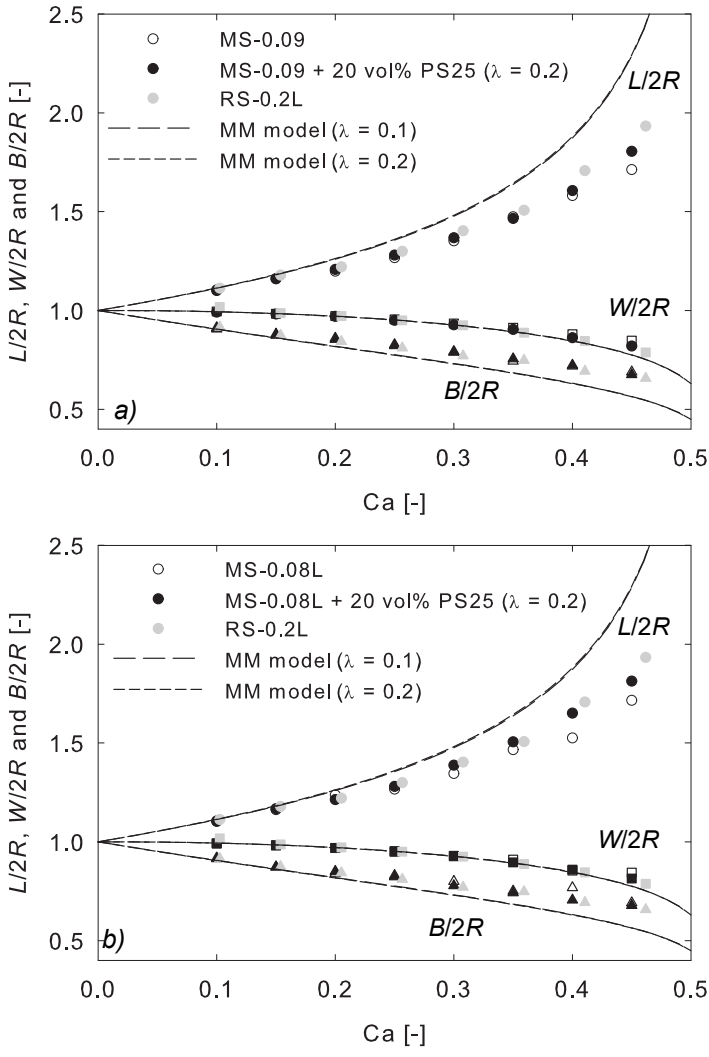

Figure 5.12: Dimensionless droplet axes $L/2R$, $W/2R$, and $B/2R$ of systems RS-0.2L and (a) MS-0.09 (+ 20 vol% PS25) or (b) MS-0.08L (+ 20 vol% PS25) as function of the applied capillary number.

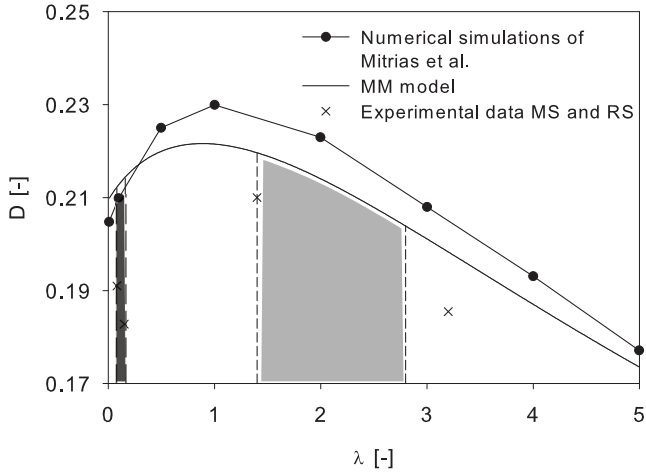

Figure 5.13: Steady-state droplet deformation parameter D as function of the viscosity ratio λ at Ca = 0.20. Experimental data points (x) of particle-free systems MS-0.08L, RS-0.2L, MS-1.4, and RS-3.2 together with results of numerical simulations (dots) taken from Mitrias et al. [117]. The full line represents the MM model predictions. Dashed lines indicate the viscosity ratio ranges of the systems based on MS-1.4 (grey area), MS-0.09 and MS-0.08L (black area).

The results for the other particle concentrations and particle sizes are similar. Up to intermediate capillary numbers (Ca = 0.35), all particle-free systems in Figure 5.12 (MS-0.09, MS0.08L, and RS-0.2L) show similar deformation behavior (deviations < 5%), hence there is no effect of the differences in viscosity ratio. Also, the MM model predicts only a very small increase of the droplet deformation (< 1%) when the viscosity ratio increases from 0.08 to 0.2.

The reason why we do not observe a particle effect on the droplet deformation for the systems based on MS-0.09 or MS-0.08L is further clarified in Figure 5.13. In the range of low viscosity ratios, the MM model predicts only a very small (< 1 %) increase in droplet deformation due to an increase in viscosity ratio of approximately 40 %. Consequently, if the particles added to MS-0.09 or MS-0.08L would show similar effects on the steady-state deformation as observed for systems based on MS-1.4, we would not be able to observe these effects. In general, an increase of 50 % in viscosity ratio is only substantial in the region of $\lambda \sim 1$ and only large changes in viscosity ratio affect the droplet deformation. However, small oscillations and irregular droplet shapes similar to the ones observed for particle systems based on MS-1.4 (section 5.2.2) are

observed at high particle concentrations and larger particle sizes due to the circulation and confinement of the particles inside the droplet.

The transient droplet dynamics after startup and cessation of shear flow of particle system MS-0.08L + 20 vol% PS25 are compared with the dynamics of the corresponding mother system MS-0.08L in Figure 5.14. No significant differences are observed between the transient dynamics of the particle system and the mother system. In addition, the breakup behavior of MS-0.08L + 20 vol% PS25 is studied. As can be seen in Figure 5.15, the particle-filled droplet breaks up by necking into two similar daughter droplets and a particle-free satellite droplet.

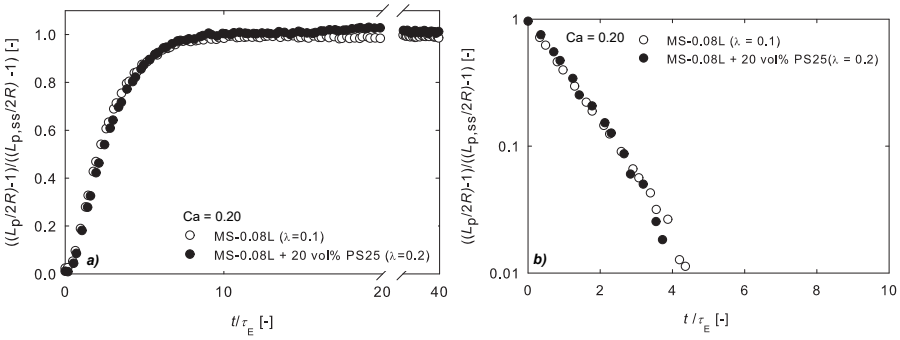

Figure 5.14: Dimensionless parameter $((L_\mathrm{p}/2R)\text{-}1)$ normalized by its steady-state value $((L_\mathrm{p,ss}/2R)\text{-}1)$ as function of dimensionless time t/τ_E after (a) startup of shear flow and (b) cessation of shear flow for MS-0.08L (+ 20 vol% PS25). All data are for Ca = 0.20.

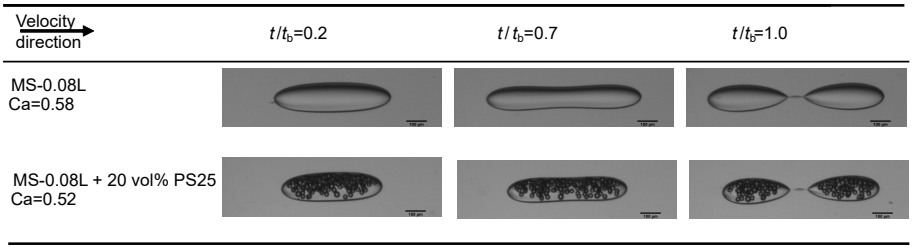

Figure 5.15: Images of MS-0.08L (+ 20 vol% PS25) taken during droplet breakup at $\mathrm{Ca_{crit}}$ (indicated in the first column) in top view (velocity - vorticity plane). Second and third column show images taken at time $t/t_\mathrm{b} = 0.2$ and $t/t_\mathrm{b} = 0.7$, respectively, with t_b the breakup time. Last column shows the droplets just after breakup ($t/t_\mathrm{b} = 1$).

In general, we do not observe significant particle effects on the droplet dynamics in this viscosity ratio range ($\lambda < 1$). Therefore, it is decided to not perform further experiments with other volume concentrations or particle sizes. In addition, the exact particle concentration inside the droplet is also less important for these systems as it hardly makes a difference in the final predicted droplet dynamics. Consequently, the actual particle concentration of the injected droplets is not determined for these systems.

5.4 Conclusion

In this chapter, the intrinsic effects of non-Brownian particles localized in the droplet phase on the single droplet dynamics are experimentally investigated in shear flow. In general, the particles increase the droplet phase viscosity and thus the viscosity ratio. Therefore, the results are compared with data of particle-free reference systems with comparable viscosity ratios which allows us to quantitatively verify the hypothesis that the particle-filled droplets can be treated as a homogenous medium with a viscosity governed by the particle concentration. The particle effects observed depend on the viscosity ratio of the system.

For particle systems based on MS-0.09 and MS-0.08L, with a viscosity ratio much lower than one, the increase in viscosity ratio has no significant effect on the droplet dynamics and hence, it was not possible to quantitatively verify the proposed hypothesis. For particle systems based on MS-1.4 and hence, with a viscosity ratio around one, the increase in viscosity ratio results in a suppressed droplet deformation, slower transient dynamics (after startup and cessation of shear flow), and a higher critical capillary number for breakup as compared to the neat system, which is expected based on the viscosity ratio increase due to the addition of the particles to the droplet phase. For this system, the particle concentration and ratio of particle to droplet size are systematically varied.

At first glance, these particle effects can indeed be predicted by the viscosity ratio λ of the system governed by the particle concentration. However, the presented results demonstrate that this is only possible at low particle over droplet size ratios ($r/R = 0.02$). The quantitative comparison of the dimensionless deformation axes $L/2R$ and characteristic time scales of the particle systems with those of the corresponding particle-free reference systems show that the droplet dynamics of particle systems with $r/R \geq 0.1$ are not completely governed by their viscosity ratio. Instead, the droplet dynamics are similar to those of a particle-free system with a viscosity ratio λ^* slightly higher than its bulk viscosity ratio λ. Accordingly, the particle-filled droplets behave slightly more

viscous than expected based on the proposed hypothesis, although differences between λ^* and λ remain limited.

Furthermore, additional intrinsic particle effects come into play for particle over droplet size ratios exceeding 0.1, similar to the local disturbances observed by Kaur and Leal [83] for particles present in the matrix phase and higher particle over droplet size ratios. For these particle systems, individual particles or a particle cluster bulging out of the droplet result in asymmetric droplet shapes and oscillations in the dimensionless droplet axes during steady-state shear flow. A different breakup mechanism which is similar to tip streaming for surfactant-covered droplets is also observed at high particle concentrations. Particle-free droplets are ejected from the droplet tips, while breakup of the central particle cluster seems to be impossible under the current operating window of the CR setup.

These intrinsic effects increase with particle concentration and particle over droplet size ratio. However, due to different intrinsic particle effects for steady-state deformation, startup, retraction, and breakup, it can be concluded that the complete droplet dynamics can not be described by a single correction factor for the viscosity ratio.

Chapter 6

Effects of nanoparticles localized at the droplet interface

This chapter focuses on the effects of nanoparticles localized at the droplet interface. As stated in Chapter 2, previous studies already demonstrated a reduced or even suppressed droplet deformation and breakup and slower droplet retraction when a particle network is formed at the droplet interface. Similar behaviour is observed for the steady-state droplet deformation and breakup of the system used in this study as described in the first section of this chapter. However, this study focuses on finding a quantitative link between the rheological properties of the particle-covered interface and the corresponding droplet dynamics in order to be able to predict the single droplet dynamics based on the interfacial properties. In a second part, the rheological properties of the particle-filled interface are therefore discussed and the behavior is compared with the corresponding droplet dynamics observed in the first section.

The work presented in this chapter is performed in collaboration with Y. Mei, who designed, performed, and post-processed the major part of the single droplet dynamics experiments. Y. Mei and H. Van Ammel both designed the rheological experiments, H. Van Ammel performed the major part of these experiments and the data post-processing. The following chapter is based on a manuscript in preparation:

Y. Mei, H. Van Ammel, P. Moldenaers, and R. Cardinaels. Deformation and breakup of single nanoparticle-armoured droplets in the shear flow.

6.1 Effects on single droplet dynamics

Nanoparticles localized at the droplet interface replace part of the liquid-liquid interface and hence, affect the interfacial energy [143]. Therefore, the (apparent) interfacial tension is first measured and discussed. Thereafter, these results are used to correctly compare the steady-state droplet deformation and breakup behavior of systems with various particle coverages. The last part of this section demonstrates the effect of the breakup of the interfacial elastic particle shell, resulting in a hysteresis or memory effect of the droplet deformation.

6.1.1 Apparent interfacial tension

Two opposite effects are observed in the measured interfacial tension values summarized in Figure 6.1 as function of the droplet residence time in the 0.4 vol% suspension of silica nanoparticles. A droplet with a residence time of 0 h corresponds to the neat, particle-free, system and a longer residence time in the suspension results in a higher particle coverage at the droplet interface. First, at low particle concentrations, the interfacial tension decreases as compared to that of the neat system. The nanoparticles located at the interface reduce the liquid-liquid interfacial area and hence, decrease the interfacial energy. Then, at higher particle concentrations, the interfacial tension increases again and becomes higher than the interfacial tension of the neat system. However, this is not an increase of the thermodynamic interfacial tension, but a result of the formation of an elastic particle network at the interface. This elastic particle shell results in an increase in interfacial elasticity and forms a rigid particle network, which inhibits droplet deformation. As explained in detail in section 3.4 of Chapter 3, the interfacial tension Γ is in this work determined by fitting the droplet axes at small deformations to the second order theory of Greco [61]. Hence, the elastic response of the interfacial particle network interferes with the interfacial tension measurement and the values in Figure 6.1 do not represent the real thermodynamic interfacial tension. Therefore, these measured values are called the apparent interfacial tension, Γ_{app}.

Since it is difficult to fully separate the thermodynamic and elastic contributions, we assume that the minimum value obtained, $\Gamma_{\mathrm{eff}} = 1.24$ mN/m, is a good

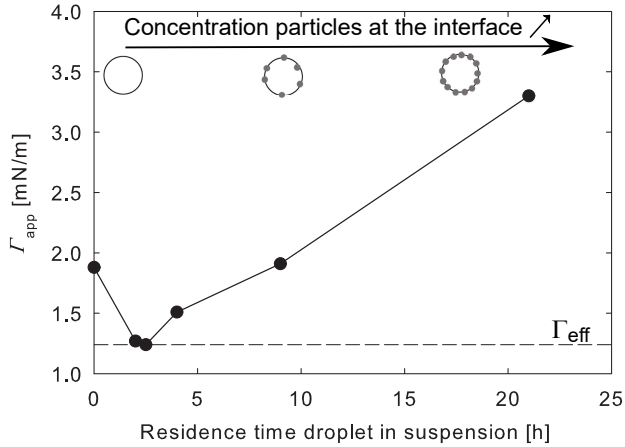

Figure 6.1: Apparent interfacial tension Γ_{app} of particle-covered droplets (MS-0.1 + 0.4 vol% silica) determined by fitting the droplet axes at small deformations to the second order theory of Greco [61]. The particle concentration at the interface increases with the residence time of the droplet in the 0.4 vol% suspension of silica nanoparticles. The dashed line indicates the minimum, Γ_{eff}.

approximation of the thermodynamic effect of the particles. This value is used to calculate the applied effective capillary numbers in the following sections:

$$\mathrm{Ca}_{\mathrm{eff}} = \frac{\eta_{\mathrm{m}} \cdot R \cdot \dot{\gamma}}{\Gamma_{\mathrm{eff}}} \tag{6.1}$$

6.1.2 Steady-state deformation

The steady-state droplet deformation and orientation behavior of particle-covered droplets is summarized in Figure 6.2 by means of the dimensionless droplet axes $L/2R$ (a), $W/2R$ (b), $B/2R$ (c) and orientation angle θ (d). Droplets with a different residence time in the 0.4 vol% silica nanoparticle suspension, and hence different particle coverage, are measured. As a reference, a droplet with a particle-free interface, indicated with a residence time of 0 h, is also measured. The effect of particles on the interfacial tension is taken into account by presenting the droplet deformation as function of the applied effective capillary number as defined in Equation 6.1.

After a small residence time (2.5 h) in the suspension, only a small amount of particles cover the droplet interface. As demonstrated in Figure 6.2, this

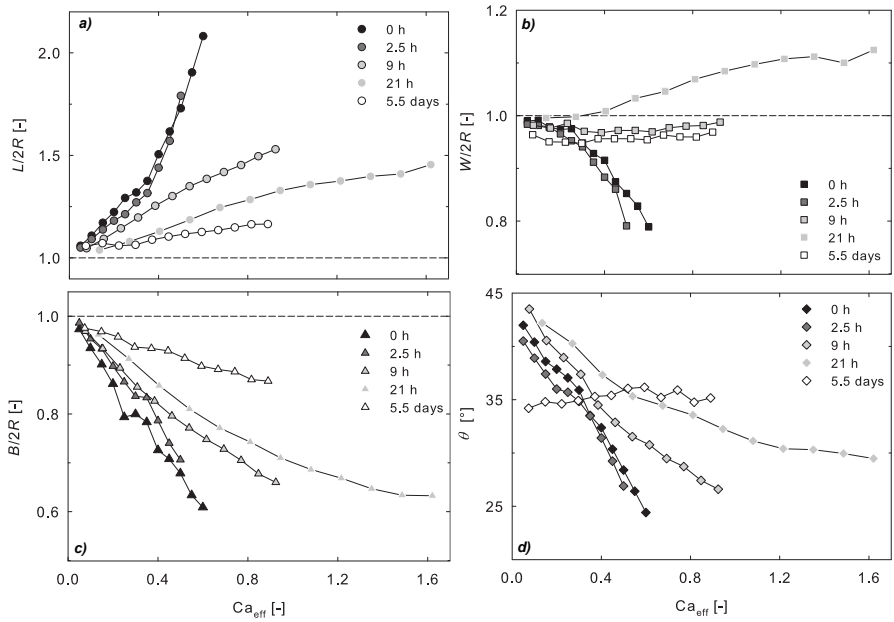

Figure 6.2: Dimensionless droplet axes (a) $L/2R$, (b) $W/2R$, (c) $B/2R$, and (d) orientation angles θ of particle-covered droplets (MS-0.1 + 0.4 vol% silica) with a different residence time in the 0.4 vol% suspension of silica nanoparticles as function of effective capillary number $\mathrm{Ca_{eff}}$.

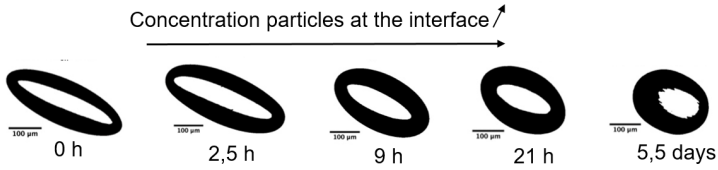

Figure 6.3: Images of particle-covered droplets (MS-0.1 + 0.4 vol% silica) with a different residence time in the 0.4 vol% suspension of silica nanoparticles. Images are taken in the side view (velocity - velocity gradient plane) at $\mathrm{Ca_{eff}} \sim 0.50$.

small amount of particles only has a limited effect on the steady-state droplet dynamics as compared to that of the neat droplet. However, the droplet shape differs slightly from the ellipsoidal shape of the particle-free droplet and rather has a sigmoidal shape, as shown in Figure 6.3.

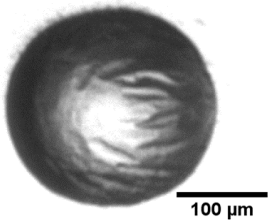

Figure 6.4: Example of buckling and wrinkling of the particle-covered interface. Image is taken in the top view (velocity - vorticity plane) at rest.

When the particle concentration at the droplet interface gradually increases, it can be seen in Figure 6.2 that the behavior becomes different as the droplet deformation gradually decreases until almost no deformation is observed for a droplet with a residence time of 5.5 days in the suspension. As demonstrated in Figure 6.3, this droplet remains almost spherical, even at very high capillary numbers. The droplet thus behaves as a rigid particle and hence, a more suspension-like behavior is observed. In addition, particle-covered droplets show less orientation towards the flow direction, especially at high capillary numbers. Finally, after 5.5 days inside the suspension, the droplet orientation becomes independent of the applied capillary number.

As already mentioned in the previous section, an elastic particle network is formed at higher interfacial particle coverage. This network is responsible for the almost complete suppression of the droplet deformation. The formed elastic shell could also been observed during the experiments by wrinkling and buckling of the droplet interface, as illustrated in Figure 6.4.

Another effect is observed for droplets with a residence time of 21 h or 3 days in the suspension. For these droplets, $W/2R$ becomes larger than 1 and hence, elongation in the vorticity direction is observed. Mao et al. [107] also reported vorticity alignment for ellipsoidal particle filled systems which form a rigid network at the interface. A similar phenomenon is earlier reported for viscoelastic systems and attributed to normal stress differences [115, 185, 97].

6.1.3 Droplet breakup

As illustrated in the previous section, the elastic particle network formed at the interface substantially suppresses droplet deformation until suspension-like behavior is observed at high particle concentrations. However, in contrast with rigid particles, it is still possible to damage the particle network and hence,

break up the droplets. In this section, breakup is studied in detail by increasing the applied capillary number in small discrete steps until breakup occurs. After every applied capillary number, the shear flow is stopped and hence, the droplet is allowed to retract back to its spherical shape before the next capillary number is applied.

Two opposites effects are again observed in the evolution of the critical capillary number at which breakup occurs as function of the residence time of the droplet in the suspension, presented in Figure 6.5. First, at low particle concentrations, the critical capillary number slightly decreases. Hence, the few particles present at the droplet interface slightly destabilize the droplet against breakup by disturbing the free surface. Then, at higher particle concentrations, a strong stabilization effect against droplet breakup is observed and droplets only break up at very high capillary numbers as compared to the neat system. These results are also expected from the results of the steady-state droplet deformation (section 6.1.2).

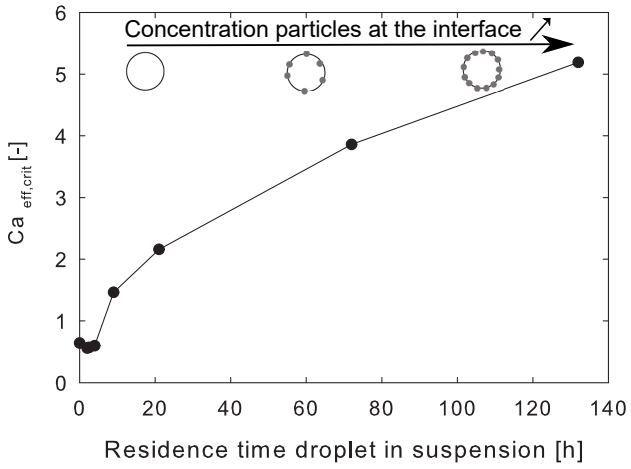

Figure 6.5: Critical effective capillary number at which breakup occurs for particle-covered droplets (MS-0.1 + 0.4 vol% silica). The particle concentration at the interface increases with the residence time of the droplet in the 0.4 vol% suspension of silica nanoparticles.

Also the breakup behavior of the particle-filled systems is compared with that of the neat system. The first column in Figure 6.6 shows the particle-free system which breaks up, as expected, by necking into two daughter droplets and some satellite droplets. The breakup behavior of droplets with a low concentration of particles at the interface is very similar to this breakup by necking observed for

the neat system. This is illustrated in Figure 6.6 for a droplet with a residence time of 4 h in the suspension. However, a longer thread is formed before breakup occurs, which also affects the satellite droplets formed.

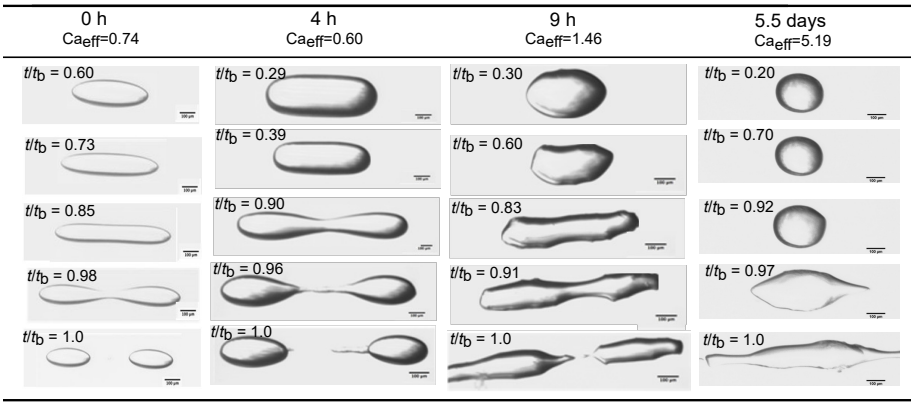

Figure 6.6: Images of particle-covered droplets (MS-0.1 + 0.4 vol% silica) taken during droplet breakup at $Ca_{eff,\,crit}$ (indicated in table) in top view (velocity - vorticity plane). The particle concentration at the interface increases with the residence time of the droplet in the 0.4 vol% suspension of silica nanoparticles, indicated in the table. Images are taken at time t/t_b, with t_b the breakup time.

At higher particle concentrations, the breakup behavior is completely different. First, a smooth droplet surface and reduced deformation is observed. At a certain moment, however, local instabilities in the particle network arise. These local instabilities further grow and cause irregular droplet deformation. Finally, the droplet bursts in a very short period of time. Figure 6.6 demonstrates this typical breakup behavior for a droplet with a residence time of 9 h in the suspension and for a droplet that spent 5.5 days in the suspension. The latter breaks up into several fragments, while the first droplet still breaks up into two main daughter droplets. In contrast to the determined critical capillary number, the shape dynamics observed during breakup are irreproducible and specific for a certain droplet.

6.1.4 Hysteresis effect

The previous section demonstrated the possibility to plastically deform and damage the formed elastic particle shell at the interface. A damaged particle network will have another effect on the droplet dynamics as compared to the perfect smooth particle network obtained by keeping the droplet in the

suspension. Therefore, the droplet behavior will depend on the flow history. This effect is systematically studied in Figure 6.7 for a droplet with a residence time of 9 h in the suspension. This figure shows the steady-state deformation by means of the dimensionless droplet axis $L/2R$ as function of the applied capillary number. Appendix C.1 shows the corresponding dimensionless droplet axes $B/2R$ and $W/2R$.

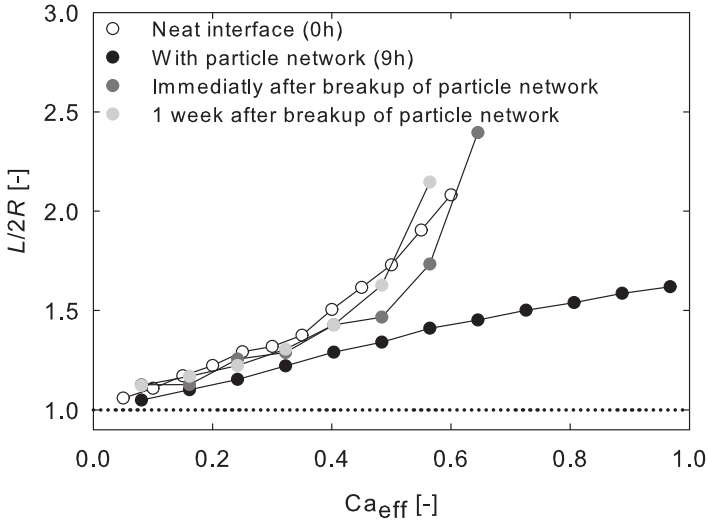

Figure 6.7: Dimensionless droplet axes $L/2R$ of particle-covered droplets (MS-0.1 + 0.4 vol% silica) as a function of the effective capillary number Ca_{eff}. White data points refer to a droplet with a neat interface. Other measurements are performed with a droplet with a residence time of 9 h in the 0.4 vol% suspension of silica nanoparticles, immediately after droplet transfer (black data points), immediately after breakup of the particle network by shear (dark grey data points), and 1 week after breakup of the particle network (light grey data points).

First, the steady-state droplet deformation is measured immediately after the droplet transfer from the suspension. Hence, the droplet has a smooth and homogeneous particle layer at the interface which forms a network. These results are shown in Figure 6.7 by the black data points and agree with these shown in Figure 6.2. Then, the capillary number is further increased until near breakup. However, just before complete breakup of the droplet, the flow is stopped and the droplet is allowed to retract. The elastic shell is thus deformed outside its elastic deformation region and is damaged. Thereafter, the steady-state deformation of this droplet is measured again as function of the capillary

number. The results are represented by the dark grey data points in Figure 6.7. As can be seen, a higher steady-state droplet deformation is observed, comparable to that of the particle-free system. Even after 1 week, the damage is not restored and hence, the droplet deformation is still larger as compared to that of the droplet with an intact particle network. Hence, the droplet has a time-dependent (thixotropic) interface and the droplet response is thus depending on the flow history.

Before the elastic shell is plastically damaged, the droplet evolves towards a stable droplet shape as demonstrated in Figure 6.8. This figure shows the main dimensionless droplet axis in top view ($L_p/2R$) for $Ca_{eff} = 0.23$ as function of dimensionless time from the moment shear flow is started. The corresponding droplet image in the inset (i) illustrates this stable droplet shape and the smooth and homogenous particle network at the interface. In contrast, the results shown by the grey data points in Figure 6.8, obtained after deforming the particle shell outside its elastic deformation region, show clear shape oscillations and irregular droplet shapes which are similar to the observations for a viscoelastic capsule [87]. The corresponding inset (ii) of Figure 6.8 demonstrates that the network has been broken at different points, resulting in accumulated aggregates. By this accumulation and the lack of mobility, a heterogeneous particle distribution and non-spherical particle shell exists at the droplet interface.

It is also noticed that applying too high shear forces during the transfer of a droplet from the suspension to the particle-free matrix can irreversibly damage the particle network. This damage affects the steady-state deformation and droplet shape observed. The droplet will deform more as compared to a similar droplet with a homogeneous particle shell and hence, will also break at smaller capillary numbers. In addition, clear oscillations in the measured dimensionless droplet axes are observed due to the irregular droplet shapes. This effect is illustrated in Figure 6.9 which shows the dimensionless droplet axes $L_p/2R$ as function of dimensionless time for two droplets with a similar residence time in the suspension, but with different behavior due to the different applied forces during droplet transfer. Application of too high forces during droplet transfer can even result in an irregular, non-spherical droplet shape at rest.

6.2 Link with rheological properties of the particle-covered interface

In this section, the rheological properties of the flat interface are studied in order to link the droplet dynamics observed, described in the previous section to these properties. First, the interfacial shear properties are studied by using a

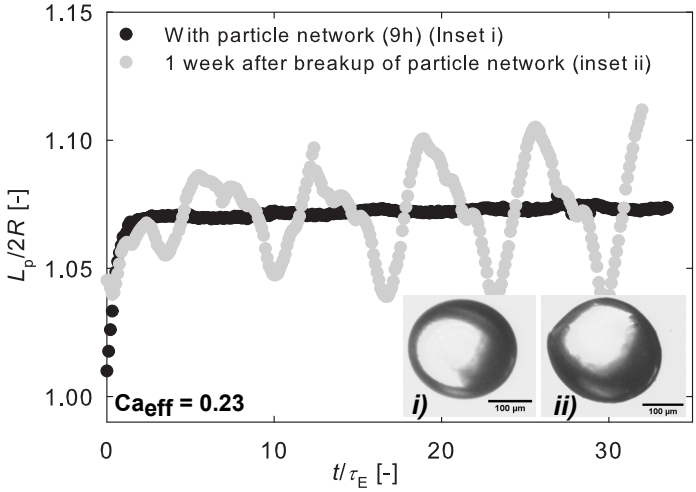

Figure 6.8: Dimensionless droplet axes $L_p/2R$ of particle-covered droplets (MS-0.1 + 0.4 vol% silica) as function of dimensionless time t/τ_E. Measurements are performed with a droplet with a residence time of 9 h in the 0.4 vol% suspension of silica nanoparticles, immediately after droplet transfer (black data points) and 1 week after breakup of the particle network (light grey data points). Inset: Images of the droplets in the top view (velocity - vorticity plane) during steady-state deformation (i) immediately after droplet transfer and (ii) 1 week after breakup of the particle network. All data and images are for Ca_{eff} = 0.23.

double-wall ring set-up (Figure 3.6). As mentioned in section 3.3 of Chapter 3, the viscosities of PDMS and PIB and the layer thickness of the PIB suspension is equal to that used during the preparation of the particle-covered droplets. Hence, we can assume that the flat particle-covered interface studied in this section, is identical to the particle-covered droplet interface.

6.2.1 Interfacial shear rheology

Interfacial shear rheology is a very useful tool to characterize the particle network and to compare different particle networks. In addition, several authors already showed by interfacial shear experiments that these properties can have a significant effect on the droplet deformation of protein-covered droplets [44, 45] or morphology control of polymer blends [183]. The interfacial moduli G''_s and

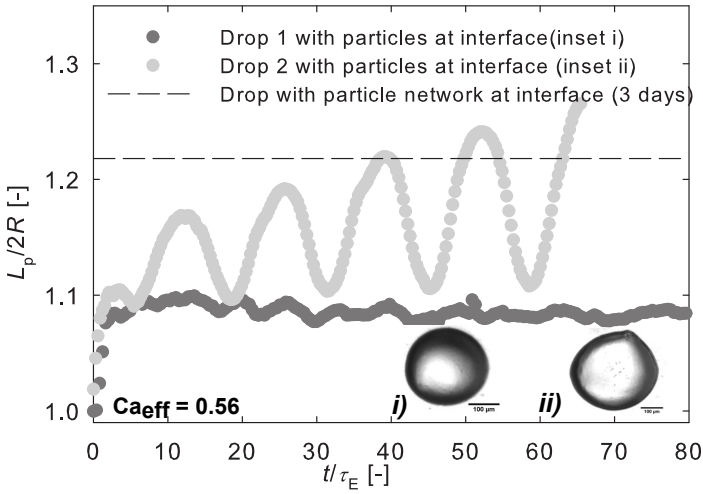

Figure 6.9: Dimensionless droplet axes $L_p/2R$ of particle-covered droplets (MS-0.1 + 0.4 vol% silica) as function of dimensionless time t/τ_E. Measurements are performed with droplets with a residence time of 4.6-4.8 days in the 0.4 vol% suspension of silica nanoparticles, immediately after a failed droplet transfer. The dashed line represents $L_p/2R$ of a droplet with a residence time of 3 days in the 0.4 vol% suspension of silica nanoparticles at $Ca_{eff} = 0.59$ after a successful droplet transfer. The insets show images during shear flow of the two droplets in the top view (velocity - vorticity plane). All data and images are for $Ca_{eff} = 0.56$.

G'_s are measured as a function of time, strain and angular frequency. Finally, also the yield stress of the particle network is determined by performing creep experiments.

The Boussinesq number, defined in Equation 3.4, for the neat interface is equal to 7. Therefore, all results shown in this section are sub-phase corrected. The iterative procedure applied to perform this correction is explained in detail in the work of Vandebril et al. [182]. However, the corrections are relatively small for all experiments. It has to be noted, however, that this correction is valid for a volume of 20 ml as upper subphase, while a volume of 23.3 ml is added in the performed experiments to achieve a 1 cm thick layer. Additionally, the density and viscosity of the PIB suspension with 0.4 vol% of silica nanoparticles used as upper phase are approximated by these of the pure PIB.

Shear moduli and timescales

A viscoelastic particle network builds up at the interface as a function of time as can be seen in Figure 6.10 which shows the sub-phase corrected interfacial response at a constant angular frequency of 0.5 rad/s and strain of 0.025% as a function of time. Time zero corresponds to the time the measurement is started, directly after the addition of the PIB suspension as top phase. As G'_{s} becomes larger than G''_{s}, the particle network becomes predominantly elastic. As a reference, the response of the neat interface is also shown by a dashed line. However, caution is needed as the interfacial response of the neat system is small and hence, close to the machine limits. Consequently, the interfacial characteristics of the formed particle-covered interface are substantially different as compared to that of the neat interface and the formed network corresponds to the elastic network responsible for the suppression observed for droplet deformation, described in the previous section. Steady-state is reached after approximately 4 h . Therefore, a waiting time of at least 10 h is applied and the moduli at steady-state are compared before every experiment to ensure steady-state is reached and the particle network is fully developed.

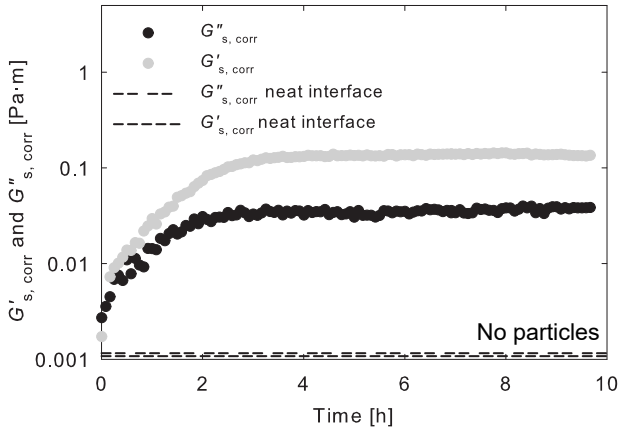

Figure 6.10: Corrected interfacial loss modulus $G''_{\mathrm{s,\,corr}}$ and storage modulus $G'_{\mathrm{s,\,corr}}$ as function of time (strain amplitude of 0.025% and angular frequency of 0.5 rad/s). Time zero corresponds to the moment the 0.4 vol% suspension of silica nanoparticles is added as the top phase and the measurement is started. The dashed lines show the corrected interfacial moduli of the particle-free system as a reference.

An estimation of the surface coverage at steady-state can be made with the steady-state moduli obtained according to the Krieger-Dougherty equation,

modified for 2D suspensions of hard spheres [114]:

$$\left|\eta^*_{s,r}\right| = \left(1 - \frac{\phi}{\phi_{max}}\right)^{-2\phi_{max}} \tag{6.2}$$

With $\eta^*_{s,r}$ the complex relative interfacial viscosity and ϕ_{max} equal to 0.907 for a hexagonal packing of a 2D monolayer of hard spheres [138]. According to this equation, the interfacial moduli obtained at steady-state correspond to a surface coverage of 0.84. However, it has to be noted that this approach is only valid in the high frequency range where the moduli G' and G_J of the particle system and neat system approach the same slope of 2 and 1, respectively [55]. However, the steady-state moduli obtained are determined at an angular frequency of only 0.5 rad/s and hence, this surface coverage is only a rough estimation.

In order to further quantitatively link the droplet dynamics observed to the interfacial shear characteristics of the flat interface, the Young's modulus of the particle shell at the droplet interface is determined according to the Barthès-Biesel and Sgaier (BBS) model [9]. This model predicts the deformation of a soft capsule, i.e. a liquid droplet surrounded by a deformable membrane, based on the viscoelastic characteristics of the membrane. The model is however not yet validated for particle-covered droplets. The perturbation analysis gives following prediction for the deformation parameter, defined in Equation 2.4, of a soft capsule subjected to a weak, simple shear flow:

$$D = \frac{25}{4}\frac{\eta_m \cdot R}{E \cdot h} \cdot \dot{\gamma}, \tag{6.3}$$

with E the Young's modulus and h the thickness of the membrane. This equation is only valid for capsules with a membrane modulus over viscosity ratio of order $O(1)$ and at small deformations in the elastic region [45, 9].

We can approach the particle-covered droplets as soft capsules and determine the Young's modulus of the rigid particle shell at the droplet interface. Figure 6.11a illustrates the linear relationship (Equation 6.3) between the droplet deformation parameter and the applied shear rate for particle-covered droplets. As the residence time in the suspension increases and hence, the particle coverage at the droplet interface increases, the slope decreases, indicating a higher modulus of the particle shell. Figure 6.11b summarizes the determined Young's modulus multiplied by the particle layer thickness as function of the residence time of the droplet in the 0.4 vol% silica nanoparticle suspension. Erni et al. [45] followed the same approach for protein-covered droplets and found a Young's modulus of 0.245 Pa·m. Hence, as compared to protein-covered droplets the Young's modulus of the particle shell is rather small.

The modulus determined from droplet deformation (Figure 6.11b) can be compared with the interfacial shear modulus of the particle network (Figure

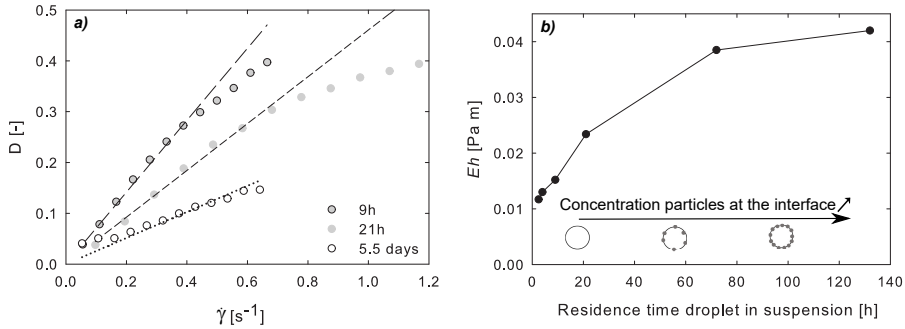

Figure 6.11: (a) Deformation parameter D of particle-covered droplets (MS-0.1 + 0.4 vol% silica) with different residence times in the 0.4 vol% suspension of silica nanoparticles as function of the applied shear rate. The dashed lines indicate the corresponding linear fits. (b) Young's modulus E multiplied with particle layer thickness h determined according to the BBS model [9] from the deformation of particle-covered droplets (MS-0.1 + 0.4 vol% silica) with different residence times in the 0.4 vol% suspension of silica nanoparticles.

6.10). It is expected that the Young's modulus is approximately equal to 3 times the shear modulus. It can be seen that this is not exactly valid, but both moduli are of the same order of magnitude. However, the time scales are completely different. The shear moduli already reach steady-state after approximately 4 h, whereas the Young's modulus determined from the droplet deformation is still increasing after a few days. No direct link between the shear moduli and the droplet deformation behavior is thus found.

Rebuilt particle network

The interfacial shear moduli G'_s and G''_s are measured at a fixed strain amplitude of 0.025% as function of the angular frequency. This measurement is performed after the particle network is completely developed. Figure 6.12 shows the values of G'_s obtained as function of the angular frequency. G'_s is only weakly dependent on the angular frequency ($G'_s \sim \omega^{0.16}$), which is typical for a gel-like system. Hence, the aggregated particle network forms a rigid shell at the interface. This rigid shell is broken by the application of a high shear rate (1 s^{-1}). The results of the subsequent experiment, a frequency sweep, is also shown in Figure 6.12. As can be seen in this figure, the elastic particle network is indeed almost completely broken down as G'_s decreased substantially.

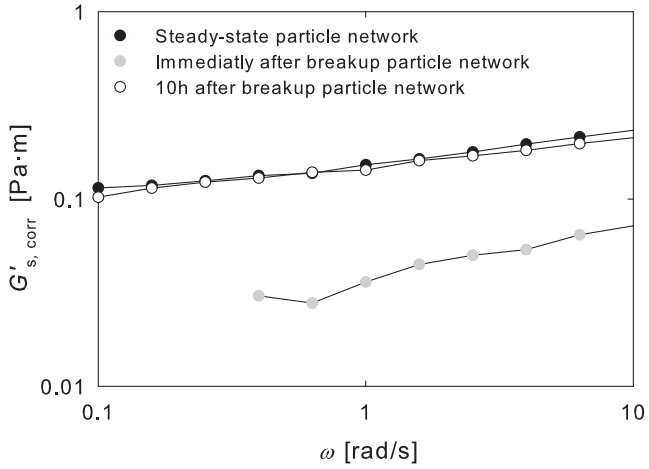

Figure 6.12: Corrected interfacial storage modulus $G'_{\mathrm{s,\,corr}}$ as function of angular frequency (strain amplitude of 0.025%). Black data points are measured 10 h after addition of 0.4 vol% suspension of silica nanoparticles as the top phase, hence steady-state in particle interfacial coverage is reached. Grey data points are measured after breakup of the particle network by applying a shear rate of 1 s^{-1} for 60 s. Frequency sweep indicated by white data points is performed 10 h after breakup of the particle network.

Thereafter, the ability to rebuilt the interfacial particle network is followed in time by measuring the surface moduli as function of angular frequency every hour. After a period of 10 h, the particle network has almost completely recovered. These results are in clear contrast with the results of the droplet deformation suppression which is not restored after a resting period of one week (section 6.1.4). However, during the resting period of the flat interface, the top layer still contained particles, while the particle-covered droplets were isolated in a particle-free matrix during this resting period. It was not possible to remove the suspension top layer and replace it by a particle-free PIB top phase without damaging the interfacial network. Hence, additional particles were able to migrate towards the flat interface, which was impossible during the single droplet experiments. Vandebril et al. [181] also reported the ability of a 2D particle network consisting of ellipsoidal particles to rebuilt. In these experiments, only a small diffusive particle layer just above the flat interface was present.

Linear strain limit

The interfacial response as function of the strain amplitude is determined at a constant angular frequency of 0.5 rad/s. The experiment is performed 10 h after the addition of the 0.4 vol% suspension of silica nanoparticles as top phase and hence, the particle network is fully developed at the start of this experiment. Indeed, the results in Figure 6.13 demonstrate that the sub-phase corrected moduli are comparable with the results of Figure 6.10 at steady-state in the linear viscoelastic region at low strain amplitudes and the interface is predominantly elastic.

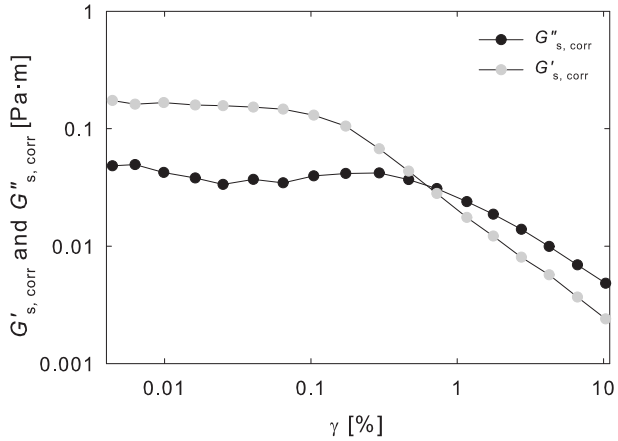

Figure 6.13: Corrected interfacial loss modulus $G''_{\mathrm{s,\,corr}}$ and storage modulus $G'_{\mathrm{s,\,corr}}$ as function of strain amplitude (angular frequency of 0.5 rad/s). Strain sweep is performed 10 h after addition of 0.4 vol% suspension of silica nanoparticles as the top phase, hence steady-state in particle interfacial coverage is reached.

The linear strain limit is approximately equal to 0.06 %. The linear strain limit of an aggregated 2D suspension strongly depends on the surface coverage and decreases with surface coverage [138, 105]. For an air-water interface covered with spherical polystyrene particles (3.1 μm), Reynaert et al. [138] found a linear strain limit around 0.15% for a particle coverage of 0.50. According to Equation 6.2, the surface coverage in our experiments is roughly equal to 0.84. The linear strain limit of this 2D network is also similar to the value of 0.05% reported by Buscall et al. [19] for a 3D aggregated suspension consisting of silica nanoparticle (26 nm).

The corresponding linear stress limit can also be calculated from these results, and equals $0.97 \cdot 10^{-4}$Pa·m. This value can be considered as an approximation of the yield stress of the particle network. However, the yield stress is determined more accurately in the next subsection by performing step stress or creep experiments. This value will be compared with the stress applied in the single droplet dynamics experiments.

When the strain exceeds the linear limit, G'_s starts to decrease monotonically, while G''_s first slightly increases before it starts to decrease. This small increase can be attributed to particle rearrangements and is typical for the breakup of an aggregated network [181, 104]. Finally, the particle network breaks down at higher strain amplitudes, which results in a more viscous interface ($G''_s > G'_s$).

Yield stress

The yield stress is determined by performing creep(-recovery) tests in which a step stress signal is applied to the interface, while the material response or strain is measured as a function of time. During the recovery phase, this stress is instantaneously released, while the strain is still measured. Imperiali et al. [77] noticed that these recovery measurements are very sensitive and small offsets in recovery are possible.

The measured response of the flat particle-covered interface for the different applied surface stresses ranging from $0.5 \cdot 10^{-4}$ to $0.8 \cdot 10^{-4}$Pa · m as shown in Figures 6.14a and b is typical for a viscoelastic liquid. The incomplete recovery can be the result of rearrangements in the particle network and plastic flow [77]. The material strain response for applied surface stresses smaller or equal to $1.0 \cdot 10^{-4}$Pa · m is very small as demonstrated in Figure 6.14c. When a surface stress of $2.0 \cdot 10^{-4}$Pa · m is applied, the measured strain is, however, much larger. It can be concluded that the particle network formed at the interface breaks when a stress of $2.0 \cdot 10^{-4}$Pa · m is applied, which results in a sudden decrease in interfacial elasticity and viscosity and hence, flow of the interface. Hence, the yield stress of the particle network ranges between $1.0 \cdot 10^{-4}$ and $2.0 \cdot 10^{-4}$Pa · m. This value is similar to the linear stress limit determined in the previous subsection, which can also be considered as an indication of the network's yield stress.

This surface yield stress can be compared with bulk values by dividing this value by the interfacial thickness. If we assume a particle layer thickness equal to the diameter of the nanoparticles, i.e. 50 nm, an apparent bulk yield stress between 2000 and 4000 Pa is obtained.

This yield stress can be compared with the stress required in the single droplet

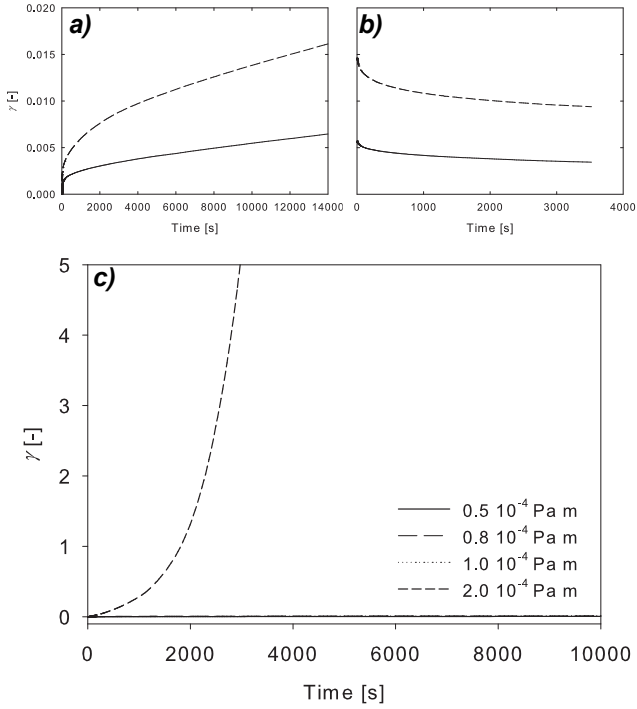

Figure 6.14: Material response (strain γ) as function of time during the application of a shear stress σ to the interface (creep curves: a and c) and after the release of this step stress signal (recovery curves: b).

experiments to breakup the particle network at the droplet interface. The applied hydrodynamic stress σ on a spherical particle can be calculated with the following equation [82]:

$$\sigma = 2.5 \cdot \eta_{\mathrm{m}} \cdot \dot{\gamma}. \tag{6.4}$$

The maximum stress applied during droplet breakup ($\mathrm{Ca}_{\mathrm{crit}}$) is then equal to 161 Pa. Hence, the applied stresses to the droplet surface during the breakup experiments are an order of magnitude smaller as compared to the determined yield stress of the interfacial particle network.

6.2.2 Dilatational rheology

The dilatational properties of the interface also have an important contribution during droplet deformation. Experiments are performed to measure the surface pressure-area isotherms during compression of the particle laden interface in a Langmuir trough using a Wilhelmy balance. However, as illustrated in Figure 6.15, we could conclude from these experiments that the PDMS-PIB system is not suitable to measure surface pressure-area isotherms with the current available techniques due to the low interfacial tension between PDMS and PIB and the small effect of the particles on this interfacial tension. In addition, the flat interface is compressed during these experiments, while the droplet interface is also subjected to extension and shear during deformation.

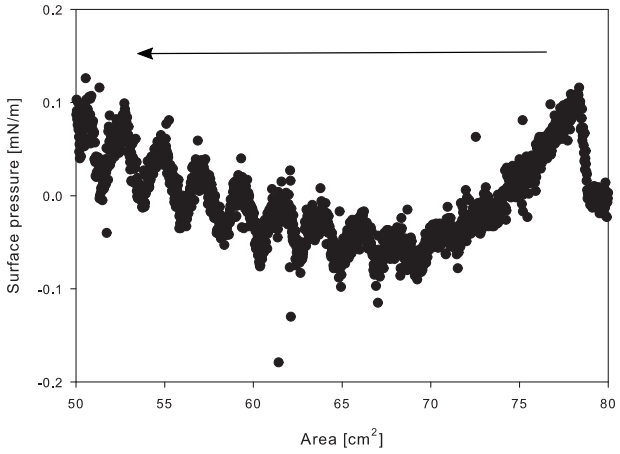

Figure 6.15: Example of surface pressure-area isotherm during compression of a particle laden interface. PDMS is used as bottom phase, while the upper phase consists of PIB with 0.1 vol% silica nanoparticles. A waiting period of 24 h is applied before the experiment to allow particles to migrate towards the interface.

6.3 Conclusion

We first observed the interesting dynamics of particle-covered droplets which are qualitatively different as compared to the dynamics of neat droplets. At high particle coverage, the particles form a particle network at the droplet interface. As expected from previous studies described in literature, this network is

responsible for an almost complete suppression of the droplet deformation and stabilizes the droplet against breakup. Hence, a suspension-like behavior of the droplets is observed with limited droplet deformation and orientation. However, the droplet deformation becomes comparable to that of the particle-free system when the particle network is damaged. Surprisingly, even after a resting period of 1 week, the particle network is not restored. Hence, the droplets have a time-dependent (thixotropic) interface and the droplet dynamics depend on the flow history. In addition, the breakup behavior is very irregular.

The aim of this study is however to quantitatively investigate the link between the droplet dynamics observed and rheological properties of the particle-covered interface. This behavior is rather complex and no direct link is found. From the interfacial shear experiments, we could conclude that indeed, a viscoelastic interface is formed with a dominantly elastic behavior. However, the time scales observed during interfacial shear rheology experiments are different compared with the timescales observed in the droplet deformation experiments. Additionally, it is seen that the elastic network completely rebuilds after breakup of the network by shear. The particle network also exhibits a shear yield stress. However, this yield stress is an order of magnitude larger than the applied stress during droplet breakup and hence, does not explain the particle network breakup observed during droplet breakup. From these interfacial shear experiments, we could conclude that the dilatational interfacial properties probably also play an important role during droplet deformation. However, it was not possible to further investigate these dilatational interfacial properties of this system with the current techniques and selected material system.

Chapter 7

Conclusions and outlook

Particles are often incorporated in emulsions or polymer blends to improve the material performance or to tailor the blend morphology. The incorporation of solid particles significantly affects the single droplet dynamics. Due to these effects, the overall microstructure and hence, the final material properties will change with the addition of particles.

The first part of this work focuses on droplet-matrix systems containing non-Brownian particles which are initially uniformly distributed inside the droplet phase. It is shown in this work, that the particles migrate in the vorticity direction during the application of simple shear. Consequently, the system evolves towards a non-homogenous steady-state particle distribution. Surprisingly, the final steady-state distribution depends on the system's viscosity ratio. These new results could for example be used as an alternative to the acoustic field proposed by Fornell et al. [50] to control the lateral position of particles inside droplets. This is done in order to create droplets with increased particle concentrations by splitting the droplet into 3 daughter droplets after the application of simple shear flow. In addition, this work quantitatively verifies the hypothesis that the single droplet dynamics of particle-filled droplets can be predicted by the droplet viscosity governed solely by the particle concentration. Therefore, droplet deformation, retraction, and breakup of different particle-filled model systems are experimentally investigated and compared with particle-free reference systems with similar properties. It is shown that for systems with a viscosity ratio larger than one, the particles significantly affect the droplet dynamics. These results can be used to further predict the effects of particles in more concentrated systems and complex flow fields. In general, the dynamics are slowed down and deformation and breakup is suppressed by the addition

of particles. Therefore, larger droplets and possibly non-spherical droplets are expected in the final material. At high concentrations or high particle over droplet size ratios, the droplet size distribution will also become broader. Hence, the addition of particle such as carbon black as a coloring agent will also affect the microstructure and hence, the final material properties.

The second part of this work focuses on droplet-matrix systems with a particle-covered interface. In previous studies [187, 183, 167, 67] it is shown that particles at the interface stabilize the droplets against coalescence. In general, particles will have a stabilizing effect on the formed microstructure from the moment they reach the droplet interface and hence, 'freeze' the microstructure. This work shows that by the application of high shear rates the particle network and finally, also the droplet breaks up. However, the critical capillary number for breakup of particle-covered droplets is higher compared to that of the neat droplet system. The particle network thus stabilizes the droplet against breakup. Hence, the effect of particles on the average droplet size in more concentrated systems will depend on the applied shear rates, kinetics and mixing procedure. The droplet breakup occurs very irregularly and will result in a broad droplet size distribution and non-spherical daughter droplets. The main results of the different parts of this work are summarized in detail below together with some recommendations for further research.

Non-Brownian particles localized inside sheared droplets

Three model systems are selected which fulfil the requirements to enable to investigate their droplet dynamics microscopically. All model systems consist of a PDMS matrix phase. The first system (MS-1.4) consists of a PEG-*ran*-PPG droplet phase, resulting in a viscosity ratio of 1.4 ($\lambda = 1.4$). The second system (MS-0.09) consists of the same components, but the system's viscosity ratio is smaller than one ($\lambda = 0.09$). The third system (MS-0.08L) is composed of a different droplet phase material (PPG) and hence, the interfacial tension is lower in this case. However, the system's viscosity ratio is matched with the viscosity ratio of MS-0.09 ($\lambda = 0.08$). Microsized PS particles are added which remain localized inside the droplet phase during the entire course of the experiments. The particle concentration and particle to droplet size ratio is systematically varied for the different systems.

Particle migration

During rest, the particle distribution inside the droplets remains homogeneous. In contrast, this dissertation shows that during the application of shear the

particles migrate in the vorticity direction towards or away from the equatorial plane. The final steady-state particle distribution mainly depends on the system's viscosity ratio, but the migration behavior is also affected by the particle concentration. Figure 7.1 gives a schematic overview of the different steady-state particle distributions obtained. This figures shows that in the systems studied with low particle concentrations (1 vol%) most particles align on a streamline between the central plane and the droplet edge. However, for systems with a viscosity ratio smaller than one, some particles also migrate in the vorticity direction towards the droplet edges. At higher particle concentrations (5 - 20 vol%), Figure 7.1 illustrates that particles in the system with a viscosity ratio larger than one migrate towards the central droplet axis, while particles move away from this central droplet axis towards the droplet edge in the systems studied with a viscosity ratio smaller than one.

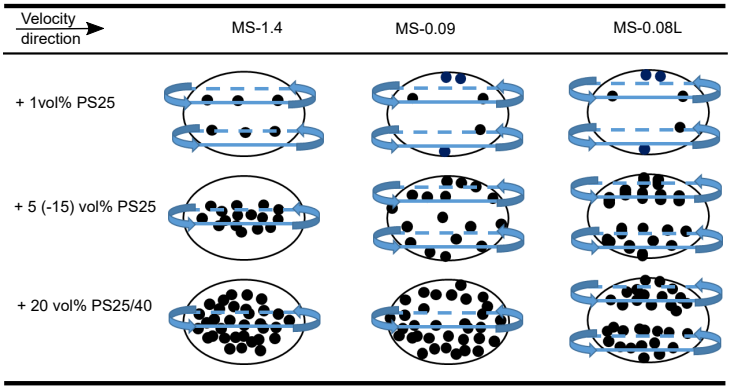

Figure 7.1: Schematic overview of the steady-state particle distributions in top view obtained after the application of shear flow for the three systems studied MS-1.4, MS-0.09 and MS-0.08L as function of the particle concentration.

An important part of this work is to further understand this surprising particle migration behavior. With a quantitative analysis, it became clear that a lower capillary number or higher particle concentration result in a larger time needed to reach the steady-state particle distribution. Furthermore, the results of numerical VOF simulations of the velocity profiles and shear rate gradients inside the particle-free mother systems (MS-1.4 and MS-0.08L) are used to discuss and evaluate possible driving forces. Buoyancy forces, centripetal forces, inertia and elasticity are eliminated as possible driving forces for the migration behavior observed. However, differences in streamlines and shear rate gradients are observed which can qualitatively explain part of the migration behavior towards zones of low shear rates and/or low streamline curvature. However,

also confinement, secondary flows, and particle disturbance flow can play a role. Hence, different mechanisms are simultaneously present and contribute to the final steady-state particle distribution which makes a quantitative analysis of the underlying mechanisms complex.

Based on these conclusions, recommendations for future work are listed below:

- In this study, the particle migration behavior in systems MS-0.09 + Y vol% PS25 is only studied for three different particle concentrations (1, 5, and 20 vol%), all with PS particles with a diameter of 25 µm. Some droplets show a similar change in particle distribution as observed for MS-0.08 + Y vol% PS25, while for MS-0.09 + 20 vol% PS25 the changes are less clear and only a very small particle-free zone arises. Therefore, an enlargement of the investigated parameter space to intermediate particle concentrations and other particle sizes would be interesting to better understand the particle migration behavior in this system and the general effect of the system's viscosity ratio and interfacial tension.

- In general, the investigated parameter space could also be expanded to smaller and larger particles, e.g. PS particles of 5 µm and 82 µm with particle concentrations ranging from 1 vol% to 20 vol%.

- In the current quantitative analysis, the time to reach a steady-state distribution is compared for different systems. Hence, this analysis does not provide the migration speed of the individual particles, but only the kinetics of the overall microstructure change. Consequently, a quantitative comparison between different systems which reach a different steady-state particle distribution is not possible. Moreover, it is difficult to compare systems with different particle sizes and particle concentrations as the number of particles that have to migrate to create a particle-free zone differs. In order to gain more insight in the underlying mechanisms, it would be interesting to be able to determine and compare the trajectories and corresponding migration speed of individual particles in the different systems. With the current setup, it is possible to determine the particle trajectories at very low particle concentrations (1 vol%), but identification of individual particles becomes impossible at higher particle concentrations. A possible alternative would be to work with fluorescence microscopy and follow a few tracer particles, while the droplet is subjected to shear flow. In addition, a 3D study with a confocal microscope of the particle-filled droplets subjected to shear flow would provide more insight in the particle trajectories. However, for a rheo-confocal 3D study the refractive indexes of the different components have to be matched.

- To get a more quantitative understanding of the underlying driving forces numerical simulations of the droplet phase containing particles, and consideration of the disturbance flow induced by the particles would be helpful. However, these simulations are complex and computationally demanding, especially at high particle concentrations.

Droplet dynamics

The addition of non-Brownian particles increases the droplet phase viscosity and hence, the viscosity ratio of the system. Therefore, the intrinsic particle effects on the droplet dynamics of the three model systems are studied by comparing the results with the dynamics of reference systems with similar viscosity ratios. It is shown that the particle distribution has no effect on the droplet dynamics. The results in this dissertation demonstrate that the particle effects on the droplet dynamics greatly depend on the viscosity ratio of the system.

For the systems with a viscosity ratio much smaller than one (MS-0.09 and MS0.08L), the increase in viscosity ratio caused by the particles has no significant effect on the droplet dynamics, as also predicted by the MM model. For the system with a viscosity ratio larger than one (MS-1.4), a reduced droplet deformation, slower transient dynamics, and stabilization against breakup as compared to breakup of the neat particle-free blend is observed. Therefore, the droplet dynamics of this system are further analyzed and a quantitative comparison between the different particle systems and corresponding reference systems is made in this work. This allows us to verify the hypothesis that particle-filled droplets can be treated as a homogeneous medium characterized by its viscosity which is governed by the particle concentration. The effects depend on the particle to droplet size ratio r/R.

The deformation, retraction, and breakup behavior of MS-1.4 + 20 vol% PS5 ($r/R = 0.02$) is similar to that of the corresponding reference system. Hence, the system behaves as a homogenous medium with a viscosity governed by the particle concentration as stated in the proposed hypothesis. However, this work demonstrates that systems with a particle over droplet size ratio larger than 0.1 ($r/R > 0.1$) behave as a slightly more viscous system, with a higher viscosity ratio than expected purely based on the particle concentration. Hence, systems with $r/R > 0.1$ show a reduced steady-state deformation and slower transient dynamics as compared to the corresponding reference systems. Additionally, a different breakup mechanism is observed wherein particle-free satellite droplets are released from the droplet tips, while breakup of the particle cluster was impossible within the possible shear rate range. These systems also show additional intrinsic particle effects like asymmetric droplet shapes

and consequently, oscillations in deformation. The intrinsic particle effects observed are rather limited, but become more pronounced at higher particle concentrations or larger particle to droplet size ratios. A single correlation factor for the viscosity ratio which can predict the overall single droplet dynamics could not be found due to the quantitatively different particle effects for steady-state deformation, startup, retraction, and droplet breakup.

As a recommendation for further work, it would also be interesting to perform experiments at different particle concentrations for systems with PS82 and PS5 particles to gain more insight in the effect of particle concentration and particle to droplet size ratio. Furthermore, coalescence experiments between two particle-filled droplets would help to further understand the larger droplet sizes observed in literature for concentrated particle-filled polymer blends. However, it was impossible to obtain two droplets with a similar size and particle concentration and controllable offset as it was impossible to break the central particle cluster at higher particle concentrations for the system of interest with a viscosity ratio larger than one.

Effects of nanoparticles localized at the droplet interface

In order to study the impact of particles localized at the droplet interface a model system consisting of a Newtonian PDMS droplet and a PIB matrix is selected. Silica nanoparticles with a diameter of 50 nm are added to the PIB matrix and migrate towards the interface of the PDMS droplets injected in the suspension. The particle concentration at the interface is varied by varying the droplet's residence time inside the suspension. This work elucidates the impact of a particle covered interface on the single droplet dynamics, in particular on steady-state deformation and breakup. Particles at the interface lower the interfacial tension by reducing the area of liquid-liquid interface. At low particle concentrations, a decreased interfacial tension is indeed observed, but the impact on the droplet deformation and breakup stays rather limited. With increasing particle concentration, the measured interfacial tension increases due to the elastic response of the particle network formed at the interface. The formation of this particle network results in a reduced droplet deformation and even total suppression of deformation at very high interfacial particle concentrations. Consequently, the droplet starts to behave as a rigid particle. However, droplet breakup is still possible, although at much higher capillary numbers. Hence, the particle network stabilizes the droplet against breakup. At the critical capillary number, local instabilities in the rigid particle shell grow and result in irregular droplet shapes. Consequently, the droplet bursts open into several daughter droplets. The breakup behavior is thus different compared to that of the neat system which breaks up by necking and end pinching. Due to the creation of

local instabilities in the particle shell at high capillary numbers, the droplet deformation also depends on the flow history and hence, the interface behaves thixotropic.

The previous findings clearly indicate the importance of the interfacial viscoelastic properties in the droplet dynamics. Therefore, interfacial shear rheology experiments on a flat interface with the same particle coverage as the particle covered droplet interface are performed to elucidate the relation between the interfacial rheological properties and the droplet dynamics. Experiments are performed with a ring geometry positioned between the two fluid phases whereby the lower phase is a neat system and the upper phase is a suspension. The particles from the suspension migrate to the interface over time as G' increases and becomes larger than G''. Hence, these results confirm the formation of an elastic particle network at the interface. Moreover, the response of the network to large strain amplitudes during a strain sweep is typical for the breakup of an aggregated particle network. This work tries to further quantify the relation between the interfacial shear rheological properties and the droplet dynamics observed. The shear modulus obtained is compared with the Young's modulus of the particle covered droplet interface determined according to the Bartès-Biesel and Sgaier model which predicts the deformation of a soft capsule. Both moduli are of the same order of magnitude. However, the time scales of both experiments are completely different as steady-state is already reached after 4 h in the interfacial shear rheology experiments. In contrast, there is still a clear increase in the Young's modulus of the droplet interface, even after several days. In addition, the determined interfacial yield stress of the flat particle network is much larger as compared to the stresses required to break up the particle covered droplets. From these results it can be concluded that interfacial shear rheology is not able to fully predict the droplet dynamics and additional interfacial measurements are necessary to relate the interfacial properties to the droplet dynamics. Hence, as the droplet interface is subjected to shear, compression and extension, the dilatational properties of the particle covered interface probably also play an important role. However, the current system is not suitable for further dilatational experiments.

Following proposals for further investigations are recommended:

- The current model system studied has a small interfacial tension and the particles only have a limited effect on the interfacial tension. Consequently, measurements of the surface-pressure area isotherms during compression of the particle-laden interface is not possible. A careful selection of another model system with higher interfacial tension would therefore help to further understand the relation between the viscoelastic interfacial properties and the droplet dynamics.

- Despite several attempts with SEM measurements and static multiple light scattering, the exact particle concentration at the interface is unknown in the current research. In order to be able to compare the flat interface used during interfacial shear rheology experiments with the particle covered interface of the droplets, both interfaces need to be prepared under exactly the same conditions. However, this approach limits the possibilities. For instance, a high matrix viscosity is required to perform counterrotating experiments, while the viscosity of the subphases has to be low in order to reduce subphase drag during interfacial rheology experiments. A method to create a particle covered interface with a variable and known particle concentration would expand possibilities for further research. Dockx et al. [37] recently proposed a method to control interfacial particle coverage by using transient double emulsions.
- The in-depth study of coalescence between two particle covered droplets would gain additional insight in the effects of particles on the structure development of polymer blends and the stabilizing mechanisms.

Appendix A

Materials and Methods

A.1 Estimation of wetting parameter

The wetting parameter can be calculated according to equation 2.31. The Owens-Wendt-Rabel-Kaelble approximation is used to estimate the interfacial energies [183, 125]:

$$\Gamma_{12} = \Gamma_1 + \Gamma_2 - 2\sqrt{\Gamma_1^d \Gamma_1^p} - 2\sqrt{\Gamma_2^d \Gamma_2^p}, \tag{A.1}$$

with Γ_i^p and Γ_i^p, respectively, the dispersive and polar component of the surface energy of component i. Table A.1 gives an overview of the surface free energies, dispersive, and polar contributions found in literature [175, 194, 118]. The values of PPG were not found in literature. Therefore, an estimation is made based on the values of propylene glycol. The calculated wetting parameters are finally summarized in Table A.2

Table A.1: Surface free energies Γ_i, polar and dispersive contributions of different polymers. Data from [175, 194, 118].

Component	Γ_i [mN/m]	Γ_i^d [mN/m]	Γ_i^p [mN/m]
Glycerol	63.4	37	26
PDMS	19.8	19	0.8
PIB	33.6	33.6	0
PPG	35.4	26.4	9
PS	40.7	34.5	6.1

Table A.2: Wetting parameter ω_{12} for PS particles and different combinations of droplet and matrix phase materials estimated based on interfacial energy values found in literature.

Droplet phase	Matrix phase	ω_{12} [-]
Glycerol	PDMS	-0.12
PPG	PDMS	0.78
PIB	PDMS	-0.46
PDMS	PIB	0.46

A.2 Settling velocity of non-Brownian PS particles

Table A.3: Settling velocity of non-Brownian PS particles in the different systems calculated according to Stokes' law (Equation 2.18). A negative settling velocity corresponds to creaming, while a positive settling velocity corresponds to sedimentation of the particles.

System	Particle diameter [μm]	Sedimentation velocity [μm/h]
MS-1.4	5	-0.02
	25	-1.4
	82	-14.8
MS-0.09	25	-50.2
MS-0.08L	25	-56.4
	44	-174.7

A.3 Conservation of volume equation and the equations for projection of an ellipsoid on a plane

At capillary numbers higher than 0.20, the rescaling method is not accurate enough to determine L, B, and θ from the images in the velocity-velocity gradient plane. Therefore, these parameters are calculated from L_g, L_p, W, and R by using the conservation of volume equation and the equations for projection of an ellipsoid on a plane [21]:

$$R^3 = \frac{LBW}{8}, \tag{A.2}$$

$$\left(\frac{L_p}{2R}\right)^2 = \left(\frac{L}{2R}\right)^2 \cos^2(\theta) + \left(\frac{B}{2R}\right)^2 \sin^2(\theta), \tag{A.3}$$

$$\left(\frac{L_g}{2R}\right)^2 = \left(\frac{B}{2R}\right)^2 \cos^2(\theta) + \left(\frac{L}{2R}\right)^2 \sin^2(\theta). \tag{A.4}$$

A.4 Second order coefficients in the model of Greco

The interfacial tension is determined by fitting the dimensionless droplet axes at small deformations to the second order theory of Greco. For a droplet-matrix

system consisting of a Newtonian droplet in a Newtonian matrix phase, the following equation is applied [61]:

$$\frac{L_\mathrm{p}}{2R} = 1 + \dot{\gamma}^2 \left(\frac{\eta_\mathrm{m} R}{\Gamma}\right)^2 (\frac{1}{4}\mathrm{F}^2 + \frac{1}{4}\mathrm{s}_2 + \frac{1}{2}\mathrm{s}_3). \tag{A.5}$$

F, s_2 and s_3 are scalar functions which only depend on the system's viscosity ratio:

$$\mathrm{F} = \frac{16 + 19\lambda}{8 + 8\lambda}, \tag{A.6}$$

$$\mathrm{s}_2 = \frac{(16 + 19\lambda)(4712 + \lambda(17967 + \lambda(16360 + 3591\lambda)))}{(8 + 8\lambda)(1890(1 + \lambda)^2)}, \tag{A.7}$$

$$\mathrm{s}_3 = -\frac{(16 + 19\lambda)(2656 + \lambda(8835 + 5855\lambda))}{(8 + 8\lambda)(3780(1 + \lambda)^2)}. \tag{A.8}$$

A.5 Calculating closed streamlines from a coarse mesh velocity field

When post-processing the numerical calculations, it is observed that the streamlines inside a droplet spiral outwards from the center. These streamlines eventually cross the liquid-liquid interface into the surrounding continuous phase. Hence, it would appear as if the droplet is losing mass, which is in contradiction with the model equations. This inconsistent behavior is most likely due to numerical inaccuracies in the calculated velocity field. Indeed, the rate at which streamlines spiral outwards, decreases by refining the mesh. Unfortunately, the very fine mesh needed for closing the streamlines requires an excessively large computational effort. To reduce the computational burden, this section describes an alternative method for generating closed streamlines as opposed to the numerical integrators ordinarily used in visualization software such as ParaView [126]. At this point, it must be stressed that the streamlines inside a droplet do not have to be closed curves and may behave chaotically. However, when a droplet is deformed under uniform shear, such chaotic behavior does not occur [157].

The different steps of the procedure are as follows. The main idea for imposing closed streamlines is first introduced. This results in a least-squares problem that is solved by using, for example, the iterative Levenberg-Marquardt algorithm. Then a reasonably robust initial guess to start the iterative procedure is provided, which ensures convergence to the global minimum. As a validation for the proposed method, the streamlines inside a neutrally buoyant, spherical droplet in uniform shear flow are calculated as a test case. To emulate an actual

simulation, the exactly known velocity field [10] is discretized and a non-zero divergence is artificially added.

A.5.1 Ensuring periodic orbits

Streamlines are at any location tangent to the velocity field. This means that a streamline going through the point $\mathbf{x}_0 = (x_0, y_0, z_0)$ at $t = 0$ s will evolve according to:

$$\frac{\mathrm{d}x(t)}{\mathrm{d}t} = u_\mathrm{x}(x, y, z), \tag{A.9a}$$

$$\frac{\mathrm{d}y(t)}{\mathrm{d}t} = u_\mathrm{y}(x, y, z), \tag{A.9b}$$

$$\frac{\mathrm{d}z(t)}{\mathrm{d}t} = u_\mathrm{z}(x, y, z), \tag{A.9c}$$

where u_x, u_y, and u_z are the components of the velocity $\mathbf{u}$.

By requiring that the components of the position $\mathbf{x}$ are periodic, they can be approximated by a Fourier series:

$$x(t) = x_0 + \sum_{\mathrm{k}=1}^{\infty} \left(a_{2\mathrm{k}-1} \sin(\mathrm{k}\phi) + a_{2\mathrm{k}}(\cos(\mathrm{k}\phi) - 1) \right), \tag{A.10a}$$

$$y(t) = y_0 + \sum_{\mathrm{k}=1}^{\infty} \left(b_{2\mathrm{k}-1} \sin(\mathrm{k}\phi) + b_{2\mathrm{k}}(\cos(\mathrm{k}\phi) - 1) \right), \tag{A.10b}$$

$$z(t) = z_0 + \sum_{\mathrm{k}=1}^{\infty} \left(c_{2\mathrm{k}-1} \sin(\mathrm{k}\phi) + c_{2\mathrm{k}}(\cos(\mathrm{k}\phi) - 1) \right), \tag{A.10c}$$

with ϕ ranging from 0 to 2π. The problem is then reduced to finding the unknown coefficients a_k, b_k, c_k, so that the vector $\mathbf{s}$ with components:

$$s_\mathrm{x} = \frac{\mathrm{d}x}{\mathrm{d}\phi} = \sum_{\mathrm{k}=1}^{\infty} \mathrm{k} \left(a_{2\mathrm{k}-1} \cos(\mathrm{k}\phi) - a_{2\mathrm{k}} \sin(\mathrm{k}\phi) \right), \tag{A.11a}$$

$$s_\mathrm{y} = \frac{\mathrm{d}y}{\mathrm{d}\phi} = \sum_{\mathrm{k}=1}^{\infty} \mathrm{k} \left(b_{2\mathrm{k}-1} \cos(\mathrm{k}\phi) - b_{2\mathrm{k}} \sin(\mathrm{k}\phi) \right), \tag{A.11b}$$

$$s_\mathrm{z} = \frac{\mathrm{d}z}{\mathrm{d}\phi} = \sum_{\mathrm{k}=1}^{\infty} \mathrm{k} \left(c_{2\mathrm{k}-1} \cos(\mathrm{k}\phi) - c_{2\mathrm{k}} \sin(\mathrm{k}\phi) \right), \tag{A.11c}$$

has the same direction as the velocity $\mathbf{u}$. Because the velocity field might not be solenoidal, the equality between the direction of $\mathbf{s}$ and $\mathbf{u}$ is not enforced exactly. Instead, the angle ζ between $\mathbf{s}$ and $\mathbf{u}$ is minimized. Thus, the coefficients a_k, b_k, c_k are found by minimizing the objective function:

$$\int_0^{2\pi} (1 - \cos(\zeta))^2 \, d\phi = \int_0^{2\pi} \left(1 - \frac{\mathbf{s} \cdot \mathbf{u}}{\|\mathbf{s}\| \cdot \|\mathbf{u}\|}\right)^2 d\phi. \tag{A.12}$$

It is straightforward to convert this integral to a least-squares problem by discretizing ϕ and using any appropriate quadrature rule. In particular, we found that the trapezoidal rule already gave sufficiently satisfying results.

The proposed algorithm therefore consists of i) guessing a_k, b_k, and c_k so that the streamline follows from Equation A.9 ii) evaluating the velocity components $\mathbf{u}(\mathbf{x})$ on these newly calculated positions, iii) calculating $\mathbf{s}$ via substitution of a_k, b_k, and c_k into Equation A.11, and finally iv) calculating the objective function Equation A.12 for the minimization procedure. By using Levenberg-Marquardt as implemented in the Matlab or Octave function *lsqnonlin* [123, 109], the coefficients a_k, b_k, and c_k are updated until a local minimum is found. As it is not guaranteed that this local minimum also is a global minimum, the success of this method critically relies on the initial guess of the coefficients a_k, b_k, and c_k.

A.5.2 Providing the initial guess

The initial guess is provided by numerical integration of Equation A.12 by an explicit Dormand-Prince method of order 4, as implemented by *ode45* in Octave [124]. The velocity vector $\mathbf{u}$ for any position $\mathbf{x}$ is obtained by linear interpolation between its values on the nearest grid points. Essentially, this is the same as the ordinary method used for calculating the streamlines in, for example, ParaView [126]. The integration is stopped when one cycle is nearly complete. In fact, as this streamline does not form a closed curve, the integration is stopped when the distance between the starting point $\mathbf{x}_0$ and endpoint $\mathbf{x}_{t_\mathrm{f}}$ is decreasing and smaller than a predefined value.

The above initial guess for the streamline is improved slightly further. If this streamline spirals outward, then calculating the streamline corresponding to the reversed velocity $-\mathbf{u}$ results in an inward spiral, as if the tracer particle moves back in time. Similar to the outward spiraling streamline, the integration is terminated when the starting point $\mathbf{x}_{\mathbf{r},0}$ and endpoint $\mathbf{x}_{\mathbf{r},t_\mathrm{f}}$ is decreasing and smaller than a predefined value. It is clear that some sort of averaging between both trajectories improves the initial guess. Also note that in the absence of numerical errors, both streamlines coincide and would be traversed in opposite directions by tracer particles.

Once the initial guesses $\mathbf{x}(t)$ and $\mathbf{x}_\mathbf{r}(t)$ are made for one cycle of the respectively out- and inward spiraling streamlines, it is straightforward to find the

corresponding coefficients a_{k}, b_{k}, and c_{k}. For the outward spiraling streamlines, one finds:

$$\begin{bmatrix} a_{2\mathrm{k}-1} \\ b_{2\mathrm{k}-1} \\ c_{2\mathrm{k}-1} \end{bmatrix} = \frac{2}{t_{\mathrm{f}}} \int_0^{t_{\mathrm{f}}} \mathbf{x}(t) \sin\left(\frac{2\pi \mathrm{k} t}{t_{\mathrm{f}}}\right) dt, \tag{A.13a}$$

$$\begin{bmatrix} a_{2\mathrm{k}} \\ b_{2\mathrm{k}} \\ c_{2\mathrm{k}} \end{bmatrix} = \frac{2}{t_{\mathrm{f}}} \int_0^{t_{\mathrm{f}}} \mathbf{x}(t) \cos\left(\frac{2\pi \mathrm{k} t}{t_{\mathrm{f}}}\right) dt, \tag{A.13b}$$

and for the inward spiraling streamlines, one finds:

$$\begin{bmatrix} a_{2k-1} \\ b_{2k-1} \\ c_{2k-1} \end{bmatrix} = -\frac{2}{t_{\mathrm{f}}} \int_0^{t_{\mathrm{f}}} \mathbf{x_r}(t) \sin\left(\frac{2\pi \mathrm{k} t}{t_{\mathrm{f}}}\right) dt, \tag{A.14a}$$

$$\begin{bmatrix} a_{2k} \\ b_{2k} \\ c_{2k} \end{bmatrix} = \frac{2}{t_{\mathrm{f}}} \int_0^{t_{\mathrm{f}}} \mathbf{x_r}(t) \cos\left(\frac{2\pi \mathrm{k} t}{t_{\mathrm{f}}}\right) dt, \tag{A.14b}$$

so that the initial guess for the coefficients a_{k}, b_{k}, and c_{k} ultimately follows from averaging Equations A.13 and A.14.

A.5.3 Validation with an analytical result

The velocity components u_{x}, u_{y}, and u_{z} inside a spherical drop with radius R subjected to a uniform shear flow with shear rate $\dot{\gamma}$ are given by [10]:

$$\frac{u_{\mathrm{x}}}{R\dot{\gamma}} = \frac{y}{4R(1+\lambda)} \left(\frac{5r^2}{R^2} - \frac{4x^2}{R^2} + 2\lambda - 1\right) \tag{A.15a}$$

$$\frac{u_{\mathrm{y}}}{R\dot{\gamma}} = \frac{x}{4R(1+\lambda)} \left(\frac{5r^2}{R^2} - \frac{4y^2}{R^2} - 2\lambda - 5\right) \tag{A.15b}$$

$$\frac{u_{\mathrm{z}}}{R\dot{\gamma}} = -\frac{z}{R(1+\lambda)} \frac{xy}{R^2} \tag{A.15c}$$

where λ is the droplet to continuous phase viscosity ratio and $r^2 = x^2 + y^2 + z^2$. Note that the shape of the streamlines is independent of $\dot{\gamma}$ and R if the coordinates x, y, and z are replaced by x/R , y/R, and z/R. Then the magnitude of $\dot{\gamma}$ and R only determine the duration of one cycle. To mimic the artificial divergence observed in actual numerical calculations, the velocity field

is given a small divergence D_i by virtue of adding D_x, D_y, and D_z respectively to the components of $\mathbf{u}$ given by Equation A.15. Figure A.1 shows a streamline calculated with the proposed algorithm using $D_i = 0.05$ and a viscosity ratio $\lambda = 0.1$. Note that even with a little divergence added, the normal procedure quickly spirals outward whereas the proposed algorithm remains robust and largely unaffected by the presence of this artificially added divergence.

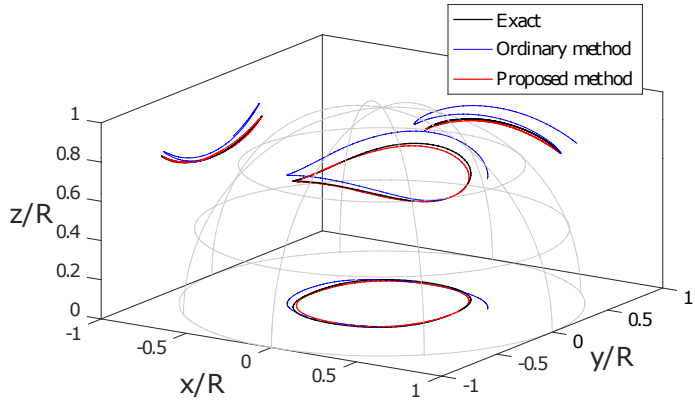

Figure A.1: A comparison between the ordinary method for integrating a streamline inside a droplet (only upper half is shown here) and the proposed alternative method when the divergence is nonzero ($D_i = 0.05$) due to numerical errors in the calculated velocity field. As a reference, the exact streamline is also displayed and is closely approximated by the alternative method.

Appendix B

Migration of non-Brownian particles localized inside sheared droplets

B.1 Steady-state particle distribution of MS-1.4 with intermediate particle concentrations

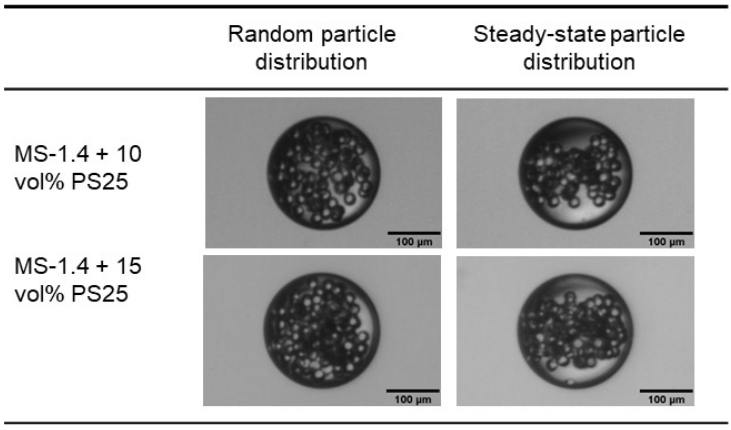

Figure B.1: Images of particle-filled droplets (10 - 15 vol% PS25) added to MS-1.4 captured after droplet injection (random particle distribution) and after cessation of shear flow (Ca = 0.30) when steady-state particle distribution is reached. All images are taken in the top view (velocity - vorticity plane).

B.2 Particle distribution after cessation of shear flow

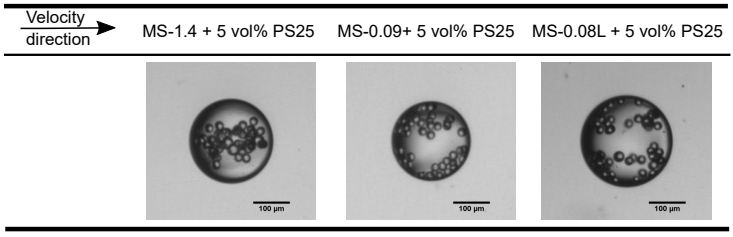

Figure B.2: Images of particle-filled droplets (5 vol% PS25) added to MS-1.4, MS-0.09, and MS-0.08L captured after cessation of shear flow (Ca = 0.30). Steady-state particle distribution is reached. All images are taken in the top view (velocity - vorticity plane).

B.3 Numerical simulations: velocity field

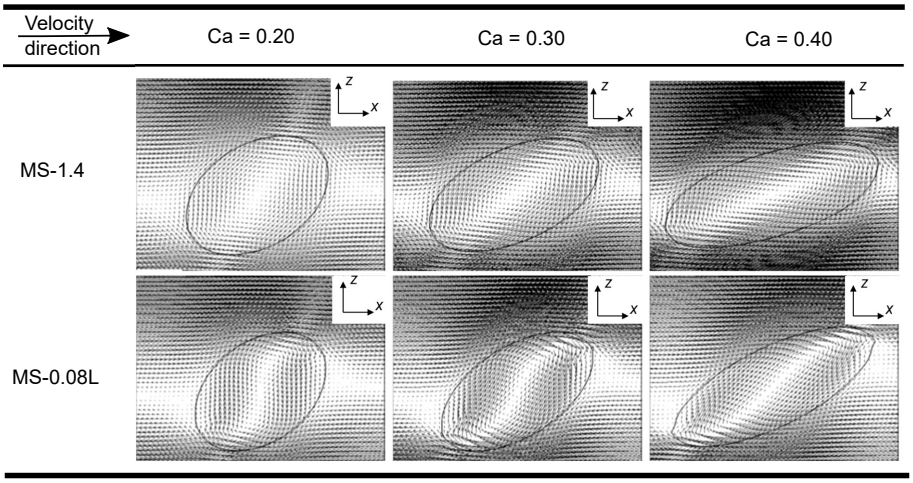

Figure B.3: Steady-state velocity field and droplet contour at $t = 10$ s for MS-1.4 and MS-0.08L at Ca = 0.20, Ca = 0.30, and Ca = 0.40. Cross-sectional slice in the velocity (x)-velocity gradient (z) plane through the centre of the droplet.

B.4 Numerical simulations: vorticity magnitude

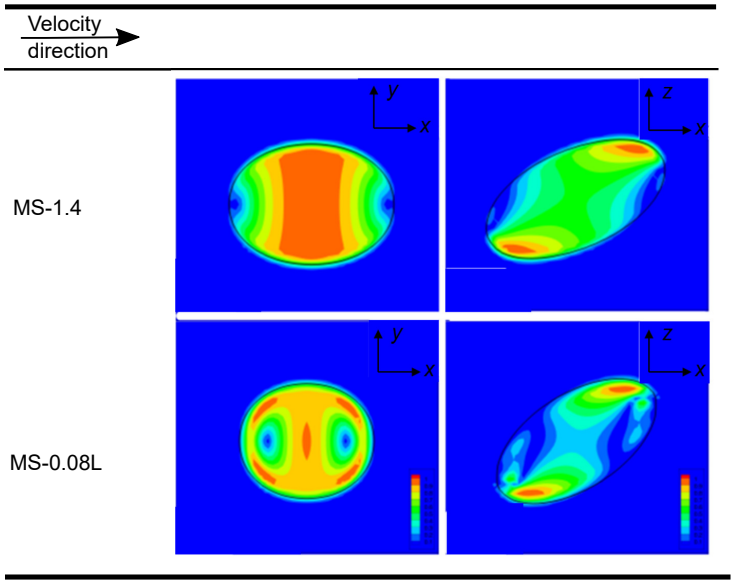

Figure B.4: Vorticity magnitude normalized by the maximum value in that slice and droplet contour at $t = 10$ s (Ca $= 0.30$) for MS-1.4 and MS-0.08L. Cross-sectional slices in the velocity (x)–vorticity (y) and velocity (x)–velocity gradient (z) planes through the centre of the droplet.

Appendix C

Effects of nanoparticles localized at the droplet interface

C.1 Hysteresis effect

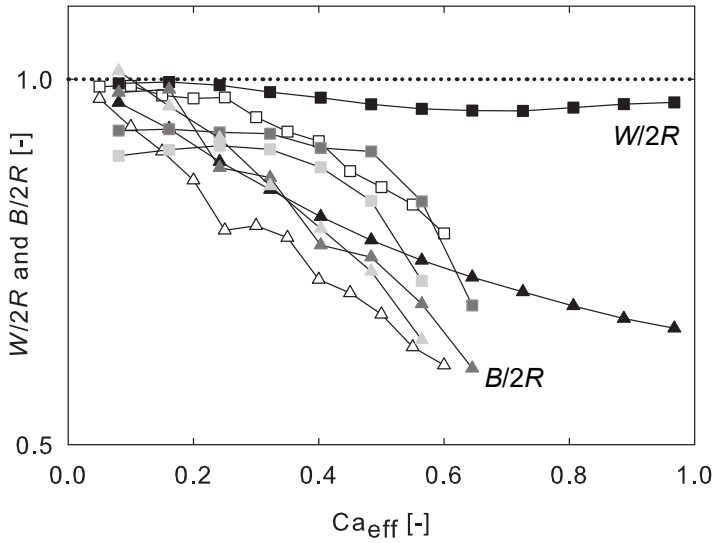

Figure C.1: Dimensionless droplet axes $B/2R$ and $W/2R$ of particle covered droplets (MS-0.1 + 0.4 vol% silica) as function of effective capillary number $\mathrm{Ca}_{\mathrm{eff}}$. White data points refer to a droplet with a neat interface. Other measurements are performed with a droplet with a residence time of 9h in the 0.4 vol% suspension of silica nanoparticles, immediately after droplet transfer (black data points), immediately after breakup of the particle network by shear (dark grey data points), and 1 week after breakup of the particle network (light grey data points).

Bibliography

[1] J. R. Abbott, N. Tetlow, A. L. Graham, S. A. Altobelli, E. Fukushima, L. A. Mondy, and T. S. Stephens. Experimental observations of particle migration in concentrated suspensions: Couette flow. *Journal of Rheology*, 35(5):773–795, 1991.

[2] A. R. Ajitha, P. M. Lovely, and T. Sabu. *Compatibilization of polymer blends by micro and nanofillers*, pages 179–203. 2020.

[3] A. Amani, N. Balcázar, J. Castro, and A. Oliva. Numerical study of droplet deformation in shear flow using a conservative level-set method. *Chemical Engineering Science*, 207:153–171, 2019.

[4] D. Amoabeng, D. Roell, K. M. Clouse, B. A. Young, and S. S. Velankar. A composition-morphology map for particle-filled blends of immiscible thermoplastic polymers. *Polymer*, 119:212–223, 2017.

[5] A. M. Ardekani, S. Dabiri, and R. H. Rangel. Deformation of a droplet in a particluate shear flow. *Physics of Fluids*, 21(9):1–8, 2009.

[6] S. Asakura and F. Oosawa. On interaction between two bodies immersed in a solution of macromolecules. *Journal of Chemical Physics*, 22:1255–1256, 1954.

[7] R. Aveyard, B. P. Binks, and J. H. Clint. Emulsions stabilised solely by colloidal particles. *Advances in Colloid and Interface Science*, 100-102:503–546, 2003.

[8] D. Barthes-Biesel and A. Acrivos. Deformation and burst of a liquid droplet freely suspended in a linear shear field. *Journal of Fluid Mechanics*, 61(1):1–22, 1973.

[9] D. Barthes-Biesel and H. Sgaier. Role of membrane viscosity in the orientation and deformation of a spherical capsules suspended in shear flow. *Journal of Fluid Mechanics*, 160:119–135, 1985.

[10] W. Bartok and S. G. Mason. Particle motions in sheared suspensions: Vii. internal circulation in fluid droplets (theoretical). *Journal of Colloid Science*, 13:293–307, 1958.

[11] L. Becu and L. Benyahia. Strain-induced droplet retraction memory in a pickering emulsion. *Langmuir*, 25(12):6678–6682, 2009.

[12] C. Berdan and L. G. Leal. Motion of a sphere in the presence of a deformable interface: I. perturbation of the interface from flat: the effects on drag and torque. *Journal of Colloid and Interface Science*, 87(1):62–80, 1981.

[13] T. Bertrand, C. Bonnoit, E. Clément, and A. Lindner. Dynamics of drop formation in granular suspensions: the role of volume fraction. *Granular Matter*, 14(2):169–174, 2012.

[14] A. Bharati, R. Cardinaels, J. W. Seo, M. Wübbenhorst, and P. Moldenaers. Enhancing the conductivity of carbon nanotube filled blends by tuning their phase separated morphology with a copolymer. *Polymer*, 79:271–282, 2015.

[15] B. P. Binks. Particles as surfactants - similarities and differences. *Colloidal and Interface Science*, 7:21–41, 2002.

[16] B. P. Binks. *Colloidal Particles at Liquid Interfaces: An Introduction*, pages 1–74. 2006.

[17] C. Bonnoit, T. Bertrand, E. Clément, and A. Lindner. Accelerated drop detachment in granular suspensions. *Physics of Fluids*, 24(4):043304, 2012.

[18] F. Bresme and M. Oettel. Nanoparticles at fluid interfaces. *Journal of Physics: Condesed Matter*, 19(41):413101, 2007.

[19] R. Buscall, D. A. Mills, J. W. Goodwin, and J. W. Lawson. Scaling behaviour of the rheology of aggregate networks formed from colloidal particles. *Journal of Chemical Society*, 84(12):4249–4260, 1988.

[20] H. Butt, K. Graf, and M. Kappl. *Physics and Chemistry of Interfaces*. Wiley-VCH GmbH and Co. KGaA, Weinheim, 2003.

[21] R. Cardinaels. *Droplet deformation, breakup and coalescence in shear flow: effects of confinement and component viscoelasticity*. Thesis, 2010. PhD thesis KU Leuven.

[22] R. Cardinaels, S. Afkhami, Y. Renardy, and P. Moldenaers. An experimental and numerical investigation of the dynamics of microconfined droplets in systems with one viscoelastic phase. *Journal of Non-Newtonian Fluid Mechanics*, 166(1-2):52–62, 2011.

[23] R. Cardinaels and P. Moldenaers. *Morphology Development in Immiscible Polymer Blends*. Polymer Morphology (Guo, Q.). 2016.

[24] C. E. Chaffey and H. Brenner. A second-order theory for shear deformation of drops. *Journal of Colloid and Interface Science*, 24(2):258–269, 1967.

[25] J. Choi, K. W. Oh, J. H. Thomas, W. R. Heineman, H. B. Halsall, J. H. Nevin, A. Helmicki, H. T. Henderson, and C. H. Ahn. An integrated microfluidic biochemical detection system for protein analysis with magnetic bead-based sampling capabilities. *Lab Chip*, 2:27–30, 2002, type = Journal Article.

[26] R. G. Cox. The deformation of a drop in a general time-dependent fluid-flow. *Journal of Fluid Mechanics*, 37(3):601–623, 1969.

[27] R. G. Cox and S. G. Mason. Suspended particles in fluid flow through tubes. *Annual Review of Fluid Mechanics*, 3:291–316, 1971.

[28] S. S. Datta, H. C. Shum, and D. A. Weitz. Controlled buckling and crumpling of nanoparticle-coated droplets. *Langmuir*, 26(24):18612–18616, 2010.

[29] G. D'Avino, F. Snijkers, R. Pasquino, M. A. Hulsen, F. Greco, P. L. Maffettone, and J. Vermant. Migration of a sphere suspended in viscoelastic liquids in couette flow: experiments and simulations. *Rheologica Acta*, 51(3):215–234, 2011.

[30] R. A. de Bruijn. *Deformation and breakup of drops in simple shear flow*. Thesis, 1991. PhD Thesis TU Eindhoven.

[31] P. De Bruyn. *Understanding the effect of confinement on droplet coalescence in shear flow*. Thesis, 2014. PhD Thesis KU Leuven.

[32] M. Desse, J. Mitchell, B. Wolf, and T. Budtova. Droplet deformation and break-up under shear: Hydrocolloid solution vs. suspension of starch granules. *Food Hydrocolloids*, 25(3):495–502, 2011.

[33] M. Desse, B. Wolf, J. Mitchell, and T. Budtova. Experimental study of the break-up of starch suspension droplets in step-up shear flow. *Journal of Rheology*, 53(4):943–955, 2009.

[34] M. Destribats, M. Rouvet, C. Gehin-Delval, C. Schmitt, and B. P. Binks. Emulsions stabilised by whey protein microgel particles: towards food-grade pickering emulsions. *Soft Matter*, 10:6941–6954, 2014.

[35] E. Dickinson. Use of nanoparticles and microparticles in the formation and stabilization of food emulsions. *Trends in Food Science and Technology*, 25:4–12, 2012.

[36] A. D. Dinsmore, M. F. Hsu, M. G. Nikolaides, M. Marquez, A. R. Bauscsh, and D. A. Weitz. Colloidosomes: Selectively permeable capsules composed of colloidal particles. *Science*, 298(5595):1006–1009, 2002.

[37] G. Dockx, S. Geisel, D. G. Moore, E. Koos, A. R. Studart, and J. Vermant. Designer liquid-liquid interfaces made from transient double emulsions. *Nat Commun*, 9(1):4763, 2018.

[38] A. Dörr, A. Sadiki, and A. Mehdizadeh. A discrete model for the apparent viscosity of polydisperse suspensions including maximum packing fraction. *Journal of Rheology*, 57(3):473–765, 2013.

[39] D. A. Edwards, H. Brenner, and D. T. Wasan. *Interfacial Transport Processes and Rheology*. Butterworth-Heinemann, 1991.

[40] A. Einstein. Eine neue bestimmung der molekeuldimensionen. *Annalen der Physik*, 324(2):289–306, 1906.

[41] A. Einstein. Berichtigung zu meiner arbeit: 'eine neue bestimmung der molekeuldimensionen'. *Annalen der Physik*, 339(3):591–592, 1911.

[42] L. Elias, F. Fenouillot, J. Majesté, P. Alcouffe, and P. Cassagnau. Immiscible polymer blends stabilized with nano-silica particles: Rheology and effective interfacial tension. *Polymer*, 49(20):4378–4385, 2008.

[43] L. Elias, F. Fenouillot, J. C. Majesté, and P. Cassagnau. Morphology and rheology of immiscible polymer blends filled with silica nanoparticles. *Polymer*, 48(20):6029–6040, 2007.

[44] P. Erni, P. Fiscer, and E. J. Windhab. Deformation of single emulsion drops covered with a viscoelastic adsorbed protein layer in simple shear flow. *Applied Physics Letters*, 87:244104, 2005.

[45] P. Erni, E. J. Windhab, and P. Fischer. Emulsion drops with complex interfaces: Globular versus flexible proteins. *Macromolecular Materials and Engineering*, 296(3-4):249–262, 2011.

[46] J. Feng, C. Chan, and J. Li. A method to control the dispersion of carbon black in an immiscible polymer blend. *Polymer Engineering & Science*, 43(5):1058–1063, 2003.

[47] F. Fenouillot, P. Cassagnau, and J. C. Majesté. Uneven distribution of nanoparticles in immiscible fluids: Morphology development in polymer blends. *Polymer*, 50(6):1333–1350, 2009.

[48] J. Ferreira, F. Castro, F. Rocha, and S. Kuhn. Protein crystallization in a droplet-based microfluidic device: Hydrodynamic analysis and study of the phase behaviour. *Chemical Engineering Science*, 191:232–244, 2018.

[49] G. Filippone, N. T. Dintcheva, F. La Mantia, and D. Acierno. Using organoclay to promote morphology refinement and co-continuity in high-density polyethylene/polyamide 6 blends – effect of filler content and polymer matrix composition. *Polymer*, 51(17):3956–3965, 2010.

[50] A. Fornell, J. Nilsson, L. Jonssen, R. P., H. N. Joensson, and M. Tenje. Controlled lateral positioning of microparticles inside droplets using acoustophoresis. *Analytical Chemistry*, 87:10521–10526, 2015.

[51] S. Frijters, F. Günther, and J. Harting. Effects of nanoparticles and surfactant on droplets in shear flow. *Soft Matter*, 8(24):6542–6556, 2012.

[52] R. J. Furbank and J. F. Morris. An experimental study of particle effects on drop formation. *Physics of Fluids*, 16(5):1777–1790, 2004.

[53] F. Gadala-Maria and A. Acrivos. Shear-induced structure in a concentrated suspension of solid spheres. *Journal of Rheology*, 24(6):799–814, 1980.

[54] M. Gahleitner, B. Kretzschmar, D. Pospiech, E. Ingolic, N. Reichelt, and K. Bernreitner. Morphology and mechanical properties of polypropylene/polyamide 6 nanocomposites prepared by a two-step melt-compounding process. *Journal of Applied Polymer Science*, 100(1):283–291, 2006.

[55] F. J. Galindo-Rosales, P. Moldenaers, and J. Vermant. Assessment of the dispersion quality in polymer nanocomposites by rheological methods. *Macromolecular Materials and Engineering*, 296(3-4):331–340, 2011.

[56] G. Geuskens, J. L. Gielens, D. Geshef, and R. Deltour. The electrical conductivity of polymer blends filled with carbon-black. *European Polymer Journal*, 27(11):1261–1264, 1987.

[57] H. L. Goldsmith and S. G. Mason. *The microrheology of dispersions*, volume 4. Academic Press Inc., London (UK), 1967.

[58] A. Gooneie, H. Nazockdast, and F. Shahsavan. Effect of selective localization of carbon nanotubes in pa6 dispersed phase of pp/pa6 blends

on the morphology evolution with time, part 1: Droplet deformation under simple shear flows. *Polymer Engineering and Science*, 55(7):1504–1519, 2015.

[59] A. Gooneie, H. Nazockdast, and F. Shahsavan. Effect of selective localization of carbon nanotubes in pa6 dispersed phase of pp/pa6 blends on the morphology evolution with time, part 2: Relaxation of deformed droplets after cessation of flow. *Polymer Engineering and Science*, 56(1):51–60, 2016.

[60] H. P. Grace. Dispersion phenomena in high viscosity immiscible fluid systems and application of static mixers as dispersion devices in such systems. *Chemical Engineering Communications*, 14:225–277, 1982.

[61] F. Greco. Second-order theory for the deformation of a newtonian drop in a stationary flow field. *Physics of Fluids*, 14(3):946–954, 2002.

[62] S. Guido and M. Villone. Three-dimensional shape of a drop under simple shear flow. *Journal of Rheology*, 42(2):395–415, 1998.

[63] S. Guido and M. Villone. Measurement of interfacial tension by drop retraction analysis. *Journal of Colloid and Interface Science*, 209(1):247–250, 1999.

[64] A. Gupta, P. Magaud, C. Lafforque, and M. Abbas. Conditional stability of particle alignment in finite-reynolds-number channel flow. *Physical Review Fluids*, 3(11):114302, 2018.

[65] M. Han and C. Kim. Particle migration in tube flow of suspensions. *Journal of Rheology*, 43(5):1157–1174, 1999.

[66] C. Harrats, S. Thomas, and G. Groeninckx. *Micro-and nanostructured multiphase polymer blend systems: phase morphology and interfaces*. CRC press, 2005.

[67] Y. He, Y. Huang, Q. Li, Y. Mei, M. Kong, and Q. Yang. Morphological hysteresis in immiscible pib-pdms blends filled with fumed silica nanoparticles. *Colloid and Polymer Science*, 290(11):997–1004, 2012.

[68] M. Hein, M. Moskopp, and R. Seemann. Flow field induced particle accumulation inside droplets in rectangular channels. *Lab Chip*, 15:2879–2886, 2015.

[69] B. P. Ho and L. G. Leal. Migration of rigid spheres in a two-dimensional unidirectional shear flow of a second-order fluid. *Journal of Fluid Mechanics*, 76(4):783–799, 1976.

[70] D. A. Hoang, V. van Steijn, L. M. Portela, M. T. Kreutzer, and C. R. Kleijn. Benchmark numerical simulations of segmented two-phase flows in microchannels using the volume of fluid method. *Computers and Fluids*, 86:28–36, 2013.

[71] J. S. Hong, Y. K. Kim, K. H. Ahn, and S. J. Lee. Shear-induced migration of nanoclay during morphology evolution of pbt-ps blend. *Journal of Applied Polymer Science*, 108(1):565–575, 2008.

[72] J. S. Hong, H. Namkung, K. H. Ahn, S. J. Lee, and C. Kim. The role of organically modified layered silicate in the breakup and coalescence of droplets in pbt-pe blends. *Polymer*, 47(11):3967–3975, 2006.

[73] J. B. Hooper and K. S. Schweizer. Structure, surface excess and effective interactions in polymer nanocomposite melts and concentrated solutions. *Journal of Chemical Physics*, 121(14):6986–6997, 2004.

[74] J. B. Hooper and K. S. Schweizer. Contact aggregation, bridging, and steric stabilization in dense polymer-particle mixtures. *Macromolecules*, 38:8858–8869, 2005.

[75] J. Huang. Carbon black filled conducting polymers and polymer blends. *Advances in Polymer Technology*, 21(4):299–313, 2002.

[76] S. Huang, L. Bai, M. Trifkovic, X. Cheng, and C. W. Macosko. Controlling the morphology of immiscible cocontinuous polymer blends via silica nanoparticles jammed at the interface. *Macromolecules*, 49(10):3911–3918, 2016.

[77] L. Imperiali, K. H. Liao, C. Clasen, J. Fransaer, C. W. Macosko, and J. Vermant. Interfacial rheology and structure of tiled graphene oxide sheets. *Langmuir*, 28(21):7990–8000, 2012.

[78] N. Ioannou, H. Liu, and Y. H. Zhang. Droplet dynamics in confinement. *Journal of Computational Science*, 17:463–474, 2016.

[79] P. J. A. Janssen and P. D. Anderson. Boundary-integral method for drop deformation between parallel plates. *Physics of Fluids*, 19(4):043602, 2007.

[80] D. B. Jones and P. J. Middelberg. Interfacial protein networks and their impact on droplet breakup. *AIChE Journal*, 49(6):1533–1541, 2003.

[81] P. Jyotishkumar, S. Thomas, and Y. Grohens. *Polymer Blends: State of the Art, New Challenges, and Opportunities*, book section 1. 2014.

[82] G. R. Kasaliwal, S. Pegel, A. Goldel, P. Potschke, and G. Heinrich. Analysis of agglomerate dispersion mechanisms of multiwalled carbon nanotubes during melt mixing in polycarbonate. *Polymer*, 51(12):2708–2720, 2010.

[83] S. Kaur and L. G. Leal. Drop deformation and break-up in concentrated suspensions. *Journal of Rheology*, 54(5):981–1008, 2010.

[84] I. Kelnar, V. Khunová, J. Kotek, and L. Kaprálková. Effect of clay treatment on structure and mechanical behavior of elastomer-containing polyamide 6 nanocomposite. *Polymer*, 48(18):5332–5339, 2007.

[85] M. R. Kennedy, C. Pozrikidis, and R. Skalak. Motion and deformation of liquid drops, and the rheology of dilute emulsions in simple shear flow. *Computers and Fluids*, 23(2):251–278, 1994.

[86] M. Khemakhem, K. Lamnawar, A. Maazouz, and M. Jaziri. Effect of core-shell acrylate rubber particles on the thermomechanical and physical properties of biocomposites from polylactic acid and olive solid waste. *Polymer Engineering and Science*, 58(6):894–902, 2018.

[87] I. Koleva and H. Rehage. Deformation and orientation dynamics of polysiloxane microcapsules in linear shear flow. *Soft Matter*, 8(13):3681–3693, 2012.

[88] A. E. Komrakova, O. Shardt, D. Eskin, and J. J. Derksen. Lattice boltzmann simulations of drop deformation and breakup in shear flow. *International Journal of Multiphase Flow*, 59:24–43, 2014.

[89] M. Kong, Y. Huang, G. Chen, Q. Yang, and G. Li. Retarded relaxation and breakup of deformed pa6 droplets filled with nanosilica in ps matrix during annealing. *Polymer*, 52(22):5231–5236, 2011.

[90] M. Kontopoulou, Y. Liu, J. R. Austin, and J. S. Parent. The dynamics of montmorillonite clay dispersion and morphology development in immiscible ethylene–propylene rubber/polypropylene blends. *Polymer*, 48(15):4520–4528, 2007.

[91] P. Kralchevky and K. Nagayama. Capillary interactions between particles bound to interfaces, liquid films and biomembranes. *Advances in Colloidal and Interface Science*, 85:145–192, 2000.

[92] I. M. Krieger. Rheology of monodisperse latices. *Advances in Colloid and Interface Science*, 3(2):111–136, 1972.

[93] G. P. Krishnan, S. Beimfohr, and D. Leighton. Shear-induced radial segregation in bidisperse suspensions. *Journal of Fluid Mechanics*, 321:371–393, 1996.

[94] M. Kroll, B. Langer, S. Schumacher, and W. Grellmann. The influence of carbon black batches on the fracture behavior of glass fiber reinforced pa6-pa66 blends. *Journal of Applied Polymer Science*, 116:610–618, 2010.

[95] L. G. Leal. Particle motions in a viscous fluid. *Annual Review of Fluid Mechanics*, 12:435–476, 1980.

[96] D. Leighton and A. Acrivos. The shear-induced migration of particles in concentrated suspensions. *Journal of Fluid Mechanics*, 181:415–439, 1987.

[97] L. Levitt and C. W. Macosko. Influence of normal stress difference on polymer drop deformation. *Polymer Engineering and Science*, 36(12):1647–1655, 1996.

[98] T. B. Lewis and L. E. Nielsen. Viscosity of dispersed and aggregated suspensions of spheres. *Transactions of the Society of Rheology*, 12(3):421–443, 1968.

[99] J. Li, Y. Y. Renardy, and M. Renardy. Numerical simulation of breakup of a viscous drop in simple shear flow through a volume-of-fluid method. *Physics of Fluids*, 12(2):267–278, 2000.

[100] L. Li, C. Miesch, P. K. Sudeep, A. C. Balazs, T. Emrick, T. P. Russell, and R. C. Hayward. Kinetically trapped co-continuous polymer morphologies through intraphase gelation of nanoparticles. *Nano Letters*, 11:1997–2003, 2011.

[101] Q. Liu, S. Xu, Z. Chen, and J. Wang. Analysis of rheological behaviors of two-dimensional emulsion globules with asymmetric internal structures in modes extensional flows. *Physics of Fluids*, 31(4):042003, 2019.

[102] Y. Liu and M. Kontopoulou. The structure and physical properties of polypropylene and thermoplastic olefin nanocomposites containing nanosilica. *Polymer*, 47(22):7731–7739, 2006.

[103] C. W. Macosko. Morphology development and control in immiscible polymer blends. In *Macromolecular Symposia*, volume 149, pages 171–184. Wiley Online Library.

[104] B. Madivala, J. Fransaer, and J. Vermant. Self-assembly and rheology of ellipsoidal particles at interfaces. *Langmuir*, 25(5):2718–2728, 2009.

[105] B. Madivala, S. Vandebril, J. Fransaer, and J. Vermant. Exploiting particle shape in solid stabilized emulsions. *Soft Matter*, 5(8):1717–1727, 2009.

[106] P. L. Maffettone and M. Minale. Equation of change for ellipsoidal drops in viscous flow. *Journal of Non-Newtonian Fluid Mechanics*, 78(2-3):227–241, 1998.

[107] C. Mao, M. Kong, Q. Yang, G. Li, and Y. Huang. Vorticity deformation in polymeric emulsions induced by anisotropic ellipsoids. *ACS Macro Letters*, 5(8):900–903, 2016.

[108] J. S. Marshall and S. Li. *Adhesive particle flow. A discrete-element approach.* Camebridge University Press, New York (US), 2014.

[109] matlab release R2019a. lsqnonlin. The MathWorks, Inc., Natick, Massachusetts, United States. [online] Available on: //nl.mathworks.com/help/optim/ug/lsqnonlin.html.

[110] D. Megias-Alguacil. Surface rotation of liquid droplets under a simple shear flow: Experimental observations in 3d. *Soft Materials*, 11(1):1–5, 2010.

[111] S. Mehrabian, M. Bussmann, and E. Acosta. Breakup of high solid volume fraction oil–particle cluster in simple shear flow. *Colloids and Surfaces A: Physicochemical and Engineering Aspects*, 483:25–35, 2015.

[112] Y. Mei, G. Li, P. Moldenaers, and R. Cardinaels. Dynamics of particle-covered droplets in shear flow: unusual breakup and deformation hysteresis. *Soft Matter*, 12(47):9407–9412, 2016.

[113] T. Merkel, J. Henne, L. Hecht, V. Gräf, E. Walz, and H. P. Schuchmann. Emulsification of particle loaded drops in simple shear flow. *Colloids and Surfaces A: Physicochemical and Engineering Aspects*, 470:179–187, 2015.

[114] J. Mewis and N. J. Wagner. *Colloidal Suspension Rheology.* Cambridge University Press, New York, 2011.

[115] K. B. Migler. Droplet vorticity alignment in model polymer blends. *Journal of Rheology*, 44(2):277–290, 2000.

[116] M. Minale, P. Moldenaers, and J. Mewis. Effect of shear history on the morphology of immiscible polymer blends. *Macromolecules*, 30:5470–5475, 1997.

[117] C. Mitrias. *Modelling interfaces in fluids with applications to foams and blends.* Thesis, 2018. PhD Thesis TU Eindhoven.

[118] I. Moutinho, M. Figueiredo, and P. Ferreira. Evaluating the surface energy of laboratory-made paper sheets by contact angle measurements. *Tappi Journal*, 6(6):26–32, 2007.

[119] M. K. Mulligan and J. P. Rothstein. Deformation and breakup of micro- and nanoparticle stabilized droplets in microfluidic extensional flows. *Langmuir*, 27(16):9760–9768, 2011.

[120] S. Nagarkar and S. Velankar. Rheology and morphology of model immiscible polymer blends with monodisperse spherical particles at the interface. *Journal of Rheology*, 57(3):901–926, 2013.

[121] S. P. Nagarkar and S. S. Velankar. Morphology and rheology of ternary fluid–fluid–solid systems. *Soft Matter*, 8(32):8464, 2012.

[122] A. Nuzzo, E. Bilotti, T. Peijs, D. Acierno, and G. Filippone. Nanoparticle-induced co-continuity in immiscible polymer blends – a comparative study on bio-based pla-pa11 blends filled with organoclay, sepiolite, and carbon nanotubes. *Polymer*, 55(19):4908–4919, 2014.

[123] octave forge community. Function reference: lsqnonlin. GNU Octave Forge, [Online] Available on: https://octave.sourceforge.io/optim/function/lsqnonlin.html.

[124] octave forge community. Function reference: ode45. GNU Octave Forge, [Online] Available on: https://octave.sourceforge.io/octave/function/ode45.html.

[125] D. K. Owens and R. C. Wendt. Estimation of the surface free energy of polymers. *Journal of applied polymer science*, 13(8):1741–1747, 1969.

[126] Paraview. paraview.simple.streamtracer. Kitware, Inc., New York, United States. [online] Available on: https://kitware.github.io/paraview-docs/latest/python/paraview.simple.StreamTracer.html.

[127] P. Peyla and C. Verdier. New confinement effects on the viscosity of suspensions. *EPL (Europhysics Letters)*, 94(4):44001, 2011.

[128] R. J. Phillips, R. C. Armstrong, R. A. Brown, A. L. Graham, and J. R. Abbott. A constitutive equation for concentrated suspensions that accounts for shear-induced particle migration. *Physics of Fluids A: Fluid Dynamics*, 4(1):30–40, 1992.

[129] W. J. Phillips, G. R. W., and F. R. W. Experimental studies of drop dynamics in shear fields: Role of dynamic interfacial effects. *Journal of Colloid and Interface Science*, 76(2):350–370, 1980.

[130] S. U. Pickering. Sxcvi.-emimsions. *Journal of the Chemical Society, Transactions*, 91:2001–2021, 1907.

[131] J. Plattier, L. Benyahia, M. Dorget, F. Niepceron, and J. Tassin. Viscosity-induced filler localisation in immiscible polymer blends. *Polymer*, 59:260–269, 2015.

[132] R. L. Powell and S. G. Mason. Dispersion by laminar flow. *AlChE Journal*, 28(2):286–293, 1982.

[133] J. M. Rallison. Note on the time-dependent deformation of a viscous drop which is almost spherical. *Journal of Fluid Mechanics*, 98(3):625–633, 1980.

[134] J. M. Rallison. The deformation of small viscous drops and bubbles in shear flow. *Annual Review of Fluid Mechanics*, 16:45–66, 1984.

[135] J. M. Rallison and A. Acrivos. A numerical study of the deformation and burst of a viscous drop in an extensional flow. *Journal of Fluid Mechanics*, 89(1):191–200, 1978.

[136] S. S. Ray, S. Pouliot, M. Bousmine, and L. Utracki. Role of organically modified layered silicate as an active interfacial modifier in immiscible polystyrene/polypropylene blends. *Polymer*, 45(25):8403–8413, 2004.

[137] Y. Renardy. The effects of confinement and inertia on the production of droplets. *Rheologica Acta*, 46(4):521–529, 2006.

[138] S. Reynaert, P. Moldenaers, and J. Vermant. Interfacial rheology of stable and weakly aggregated two-dimensional suspensions. *Physical Chemisty Chemical Physics*, 9:6463–6475, 2007.

[139] M. Rhodes and N. J. Wagner. *Introduction to Particle Technology.* John Wiley and Sons, Ltd, England, 2008.

[140] L. M. Robeson. *Polymer blends: a comprehensive review.* Munich: Hanser, 2007.

[141] F. D. Rumscheidt and S. G. Mason. Particle motions in sheared suspensions. xii. deformation and burst of fluid drops in shear and hyperbolic flow. *Journal of colloid Science*, 16(3):238–261, 1961.

[142] L. Salvia-Trujillo, M. Artiga-Artigas, A. Molet-Rodrigues, A. Turmo-Ibarz, and O. Martin-Belloso. mulsion-based nanostructures for the delivery of active ingredients in foods. *Frontiers Sustainable Food Systems*, 2(79):1–7, 2018.

[143] M. Salzano de Luna and G. Filippone. Effects of nanoparticles on the morphology of immiscible polymer blends. *European Polymer Journal*, 79:198–218, 2016.

[144] M. Salzano de Luna and G. Filippone. Effects of nanoparticles on the morphology of immiscible polymer blends – challenges and opportunities. *European Polymer Journal*, 79:198–218, 2016.

[145] L. L. Schramm. *Emulsions, foams, and suspensions: fundamentals and applications*. John Wiley and Sons, 2006.

[146] R. Scirocco, J. Vermant, and J. Mewis. Effect of the viscoelasticity of the suspending fluid on structure formation in suspensions. *Journal of non-Newtonian Fluid Mechanics*, 117(2-3):183–192, 2004.

[147] G. Segré and A. Silberberg. Radial particle displacements in poiseuille flow of suspensions. *Nature*, 189:209–210, 1961.

[148] G. Segré and A. Silberberg. Behaviour of macroscopic rigid spheres in poiseuille flow part 2. experimental results and interpretation. *Journal of Fluid Mechanics*, 14(1):136–157, 1962.

[149] P. Siahcheshm, F. Goharpey, and R. Foudazi. Droplet retraction in the presence of nanoparticles with different surface modifications. *Rheologica Acta*, 57(11):729–743, 2018.

[150] I. R. Siqueira, R. B. Reboucas, and M. S. Carvalho. Particle migration and alignment in slot coating flows of elongated particle suspensions. *Americal Institute of Chemical Engineers*, 63(7):3187 – 3198, 2017.

[151] P. G. Smith and T. G. M. Van de Ven. Interactions between drops and particles in simple shear. *Colloids and Surfaces*, 15:211 – 231, 1985.

[152] P. G. Smith and T. G. M. van de Ven. Shear-induced deformation and rupture of suspended solid/liquid clusters. *Colloids and Surfaces*, 15:191–210, 1985.

[153] F. Snijkers. *Effects of viscoelasticity on particle motions in sheared suspensions*. Thesis, 2009. PhD Thesis KU Leuven.

[154] G. Soligo, A. Roccon, and A. Soldati. Deformation of clean and surfactant-laden droplets in shear flow. *Meccanica*, 9:1–16, 2019.

[155] E. J. Stancik, G. T. Gavranovic, M. J. O. Widenbrant, A. T. Laschitsch, J. Vermant, and G. G. Fuller. Structure and dynamics of particle monolayers at a liquid–liquid interface subjected to shear flow. *Polymer*, 48(15):4520–4528, 2007.

[156] S. Steinmann, W. Gronski, and C. Friedrich. Influence of selective filling on rheological properties and phase inversion of two-phase polymer blends. *Faraday Discuss.*, 123:145–156, 2003.

[157] H. A. Stone, A. Nadim, and S. H. Strogatz. Chaotic streamlines inside droplet immersed in steady stokes flows. *Journal of Fluid Mechanics*, 232:629–646, 1990.

[158] Z. B. Stone and H. A. Stone. Imaging and quantifying mixing in a model droplet micromixer. *Physics of fluids*, 17(063103), 2005.

[159] A. B. Subramaniam, M. Abkarian, and H. A. Stone. Controlled assembly of jammed colloidal shells on fluid droplets. *Nature Materials*, 4(7):553–556, 2005.

[160] A. B. Subramaniam, M. Abkarina, L. Mahadevan, and H. A. Stone. Non-spherical bubbles. *Nature*, 438:930, 2005.

[161] A. Taguet, P. Cassagnau, and J. M. Lopez-Cuesta. Structuration, selective dispersion and compatibilizing effect of (nano)fillers in polymer blends. *Progress in Polymer Science*, 39(8):1526–1563, 2014.

[162] G. I. Taylor. The viscosity of a fluid containing small drops of another fluid. *Proceedings of the Royal Society A: Mathematical, Physical and Engineering Sciences*, 138(834):41–48, 1932.

[163] G. I. Taylor. The formation of emulsions in definable fields of flow. *Proceedings of the Royal Society A: Mathematical, Physical and Engineering Sciences*, 146(858):501–523, 1934.

[164] S. Tcholakova, N. D. Denkov, and A. Lips. Comparison of solid particles, globular proteins and surfactants as emulsifiers. *Physical Chemistry Chemical Physics*, 10:1608–1627, 2008.

[165] P. Thareja, K. Moritz, and S. S. Velankar. Interfacially active particles in droplet/matrix blends of model immiscible homopolymers: Particles can increase or decrease drop size. *Rheologica Acta*, 49(3):285–298, 2010.

[166] K. M. C. Tjorve and E. Tjrove. The use of gompertz models in growth analyses, and new gompertz-model approach: An addition to the unified-richards family. *PLoS ONE*, 12(6), 2017.

[167] W. Tong, Y. Huang, C. Liu, X. Chen, Q. Yang, and G. Li. The morphology of immiscible pdms/pib blends filled with silica nanoparticles under shear flow. *Colloid and Polymer Science*, 288(7):753–760, 2010.

[168] S. Torza, R. G. Cox, and S. G. Mason. Particle motions in sheared suspensions xxvii. transient and steady deformation and burst of liquid drops. *Journal of Colloid and Interface Science*, 38(2):395–411, 1972.

[169] S. Torza, C. P. Henry, R. G. Cox, and S. G. Mason. Particle motions in sheared suspensions xxvi. streamlines in and around liquid drops. *Journal of Colloid and Interface Science*, 35(4):529–543, 1971.

[170] C. L. Tucker and P. Moldenaers. Microstructural evolution in polymer blends. *Annual Review of Fluid Mechanics*, 34(1):177–210, 2002.

[171] O. B. Usta, D. Perchak, A. Clarke, J. M. Yeomans, and A. C. Balazs. Shear and extensional deformation of droplets containing polymers and nanoparticles. *The Journal of Chemical Physics*, 130(23):234905, 2009.

[172] L. A. Utracki and C. A. Wilkie. *Polymer blends handbook*, volume 1. Kluwer academic publishers Dordrecht, 2002.

[173] K. van As. kva-interfaceproperties, 2017. [online] Available on: https://github.com/floquation/OF-kva-interfaceProperties.

[174] M. S. van Deen, T. Bertrand, N. Vu, D. Quéré, E. Clément, and A. Lindner. Particles accelerate the detachment of viscous liquids. *Rheologica Acta*, 52(5):403–412, 2013.

[175] D. W. van Krevelen and K. te Nijenhuis. *Properties of Polymers*. Elsevier B.V., 2009.

[176] S. Van Loon, J. Fransaer, C. Clasen, and J. Vermant. String formation in sheared suspensions in rheologically complex media: The essential role of shear thinning. *Journal of Rheology*, 58(1):237–254, 2014.

[177] A. Vananroye. *Structure development in polymer blends during flow in confinements*. Thesis, 2007. PhD Thesis KU Leuven.

[178] A. Vananroye, R. Cardinaels, P. Van Puyvelde, and P. Moldenaers. Effect of confinement and viscosity ratio on the dynamics of single droplets during transient shear flow. *Journal of Rheology*, 52(6):1459–1475, 2008.

[179] A. Vananroye, P. Van Puyvelde, and P. Moldenaers. Effect of confinement on droplet breakup in sheared emulsions. *Langmuir*, 22(9):3972–3974, 2006.

[180] A. Vananroye, P. Van Puyvelde, and P. Moldenaers. Effect of confinement on the steady-state behavior of single droplets during shear flow. *Journal of Rheology*, 51(1):139–153, 2007.

[181] S. Vandebril. *Control of morphology and properties of immiscible polymer blends by addition of nanoparticles*. Thesis, 2010. PhD Thesis KU Leuven.

[182] S. Vandebril, A. Franck, G. G. Fuller, P. Moldenaers, and J. Vermant. A double wall-ring geometry for interfacial shear rheometry. *Rheologica Acta*, 49(2):131–144, 2009.

[183] S. Vandebril, J. Vermant, and P. Moldenaers. Efficiently suppressing coalescence in polymer blends using nanoparticles: role of interfacial rheology. *Soft Matter*, 6(14):3353–3362, 2010.

[184] S. Velankar and P. Moldenaers. Bidisperse polymeric mixtures for independent control of viscosity and elasticity. *Rheologica Acta*, 41:418–426, 2002.

[185] K. Verhulst, R. Cardinaels, P. Moldenaers, S. Afkhami, and M. Renardy. Influence of viscoelasticity on drop deformation and orientation in shear flow. part 2: Dynamics. *Journal of Non-Newtonian Fluid Mechanics*, 156(1-2):44–57, 2009.

[186] K. Verhulst, P. Moldenaers, and M. Minale. Drop shape dynamics of a newtonian drop in a non-newtonian matrix during transient and steady shear flow. *Journal of Rheology*, 51(2), 2007.

[187] J. Vermant, G. Cioccolo, K. Golapan Nair, and P. Moldenaers. Coalescence suppression in model immiscible polymer blends by nano-sized colloidal particles. *Rheologica Acta*, 43:529–538, 2004.

[188] J. S. Vrentas, D. Venerus, and C. M. Vrentas. An exact analysis of reservoir effects for rotational viscosimeters. *Chemical Engineering Science*, 46:33–37, 1991.

[189] M. U. Wahit, A. Hassan, A. R. Rahmat, J. W. Lim, and Z. A. Mohd Ishak. Effect of organoclay and ethylene-octene copolymer inclusion on the morphology and mechanical properties of polyamide/polypropylene blends. *Journal of Reinforced Plastics and Composites*, 25(9):933–955, 2006.

[190] L. Wang, C. Shi, Z. Guo, and J. Yu. Tailoring the morphology of polypropylene/polyamide 66 blend at an asymmetric composition by using organoclay and maleic anhydride grafted polypropylene. *Journal of Industrial and Engineering Chemistry*, 20(1):259–267, 2014.

[191] H. Weller. Openfoam-5.x, 2017. The OpenFOAM Foundation Ltd, England, [Online] Available on: https://openfoam.org/.

[192] A. Williams, J. J. M. Janssen, and A. Prins. Behaviour of droplets in simple shear flow in the presence of a protein emulsifier. *Colloids and Surfaces*, 1997:189–200, 1996.

[193] W. Wixwat, Y. Fu, and J. R. Stevens. Index of refraction, density and viscosity measurements of poly(propylene glycol)-salt complexes. *Polymer*, 32(7):1181–1185, 1991.

[194] S. Wu. *Polymer interface and adhesion*. Marcel Dekker, Inc., New York, 1982.

[195] H. Xi and C. Duncan. Lattice boltzmann simulations of three-dimensional single droplet deformation and breakup under simple shear flow. *Physical Review E*, 59(3):3022–3026, 1999.

[196] H. Yang, X. Zhang, C. Qu, B. Li, L. Zhang, Q. Zhang, and Q. Fu. Largely improved toughness of pp/epdm blends by adding nano-sio2 particles. *Polymer*, 48(3):860–869, 2007.

[197] S. Yoshida and M. Trifkovic. Unraveling the effect of 3d particle localization on coarsening dynamics and rheological properties in cocontinuous polymer blend nanocomposites. *Macromolecules*, 52(20):7678–7687, 2019.

[198] Q. Zhang, H. Yang, and Q. Fu. Kinetics-controlled compatibilization of immiscible polypropylene-polystyrene blends using nano-sio2 particles. *Polymer*, 45(6):1913–1922, 2004.

[199] X. Zhao. Drop breakup in dilute newtonian emulsions in simple shear flow: New drop breakup mechanisms. *Journal of Rheology*, 51(367):367–392, 2007.

[200] L. Zhu and F. Gallaire. Bifurcation dynamics of a particle-encapsulating droplet in shear flow. *Physical Review Letters*, 119(6):064502, 2017.

[201] H. Zou, K. Wang, Q. Zhang, and Q. Fu. A change of phase morphology in poly(p-phenylene sulfide)/polyamide 66 blends induced by adding multi-walled carbon nanotubes. *Polymer*, 47(22):7821–7826, 2006.

[202] Z. Zou, Z. Sun, and L. An. Effect of fumed silica nanoparticles on the morphology and rheology of immiscible polymer blends. *Rheologica Acta*, 53(1):43–53, 2013.

Curriculum

Helene Van Ammel
°19 February 1992, Edegem (Belgium)

Education

2015 - 2021	PhD in Engineering Science, KU Leuven
	Chemical Engineering,
2013 - 2015	Master in Engineering Science, KU Leuven
	Chemical Engineering
2010 - 2013	Bachelor in Engineering Science, KU Leuven
	Chemical Engineering - Mechanical Engineering
2004 - 2010	High School, Sint-Jozefinstituut Essen
	Science-Mathematics

Experience

2020 - ...	Process Engineer, Total Polymers Antwerp
2015 - 2020	PhD researcher, KU Leuven
	The effects of particles on the dynamics of sheared droplets
2015 - 2020	Teaching assistant, KU Leuven
	Guiding Master's theses, coaching problem solving and design projects, Lab session 16th European School on Rheology
2015	Master thesis, KU Leuven
	The impact of glucose oxidase on the rheology of bread dough
2014	Summer internship, BASF Antwerp
	GC analysis on emission measurements

List of publications

Articles in peer-reviewed international journals

- **H. Van Ammel***, J. Ferreira*, A. Kruitwagen, S. Fransen, P. Moldenaers, S. Kuhn, and R. Cardinaels. Migration of non-Brownian particles localized inside shear droplets. In preparation.
  * Equal contributions
- **H. Van Ammel**, P. Moldenaers, and R. Cardinaels. Dynamics of sheared droplets filled with non-Brownian particles. *Rheologica Acta*, 59:935-949, 2020.
- Y. Mei, **H. Van Ammel**, P. Moldenars, and R. Cardinaels. Deformation and breakup of single nanoparticle-armoured droplets in shear flow. In preparation.
- M. Meerts, **H. Van Ammel**, Y. Meeus, S. Van Engeland, R. Cardinaels, F. Oosterlinck, C. M. Courtin, and P. Moldenaers. Enhancing the rheological performance of wheat flour dough with glucose oxidase, transglutaminase or supplementary gluten. *Food and Bioprocess Technology*, 10:2188-2198, 2017.

Contributions in international conferences

- **H. Van Ammel**, R. Cardinaels, and P. Moldenaers. Effects of non-Brownian particles localized in the droplet phase: Droplet dynamics and particle distribution. *33rd Conference of the European Colloid and Interface Society (ECIS)*. Leuven, Belgium. September 2019.
- Y. Mei, **H. Van Ammel**, P. Moldenaers, and R. Cardinaels. Effects of nanoparticles localized at the interface on single droplet dynamics in

shear flow. *33rd Conference of the European Colloid and Interface Society (ECIS)*. Leuven, Belgium. September 2019.

- **H. Van Ammel**, Y. Mei, R. Cardinaels, and P. Moldenaers. Effect of nanoparticles at the droplet interface on the dynamics of a droplet subjected to shear flow. *Joint Symposium of the Belgian Group of Rheology BGR and German Rheological Society DGR*. Luxembourg, Luxembourg. March 2018.

- **H. Van Ammel**, Y. Mei, R. Cardinaels, and P. Moldenaers. Effects of nanoparticles localized at the interface on single droplet dynamics in shear flow. *Annual European Rheology Conference*. Copenhagen, Denmark. April 2017.

- **H. Van Ammel**, Y. Mei, R. Cardinaels, and P. Moldenaers. Structure development in polymer blends containing nanoparticles localized at the interface. *51ième congrès annual du groupe Français de Rhéologie*. Lille, France. October 2016.



FACULTY OF ENGINEERING SCIENCE
DEPARTMENT OF CHEMICAL ENGINEERING
SOFT MATTER, RHEOLOGY AND TECHNOLOGY
Celestijnenlaan 200J box 2424
B-3001 Leuven
http://www.cit.kuleuven.be/smart